A MID-INFRARED STUDY OF BLUE COMPACT DWARF GALAXIES

A Dissertation

Presented to the Faculty of the Graduate School

of Cornell University

in Partial Fulfillment of the Requirements for the Degree of

Doctor of Philosophy

by

Yanling Wu

January 2009

A MID-INFRARED STUDY OF BLUE COMPACT DWARF GALAXIES

Yanling Wu, Ph.D.

Cornell University 2009

Blue Compact Dwarf Galaxies (BCDs) are characterized by their blue optical colors, low luminosities and small sizes. Typically BCDs are found to have low, subsolar metallicities, and they are proposed to be local analogs to the primeval galaxies in the early universe. The unprecedented sensitivity of the *Spitzer* Space Telescope has enabled, for the first time, the detection of a large sample of these low luminosity systems. In this dissertation, I will present my work employing *Spitzer* data to study the dust properties and chemical evolution of blue compact dwarf galaxies.

Using *Spitzer/IRS* low-resolution spectra ($\lambda/\delta\lambda \sim 100$), I investigated the presence/absence of the Polycyclic Aromatic Hydrocarbon (PAH) features in low-metallicity galaxies. After exploring different physical parameters, I find that the strength of PAH emission is best correlated with a combination of formation and destruction effects. In addition, using the high-resolution spectroscopy ($\lambda/\delta\lambda \sim 600$), I study the elemental abundances of neon and sulfur in BCDs and compare with the optical studies. I find that the infrared derived elemental abundances generally agree with the optical results, though the neon abundances are slightly higher from our study. I also analyze the FIR/radio correlation in BCDs and expand the discussion to the mid-IR. I find that the infrared luminosities are well correlated with the radio luminosities even in these low luminosity systems. A study on the spectral energy distribution (SED) and star formation rates (SFRs) in low-luminosity star-forming galaxies is also included in this thesis. The SEDs

appear to be warmer than normal star-forming galaxies, and their SFRs vary over an order of magnitude. Finally, I also present a case study on the famous BCD IZw18, showing the first mid-infrared spectrum for this galaxy.

BIOGRAPHICAL SKETCH

Yanling Wu was born on the 25th of June, 1980 to Qingmin Wu and Wenqin Li in the beautiful city of Suzhou, Jiangsu province, P.R China. There she spent the first 18 years of her life before she moved to Beijing for college.

Yanling spent four years in Tiankuqian primary school, and then transferred to Dongzhongshi primary school, where she started to learn English. This turned out to be a wise decision because starting from that year, Suzhou Middle School reopened its junior high school section, and without knowing any English, Yanling would not be able to pass their entrance exams. There were four rounds of exams and Yanling ranked first in each of the rounds.

The years in Suzhou Middle School were unforgettable for Yanling. She became a member of the international class, where she met many talented fellow students. Yanling was very thankful for this healthy environment of competition. She became interested in physics with the help of her physics teacher, Yiran Wang, which finally led her to decide to study astronomy in college. She was also very grateful to her English teacher, Yi Guan, without whom Yanling's English would be inadequate to survive in the US.

After spending six years in Suzhou Middle School, Yanling joined the astronomy department of Peking University as an undergraduate student, where she received her Bachelor's Degree in physics in 2003. She did her undergraduate thesis under the supervision of Professor Zuhui Fan on the Sunyaev Zel'dovich effect, and that work was published in the Astrophysical Journal the same year.

Yanling decided to go to graduate school in the United States. Because of its prestigious infrared program, Yanling finally picked Cornell as the place to spend the next five years, without knowing how much lovely snow she would enjoy while in Ithaca. The *Spitzer* Space Telescope was successfully launched in the same week

as Yanling arrived at Cornell and she became a member of the Spitzer/IRS team half a year later, working with Professor Jim Houck. There she spent the last fours of her graduate program. Her work on the mid-infrared properties of blue compact dwarf galaxies using Spitzer observations culminated in this dissertation.

To my parents Qingming Wu and Wenqin Li.

ACKNOWLEDGEMENTS

Even though the winters in Ithaca are long, the last five years still passed quickly. Now I have a dissertation in my hand and I cannot wait to thank all the wonderful people who have helped me through my Ph.D.

I would like to thank my advisor, Jim Houck, without whom I would not have the great opportunity to explore the beauty of infrared astronomy. Jim, thank you for introducing me to those little galaxies that ended up as the objects I study for my dissertation. I am very thankful to the GTO time you gave me for my Ph.D study, as well as the valuable advice on my research. My road to becoming an infrared astronomer would not be possible without Jim's help.

My five years as a Ph.D candidate would have much less fun if I haven't met my co-advisor, Vassilis Charmandaris. Vassilis, thank you so much for being my advisor, and more importantly, as a life-long friend. I started with little understanding of astronomy and now I am finishing up my dissertation. This would not happen without your help. I still remember that in the beginning I did not dare to ask questions because I worried about my ignorance showing and it was your patience and kindness that helped me to open my mouth and talk about science. I like your style of being a very hands-on advisor. You always gave me suggestions when I was at a lost, and you have encouraged me to keep going when I need it. It is very fortunate for me to have you as my co-advisor during my last five years and I hope that our collaboration will go on forever. This is a statement based solely on your science merit, not on your charm, though it is a solid fact that you are the most handsome man in the astronomy department.

I mus thank Jeronimo Bernard-Salas, from whom I learned how to derive the elemental abundances using the infrared data. Jero not only explained the method to me very patiently, but also generously shared his code, and most importantly,

taught me how to think critically when dealing with science questions. I also have to tell you that you are astonishingly handsome which makes working with you a very pleasant experience.

There are so many people on the IRS team that I have benefited from (in alphabetical order): Don Barry, Jeronimo Bernard-Salas, Bernhard Brandl, Vassilis Charmandaris, Daniel Devost, Duncan Farrah, Elise Furlan, Shannon Gutenkunst, Peter Hall, Lei Hao, Terry Herter, James Higdon, Sarah Higdon, Jim Houck, David Levitan, Jason Marshall, Laurie McCall, Greg Sloan, Henrik Spoon, Kevin Uchida, Dan Weedman and David Whelan. I would like to thank all of you. The IRS group is a like a big family and I feel your warmness. I suspect this might be the primary reason that help me to survive in Ithaca, where the temperature could drop to -30F sometime every winter.

I would like to give my special thanks to Shannon, who shared an office with me the past three years. Shannon, thank you very much for putting up with me, always answering my questions quickly and caring about me when I am in blue. I would also have to mention my former officemate Sabrina Stierwalt, with whom I spent the first year in gradschool, and in the US. Sabrina, thank you so much for making me very comfortable even though this is the first time I have ever been to a foreign country. Please also take my thanks to your family, with whom I spent two Thanksgivings. Many thanks to Patrick, Ryan and Suniti, who shared an office with me in my second year. Patrick, you still owe me the story of how you started to call me a duck when were were in Room 110.

I am very gratetful to the American Astronomical Society, which provided me travel grants to cover the expense of attending two conferences in China. I would like to thank Yu Gao for organizing these meetings, which gave me the opportunity to explore the development of astronomy in China, as well as meeting

many scientists.

I met Rob Kennicutt at a conference in Lijiang, China, in the summer of 2005. Rob, thank you so much for making friends with a not-know-much second-year graduate student. That encouraged me and I have learned so much from you, sharing thoughts on many things, not only research, but also life. I would also like to thank Rob for bringing me into the Local Volume Legacy Survey (LVLS) team. Thanks to all the people on LVLS. Even though we have just started, I have to say that it is my great pleasure to be working with the team.

I would also like to give my thanks to Jiasheng Huang, my great mentor and friend in astronomy, as well as gastronomy. Jiasheng, thank you so much for the tremendous amount of support you gave me in the darkest part of my life. I am so glad that I have you as a friend during that period. Because of you, I now can interpret the old saying "A friend in need is a friend indeed". As your first student in gastronomy, I hope my performance will not dissapoint you.

I must also thank George Helou, who has accpeted me as a postdoctoral fellow in the sunny California. I am sure that I will make more improvements under your supervision and I hope my joining your team can yield very fruitful results.

There are so many people that have helped me on my road of science. I would like to thank all the co-authors of my papers for making the collaboration a pleasant experience, as well as those that had insightful discussion with me, no matter their names ended up in the papers or not.

Many thanks to my committee, Jim Houck, Martha Haynes, Eanna Flanagan and Jean-Luc Margot for mentoring me through my Ph.D, and for spending their precious time to read this dissertation.

Last but not the least important, I would also like to thank my family and friends in China. My father and mother, though not knowing much about physics,

supported my college education, as well as my decision to go to graduate school in the US. I would also like to thank my best friend, Jiazhi Wu and Xiao Zhu. Xiao, we have shared many ups and downs together and I believe that our values will be well recognized one day. Jiazhi, thank you so much for listening to me patiently and making me happy. I also have to thank you for the dinners we had together and I hope that you will continue taking me to dinners whenever we have a chance to meet. My thanks also go to my Chinese friends in the US, in particular Min Long, Yanjun Xia, Lulin Shen and Hui Zhang, all of whom supported me during the past five years.

The IRS was a collaborative venture between Cornell University and Ball Aerospace Corporation funded by NASA through the Jet Propulsion Laboratory and the Ames Research Center. Support for this work was provided by NASA through Contract Number 1257184 issued by JPL/Caltech.

TABLE OF CONTENTS

Biographical Sketch . . . iii
Dedication . . . v
Acknowledgements . . . vi
Table of Contents . . . x
List of Tables . . . xiii
List of Figures . . . xiv

1 Introduction **1**
1.1 The Definition of BCD . . . 3
1.2 The Physics of BCDs . . . 4
1.2.1 The Morphology of BCDs . . . 5
1.2.2 The Star Formation in BCDs . . . 5
1.2.3 The Chemical Abundances in BCDs . . . 6
1.3 Studying the BCDs in the Infrared . . . 8
1.3.1 PAH emission in BCDs . . . 9
1.3.2 The infrared spectral energy distribution . . . 10
1.3.3 Case Study: SBS0335-052E . . . 10
1.4 In this thesis . . . 12

2 Mid Infrared Properties of Low Metallicity Blue Compact Dwarf Galaxies from *Spitzer/IRS* **17**
2.1 Introduction . . . 17
2.2 Observations and Data Reduction . . . 20
2.3 Results . . . 24
2.3.1 Mid infrared Morphology . . . 27
2.3.2 Individual Objects . . . 29
2.4 Analysis . . . 36
2.4.1 The mid-infrared spectral slope of BCDs . . . 36
2.4.2 PAH and metallicity . . . 43
2.4.3 The hardness of the radiation field . . . 46
2.4.4 PAH and the [NeIII]/[NeII] ratio . . . 48
2.4.5 PAH and luminosity density . . . 49
2.4.6 PAHs: formation and destruction effects . . . 54
2.5 Conclusions . . . 56

3 Elemental Abundances of Blue Compact Dwarfs from mid-IR Spectroscopy with *Spitzer** **65**
3.1 Introduction . . . 65
3.2 Observations and Data Reduction . . . 68
3.3 Elemental Abundances of BCDs . . . 71

*Originally published as: Yanling Wu, J. Bernard-Salas, V. Charmandaris, V. Lebouteiller, Lei Hao, B. R. Brandl, J. R. Houck, (2008), *The Astrophysical Journal*, 673, 193

3.3.1 Electron density and temperature . . . 71
3.3.2 Ionized hydrogen flux estimates . . . 72
3.3.3 Extinction correction . . . 74
3.3.4 Neon and sulfur abundances determination . . . 75
3.3.5 Individual Objects . . . 80
3.4 Discussion . . . 83
3.4.1 Solar abundances . . . 84
3.4.2 Neon and sulfur abundances . . . 84
3.4.3 Comparison with optically derived abundances . . . 86
3.5 Metallicities and PAHs . . . 92
3.6 Conclusions . . . 94

4 Blue Compact Dwarf Galaxies with Spitzer: The Infrared/Radio Properties* 103
4.1 Introduction . . . 103
4.2 Observations . . . 106
4.3 Results . . . 111
4.3.1 Mid-IR and FIR to Radio Correlation in BCDs . . . 111
4.3.2 Metallicity and Dust Temperature Effects on q_{IR} . . . 116
4.3.3 Star Formation Rate Estimates . . . 118
4.3.4 The Two Extremes: IZw18 and SBS0335-052E . . . 121
4.4 Conclusions . . . 125

5 Dust Properties and Star Formation Rates in Star-Forming Dwarf Galaxies* 132
5.1 Introduction . . . 132
5.2 Data . . . 135
5.2.1 Sample selection and optical data . . . 135
5.2.2 Spitzer multiband imaging photometer data . . . 139
5.2.3 Spitzer 16 μm imaging . . . 140
5.2.4 *Spitzer* Infrared Array Camera Data . . . 141
5.2.5 Galaxy evolution explorer data . . . 141
5.3 Dust diagnostics . . . 142
5.3.1 Do star-forming dwarf galaxies have PAHs? . . . 142
5.3.2 How do dust properties relate to metallicity? . . . 152
5.4 Star formation rate indicators . . . 154
5.4.1 Description of star-formation rate indicators . . . 157
5.4.2 Comparison of star-formation rates . . . 163
5.5 Summary . . . 169

*Originally published as: Yanling Wu, V.Charmandaris, J.R.Houck, B. Bernard-Salas, V. Lebouteiller, B. R.Brandl, D. Farrah (2008), *The Astrophysical Journal*, 676, 970

*Originally published as: J. L.Rosenberg, Yanling Wu, E.Le Ffloc'h, V. Charmandaris, M. L.N.Ashby, J. R.Houck, J. J.Salzer, S. P.Willner (2008), *The Astrophysical Journal*, 674, 814

6 Dust in the Extremely Metal-Poor Blue Compact Dwarf Galaxy I Zw 18: the *Spitzer* Mid-infrared View* **182**
6.1 Introduction . . . 182
6.2 Observations . . . 185
6.2.1 Spitzer/IRS Spectroscopy . . . 185
6.2.2 Spitzer Imaging with IRAC and MIPS . . . 187
6.3 Results . . . 187
6.3.1 Mid-IR Morphology . . . 187
6.3.2 Mid-IR Spectral Features . . . 191
6.3.3 Neon and Sulfur Abundances . . . 195
6.3.4 Comparison with SBS 0335-052E and NGC7714 . . . 197
6.4 Star Formation Rate in I Zw 18 . . . 199
6.5 Conclusions . . . 201

7 Conclusions and Future Work **208**

*Originally published as: Yanling Wu, V.Charmandaris, L.K. Hunt, J. Bernard-Salas, B. R.Brandl, J. A.Marshall, V. Lebouteiller, Lei Hao, J. R.Houck (2007), *The Astrophysical Journal*, 662, 952

LIST OF TABLES

2.1 Properties of Sources 21
2.1 Properties of Sources 22
2.2 Integrated photometry of Sources 38
2.2 Integrated photometry of Sources 39
2.3 Synthetic flux density of the sources 40
2.4 Spectroscopic Data of the Sources 45
2.5 Galaxy luminosity and volume 53

3.1 Observing Parameters of the Sample 70
3.2 Optical Properties of the Sources 73
3.3 Fine-structure Line Fluxes and Ionic Abundances 77
3.4 Elemental Abundances 79
3.5 PAH measurements of the sample 95

4.1 Properties of the Sample 109
4.1 Properties of the Sample 110
4.2 Derived Quantities of the Sample 115
4.3 Comparison of SBS 0335-052E and I Zw 18 122

5.1 Properties of KISS Galaxies 137
5.2 Infrared and Ultraviolet Fluxes of KISS Galaxies 138
5.3 Properties Influenced by PAH Emission in KISS Galaxies 151
5.4 Infrared, Optical, and UV SFRs of KISS Galaxies 161
5.4 Infrared, Optical, and UV SFRs of KISS Galaxies 162

6.1 Spizer Observations of I Zw 18 186
6.2 Fluxes and ionic abundances[a] 194
6.3 Star Formation Rate Estimates of I Zw 18 199

LIST OF FIGURES

1.1 HST/ACS image of IZw18 2
1.2 MMT spectra of IZw18 7
1.3 *Spitzer/IRS* spectrum of SBS0335-052 11

2.1 Spitzer/IRS spectra of six BCDs 25
2.2 Spitzer/IRS spectra of another six BCDs 26
2.3 Mid-IR fine structure lines of 12 BCDs from Spitzer/IRS high-resolution spectra. 28
2.4 The 22 μm peak-up images of the four BCDs that display extended emission. 30
2.5 a) The ratio of the 22 to the 16 μm flux density as a function of the metallicity of the sources. b) The ratio of22 to 8 μm flux density as a function of metallicity. 41
2.6 a) The 6.2 μm PAH EWs as a function of the 24 over 8 μm flux ratios. b) The 11.2 μm PAH EWs as a function of the 24 over 8 μm flux ratios. c) The 6.2 μm PAH EWs as a function of the 22 over 16 μm flux ratios. d) The 11.2 μm PAH EWs as a function of the 22 over 16 μm flux ratios. 42
2.7 a) The 6.2 μm PAH EW vs metallicity. b) The 11.2 μm PAH EW vs metallicity. 44
2.8 Flux ratios of SIV/SIII vs NeIII/NeII 47
2.9 The flux ratio of NeIII/NeII as a function of metallicity 48
2.10 The flux ratio of SIV/SIII as a function of metallicity 49
2.11 a) The 6.2 μm PAH EW vs flux ratio of NeIII/NeII. b) The 11.2 μm PAH EW vs flux ratio of NeIII/NeII 50
2.12 a) The 6.2 μm PAH EW vs the luminosity density ($L_{22\mu m}$/V). b) The 11.22 μm PAH EW vs $L_{22\mu m}$/V 52
2.13 a) The 6.2 μm PAH EWs a function of the product of the hardness and intensity of the radiation field. b) The 11.2 μm PAH EWs a function of the product of the hardness and intensity of the radiation field) 54
2.14 a) The 6.2 μm PAH EWs as a function of the product of the hardness and intensity of the radiation field divided by its metallicity. b) The 11.2 μm PAH EWs as a function of the product of the hardness and intensity of the radiation field divided by its metallicity. 55

3.1 Ne^{++}/Ne^{+} vs S^{3+}/S^{++} 78
3.2 The abundance of Ne/H vs S/H 85
3.3 The abundance ratio of Ne/S as a function of Ne/H 87
3.4 a) The abundance of Ne/H vs O/H. b) The abundance of S/H vs O/H 89

3.5 a) The infrared derived Ne/H as a function of the optical Ne/H abundances. b) The infrared derived S/H as a function of the optical S/H abundances. 91
3.6 The abundance ratio of Ne/S as a function of O/H 93

4.1 The FIR luminosity vs 1.4 GHz radio luminosity 112
4.2 The q_{24} as a function of the the 24 μm monochromatic luminosity L_{24} 114
4.3 The q_{24} ratios as a function of the oxygen abundances for BCDs . . 117
4.4 The SFRs based on the 24 μm luminosities as a function of the SFRs estimated from the 1.4 GHz luminosities. 120

5.1 SEDs for the sample galaxies that show evidence for PAH emission. 147
5.2 SEDs for the sample galaxies that do not show evidence for PAH emission 148
5.3 SEDs for the sample galaxies for which a determination can not be made as to whether PAH emission is present 149
5.4 The flux ratio of the stellar subtracted 4.5 μm over 8 μm vs the flux ratio of 8 μm over 24 μm. 150
5.5 The mid-infrared color ratios of the sample 153
5.6 Galaxy metallicity as a function of the 8 to 24 μm flux density ratio 155
5.7 Galaxy metallicity as a function of the 22 or 24 to 16 μm flux ratio 156
5.8 Comparison of SFR indicators with respect to the SFR calculated from Hα with a correction for metallicity 167
5.9 Comparison of MIR SFR indicators as a function of the metallicity corrected Hα SFR 168
5.10 Comparison of SFR indicators, normalized by the Hα corrected SFR as a function of metallicity 169

6.1 IRAC 3.6, 5.8, 8 μm and MIPS 24 μm images of I Zw 18 as observed by Spitzer 189
6.2 a) Contour overlay of the IRAC 8 μm image on the HST/WFPC2 F555W image. b) The HST/WFPC2 image with the contours of MIPS 24 μm emission 190
6.3 Spitzer/IRS low-resolution spectrum of IZw18 192
6.4 Mid-IR fine structure lines in IZw18 from Spitzer/IRS. 193
6.5 A comparison of the mid-IR spectra of I Zw 18, SBS 0335-052E and NGC7714 198

CHAPTER 1

INTRODUCTION

Galaxies come in many types and they constitute the ingredients of the universe. In this cosmic pool, there is a group called blue compact dwarf (BCD) galaxies. These extragalactic objects are characterized by their blue optical colors, small sizes and low luminosities. In this dissertation, I will present my work on studying the mid-infrared properties of blue compact dwarf galaxies using data from the *Spitzer* Space Telescope (Werner et al. 2004), tackling problems of understanding physics of these objects, including their dust properties and chemical evolution, etc.

BCDs are interesting objects to study because they may be genuinely young galaxies in the process of formation based on the low metallicities (sub solar) measured from their HII regions (Izotov & Thuan 1999). Early studies hinted that BCDs could have dramatically different properties as compared to normal dwarf galaxies (Arp 1965; Zwicky 1966). If BCDs are indeed young galaxies, they could be used as local laboratory to study the star-formation and chemical evolution of the primeval galaxies in the early universe.

The first BCD recognized was I Zw 18 by Zwicky (1966), which was later found to have an extremely low metallicity (12+log(O/H)=7.17) observed in a galaxy (Searle & Sargent 1972), located at a distance of 18.2 Mpc (Aloisi et al. 2007). In Figure 1.1, we show an HST/ACS image of IZw18 (Izotov & Thuan 2004). Star-formation occurs mostly in the southeast region, which is called the "mainbody" of IZw18. About 22″ to the northwest of the "mainbody" is a more filamentary structure, called the "C component". The "mainbody" can further be divided into a bigger and brighter region in the northwest, and a smaller and fainter region in the southeast. The chemical abundance of IZw18 is only 12+log(O/H)=7.17

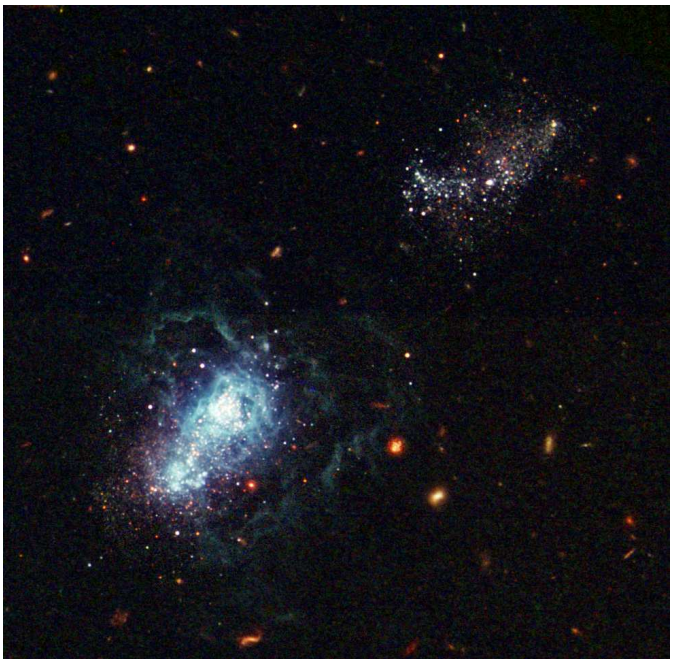

Figure 1.1 HST/ACS image of IZw18 taken by Izotov and Thuan in 2003.

(Izotov & Thuan 1999), and no other BCD has been found to have a significantly lower metallicity for several decades[1]. An infrared study on IZw18 can be found in Chapter 6 of this thesis.

In spite of the low metallicity of IZw18, a red giant brunch (RGB) has been detected from deep HST imaging of this galaxy (Aloisi et al. 2007), indicating the presence of an old stellar population. This challenges the "young age" of these objects. In fact, recent studies revealed that most BCDs are found to have an underlying population that is at least a few 10^8 yr old. Although the results of their evolutionary status remain unclear, BCDs are still very interesting objects to study. This is because despite the great success in discovering galaxy populations at high redshift, it turned out that most of these systems are already chemically polluted. BCDs, because of their low metallicities, provide an ideal laboratory to study the star-formation and galaxy evolution in a nearly pristine environment, and

[1]This record has been passed by the western component of SBS0335-052 recently, which has a metallicity of 12+log(O/H)=7.12 (Izotov et al. 2005)

thanks to their proximity, we can enjoy the advantage of having better sensitivity, precision and spatial resolution at the same time.

In this chapter, I will first review the literature for a detailed definition of BCDs, followed by a discussion on the physics of BCDs (star formation, chemical abundances, etc.), which are mostly results from optical studies. Then I will go over the infrared work on BCDs from the *Infrared Space Observatory (ISO)* (Kessler et al. 1996) and early *Spitzer* results. Finally, I will give a lay out of the thesis at the end of this chapter. Throughout this work, we assume a ΛCDM cosmology with $H_0 = 70$ km s^{-1} Mpc^{-1}, $\Omega_m = 0.3$ and $\Omega_\lambda = 0.7$.

1.1 The Definition of BCD

In the past, different studies have given different definitions on BCDs, either photometrically (Zwicky & Zwicky 1971; Thuan & Martin 1981), or spectroscopically (Gallego et al. 1996). However, these are mostly qualitative criteria that could not properly distinguish BCDs from other HII galaxies or dwarf irregular galaxies. More recently, Gil de Paz et al. (2003) have put forward a set of quantitative classifications. In this section, I discuss the definition of BCDs using information available from the literature.

Blue: According to the definition of Thuan & Martin (1981), a BCD must have a blue continuum in the optical spectrum. Since the high surface brightness component is the only component detectable in most photographic plates, Gil de Paz et al. (2003) used the peak surface brightness (PSB) and the color at this PSB to classify BCDs. They found that a limit of $\mu_{\rm B,peak} - \mu_{\rm R,peak} \leq 1$ segregates most BCDs from dwarf irregular galaxies (dIrrs) and dwarf elliptical galaxies (dEs), however, an overlap is still present and requires other criteria to identify BCDs.

Compact: Zwicky (1970) defined "compact" as any galaxy whose surface brightness is brighter than 20 mag arcsec^{-2} in any chosen wavelength range. Later on, Thuan & Martin (1981) set an upper limit of 1 kpc on the diameter. However, a very extended low surface brightness component is observed in many BCDs, thus the compactness rather refers to the size of the high surface brightness component in the galaxy. In BCDs, the presence of a current star formation event outshines the low surface brightness component while in dIrrs and dEs recent star formation (SF) is relatively less active. This results in a much brighter peak surface brightness (PSB) for BCDs. Gil de Paz et al. (2003) found that by imposing a limit of $\mu_{\rm B,peak}$ <22 mag arcsec^{-2} to the PSB, BCDs could be segregated fairly well from other types of galaxies.

Dwarf: "Dwarf" refers to the low mass of a galaxy. M_B <-18 mag imposed by Thuan & Martin (1981) was thought of as a limit on the stellar mass of BCDs, however, B band magnitude is a rather poor tracer of the stellar mass of a galaxy. Instead, K band luminosity is a much more reliable measure of stellar mass. Using evolutionary synthesis models and observational data available, Gil de Paz et al. (2003) have found an a K band luminosity limit of M_K >-21 mag for BCDs.

1.2 The Physics of BCDs

After defining the BCDs, I will give an overview on the physics of these objects in this section. Since BCDs are defined mainly based on their morphological properties, I will first discuss the morphology of BCDs.

1.2.1 The Morphology of BCDs

BCDs are small galaxies with high central surface brightness. The central morphology is usually irregular due to the presence of star formation activities. In general, the central parts of a BCD contain one or several star forming knots. The shape of the surface brightness profile is still under debate. Exponential outer profiles been found by Papaderos et al. (1996) and Telles et al. (1997), while the results from a study performed by Doublier et al. (1997) favor $r^{1/4}$ profiles. One should note that the shape of profile of a BCD probably changes with radius, thus the fitting shape will depend critically on the sensitivity limit.

1.2.2 The Star Formation in BCDs

In the family of dwarf galaxies, BCDs only account for a very small fraction. They stand out as having a much higher star formation rates (SFRs) among the dwarfs, though their SFRs are only moderate compared to normal spiral galaxies. Considering the compactness of BCDs, their SFRs normalized with the sizes can be as high as in starburst galaxies. Because of their low metallicities, BCDs offer fine laboratories to study intensive star formation in metal-poor environments.

Star formation (SF) occurs in different modes. Continuous star formation is less dramatic and occurs at a regular pace while instantaneous star formation are a number of short tense starbursts separated by extremely long intervals of time. The instantaneous mode is more often observed in BCDs (Mas-Hesse & Kunth 1999), while longer star formation episodes that successive SF takes place in individual HII regions is also possible (see the review by Kunth & Östlin 2000; Legrand et al. 2000). The low metallicity and on-going star formation in BCDs suggest that they might be very young galaxies forming their stars for the time, which will be very helpful for cosmological studies. However, an underlying population of old stars

have been detected in most BCDs, leading to the conclusion that SF occurred in short bursts separated by long quiescent periods applies to the majority of BCDs. This fluctuation in SFRs could be explained by a positive feedback of star formation in combination with the small mass of BCDs (Searle et al. 1973; Gerola et al. 1980). On the other hand, mering and interaction between galaxies is also a major driver of star formation, which will also consequently affect the chemical evolution in galaxies.

1.2.3 The Chemical Abundances in BCDs

As I mentioned earlier, BCDs are metal-poor galaxies. They chemically resemble the building blocks of larger galaxies. The metallicities of BCDs can be measured from UV, optical and infrared spectra. In chapter 3 of this thesis, I will present an infrared study of elemental abundances of BCDs and discuss the advantage of using the infrared data. However, before the launch of the *Spitzer* Space Telescope, this infrared method could not be used on BCDs because with the exception of a small handful of objects (Madden 2000), the fine structure lines in BCDs are too faint to be detected by earlier infrared instruments. In this subsection, I will review the optical studies of elemental abundances in BCDs.

The optical spectra of BCDs are characterized by narrow emission lines superimposed on blue continua (see Figure 1.2 for optical spectra of the two star-forming regions in IZw18). Oxygen is the most reliably determined element, since the most important ionization stages can all be observed in the optical spectrum of a BCD. N, S, Ne, Ar and He abundances can also be measured from the optical, while carbon and silicate abundances can be determined from ultraviolet regions. A direct measurement of electron temperature based on the detection of [OIII] λ4363 line is more favorable when estimating elemental abundances. When [OIII] λ4363 is not

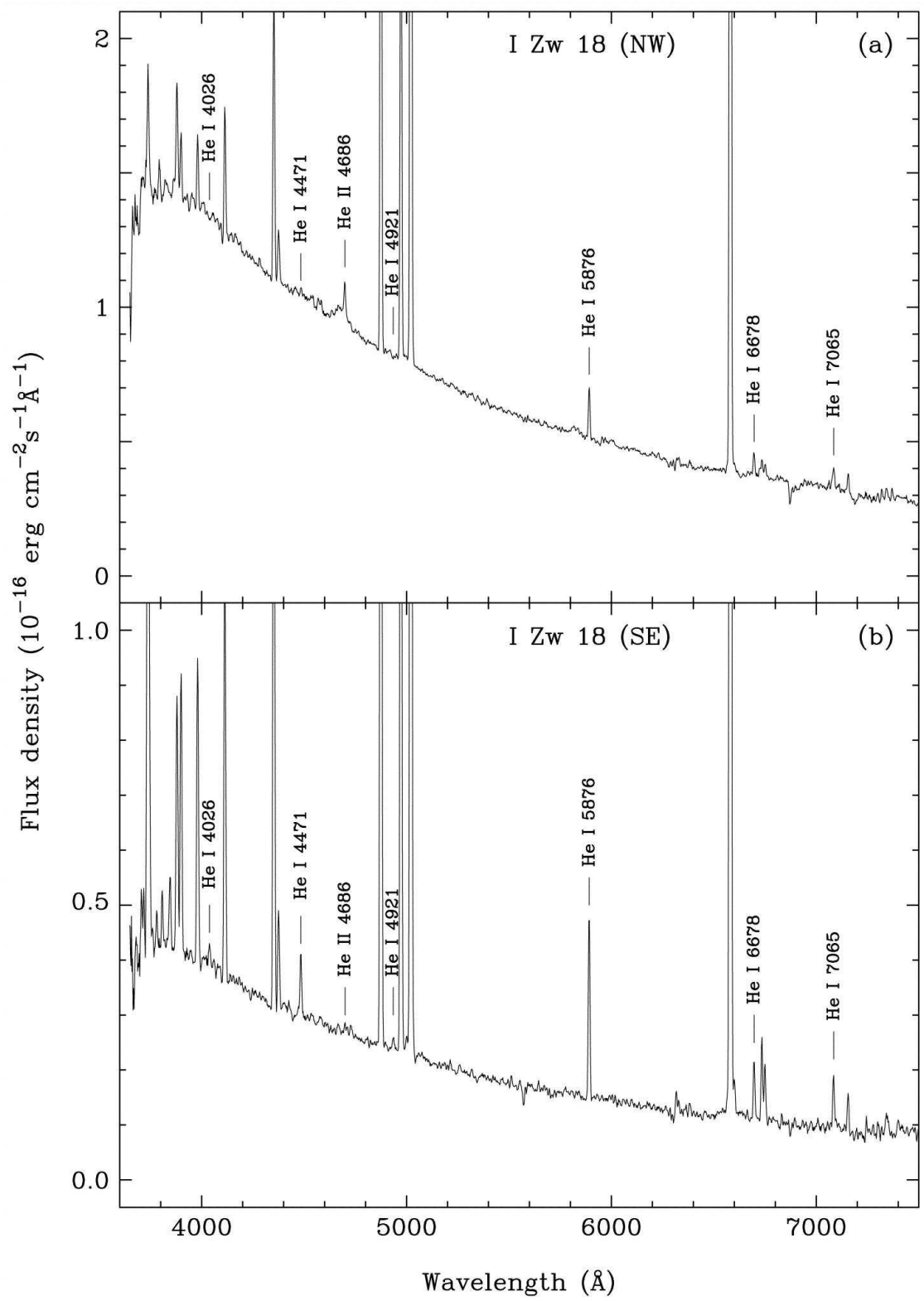

Figure 1.2 MMT spectra of the northwest and southeast components in the star-forming region of IZw18 published by Izotov et al. (1999).

detected, empirical methods based on the relationship between the oxygen abundance and the [OII] λ3727 and [OIII] $\lambda\lambda$4959,5007 strength can be used, though the uncertainty will be larger. The oxygen abundances of over 50 BCDs have been studied by Izotov & Thuan (1999) and their metallicities range between $1/2\,Z_\odot$ and $1/50\,Z_\odot$. The peak of metallicity for BCDs appears to be $\sim 1/10\,Z_\odot$, though this may partly be due to the selection effects since many surveys have selected galaxies with strong emission lines, which happen to be strongest for an oxygen abundance of around tenth of solar (see the review by Kunth & Östlin 2000). The abundance ratio of oxygen with other α-elements, such as Ne, Si, S and Ar show no dependence on oxygen abundance, which is consistent with the conception that they are all produced by the same massive stars.

1.3 Studying the BCDs in the Infrared

Recent infrared missions, such as *ISO* and *Spitzer* have opened a new window for studying the BCDs at the infrared wavelengths. For the first time, *ISO* provided 5-15 μm spectra for several BCDs, showing direct evidence that despite the low chemical abundances of BCDs, these galaxies could still have copious amount of dust emitting in the infrared (Thuan et al. 1999; Madden 2000). Furthermore, the unprecedented sensitivity of *Spitzer* is now allowing us to observe a much larger sample of BCDs to systematically study their infrared properties with a statistically more meaningful sample. I will give a brief description of the projects that I have done using this sample in the next section. In this section, I will first go over previous studies on the infrared properties of BCDs available in the literature.

1.3.1 PAH emission in BCDs

The polycyclic aromatic hydrocarbons (PAHs) are complex structures of benzene rings made by carbon and hydrogen. They are formed in the outflow of evolved or dying stars. PAHs are known to exist in the mid-IR spectra of many types of objects. Different vibrational modes (C-C stretching, C-H stretching, C-H in-plane bending and C-H out-of-plane bending) of PAH molecules are reflected as broad emission features in the $3-17\,\mu$m spectra, and this emission typically contributes $10-20\%$ to the total infrared luminosity of normal galaxies. A detailed study on the PAH features in HII regions from *ISO* data can be found in Peeters (2002).

The PAH emission is an important tracer of star formation activities. However, its strength varies significantly depending on the environment. For the few BCDs detected by *ISO*, PAH are found to be more suppressed as compared to normal star-forming galaxies. This could be due to a lack of carbon to form into PAH molecules in a metal-poor galaxy. On the other hand, the hardness of the radiation field in BCDs, as indicated by the ratio of [NeIII]/[NeII], is often 10 times times higher than that observed in starburst galaxies, indicative of a much harsher environment. Thus the hard UV photons might permeate over larger size scales within the galaxy and destroy the PAHs. An anti-correlation between the ratios of PAHs over Very Small Grains (PAHs/VSGs) and the [NeIII]/[NeII] ratios are detected, which lead Madden et al. (2006) to conclude that the hard permeating radiation field seems to play an important role in the destruction of PAHs in low metallicity regions. A detailed study on the correlation of PAH emission with different physical parameters in a much larger BCD sample can be found in chapter 2 of this thesis.

1.3.2 The infrared spectral energy distribution

Studies of the spectral energy distribution (SED) of low metallicity galaxies show that these galaxies have very different dust properties compared to the Milky Way or normal star forming galaxies. Galliano et al. (2005) and Hunt et al. (2005) have summarized some common characteristics for the infrared SED of BCDs: (i). A paucity of PAH features in the mid-IR spectra; (ii) Strong high ionization lines, such as [NeIII] and [SIV]; (iii). far-infrared (FIR) spectra which peak at or shortward of 60 μm. The standard starburst templates, M82 and Arp220, do not give a good approximation to any of the BCD SEDs studied by Hunt et al. (2005). Besides, these SEDs do not follow "canonical" scaling relations, and the "standard" star-formation indicators based on radio continuum, FIR, and MIR luminosities can be discrepant by factors of $\sim$10.

1.3.3 Case Study: SBS0335-052E

The lowest metallicity BCDs, IZw18 and SBS0335-052, share some common properties while their dust features are also very different in many ways. It is thus interesting to do case studies on these two BCDs. In this subsection, I will discuss the results on SBS0335-052 from studies in the literature. In the last chapter of this thesis, I will present our study on the infrared properties of IZw18 using *Spitzer* data.

SBS0335-052 is a nearby galaxy with M_B=16.7 mag at a distance of 58 Mpc. The western component of this BCD currently holds the record for the lowest metallicity galaxy with an oxygen abundance of 12+log(O/H)=7.12 (Izotov et al. 2005), however, it is too faint to be detected by current instruments in the infrared. Images of eastern component of SBS0335-052E from the *Hubble Space Telescope (HST)* clearly show dust patches mixed in with the six super star clusters (SSCs)

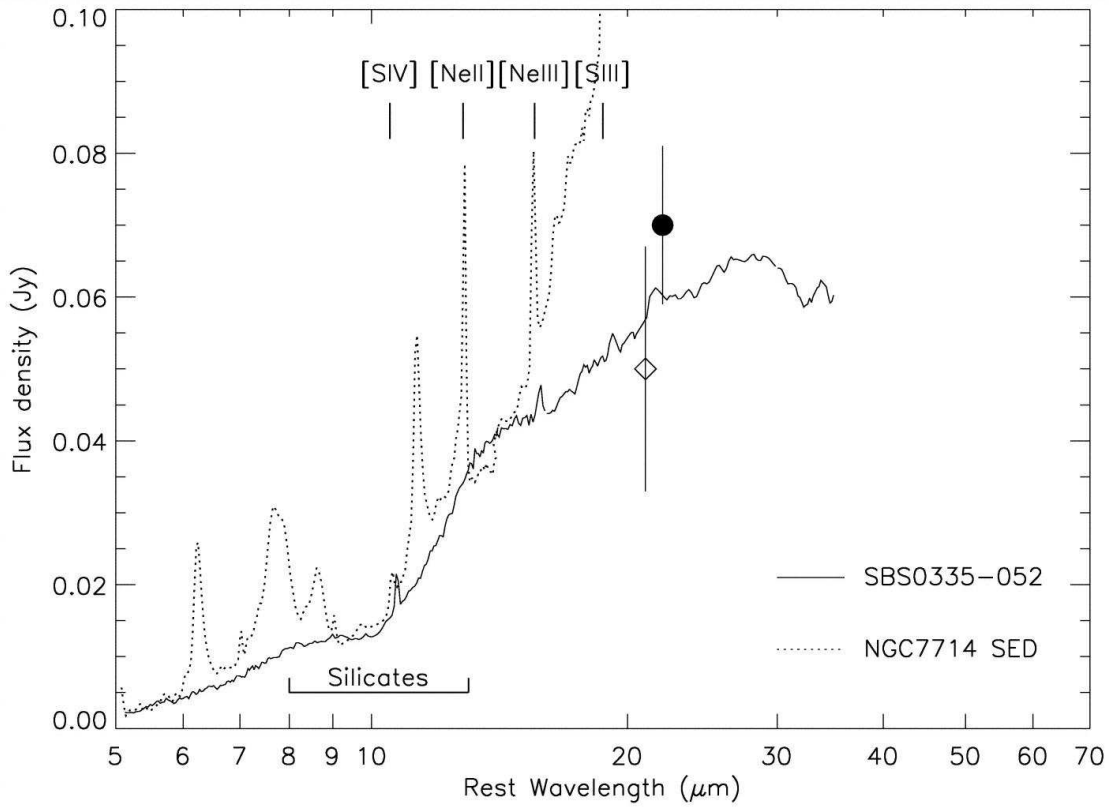

Figure 1.3 *Spitzer/IRS* low-resolution spectrum of SBS0335-052 (solid line) is presented along with the spectrum of NGC7714 (dotted line) from Brandl et al. (2004).The spectrum of NGC 7714 has been divided by 9.53 so that its 14 μm flux density matches that of SBS0335-052. [Taken from Houck et al. (2004b)].

where most of the star formation is occurring (Thuan et al. 1997).

The first mid-infrared spectrum of SBS0335-052E was published by Thuan et al. (1999), using data from ISOCAM (Cesarsky et al. 1996). As metal poor as it is, this galaxy is surprisingly bright in the mid-infrared with a $L_{12\mu m}/L_B$ ratio of 2.15. The 5−17 μm spectrum shows no sign of emission from the Polycyclic Aromatic Hydrocarbons (PAHs) and could be fit with a greybody with an extinction of A_V =19−21 mag. A large fraction (75%) of its infrared emission is contributed by an obscured SSC that is invisible from the optical (Thuan et al. 1997).

Recently, Houck et al. (2004b) have observed SBS0335-052E (see Figure 1.3) using the *Infrared Spectrograph (IRS)* (Houck et al. 2004a) on board the *Spitzer*

Space Telescope. The newly obtained $5-35\,\mu$m spectrum appear to have a relatively featureless power law shape, showing no detectable PAH emission. Silicate absorption feature at $9.7\,\mu$m is clearly present ($A_{9.7\mu m}$ $\geq$0.49 mag). Some high-ionization lines, such as [SIV] $10.51\,\mu$m and [NeIII] $15.55\,\mu$m can be seen even from the low-resolution (R$\sim$90) spectrum, while low ionization lines of [NeII] $12.81\,\mu$m and [SIII] $18.71\,\mu$m are rather weak if present. Unlike typical starburst galaxies which usually have continuum peaking near $80\,\mu$m, the flux density (f_ν) of SBS0335-052 peaks at $\sim$28 μm while the luminosity (νf_ν) peaks at $\sim$20 μm. Because of the abnormally flat spectral shape of SBS0335-052E, Houck et al. (2004b) suggest that the mass of the cold dust in this galaxy is much less than what has been previously estimated.

1.4 In this thesis

The research described in this work is targeted toward understanding the general properties of blue compact dwarf galaxies, in particular the physics of the dust in low metallicity environment.

The data presented in this thesis is taken by the *Spitzer* Space Telescope. We make use of all three instrument on board *Spitzer* in one way or another, though a large majority of the work is based on mid-IR spectra taken by the IRS.

We have compiled a large sample of BCDs ($\sim$60 objects), which we describe in more details later. The low-resolution spectra of 12 BCDs that have good signal to noise ratio for spectral analysis are presented in chapter 2. We measure the strength of PAHs from the low-resolution spectra, and analyze the PAH features by correlating with different physical parameters. We conclude that the strength of PAHs in metal-poor environment is determined by a combination of formation and destruction effects.

In Chapter 3, we use the high-resolution data of 13 BCDs to estimate the elemental abundances of neon and sulfur in these galaxies. Fluxes of fine-structure line used in this metallicity study ([SIV]10.51 μm, [NeII]12.81 μm, [NeIII]15.55 μm and [SII]18.71 μm) is also given in this chapter. We compare the infrared derived neon and sulfur abundances, with optically derived neon, sulfur and oxygen abundances for these BCDs available from the literature. A good agreement is found between the infrared and optical results. We also explore the variation in the ratio of Ne/S in the infrared and optical studies, as well as that in the solar neighborhood.

In Chapter 4, we investigate the infrared/radio correlation in low luminosity dwarf galaxies. Far-infrared (FIR) data from *IRAS*, as well as newly obtained mid-infrared data from *Spitzer* (MIPS 24 μm and IRS 22 μm), are now allowing us to explore the relationship between infrared and radio luminosities in low luminosity systems. We find that the FIR and radio luminosities of these dwarf galaxies are well-correlated, similar to that has been found in normal star-forming galaxies. The mid-infrared luminosity is also correlated with the radio luminosity, though the scatter is larger. If we examine the ratio of the infrared to radio luminosities, we find that there is a weak trend of this ratio increasing with metallicity for metal-poor sources, while this trend flattens out for sources with 12+log(O/H)>8.0.

In Chapter 5, we study the dust properties and star-formation rates in low-luminosity star-forming dwarf galaxies. Because of the relatively low metallicities of these systems, the physical properties, heating and the distribution of dust temperature/grain size in these galaxies are likely to be different from normal star-forming galaxies. We explore the variation in the presence/absence of PAH emission, IR spectral slope, etc. in low-luminosity dwarf galaxies by performing a spectral energy distribution analysis. We also compare the star-formation rates

estimated from different star-formation rate indicators from UV to the infrared. We show that the variation in the interstellar medium properties of galaxies in this sample result in over an order of magnitude spread in the computed star-formation rates.

Finally, I have also included a case study of IZw18 in Chapter 6 of this thesis. As one of the two lowest metallicity BCDs, IZw18 has been studied extensively at various wavelengths. We present the first mid-infrared spectrum of IZw18. There is no sign of PAH emission from the 5-36 μm low-resolution spectra. Strong high-ionization lines of [SIV] 10.51 μm and [NeIII] 15.55 μm are clearly detected and we use the high-resolution spectrum to estimate its neon and sulfur abundances. We also study the spectral energy distribution in IZw18. Unlike SBS0335-052E, which is also a low metallicity BCD and has a rather flat spectrum, IZw18 has a spectral slope more similar to typical starburst galaxies, such as NGC7714.

BIBLIOGRAPHY

Aloisi, A., et al. 2007, ApJ, 667, L151

Arp, H. 1965, ApJ, 142, 402

Cesarsky, C. J., et al. 1996, A&A, 315, L32

Doublier, V., Comte, G., Petrosian, A., Surace, C., & Turatto, M. 1997, A&AS, 124, 405

Gallego, J., Zamorano, J., Rego, M., Alonso, O., & Vitores, A. G. 1996, A&AS, 120, 323

Galliano, F., Madden, S. C., Jones, A. P., Wilson, C. D., & Bernard, J.-P. 2005, A&A, 434, 867

Gerola, H., Seiden, P. E., & Schulman, L. S. 1980, ApJ, 242, 517

Gil de Paz, A., Madore, B. F., & Pevunova, O. 2003, ApJS, 147, 29

Izotov, Y. I., & Thuan, T. X. 1999, ApJ, 511, 639

Izotov, Y. I., & Thuan, T. X. 2004, ApJ, 616, 768

Izotov, Y. I., Thuan, T. X., & Guseva, N. G. 2005, ApJ, 632, 210

Kessler, M. F., et al. 1996, A&A, 315, L27

Legrand, F., Kunth, D., Roy, J.-R., Mas-Hesse, J. M., & Walsh, J. R. 2000, A&A, 355, 891

Mas-Hesse, J. M., & Kunth, D. 1999, A&A, 349, 765

Papaderos, P., Loose, H.-H., Thuan, T. X., & Fricke, K. J. 1996, A&AS, 120, 207

Peeters, E. 2002, Ph.D. Thesis

Searle, L., & Sargent, W. L. W. 1972, ApJ, 173, 2

Searle, L., Sargent, W. L. W., & Bagnuolo, W. G. 1973, ApJ, 179, 427

Telles, E., Melnick, J., & Terlevich, R. 1997, MNRAS, 288, 78

Thuan, T. X., & Martin, G. E. 1981, ApJ, 247, 823

Werner, M. W., et al. 2004, ApJS, 154, 1

Zwicky, F. 1966, ApJ, 143, 192

Zwicky, F. 1970, Advances in Astronomy and Astrophysics, 7, 227

Zwicky, F., & Zwicky, M. A. 1971, Guemligen: Zwicky, —c1971,

CHAPTER 2

MID INFRARED PROPERTIES OF LOW METALLICITY BLUE COMPACT DWARF GALAXIES FROM *SPITZER/IRS*[*]

Abstract We present a *Spitzer*-based mid-infrared study of a large sample of Blue Compact Dwarf galaxies (BCD) using the Infrared Spectrograph (IRS), including the first mid-IR spectrum of IZw18, the archetype for the BCD class and among the most metal poor galaxies known. We show the spectra of Polycyclic Aromatic Hydrocarbon (PAH) emission in low-metallicity environment. We find that the equivalent widths (EW) of PAHs at 6.2, 7.7, 8.6 and 11.2 μm are generally weaker in BCDs than in typical starburst galaxies and that the fine structure line ratio, [NeIII]/[NeII], has a weak anti-correlation with the PAH EW. A much stronger anti-correlation is shown between the PAH EW and the product of the [NeIII]/[NeII] ratio and the UV luminosity density divided by the metallicity. We conclude that PAH EW in metal-poor high-excitation environments is determined by a combination of PAH formation and destruction effects.

2.1 Introduction

Galaxies formed in the early Universe are likely to have very different properties from typical evolved galaxies in the local Universe because they were formed from an environment deficient in heavy elements. Important as they are, those primeval galaxies are beyond the capability of current mid-IR instruments, thus motivating an ongoing effort to identify local analogs of the galaxy formation process in the early Universe.

Blue compact dwarfs are a group of extra-galactic objects with faint, blue optical colors, small sizes and low metallicities. They are generally dominated by

[*]Originally published as: Yanling Wu, V.Charmandaris, Lei Hao, B. Bernard-Salas, H.W.W.Spoon, J.R.Houck, (2006), *The Astrophysical Journal*, 639, 157

one or more recent bursts of star formation. Early studies hinted that BCDs have dramatically different properties compared to normal dwarf galaxies (Arp 1965; Zwicky 1966). Accumulated observational evidence over the recent years provided more details on the unique properties of these galaxies (for a review see Kunth & Östlin 2000). Early ground based observations by Roche et al. (1991) on the mid-IR spectra of 60 galaxies revealed that PAH emission is generally suppressed in low-metallicity galaxies, which could be due to hard photons destroying the particles that produce the unidentified infrared bands. Thuan et al. (1999) has shown that there is no sign of these bands in the mid-IR spectrum of SBS0335-052E taken by the Infrared Space Observatory (ISO). The suppression of the PAH emission is also seen in the mid-IR spectra of 4 BCDs discussed by Madden (2000); Galliano et al. (2005); Madden et al. (2006). Dwek (2004) proposed that the delayed injection of carbon molecules into the interstellar medium(ISM) might be partly responsible for the absence of PAH features in young star forming regions, or for the existence of a metallicity threshold below which PAHs have not formed. Hogg et al. (2005) suggested that the lack of PAH emission is closely related to the low luminosity of their sample. More recent work based on *Spitzer* observations has confirmed that PAH emission is missing in the most metal-poor galaxies (Houck et al. 2004b; Engelbracht et al. 2005; Rosenberg et al. 2006). Hunt et al. (2005) studied the global spectral energy distributions (SEDs) of 7 BCDs and confirmed that those SEDs deviate significantly from the standard templates of "classical", evolved and massive starburst galaxies, in the sense that the far-infrared (FIR) spectra peak at/or shortward of 60 μm and mid-IR spectra show little or no PAH emission. Having a relatively low metallicity, these galaxies are at an early epoch of their evolution, making them similar to samples of the distant, more massive protogalaxies, thus allowing us to study the star formation and chemical enrichment

in an environment likely to be similar to that in the early Universe.

Recently, mid-IR imaging and spectroscopy of a handful of such systems revealed the presence of dusty embedded sources as well as fine structure line emission in their spectra, consistent with a hard radiation field from massive young stars (Thuan et al. 1997; Madden 2000; Madden et al. 2006). In general, short bursts (1-5 Myr) of intensive star formation are found to best match the data (Mas-Hesse & Kunth 1999). Some BCDs appear to be very rapid star formers, and thus true dwarf analogs of giant starbursts (Kunth & Östlin 2000). The profiles and strengths of the PAHs, which might be good tracers of star formation, vary substantially (Förster Schreiber et al. 2004).

Using the unprecedented sensitivity of the Infrared Spectrograph (Houck et al. 2004a) on the *Spitzer* Space Telescope (Werner et al. 2004), we compiled a large sample of of the lowest metallicity galaxies known. Since little information on their mid-IR fluxes were available from literature, a large fraction of them were first observed with the peak-up cameras at 16 and 22 μm. As we discuss in detail in the following section, those which were bright enough were observed spectroscopically. In this paper we present 5.2–36 μm spectra of 12 galaxies for which the signal-to-noise ratio (SNR) was high enough to perform a quantitative analysis on the strength of the spectral features, as well as 16 and 22 μm broad band imaging for the remaining of the sample, covering metallicities from 1/50 $Z_\odot$ to 0.65 $Z_\odot$. Many of the remainders are scheduled for re-observation to achieve higher SNR. In Section 2, we describe the sample, the observing strategy, and the data reduction. Section 3 presents the spectral features observed in each source while our analysis on these properties is shown in Section 4. We summarize our conclusions in Section 5. Throughout this work, we assume a ΛCDM cosmology with $H_0 = 71$ km s^{-1} Mpc^{-1}, $\Omega_m = 0.3$ and $\Omega_\lambda = 0.7$.

2.2 Observations and Data Reduction

A total of 61 BCDs have been observed as part of the *IRS* Guaranteed Time Observation (GTO) program. The sample included targets from the Second Byurakan Survey (SBS), Bootes Void galaxies (Kirshner et al. 1981; Popescu & Hopp 2000), and several well-known BCDs. Some basic properties of these galaxies and the observing parameters, such as: source names, right ascension (RA), declination (Dec), redshift, *Spitzer* aorkeys, observation date, and on-source integration time for each module and peak-up mode are listed in Table 4.1.

We used all four *IRS* modules, Short-Low (SL, 5.2-14.5 μm), Long-low (LL, 14.0-38.0 μm), Short-High (SH, 9.9-19.6 μm) and Long-high (LH, 18.7-37.2 μm) to obtain spectra for 26 sources which were expected to be sufficiently bright for spectroscopy. SBS1200+589B was the only one of the targets that was not observed in SL. The low resolution modules (SL, LL) produce spectra with a resolution of 64–128 while the high-resolution modules (SH, LH) have a resolution of $\sim$600 (see Houck et al. 2004a). Nearly all targets were acquired using red peak-up (RPU) mode. In the process, an image of the source at 22μm was obtained in Double Correlated Sampling (DCS) mode and it was used to locate the mid-IR centroid of the source which was then offset to the appropriate slit (see Spitzer Observers Manual for more details). For BCDs that were too faint for spectroscopy, we only obtained broad band imaging at 16 μm (13.5-18.7 μm) and 22 μm (18.5-26.0 μm) using both *IRS* peak-up cameras in Raw Data Collection (RAW) mode. Details on this method of imaging with *IRS*, also called CHEAP for Cornell High-Efficiency Advanced Peak-up, and its photometric advantages compared to the usual *IRS* Peakup Only mode are discussed in Charmandaris et al. (2004). Eight of our galaxies were so faint in the mid-IR that only an upper limit of $\sim$0.1mJy could be established for their 16 and 22μm flux densities.

Table 2.1. Properties of Sources

Object Name	RA (J2000)	Dec (J2000)	AORKEY	Observation Date	Redshift	On-source Time (sec) SL	LL	SH	LH	BPU	RPU
Haro11	00h36m52.5s	-33d33m19s	9007104	2004-07-17	0.0206	168	240	480	240	···	98
UM283	00h51m49.4s	+00d33m53s	8997888	2004-07-13	0.0155	···	···	···	···	28	56
UM133	01h44m41.3s	+04d53m26s	8987392	2004-07-16	0.0054	···	···	···	···	28	56
UM382	01h58m09.3s	-00d06m38s	9004032	2005-01-11	0.0118	···	···	240	120	···	···
			12628224	2005-01-14		···	···	···	···	28	56
			9003776	2004-07-16		···	···	···	···	28	56
			8993792	2005-01-11		56	120	···	···	···	···
UM408	02h11m23.4s	+02d20m30s	8997120	2004-08-07	0.0120	···	···	···	···	28	56
NGC1140	02h54m33.6s	-10d01m40s	4830976	2004-01-07	0.0050	168	240	480	240	···	98
SBS0335-052E	03h37m44.0s	-05d02m40s	11769856	2004-09-01	0.0135	···	···	1440	960	···	50
			8986880	2004-02-06		840	420	···	···	···	50
NGC1569	04h30m47.0s	+64d50m59s	9001984	2004-03-01	~ 0	112	120	480	240	···	50
IIZw40	05h55m42.6s	+03d23m32s	9007616	2004-03-01	0.0026	168	240	480	240	···	98
Tol0618-402	06h20m02.5s	-40d18m09s	4845824	2003-12-15	0.0350	···	···	···	···	28	56
SBS0743+591B	07h47m46.7s	+59d00m30s	12625920	2005-03-18	0.0211	···	···	···	···	28	56
			12622080	2005-03-20		···	···	···	···	28	56
SBS0754+570	07h58m26.4s	+56d54m22s	12630272	2005-03-20	0.0116	···	···	···	···	28	56
UGC4274	08h13m13.0s	+45d59m39s	12076032	2004-10-23	0.0015	112	240	120	56	···	50
			12626688	2004-11-11		112	240	120	56	···	50
SBS0813+582A	08h18m04.5s	+58d05m56s	12629248	2005-03-18	0.0268	···	···	···	···	28	56
HS0822+3542	08h25m55.5s	+35d32m32s	12630016	2004-11-11	0.0024	···	···	···	···	28	56
IZw18	09h34m02.0s	+55d14m28s	9008640	2004-03-27	0.0025	168	240	480	240	···	98
			12622848	2005-04-23		960	480	···	···	···	98
SBS0935+495	09h38m24.0s	+49d18m17s	12624640	2004-11-13	0.0314	···	···	···	···	28	56
SBS0940+544	09h44m16.7s	+54d11m33s	9010432	2004-03-26	0.0055	···	···	···	···	28	56
SBS0943+563	09h47m13.0s	+56d06m07s	12627200	2004-11-13	0.0253	···	···	···	···	28	56
SBS1001+555	10h04m41.8s	+55d18m43s	12624384	2005-04-15	0.0037	···	···	···	···	28	56
KUG1013+381	10h16m24.5s	+37d54m46s	4846336	2003-12-15	0.0040	···	···	···	···	28	56
			8999168	2004-04-16		···	···	120	120	···	···
			9012224	2004-04-16		56	240	···	···	···	···
			12628992	2005-04-22		960	···	···	···	50	···
SBS1116+597	11h18m47.4s	+59d26m02s	12622592	2004-11-17	···	···	···	···	···	28	56
[RC2]A1116+51	11h19m34.3s	+51d30m12s	4846592	2003-12-15	0.0044	···	···	···	···	28	56
SBS1119+586	11h22m37.8s	+58d19m43s	12631040	2005-04-15	0.0053	···	···	···	···	28	56
VIIZw403	11h27m59.9s	+78d59m39s	9005824	2004-12-09	~ 0	168	240	480	240	···	50
SBS1129+576	11h32m02.5s	+57d22m46s	12632320	2005-01-06	0.0052	···	···	···	···	28	56
SBS1135+598	11h37m43.7s	+59d35m34s	12624896	2004-11-17	0.0327	···	···	···	···	28	56
Mrk1450	11h38m35.6s	+57d52m27s	9011712	2004-12-12	0.0032	168	240	480	240	···	50
SBS1136+607	11h39m11.5s	+60d30m45s	12622336	2004-11-14	0.0116	···	···	···	···	28	56
SBS1137+589	11h40m32.0s	+58d38m32s	12630528	2004-11-17	0.0068	···	···	···	···	28	56
SBS1141+576	11h44m16.6s	+57d24m32s	12627456	2005-04-15	0.0310	···	···	···	···	28	56
UM461	11h51m33.3s	-02d22m22s	9006336	2005-01-03	0.0035	168	240	480	240	···	50
SBS1149+596	11h52m34.0s	+59d22m56s	12623360	2004-11-17	0.0112	···	···	···	···	28	56
SBS1150+599	11h53m28.9s	+59d41m57s	12621824	2004-11-17	0.0371	···	···	···	···	28	56

Table 2.1 (continued)

Object Name	RA (J2000)	Dec (J2000)	AORKEY	Observation Date	Redshift	On-source Time (sec) SL	LL	SH	LH	BPU	RPU
SBS1159+545	12h02m02.4s	+54d15m50s	4847104	2003-12-15	0.0118	···	···	···	···	28	56
			9010176	2004-04-17		···	···	120	120	···	···
			9008896	2004-04-17		56	240	···	···	···	···
			12629504	2005-04-23		960	···	···	···	50	···
SBS1200+589B	12h03m22.6s	+58d41m36s	4824064	2004-01-06	0.0321	···	240	···	···	···	98
SBS1210+537A	12h12m55.9s	+53d27m38s	8989952	2004-06-06	···	168	240	480	240	···	···
SBS1211+564	12h13m35.9s	+56d08m35s	12623104	2005-04-21	0.0107	···	···	···	···	28	56
SBS1212+563	12h14m48.5s	+56d05m19s	12633088	2005-04-21	···	···	···	···	···	28	56
Tol1214-277	12h17m17.1s	-28d02m33s	9008128	2004-06-28	0.0260	168	240	480	240	···	98
SBS1219+559	12h21m29.0s	+55d38m23s	12631296	2005-04-21	0.0308	···	···	···	···	28	56
SBS1221+545B	12h24m23.0s	+54d14m48s	12625152	2005-04-21	0.0187	···	···	···	···	28	56
HS1222+3741	12h24m36.7s	+37d24m36s	12630784	2005-01-03	0.0409	···	···	···	···	28	56
Tol65	12h25m46.9s	-36d14m01s	4829696	2004-01-07	0.0090	168	240	480	240	···	98
SBS1227+563	12h30m07.3s	+56d05m13s	12632832	2005-04-21	0.0153	···	···	···	···	28	56
[RC2]A1228+12	12h30m48.5s	+12d02m42s	8998656	2004-06-27	0.0042	···	···	···	···	28	56
SBS1235+559	12h37m36.9s	+55d41m04s	12628480	2005-04-21	0.0293	···	···	···	···	28	56
UGCA292	12h38m40.0s	+32d46m01s	4831232	2004-01-07	0.0010	168	240	480	240	···	98
			12076288	2005-01-03		···	···	···	···	28	56
Tol1304-353	13h07m37.5s	-35d38m19s	9006848	2004-06-25	0.0140	168	240	480	240	···	50
			12075520	2005-02-10		···	···	···	···	28	56
HS1319+3224	13h21m19.9s	+32d08m23s	12625664	2005-02-07	0.0182	···	···	···	···	28	56
Pox186	13h25m48.6s	-11d37m38s	9007360	2004-07-14	0.0039	168	240	480	240	···	50
			12625408	2005-02-15		···	···	···	···	28	56
SBS1415+437	14h17m01.4s	+43d30m05s	4844288	2004-01-07	0.0020	···	···	···	···	28	56
			8990464	2004-05-15		···	···	120	120	···	···
			9008384	2004-05-13		56	240	···	···	···	···
HS1424+3836	14h26m28.1s	+38d22m59s	12628736	2005-02-13	0.0226	···	···	···	···	28	56
Mrk475	14h39m05.4s	+36d48m22s	8995840	2004-02-07	0.0019	···	···	···	···	28	56
			8996864	2004-06-05		···	···	120	120	···	···
			8988672	2004-06-26		56	240	···	···	···	···
CG0598	14h59m20.6s	+42d16m10s	8992256	2005-03-19	0.0575	168	240	480	240	···	50
CG0752	15h31m21.3s	+47d01m24s	8991744	2005-03-19	0.0211	168	240	480	240	···	50
SBS1533+574B	15h34m14.1s	+57d17m04s	12627968	2005-01-09	0.0110	···	···	···	···	28	56
SBS1538+584	15h39m56.9s	+58d15m33s	12623616	2005-01-08	0.0435	···	···	···	···	28	56
SBS1541+590	15h42m55.8s	+58d55m09s	12631552	2004-12-12	0.0450	···	···	···	···	28	56
Mrk1499	16h35m21.1s	+52d12m53s	9011456	2004-06-05	0.0090	168	240	480	240	···	98
[RC2]A2228-00	22h30m33.9s	-00d07m35s	9006080	2004-06-24	0.0052	168	240	480	240	···	50

[a]The coordinates and redshifts of the objects are cited from The NASA/IPAC Extragalactic Database (NED)(NED is operated by the Jet Propulsion Laboratory, California Institute of Technology, under contract with the National Aeronautics and Space Administration).

The data were processed by the *Spitzer* Science Center (SSC) data reduction pipeline version 11.0 and 11.4[1]. The 2-D image data were converted to slopes after linearization correction, subtraction of darks, and cosmic ray removal. The DCS peak-up imaging data were processed on the ground to remove cosmic rays and the residual noise of the electronics. Fixed aperture photometry was then performed in order to obtain the counts of the science target. The conversion to flux density was based on a number of calibration stars for which peak-up images, *IRS* spectra, and reliable templates are available (Cohen et al. 2003). The reduction of the spectral data started from the intermediate pipeline products (droop files), which only lacked stray light and flat field correction. Individual pointings to each nod position of the slit were co-added using median averaging and for SL and LL spectra, and the two apertures were differenced in order to remove the contribution of the background. The 2-D images were extracted with the Spectral Modeling, Analysis, and Reduction Tool (SMART Ver. 5.5.1 Higdon et al. 2004) using a variable width aperture, which scales the extraction aperture with wavelength to recover the same fraction of the diffraction limited instrumental point-spread-function (PSF). The data from SH and LH were extracted using the full slit extraction method from the median of the combined images. Since no sky (off–position) measurements were taken, the contribution of the sky emission was not subtracted from SH and LH spectra. Then the spectra were flux calibrated by multiplication with the Relative Spectral Response Function (RSRF), which was created from the *IRS* standard stars α Lac for SL and LL and ξ Dra for SH and LH for which accurate templates were available (Cohen et al. 2003). We built our RSRFs by extracting the spectra of the calibration stars in the exact same way

[1]The usage of data products from two versions of the pipeline was a result of the extended time-span over which sample was observed and the delivery of the files from the SSC. The difference between the two versions is very small and it does not introduce any inhomogeneity in the sample or influence the conclusions of the paper.

as the science targets, and dividing the stellar templates by the extracted stellar spectra. We produced one RSRF for each nod position in order to avoid systematic flat field errors. The signal difference between the nod positions provide the error estimates. Finally, the flux calibrated spectra of each order and module of the low-resolution modules except 1st order LL (LL1) (20–36μm) were scaled, using LL1 spectrum to define the continuum (presented in Figure 2.1 and 2.2). The associated photometric points are also presented on the spectra in Figure 2.1 and 2.2.

2.3 Results

From the 26 BCDs observed spectroscopically, only 11 produced spectra with SNR sufficient for features to be measured (SNR $\geq$ 2 in the 5–8μm range of the 2nd order SL, SL2). These spectra are presented in Figure 2.1 and 2.2. We also include the first mid-IR spectrum of IZw18[2]. The 22 μm flux density of each target with an aperture radius of 7.2$''$ measured during its acquisition using the red peak-up camera (circle), as well as a "synthetic" 22 μm flux obtained by convolving the spectrum with the filter response function (square) are indicated in the Figure 2.1 and 2.2. The *IRAC* 8 μm (asterisk) and *MIPS* 24 μm (triangle) flux densities are also indicated when available (Engelbracht et al. 2005). One can see that for all point sources, including SBS0335-052E, NGC1140, Mrk1499, Mrk1450, CG0598, CG0752, UM461 and IZw18, the two broad band values for the RPU agree very well. NGC1140 is marginally saturated at 22 μm, but we correct for this effect based on the PSF profile. The agreement of the spectra and the photometric measurements indicates the internal consistency of the calibration of the instrument

[2]The overall shape of the mid-IR continuum is evident from Figure 2.1, but a measurement of spectral features is challenging due to the noise in the spectrum.

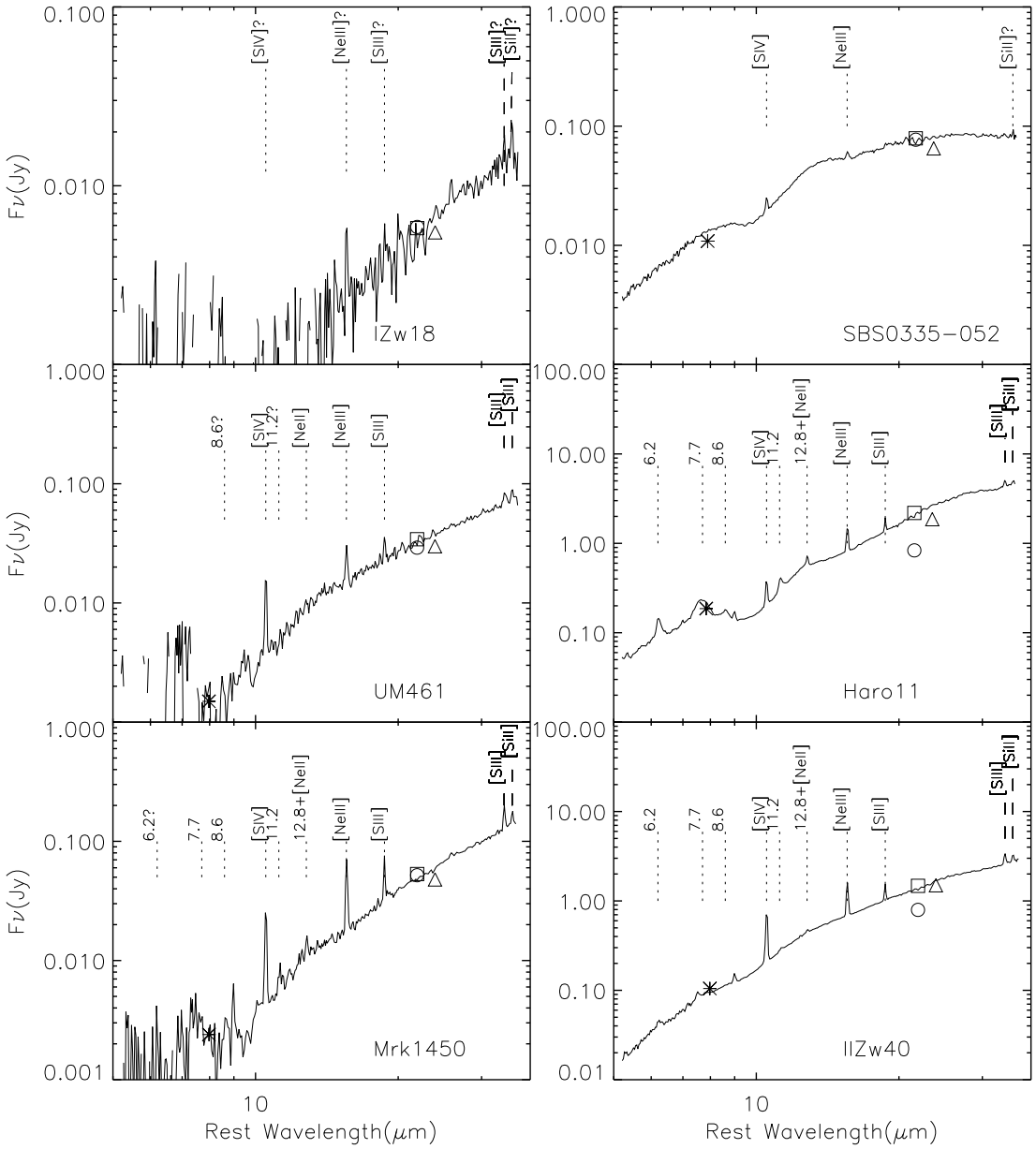

Figure 2.1 *Spitzer*/IRS mid-IR spectra of six BCDs: IZw18, SBS0335-052E, UM461, Haro11, Mrk1450 and IIZw40. The spectra of different orders were stitched and scaled to match the flux density in the 1st order LL. The circles represent the photometric flux from 22μm red peak-up camera, which has an uncertainty of 6%. The squares indicate the flux density at 22 μm measured from the spectra using "synthetic" method (See the text for detail). The asterisk and the triangle indicate the *IRAC* 8 μm and *MIPS* 24 μm measurements respectively.

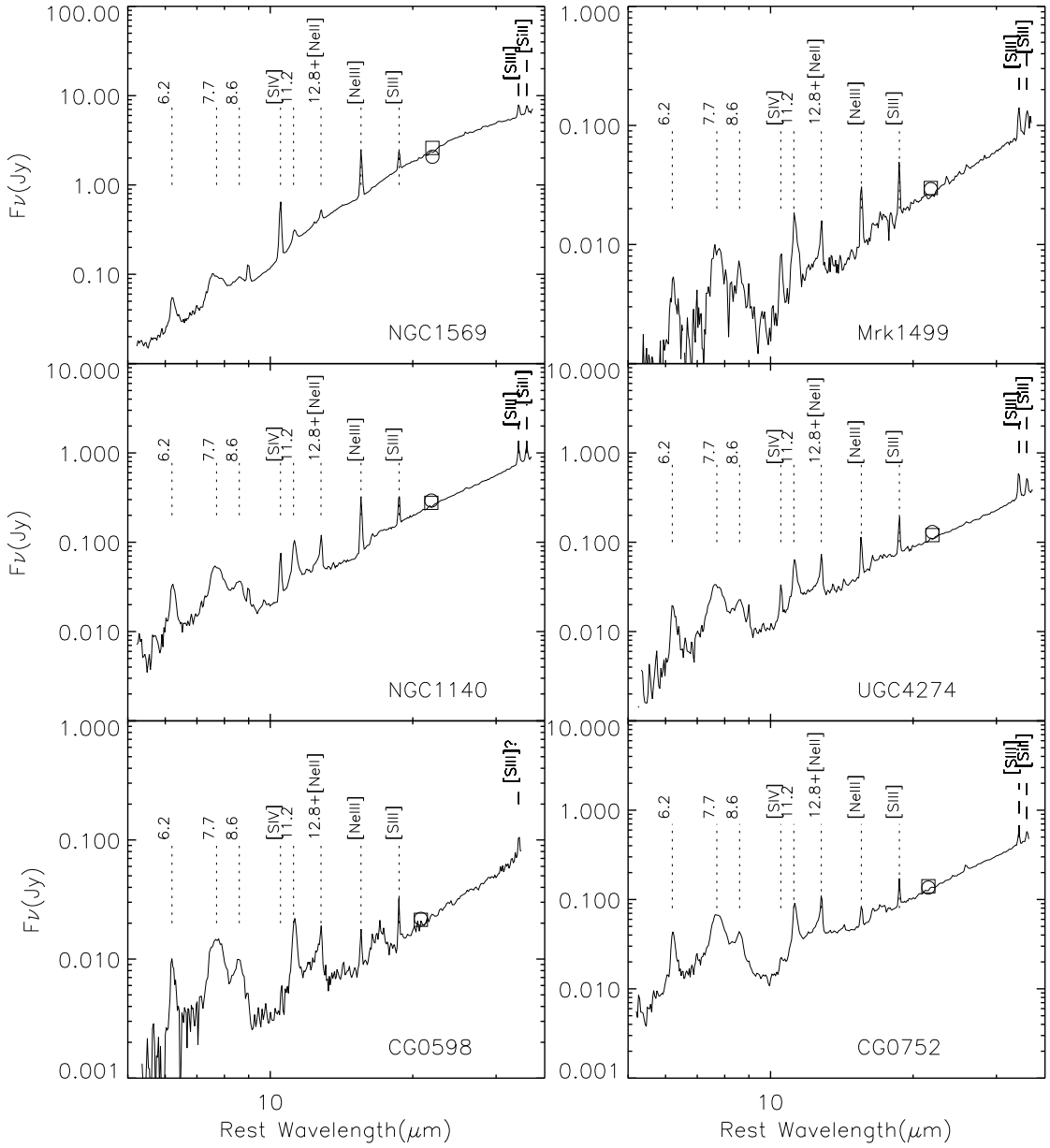

Figure 2.2 Same as Figure 1 but for another six BCDs: NGC1569, Mrk1499, NGC1140, UGC4274, CG0598 and CG0752.

between spectroscopy and peak-up photometry when all spectra are scaled to LL1. However, as expected, for sources which are extended or well above the 340 mJy saturation limit of red peak-up in a 8.4 second exposure time, such as NGC1569, IIZw40, Haro11 and UGC4274, there is a disagreement among these photometric measurements (See Figure 2.1 and 2. 2).

It is clearly seen from Figure 2.1 and 2.2 that the forbidden transitions of [SIV] at 10.51 μm and [NeIII] at 15.55 μm are visible even in the low-resolution spectra, while [NeII] at 12.81 μm, [SIII] at 18.71 μm and [SiII] at 34.8 μm lines are seen in most of them. The line fluxes used in the analysis are determined from high-resolution spectra (See Figure 2.3). The emission from PAHs at 6.2, 7.7, 8.6 11.2 and 12.8 μm are also clear in several of our targets and they are indicated in the figures but no pronounced silicate emission or absorption features are present. All PAH measurements presented in this paper were measured from the low-resolution spectra.

2.3.1 Mid infrared Morphology

As mentioned in Section 2, all spectroscopic observations were preceded by an acquisition using the 22μm peak-up camera. This provided not only more precise position of the objects for telescope pointing, but also deep 22 μm images of our targets. Analysis of those images indicates that with the exception of four galaxies: NGC1569, UGC4274, IIZw40 and Haro11, all other targets are unresolved at 22 μm (FWHM=6.5$''$) . In Figure 2.4, we display the 22 μm images of these four galaxies, overlayed with the spectrograph slits as they were placed when the spectra were obtained. Among those targets NGC1569 shows the most complex structure with two bright cores in the mid-IR. This source also has very extended emission in the optical. Therefore, not surprisingly, it requires a large scaling factor of $\leq$80% when

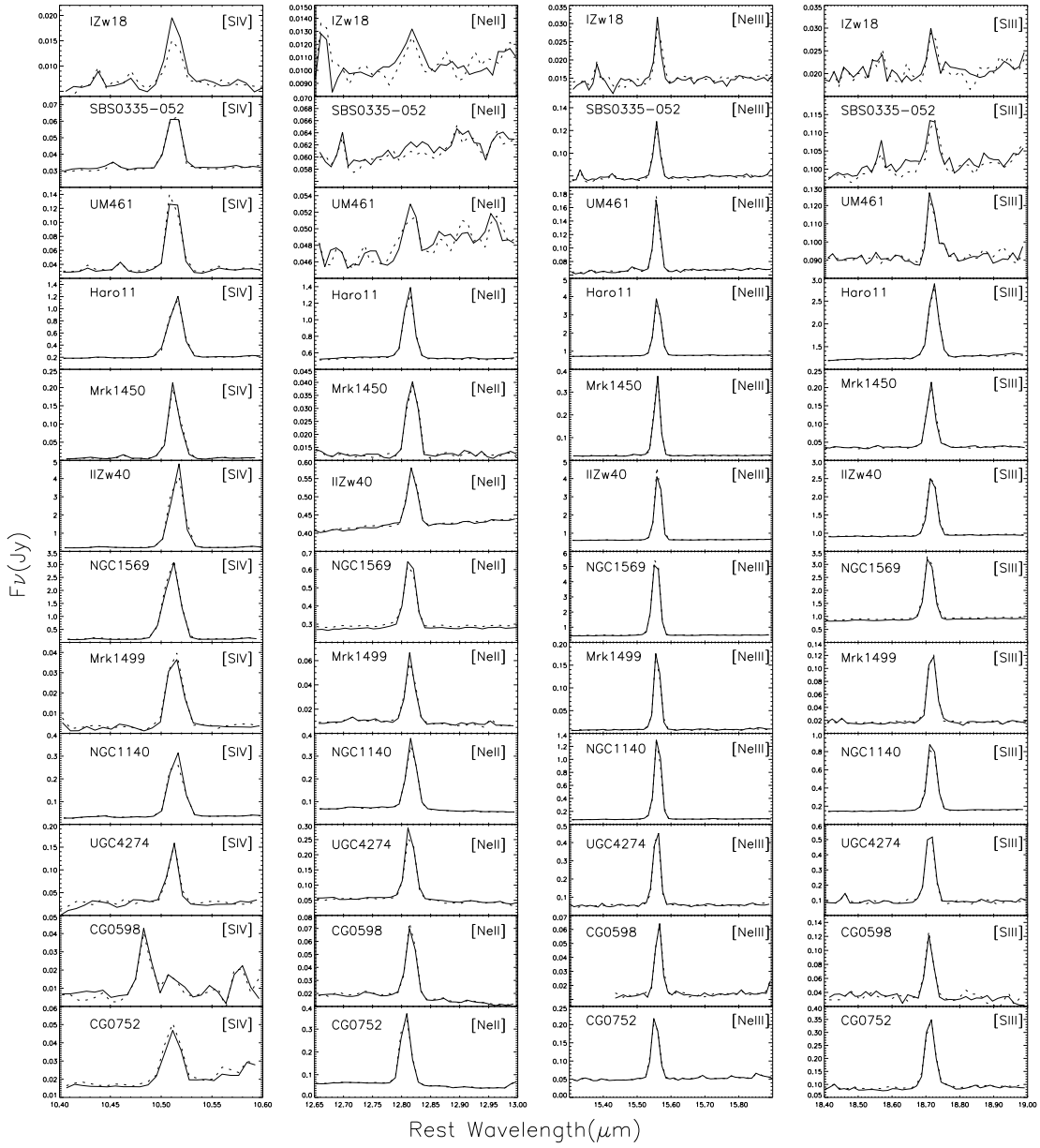

Figure 2.3 The mid-IR fine structure lines of [SIV] (10.51 μm), [NeII] (12.81 μm), [NeIII] (15.55 μm) and [SIII] (18.71 μm) from the high resolution spectra of the twelve BCDs. The solid and dotted lines denote the spectra from the first and second nod positions of the slits. Note that sky emission has not been subtracted and no stitching and scaling between different modules have been done.

we "stitch" the spectra of 1st order SL (SL1) and 2nd order LL (LL2), mostly due to the different slit widths and orientations between the two low-resolution modules. In UGC4274, we find that most of its 22 μm flux originates from a compact unresolved knot while a similar peak is seen in the near infrared which is offset by $\sim 3''$ from the mid-IR one.

2.3.2 Individual Objects

IZw18 — This is the first identified member of the blue compact dwarf galaxy class (Searle & Sargent 1972) and until recently[3] held the record of a galaxy with the lowest metallicity at Z $\sim$0.02 $Z_\odot$ (Skillman & Kennicutt 1993). IZw18 is located at a distance of 12-15 Mpc and is a bona fide young galaxy and no red giant branch stars are seen(Izotov & Thuan 2004). Zwicky (1966) described it as a double system of compact galaxies, which are in fact two star-forming regions, a northwest component and a southeast one, separated by an angular distance of $5.8''$. Examination of the spatial distribution of the stellar populations suggest that the star formation process is still building the main body from inside out (Izotov & Thuan 2004). Both Izotov et al. (1997a) and Legrand et al. (1997) detected several broad emission components in this BCD, suggesting that Wolf-Rayet (WR) features can also exist in extremely low metallicity environment. It is intrinsically very faint in the infrared. The first mid-IR spectrum of IZw18 is presented in Figure 2.1. As we discuss in the subsequent sections we are able to estimate the mid-IR spectral slope from its low-resolution spectrum. The fine structure lines of [SIV] and [NeIII] can clearly be seen in its high-resolution spectrum, though the identification of [NeII] and [SIII] is not yet

[3]Only this year (2005) measurements of Izotov et al. (2005) showed that the brightest star formation region of the western component of SBS0335-052 has an oxygen abundance of only 12+log(O/H)=7.12$\pm$0.03 ($\sim$0.017 $Z_\odot$), suggesting it is the most metal poor galaxy known.

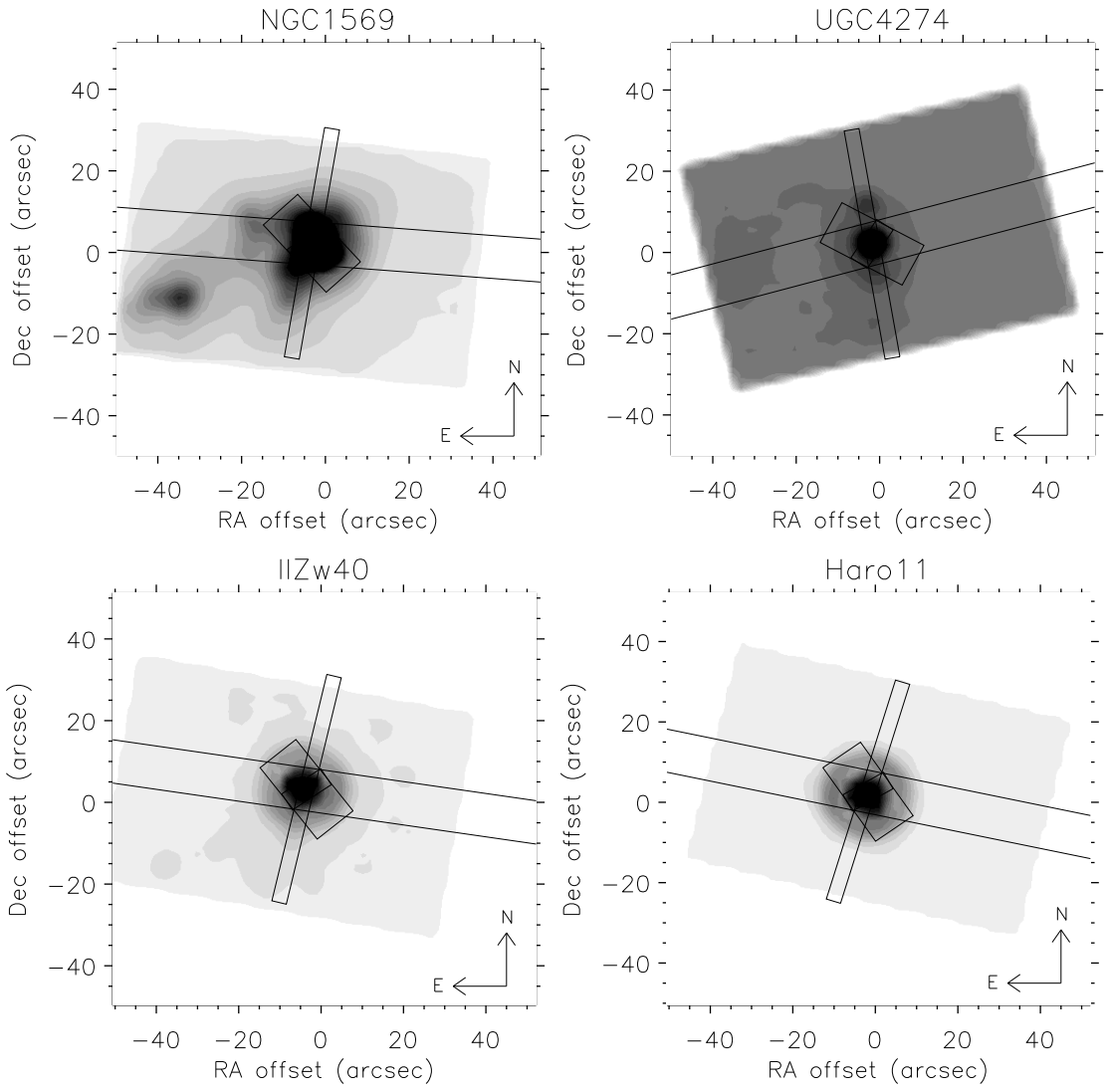

Figure 2.4 The 22 μm peak-up images of the four sources from our sample, NGC1569, UGC4274, IIZw40 and Haro11, which display extended emission. The images are overlayed with the *IRS* slits at the location from where the spectrum was obtained. The widths of the slits increase in the order of: SL, SH, LL, LH and their length in the order of: SH, LH, SL, LL.

firm. A much deeper observation with more exposure time has been scheduled and the new spectrum will be presented in a future paper (Wu et al. in prep 2006).

SBS0335-052E — Currently the third most metal-poor galaxy known with 0.024 $Z_\odot$ (Izotov et al. 1997b), SBS0335-052E is at a distance of 58 Mpc. Thuan et al. (1997) found that stars in SBS0335-052E are younger than ∼100 Myr and the current burst of star formation is no older than 5 Myrs, thus making it a truly young system. This galaxy is unexpectedly bright in the mid-IR (Thuan et al. 1999; Houck et al. 2004b) with roughly 75% of the total luminosity coming from the mid-IR (Plante & Sauvage 2002). It has six compact regions of massive star formation, five of which are visible and one obscured, and all of them lying within a diameter of 526 pc (Thuan et al. 1997). There is no sign of PAH emission in its spectrum and silicate absorption at 9.7 μm is clearly seen. The SED of the galaxy is dominated by a very strong continuum, which unlike typical star forming galaxies, such as NGC7714 (Brandl et al. 2004), peaks at ∼28 μm (f_ν), indicating the presence of little cold dust. The fine structure lines of [NeIII] and [SIV] are present, though not very strong.

UM461 — This is a dwarf galaxy with a double nucleus and is found at a distance of 15 Mpc. It has an external envelope which is strongly distorted towards the South-West, suggesting a recent tidal event (Doublier et al. 1999). The metallicity of UM461 is ∼0.087 $Z_\odot$ (Kniazev et al. 2004). With only 168 seconds of integration time in SL module, the obtained spectrum is very noisy. However, the fine structure lines, such as [SIV], [NeIII] and [SIII] can be clearly seen longward of 10 μm. The identification of PAH emission is doubtful and an upper limit of 0.199 μm for the PAH EW at 11.2 μm is indicated in Table 2.4.

Haro11 — This is a metal poor galaxy with ∼0.1 $Z_\odot$ (Bergvall et al. 2000). Its distance is ∼88 Mpc and it has an infrared luminosity, L_{IR} of 1.8×10^{11} $L_\odot$[4]. Haro11 is a moderately strong radio source, with spatially extended continuum emission at 6 and 20 cm(Vader et al. 1993; Heisler & Vader 1995). Multiple nuclei are apparent on optical broad band images (Heisler & Vader 1994) as well as narrow-band Hα images (Heisler & Vader 1995). All three nuclei are similar in continuum stellar emission (Heisler & Vader 1995) and spectra of the nuclei confirm that they are all at the same distance (Vader et al. 1993). The PAH features are much weaker compared with NGC1140 but the fine structure lines of [SIV], [SIII], [NeIII] and [NeII] lines are clearly present.

Mrk1450 — A dwarf compact object with a projected dimension less than 1 kpc, Mrk1450 is located at a distance of ∼14 Mpc. Its optical images display moderately deformed circular isophotes and a central star forming component. A strong color gradient is present reaching a $B-R$ ∼2.2 mags at the outskirts of the galaxy, while the surface brightness distribution obeys an $r^{1/4}$ law (Doublier et al. 1997). This galaxy has an L_{IR}[5] less than 1.8×10^8 $L_\odot$. Its metallicity is ∼0.12 $Z_\odot$ (Izotov & Thuan 1999). Due to the low SNR in SL2, PAH emission can not be identified clearly below 10μm, even though the 11.2 μm and possibly 12.8 μm PAHs are present. The fine structure lines of [SIV] and [NeIII] are strong.

[4]Calculated from the *IRAS* flux densities following the prescription of Sanders & Mirabel (1996): $L_{IR}=5.6\times10^5 D^2_{Mpc}(13.48S_{12}+5.16S_{25}+2.58S_{60}+S_{100})$.

[5]For this galaxy, the *IRAS* 12 μm and 25 μm flux densities are calculated by convolving our spectrum with the *IRAS* filters. The 100 μm flux density is an upper limit, thus making the L_{IR} also an upper limit.

IIZw40 — This is a prototypical H II galaxy (Sargent & Searle 1970) with L_{IR}[6] less than 2.9×10^9 $L_\odot$ at a distance of ∼10 Mpc. The metallicity of this galaxy is ∼0.17 $Z_\odot$ (Cerviño & Mas-Hesse 1994). It consists of a compact, extremely bright core and two fan-like structures, which have been interpreted as the result of a merger between two small galaxies (Baldwin et al. 1982; Brinks & Klein 1988). Star formation is concentrated in the nucleus while the double structure is quite red and shows no star formation activity (Cairós et al. 2001). Hα emission is very strong, contributing 40% to the $R-$band flux at the nucleus. The starburst could be very young and its strength is rather extraordinary (Deeg et al. 1997). It also displays WR features (Conti 1991). Our mid-IR spectrum indicates that the PAHs are present, though extremely weak. The fine structure lines of [SIV], [SIII], [NeII] and [NeIII], have been detected.

NGC1569 — A nearby dwarf galaxy (D∼2.2 Mpc Israel 1988) which has a metallicity of ∼0.19 $Z_\odot$ (Kobulnicky & Skillman 1997) and is currently in the aftermath of a massive burst of star formation (Waller 1991), with L_{IR} of $5.8\times10^8\,L_\odot$. It lies close to the plane of the Galaxy and therefore its optical properties are strongly affected by the Galactic dust extinction (Kinney et al. 1993). The presence of a broad emission feature around 4650 Å and a broad base to the Hα line indicate that WR stars are present in the nucleus of NGC1569 (Ho et al. 1995). It contains two bright super star clusters. The very hot, bright nucleus of this galaxy resembles a superluminous, young star cluster (Arp & Sandage 1985). The fine structure lines of [SIV] and [NeIII] are stronger compared to [SIII] and [NeII], which can be seen clearly even in the low-resolution spectrum (See Figure 2.2). The PAH features are clearly present. As discussed by Galliano

[6]For this galaxy, only upper limit exists for *IRAS* 100 μm, thus making the L_{IR} also an upper limit.

et al. (2003, 2005), the mid-IR emission is dominated by small grains.

Mrk1499 — This is an irregular galaxy displaying a very blue elongated central structure with two components in the optical, the brightest being off-centered with respect to the outer contours (Doublier et al. 1997). These authors suggested that this structure is reminiscent of "double nuclei" objects, while Petrosian et al. (2002) argued that this could be just an observational artifact. It has an L_{IR}[7] of 1.3×10^9 $L_\odot$ and is at a distance of ∼38 Mpc. An oxygen abundance of ∼ 0.3 $Z_\odot$ has been derived from the line measurements of Petrosian et al. (2002), using the N2 calibrator (Denicoló et al. 2002), which allows us to calculate the oxygen abundance based on the [NII]/Hα ratio. PAH features are prominent and several fine structure lines are detected. In this particular galaxy, the SNR in SL2 is rather poor, thus making the definition of the continuum challenging. We measured the 6.2 μm PAH EW by defining a maximum and minimum local continuum and then averaging the two measurements.

NGC1140 —This is a blue irregular galaxy at a distance of ∼25 Mpc, containing large mass of ionized gas in its center (Kinney et al. 1993). Its metallicity is ∼0.4 $Z_\odot$ (Calzetti 1997). Lamb et al. (1986) concluded that NGC1140 has experienced a single burst of star formation and its population mainly consists of main-sequence stars with a contribution from supergiants and, possibly, WR stars. Hunter et al. (1994) used the Hubble Space Telescope (*HST*) Planetary Camera to study the central supergiant H II region and found that the central 1/2 kpc of NGC1140 contains ∼7 blue, luminous, compact super star clusters. It has a very small average size of grains (Galliano et al. 2003, 2005) and a L_{IR}

[7]For this galaxy, only *IRAS* 60 μm and 100 μm are available. For *IRAS* 12 μm and 25 μm, we convolved our spectrum with the two *IRAS* filters and calculated their values.

of 4.3×10^9 $L_\odot$. The low resolution mid-IR spectrum shows pronounced PAH emission, almost comparable to that in the typical starburst galaxy NGC7714, while the fine structure lines are stronger compared with NGC7714.

UGC4274 — A galaxy also known as NGC2537 and Mrk86, UGC4274 is extended in the mid-IR (see Figure 2.3) and is located at a distance of ∼7 Mpc. It has a large, very irregular nucleus consisting of ∼80 star-forming knots distributed in a circular region which is surrounded by a red envelope (Gil De Paz 2000). The Hα image shows a very complex gas distribution, with multiple filaments, loops and twisted features (Cairós et al. 2001). It has an L_{IR} of 5.0×10^8 $L_\odot$ and emission from PAHs dominates its spectrum. An oxygen abundance of 12+log(O/H)=8.05 (Z∼0.13 $Z_\odot$) has been derived by Meier et al. (2001) based on the relationship between B magnitude and metallicity. Since this method has a large uncertainty and there is no direct spectroscopically measured oxygen abundance available, we calculated the metallicity using the N2 calibrator. A value of 12+log(O/H)=8.52±0.13 (Z∼0.41 $Z_\odot$) has been derived from the line measurement in Ho et al. (1997). All major mid-IR fine structure lines of the galaxy are very strong.

CG0598 — This is a galaxy selected from the Bootes Void sample. It is at a distance of 253 Mpc and it has an L_{IR}[8] less than 5.9×10^{10} $L_\odot$. In the optical, this galaxy is a flattened disk system with a bright, round nucleus. It has a smooth, elongated surrounding disk which is asymmetric with respect to the nucleus (Cruzen et al. 1997). The metallicity of this galaxy is ∼ 0.65 $Z_\odot$ (Peimbert & Torres-Peimbert 1992). In Figure 2.2, we can see that CG0598 shows very strong

[8]The *IRAS* 12 μm and 25 μm flux densities are calculated by convolving the spectrum with the *IRAS* filters. The *IRAS* 100 μm flux density is an upper limit thus making L_{IR} an upper limit as well.

PAH emission in all bands and the usual fine structure lines of [NeII], [NeIII], [SIV] and [SIII] can be identified.

CG0752 — This galaxy is ∼91 Mpc away with an L_{IR}[9] of 2.2×10^{10} $L_{\odot}$. It has remained uncatalogued for a long time because of its proximity to bright star (Sanduleak & Pesch 1987). PAH emission is moderately strong and the fine structure lines of [SIV], [SIII], [NeIII] and [NeII] are present. There is no measured oxygen abundance available from literature for this galaxy.

2.4 Analysis

2.4.1 The mid-infrared spectral slope of BCDs

The photometric properties and metallicities of the 53 galaxies in our BCD sample (excluding the 8 objects that were too faint in mid-IR) are listed in Table 2.2. The 16 and 22 μm flux densities of the sources are based on broad band imaging using the blue or red peak-up cameras, while the B and K magnitudes are taken from literature. For the 12 BCDs with good IRS spectra, we also calculated their "synthetic" 16 and 22 μm flux densities by convolving the spectra with the *IRS* peak-up filters. For comparison, we list those values in Table 2.3. We also present the 22 to 16 μm flux density ratio, f_{22}/f_{16} ($f_{22} \equiv f_{\nu}(22\,\mu m)$)in Table 2.2. This ratio provides the mid-IR slope of the spectrum and can be a useful probe of the shape of the mid-IR SED even if the galaxy are too faint to obtain a spectrum. One of our sources, SBS0335-052E, has a particularly low value of f_{22}/f_{16}, indicating the absence of cold dust around the central star forming region. As discussed by

[9]The *IRAS* 12 μm flux density is calculated by convolving the spectrum with the *IRAS* filter.

Houck et al. (2004b), the flux density of SBS0335-052E peaks at a much shorter wavelength of $\sim 28\,\mu$m while most normal galaxies peak longward of $60\,\mu$m.

We explore the variation on the f_{22}/f_{16} ratio as a function of metallicity in Figure 2.5a. In addition to the 12 BCDs, we include in this figure a typical starburst galaxy NGC7714 (Brandl et al. 2004), and an Ultra-Luminous Infrared Galaxy (ULIRG), UGC5101 (Armus et al. 2004), in order to sample a wider range of different types of galaxies forming massive young stars. The BCDs with only photometric CHEAP images are included using crosses as well when their metallicities are available from literature. It has been pointed out by Hunter et al. (1989) that no clear metallicity dependence is observed in mid-IR and FIR colors of normal galaxies. This is also confirmed in Figure 2.5a where the f_{22}/f_{16} ratio for all the BCDs seems to have an average value of $\sim$2.5 and shows no metallicity dependence.

In Figure 2.5b and 2.5c, we plot the ratio of the flux density at $22\,\mu$m to the *IRAC* $8\,\mu$m band, f_{22}/f_8, as well as the *MIPS* $24\,\mu$m to the *IRAC* $8\,\mu$m, f_{24}/f_8, as a function of their metallicities. The *IRAC* $8\,\mu$m and *MIPS* $24\,\mu$m flux densities are calculated by convolving the mid-IR spectra of these BCDs with the appropriate filter profiles. Engelbracht et al. (2005) observed that the $8\,\mu$m to $24\,\mu$m color changes markedly between 1/3 to 1/5 solar metallicity and suggested that this change is predominantly due to a decrease in the $8\,\mu$m emission. Our Figure 2.5b and 5c are very similar to Figure 2.2 in their paper. It appears that there is a separation on the f_{24}/f_8 ratio around 1/5 $Z_\odot$ on our plots with the exception of SBS0335-052, which as mentioned earlier shows no PAH detection.

Table 2.2. Integrated photometry of Sources

Object Name	$f_{8\mu m}$ (mJy)	$f_{16\mu m}$ (mJy)	$f_{22\mu m}$ (mJy)	$f_{24\mu m}$ (mJy)	B (mag)	K (mag)	$f_{22\mu m}/f_{16\mu m}$	$Z/Z_{\odot}$	References B/K	References Z
Haro11	190.0	···	851.2[a]	1900	14.31	12.0	···	0.1	1) , 2)	19)
UM283	···	3.0	8.2	···	17.38	···	2.7	0.110	9)	34)
UM133	···	2.0	6.6	···	15.41	···	3.4	0.052	3)	25)
UM382	···	0.7	1.5	···	18.20	···	2.2	0.081	3)	34)
UM408	···	1.3	3.5	···	17.46	···	2.7	0.105	3)	35)
NGC1140	···	···	294.4	···	12.56	10.51	···	0.4	4) , 5)	14)
SBS0335-052E	11.2	···	78.0	66	17.07	···	···	0.024	10	17)
NGC1569	···	···	2067.5[a]	···	9.42	7.86	···	0.19	4) , 6)	16)
IIZw40	105.0	···	796.1[a]	1500	11.87	12.35	···	0.17	3) , 5)	15)
SBS0743+591B	···	2.3	4.7	···	···	···	2.1	···		
SBS0754+570	···	0.8	2.4	···	···	···	2.9	···		
UGC4274	···	···	130.2	···	12.07	9.13	···	0.41	4) , 6)	18)[c]
HS0822+3542	0.2	1.3	4.1	2.7	17.92	···	3.1	0.028	26)	26)
IZw18	0.7	···	4.1	5.5	16.05	15.92	···	0.018	3) , 11)	27)
SBS0935+495	···	1.2	2.9	···	···	···	2.3	···		
SBS0940+544	···	1.1	2.3	···	17.18	···	2.1	0.033	3)	21)
SBS0943+563	···	1.4	3.8	···	···	···	2.8	···		
KUG1013+381	···	6.4	17.1	···	16.04	···	2.7	0.047	28)	28)
SBS1116+597	···	1.0	1.1	···	···	13.28	1.2	···	5)	
[RC2]A1116+51	···	0.5	1.7	···	17.46	···	3.6	0.049	12)	29)
SBS1119+586	···	0.6	1.5	···	···	···	2.6	···		
VIIZw403	2.5	···	7.7	28	14.11	12.7	···	0.060	3) , 7)	21)
SBS1129+576	···	0.3	1.4	···	···	···	4.0	0.032		30)
SBS1135+598	···	0.2	0.8	···	···	···	3.7	···		
Mrk1450	2.4	···	52.1	48	15.75	···	···	0.117	3)	21)
SBS1136+607	···	0.5	1.8	···	···	···	3.8	···		
SBS1137+589	···	0.5	1.0	···	···	···	2.2	···		
SBS1141+576	···	1.1	2.9	···	···	···	2.5	···		
UM461	1.6	···	29.2	30	···	···	···	0.087		22)
SBS1149+596	···	1.5	4.4[b]	···	···	···	3.1	···		
SBS1150+599	···	0.3	0.6	···	···	12.67	1.8		5)	
SBS1159+545	···	2.6	6.4	···	···	···	2.5	0.038		21)
SBS1212+563	···	1.0	1.2	···	···	···	1.2	···		
Tol1214-277	0.2	···	3.5	5.5	···	···	···	0.045		24)
SBS1219+559	···	1.0	2.1	···	···	···	2.1	···		
SBS1221+545	···	0.6	1.9	···	···	···	3.0	···		
HS1222+3741	···	3.0	6.9	···	18.40	···	2.3	0.054	13)	32)
Tol65	0.9	···	15.7	15	17.26	···	···	0.031	3)	24)
SBS1227+563	···	1.0	1.7	···	···	···	1.7	···		
[RC2]A1228+12	···	1.2	3.4	···	17.96	···	2.9	0.066	8)	35)
SBS1235+559	···	0.3	1.0	···	···	···	2.9	···		
Tol1304-353	···	6.0	10.8	···	···	···	1.8	0.058		33)

Table 2.2 (continued)

Object Name	$f_{8\mu m}$ (mJy)	$f_{16\mu m}$ (mJy)	$f_{22\mu m}$ (mJy)	$f_{24\mu m}$ (mJy)	B (mag)	K (mag)	$f_{22\mu m}/f_{16\mu m}$	$Z/Z_{\odot}$	References B/K	References Z
HS1319+3224-	···	1.3	2.1	···	19.0	···	1.6	0.048	13)	32)
Pox186	···	5.8	13.1	···	17.0	···	2.3	0.066	14)	31)
SBS1415+437	···	6.0	19.6	···	15.43	···	3.2	0.048	3)	21)
HS1424+3836-	···	0.5	1.5	···	18.68	···	2.8	0.115	13)	32)
Mrk475	···	3.2	10.8	···	16.20	···	3.3	0.105	3)	21)
CG0598	···	···	23.0	···	···	13.17	···	0.65	5)	23)
CG0752	···	···	138.9	···	···	11.73	···	···	5)	
SBS1533+574B	···	21.2	53.4	···	16.02	···	2.5	0.158	3)	21)
SBS1538+584	···	1.4	3.9	···	···	···	2.8	···		
SBS1541+590	···	1.3	3.3	···	···	···	2.5	···		
Mrk1499	···	···	29.5	···	16.00	···	···	0.3	4)	20) [c]

Note. — *IRAC* 8 μm and *MIPS* 24 μm flux densities are quoted from Engelbracht et al. (2005). The metallicity we list here is converted from the oxygen abundance using 12+log[O/H]=8.91 for solar metallicity (Kunth & Östlin 2000).

[a]The 22μm peak-up is saturated.

[b]The error in this value is higher ∼10% in the blue and ∼15% in the red due to the presence of a bright star.

[c]The oxygen abundance is calculated from [NII]/Hα measurement using the method proposed by Denicoló et al. (2002)

References. — 1) Lauberts & Valentijn (1989), 2) Spinoglio et al. (1995), 3) Gil de Paz et al. (2003), 4) De Vaucouleurs et al. (1991), 5) 2Mass Extended Objects. Final Release (2003), 6)Jarrett et al. (2003), 7) Tully et al. (1981), 8) Young & Currie (1998), 9) Vitores et al. (1996), 10) Papaderos et al. (1998), 11) Thuan (1983), 12) Arp & Oconnell (1975), 13) Vennik et al. (2000), 26) Kniazev et al. (2000), 28) Kniazev et al. (1998), 14) Calzetti (1997), 15) Cerviño & Mas-Hesse (1994), 16) Kobulnicky & Skillman (1997), 17) Izotov et al. (1997b), 18) Ho et al. (1997), 19) Bergvall et al. (2000), 20) Petrosian et al. (2002), 21) Izotov & Thuan (1999), 22) Kniazev et al. (2004), 23) Peimbert & Torres-Peimbert (1992), 24) Gallego et al. (1997), 25) Masegosa et al. (1994), 26) Kniazev et al. (2000), 27) Skillman & Kennicutt (1993), 28) Kniazev et al. (1998), 29) Kinman & Davidson (1981), 30) Guseva et al. (2003), 31) Guseva et al. (2003), 32) Popescu & Hopp (2000), 33) Stasinska & Leitherer (1996), 34) Kniazev et al. (2001), 35) Pustilnik et al. (2002)

Table 2.3. Synthetic flux density of the sources

Object Name	*IRAC* 8 μm (mJy)	*IRS* 16 μm (BPU) (mJy)	*IRS* 22 μm (RPU) (mJy)	*MIPS* 24 μm (mJy)
IZw18	···	2.6±0.1	5.9±0.3	6.5±0.1
SBS0335-052	12.3±0.2	58.1±0.3	79.8±0.3	81.5±0.2
UM461	1.8±0.1	16.9±0.3	34.5±0.2	37.7±0.2
Haro11	164.2±0.1	932.6±0.3	2307.0±4.5	2640.4±6.5
Mrk1450	2.4±0.2	22.0±0.1	53.5±0.2	59.7±0.1
IIZw40	90.1±0.6	763.7±2.4	1481.9±6.9	1624.0±11.5
NGC1569	72.2±0.2	921.8±0.6	2596.0±1.0	2991.0±4.6
Mrk1499	4.2±0.1	12.4±0.1	30.4±0.1	33.8±0.1
NGC1140	28.7±0.3	103.5±0.1	279.5±0.3	316.6±0.2
UGC4274	17.0±0.2	53.1±0.2	120.5±0.7	132.5±0.5
CG0598	7.2±0.1	11.2±0.1	24.8±0.1	28.3±0.1
CG0752	32.9±0.6	63.6±0.2	148.6±0.1	169.9±0.1

It is very important to note that, as shown by our data, using the f_{22}/f_8, or f_{24}/f_8 ratios to infer the strength of the PAH emission is not a very robust method. Since the 7.7 μm and 8.6 μm PAH emission is included in the *IRAC* 8 μm band, one might expect that a lower f_{22}/f_8 ratio would indicate the presence of a stronger PAH emission from the galaxy. However, a low f_{22}/f_8 ratio can also be due to decreased emission at 22 μm, resulting from the lack of cooler dust. A galaxy with a flat continuum but no PAH emission can have the same f_{22}/f_8 ratio as a galaxy which shows strong PAH emission and a steep continuum. If we consider SBS0335-052E and UGC4274, we can see that they have a very similar f_{22}/f_8 ratio, even though no PAHs are detected in SBS0335-052E while PAHs are prominent in UGC4274. This can be understood when we take into account the f_{22}/f_{16} ratio. It is evident from Figure 2.5a that these two sources have very different mid-IR spectral slopes. This explains why SBS0335-052E lies away from the upper left corner of Figure 2.5a. We have also plotted the PAH EW at 6.2 μm

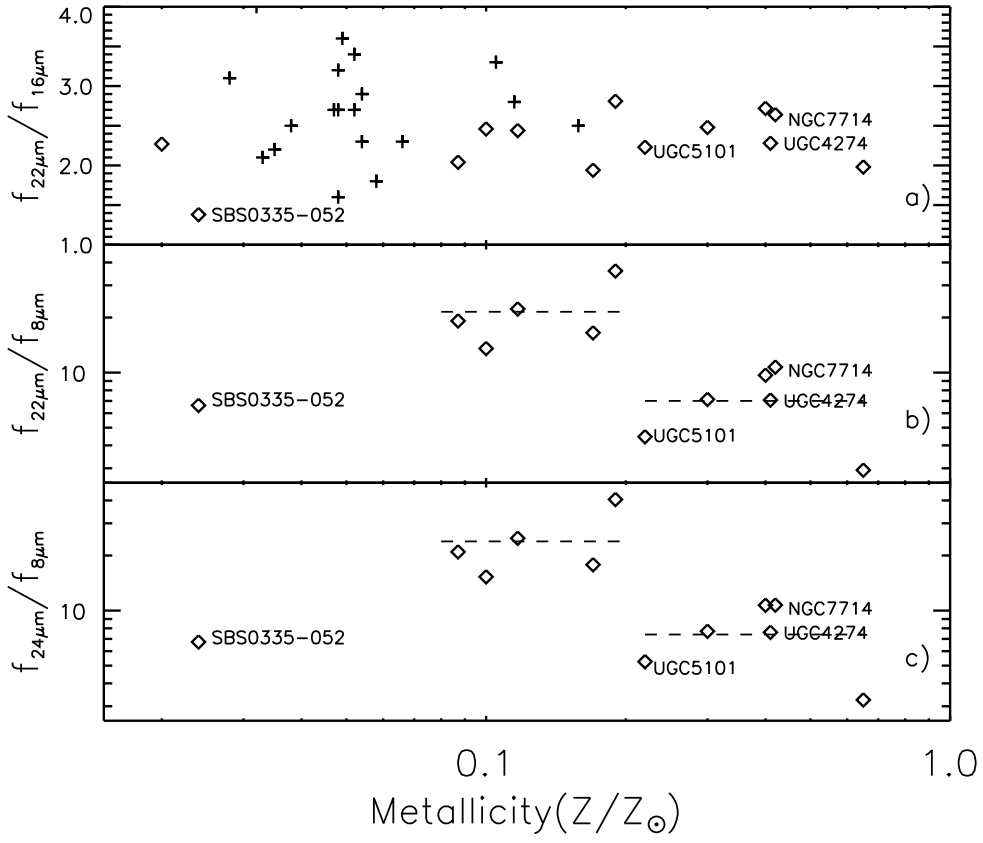

Figure 2.5 a) This figure shows the ratio of the 22 to the 16 μm flux density as a function of the metallicity of the sources. For sources with an IRS spectrum available, the ratio was calculated by convolving the spectrum with the 22 and 16μm filter curves. A starburst galaxy, NGC7714, and a ULIRG, UGC5101, are also included for comparison. Diamonds denote sources for which we have obtained spectra. The crosses indicate galaxies for which the photometric points were obtained using IRS broad band imaging (see Section 2). b) The same as a) but for the 22 to 8 μm flux density as a function of metallicity. Here we include only the galaxies for which we have full *IRS* spectra since we measure the 8 μm flux density from the spectra. SBS0335-052 clearly departs from the general trend. We indicate the average flux ratios by the dashed lines.c) Same as b) but for 24 over 8 μm flux density as a function of metallicity.

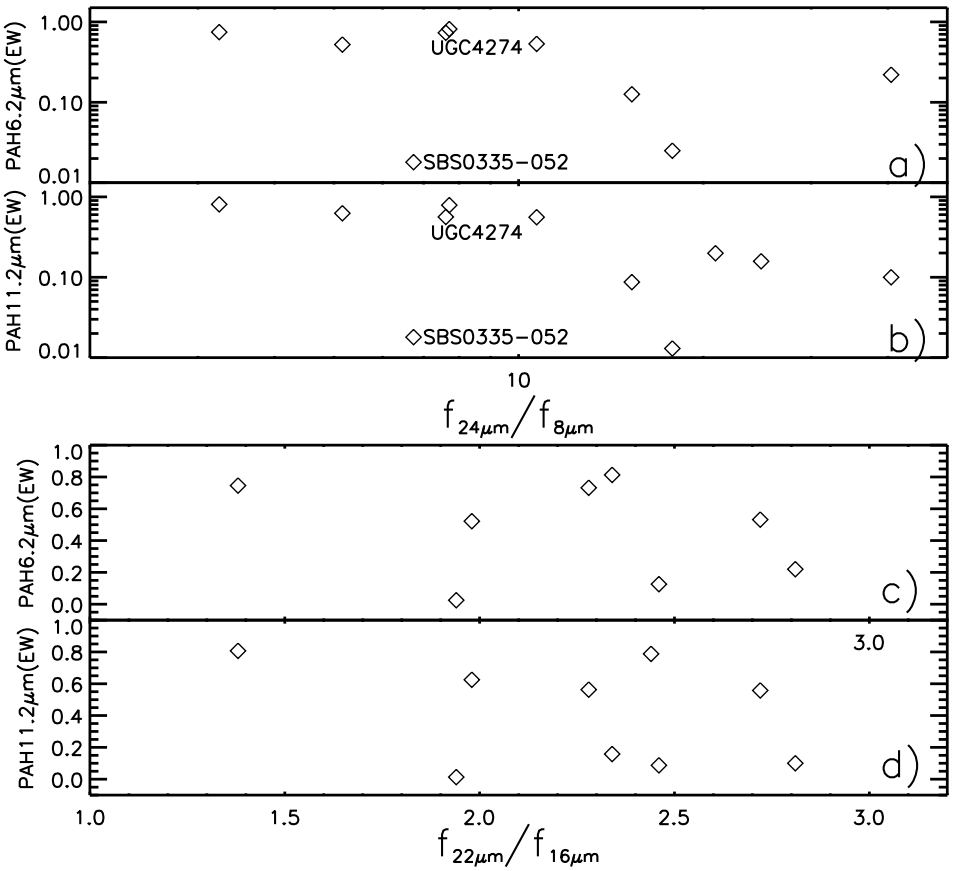

Figure 2.6 a) This figure presents the 6.2 μm PAH EW of our galaxies as a function of the 24 over 8 μm flux ratio. We note that with some scatter generally a lower f_{24}/f_8 indicates a larger PAH EW. b) Same as a) but for the 11.2 μm PAH EW. c) Same as a) but for using the 22 over 16 μm flux density ratio as the variable. There is no clear relation between the mid-IR spectral slope as indicated by f_{22}/f_{16} and the PAH strength. d) Same as c) but for 11.2 μm PAH EW.

and 11.2 μm as a function of the f_{24}/f_8 ratio in Figure 2.6a and 2.6b. We can see that overall a lower f_{24}/f_8 value indicates a stronger PAH emission, but there are some measurements that deviate from this trend. For completeness we also present the PAH EW at 6.2 μm and 11.2 μm as a function of f_{22}/f_{16} in Figure 2.6c and 2.6d but no clear correlation can be seen.

2.4.2 PAH and metallicity

In Section 1, we mentioned that the absence of PAH emission could be due to the low abundance of carbon and/or nucleating grains. In SBS0335-052E, the most metal poor galaxy for which a high quality mid-IR spectrum is available, there is an upper limit of just 0.018 μm in the EW of the 6.2μm feature (Houck et al. 2004b). To examine a possible variation in the PAH EW with metallicity, we plotted the PAH EW of 6.2 μm and 11.2 μm for our sample as function of their metallicity in Figure 2.7. The PAH EW were derived by integrating the flux of the feature in the mean spectra of both nod positions above an adopted continuum, and then divided by the average continuum flux in the integration range. The baseline was determined by fitting a spline function to the selected points. The wavelength limits for the integration of the features were approximately 5.95 μm to 6.55 μm for the 6.2 μm PAH, 7.15 μm to 8.20 μm for the 7.7 μm PAH, 8.20 μm to 8.90 μm for the 8.6 μm PAH and 10.80 μm to 11.80 μm for the 11.2 μm PAH feature. Here we only plot the 6.2 μm and 11.2 μm PAH EW, but measurements on the 7.7 μm and 8.6 μm PAH EW can be found in Table 2.4. We can see that PAH emission is absent in the most metal-poor BCDs and its strength is generally suppressed in a low metallicity environment. This result is contrary to what has been found in typical starburst galaxies where the PAH EW is much stronger with values greater than 0.5 μm for the 6.2 μm and 7.7 μm PAH bands (i.e. Brandl et al. 2004; Brandl et al. submitted 2005). In Figure 2.7, it appears that there is a trend showing that galaxies with a lower metallicity may have smaller PAH EW. Except for the two galaxies which have large uncertainty in their oxygen abundance, the PAH EW and metallicity seem to correlate quite well. The errors in the EW indicated in Figure 2.7 vary from one source to the other and are mainly due to the different SNR among the sources. Quantifying this relation by a least-squares (logarithmic)

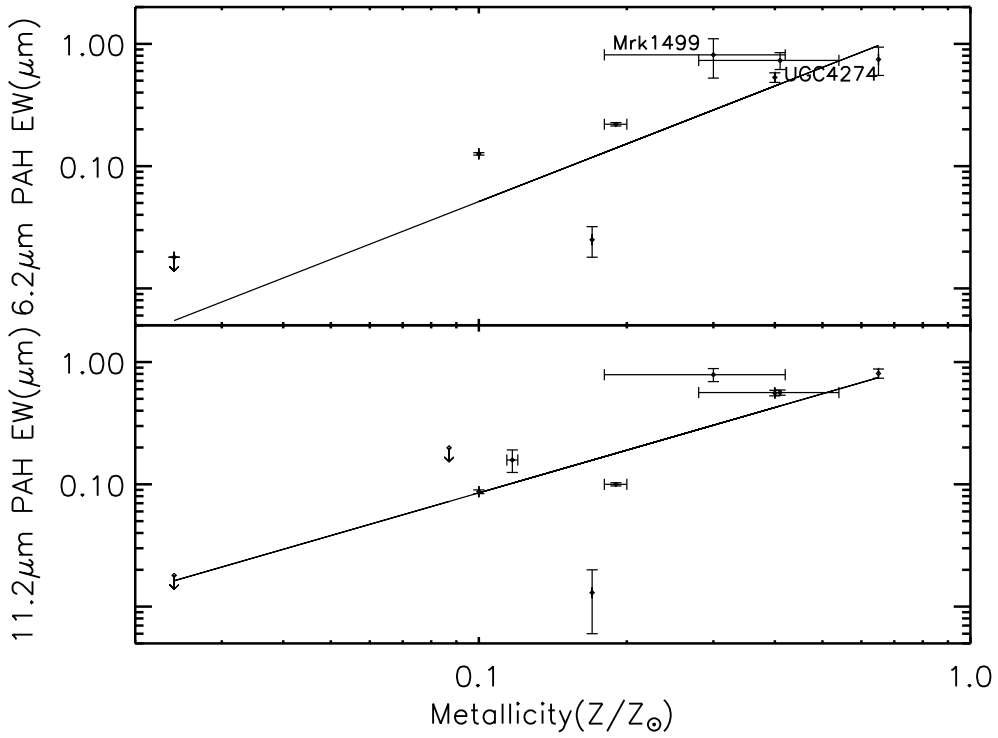

Figure 2.7 a) This figure shows the PAH EW at 6.2 μm vs metallicity. Note that the downward arrow indicates the upper limit for the PAH emission in SBS0335-052E. In some cases the extracted spectra of a target from the two nod positions of the slit differ. These uncertainties are translated into the error bars for the EW which, as we can see in Mrk1499, can be fairly large (also see text). b) Same as in a) but for the 11.2 μm PAH feature.

fit gives us a slope of N=1.57±0.63 for the 6.2 μm PAH EW and N=1.16±0.36 for the 11.2 μm PAH EW, where N is the exponent of a power law distribution. This weak trend we are seeing that the PAH EW is probably related to metallicity effects agrees with the relation suggested by Hogg et al. (2005) and Engelbracht et al. (2005).

Table 2.4. Spectroscopic Data of the Sources

Object Name	PAH EW (μm)				Flux[a]($\times 10^{-16}$W m^{-2})			
	6.2 μm	7.7 μm	8.6 μm	11.2 μm	[SIV](10.51 μm)	[NeII](12.81 μm)	[NeIII](15.55 μm)	[SIII](18.71 μm)
IZw18	···	···	···	···	0.06±0.01	<0.011	0.05±0.01	0.021±0.001
SBS0335-052	<0.018	···	···	<0.018	0.16±0.01	<0.016	0.135±0.004	0.045±0.004
UM461	···	···	···	<0.199	0.47±0.03	<0.021	0.29±0.01	0.09±0.01
Haro11	0.126±0.003	0.241±0.006	0.055±0.003	0.087±0.003	4.6±0.1	3.2±0.1	10.1±0.1	4.81±0.02
Mrk1450	···	···	···	0.158±0.033	0.75±0.02	0.13±0.01	0.96±0.02	0.46±0.01
IIZw40	0.025±0.007	0.069±0.005	0.009±0.003	0.013±0.007	18.6±0.4	0.60±0.03	11.4±0.3	4.7±0.2
NGC1569	0.220±0.007	0.402±0.012	0.045±0.004	0.100±0.003	14.8±0.4	1.55±0.08	17.4±0.3	7.2±0.2
Mrk1499	0.831±0.288	0.997±0.189	0.345±0.049	0.788±0.096	0.18±0.01	0.19±0.01	0.50±0.02	0.30±0.01
NGC1140	0.532±0.048	0.579±0.025	0.142±0.008	0.558±0.029	1.30±0.04	1.17±0.02	3.8±0.1	2.17±0.04
UGC4274	0.732±0.115	0.671±0.040	0.191±0.010	0.563±0.028	0.46±0.02	0.88±0.03	1.31±0.04	1.30±0.03
CG0598	0.746±0.194	0.954±0.075	0.331±0.036	0.807±0.070	0.13±0.02	0.206±0.004	0.18±0.03	0.23±0.01
CG0752	0.522±0.038	0.645±0.024	0.171±0.008	0.625±0.042	0.15±0.01	1.23±0.03	0.58±0.01	0.82±0.02

[a]The integrated fluxes are measured from the high resolution spectra of the targets. Background emission hasn't been subtracted and no scaling between the two modules, SH and LH has been applied.

[b] ··· indicates no available PAH EW measurement. It is mostly due to the low SNR of the spectrum. In this case, the determination of the continuum is highly uncertain and will significantly change the PAH EW. A much deeper observation with more exposure time has been submitted and more analysis will follow when data come in. For SBS0335-052, the SNR is high enough, but no PAH features can be identified in its mid-IR spectrum. We do not have a template to derive the upper limit of PAH EW at 7.7 μm and 8.6 μm.

2.4.3 The hardness of the radiation field

The presence of a young starburst in a low metallicity environment results in the production of high energy photons which can propagate relatively large distances before being absorbed by the metals in the ISM. High-resolution *IRS* spectra were taken of 26 galaxies and the results for the 12 BCDs that we discussed above are summarized in Figure 2.3 and Table 2.4. Because of the rather large difference in the ionization potentials of Ne^{++} (41eV) and Ne^{+} (22eV), the ratio of [NeIII]/[NeII] is a good tracer of the hardness of the interstellar radiation field (Thornley et al. 2000). The [SIV]/[SIII] ratio, another indicator of the hardness of the radiation field has also been studied in this paper. Given the fact that extinction in mid-IR is only a few percent of the optical extinction (Draine 2003), those line ratios are far less sensitive to the differential extinction compared to optical or UV lines. We plot the two line ratios in Figure 2.8. Since the extinction effects on [NeIII] (15.55 μm) and [NeII] (12.81 μm) are similar, the ratio of [NeIII]/[NeII] is only weakly affected by extinction, while for [SIV]/[SIII], we indicate the effect of differential extinction by the arrow on the upper left corner of the plot for an A_v of $\sim$13 mag.

We also studied the dependence of [NeIII]/[NeII] ratio on metallicity and the results are presented in Figure 2.9. We find that our 11 BCDs (CG0752, which has no metallicity measurements in literature, is not included.) appear to define a band, where galaxies with lower metallicity display a higher [NeIII]/[NeII] ratio, thus harboring a harder radiation field. For a given [NeIII]/[NeII] ratio, there is significant scatter within metallicities. This scatter could be due to local variations or differential/patchy dust extinction in these systems. It also suggests that the metallicity may not be the only factor that affects the hardness of the radiation field. The results on the [SIV]/[SIII] ratio are plotted in Figure 2.10 and we can see that it shares a similar trend as the [NeIII]/[NeII] ratio. For the discussion

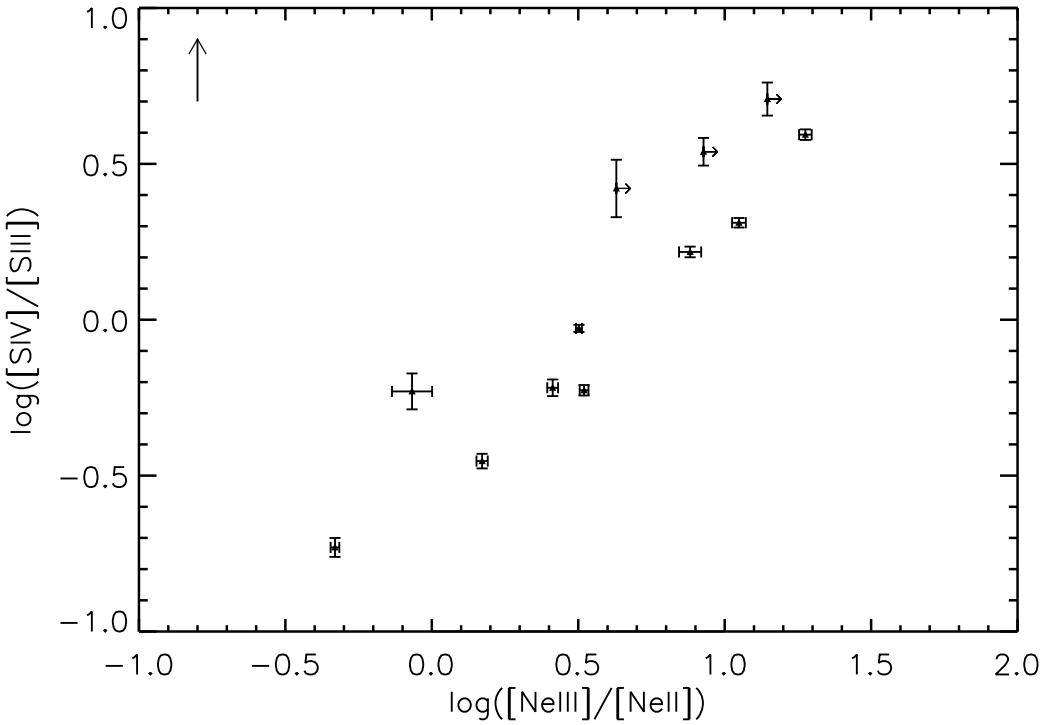

Figure 2.8 This plot shows the log([SIVλ10.51 μm]/[SIIIλ18.71 μm]) ratio as a function of log([NeIIIλ15.55 μm]/[NeIIλ12.81 μm]) for our sample. Both ratios are indicators of the hardness of the ionization field. Since no [NeII] has been detected in the high resolution spectrum of SBS0335-052, IZw18 and UM461, the lower limits of the [NeIII]/[NeIII] ratios are represented by arrows. No correction has been made for extinction. The effect of the differential extinction on the ratio of [SIV]/[SIII] is indicated by the arrow on the upper left corner for A_v $\sim$13 mag.

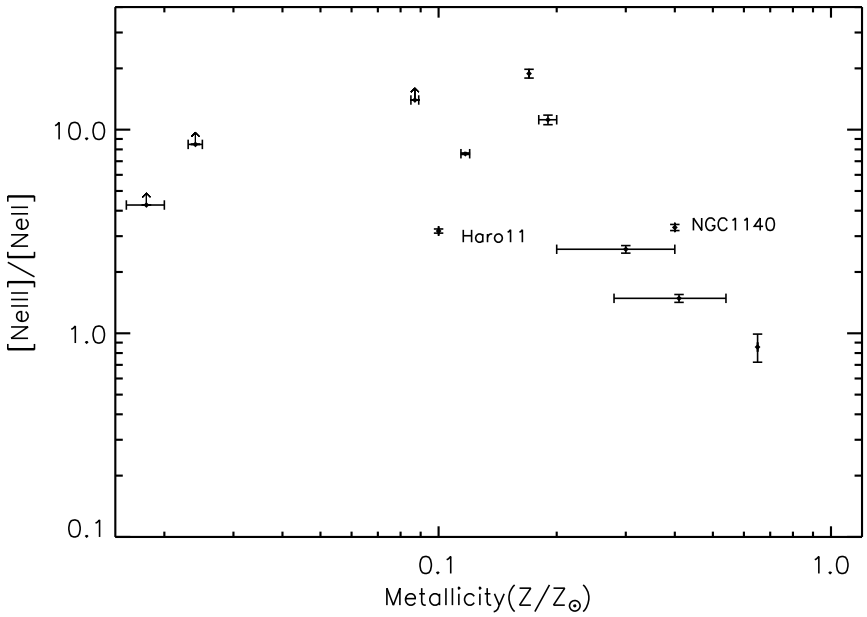

Figure 2.9 The strength of the [NeIIIλ15.55 μm]/[NeIIλ12.81 μm] ratio as a function of metallicity for our sample. The fluxes of [NeIII] and [NeII] were measured using the high resolution spectra of the sources and the metallicity (and its uncertainty) were obtained from the literature (see Table 2). Note that no [NeII] has been detected in SBS0335-052E, IZw18 and UM461, so we are showing the lower limit of [NeIII]/[NeII] by an up-pointing arrow.

that follows we choose the [NeIII]/[NeII] ratio since it is less dependent on the extinction and the neon lines are generally stronger. Further more, the [NeIII] and [NeII] lines span a wider range in ionization potential than [SIV] and [SIII].

2.4.4 PAH and the [NeIII]/[NeII] ratio

As discussed by Madden (2000), PAHs are at best a minor dust component in dwarf galaxies. In Figure 2.11, we plot the EW of the 6.2 and 11.2 μm PAHs as a function of the hardness of the radiation field, using [NeIII]/[NeII] as an indicator. We observe that the PAH EWs at 6.2 and 11.2 μm are generally suppressed in a harder radiation field as indicated by a larger [NeIII]/[NeII] ratios, suggesting

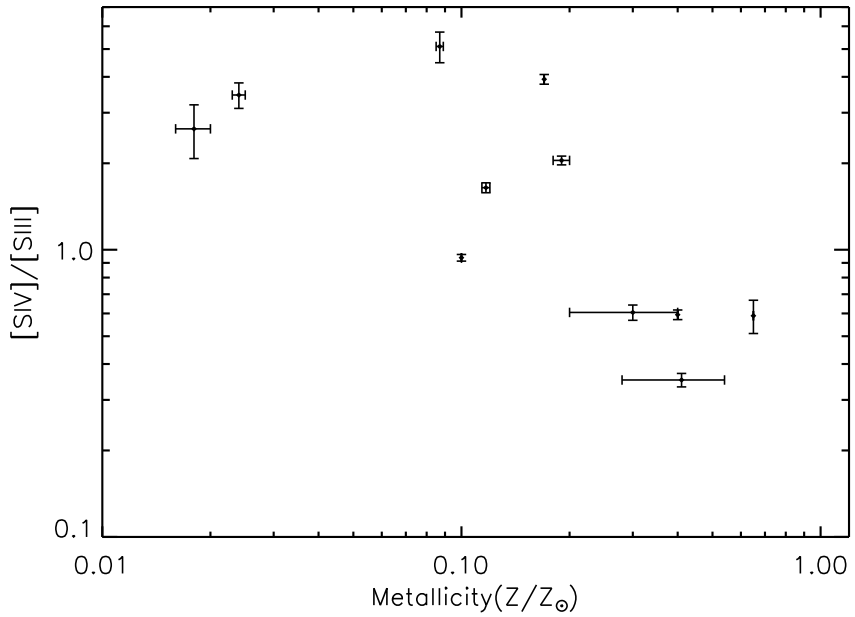

Figure 2.10 Same as Figure 8 but for [SIVλ10.51 μm]/[SIIIλ18.71 μm].

that the deficiency in PAH emission may be related to the destruction of the photodissociation region (PDR) by hard UV photons. However, the trend we see is weak. A conventional least-squares fit that minimizes (logarithmic) residuals in PAH EW yields a slope of N=-0.91±0.31 for the 6.2 μm PAH and N=-0.92±0.27 for the 11.2 μm PAH. In addition, we found that for a given [NeIII]/[NeII] ratio, we can have different PAH EW values. For example Haro11 has a considerably weaker PAH EW at both 6.2 μm and 11.2 μm as compared with NGC1140 even though they have a very similar [NeIII]/[NeII] ratio. This scatter indicates that some other or additional process is in play.

2.4.5 PAH and luminosity density

Another important parameter of the radiation field is its UV luminosity density. Does this also play a role in the destruction of PAH molecules? In young starbursts,

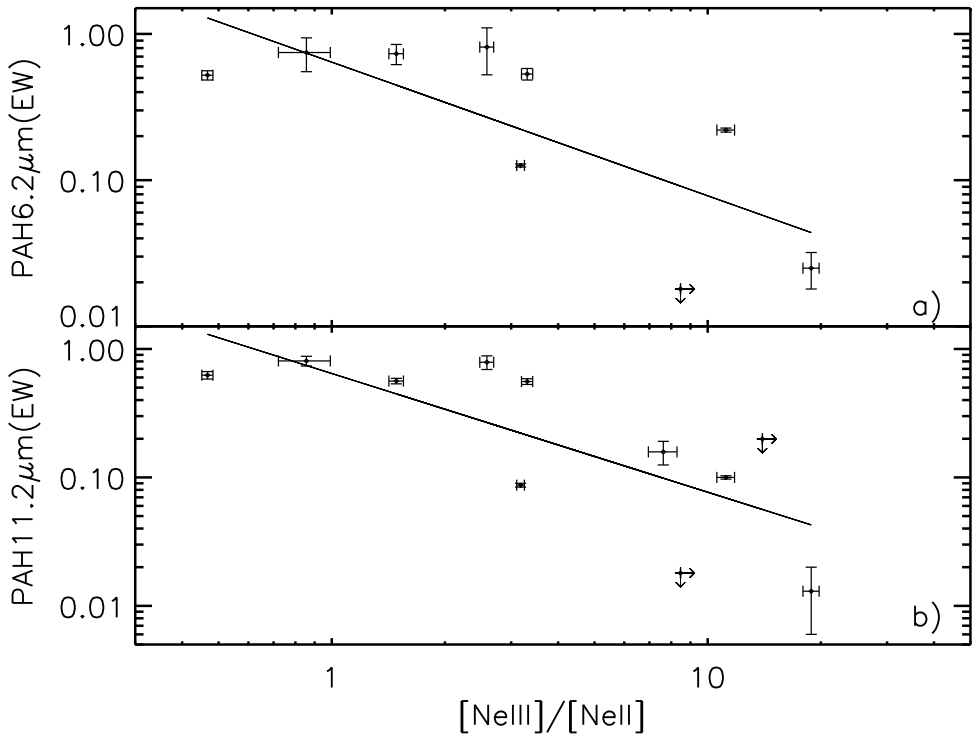

Figure 2.11 a) The EW of the 6.2 μm PAH as a function of the [NeIII]/[NeII] ratio. Note that since no PAH emission was detected in SBS0335-052E, the upper limit of its EW is indicated by a downward arrow. Similarly, the lower limit of the [NeIII]/[NeII] ratio for this source is indicated by right-pointing arrow since no [NeII] can be seen in the spectrum. b) Same as a) but for the 11.2 μm PAH.

L_{FIR} is representative of the total UV luminosity. We estimate the luminosity density of the 12 BCDs in our sample, using the 22 μm luminosity. Takeuchi et al. (2005) show that there is linear relation between the mid-IR luminosities (12 μm or 25 μm) and the total infrared luminosity, even though Dale et al. (2005) has shown a peak-to-peak uncertainty of a factor of 5 in using the 24 μm luminosity to indicate the total infrared luminosity for their sample of starburst galaxies. We calculate $L_{22\mu m}$ using the 22μm images obtained with the red peak-up camera and divide it by the estimated volume (V) of the objects from their optical or infrared images[10]. This should be proportional to the UV luminosity density. The results are listed in Table 2.5. We present the 6.2 and 11.2μm PAH EW as a function of the 22μm luminosity density in Figure 2.12. There are fewer data points on the plot compared to the table since we do not have PAH EW measurement for all the galaxies in Table 2.5. We can see that there is a trend that PAH EW decreases with increasing luminosity density. However, this relation is somewhat weak. A least-squares fit (logarithmic) of the slope returns N=-0.63$\pm$0.21 for the 6.2 μm PAH and N=-0.77$\pm$0.18 for the 11.2 μm PAH. There is considerable scatter on this plot. For instance, SBS0335-052E and Haro11 have very similar $L_{22\mu m}$/V value, but we have not found any PAH emission in SBS0335-052E while PAHs are weak but clearly present in Haro11.

A plot of the dependence of the PAH EW as a function of the product of the hardness of the radiation field and the luminosity density, [NeIII]/[NeII]*$L_{22\mu m}$/V is presented in Figure 2.13. We observed that it is better correlated than both the PAH EW vs [NeIII]/[NeII] and PAH EW vs luminosity density. A least-squares fit (logarithmic) returns N=-0.39$\pm$0.12 for 6.2 μm PAH and N=-0.47$\pm$0.10 for 11.2 μm PAH. This suggests that an increased density of harder photons destroys

[10]We use the mid-infrared images to estimate the volume for sources that are resolved at 22 μm and the optical images for the rest of the sample.

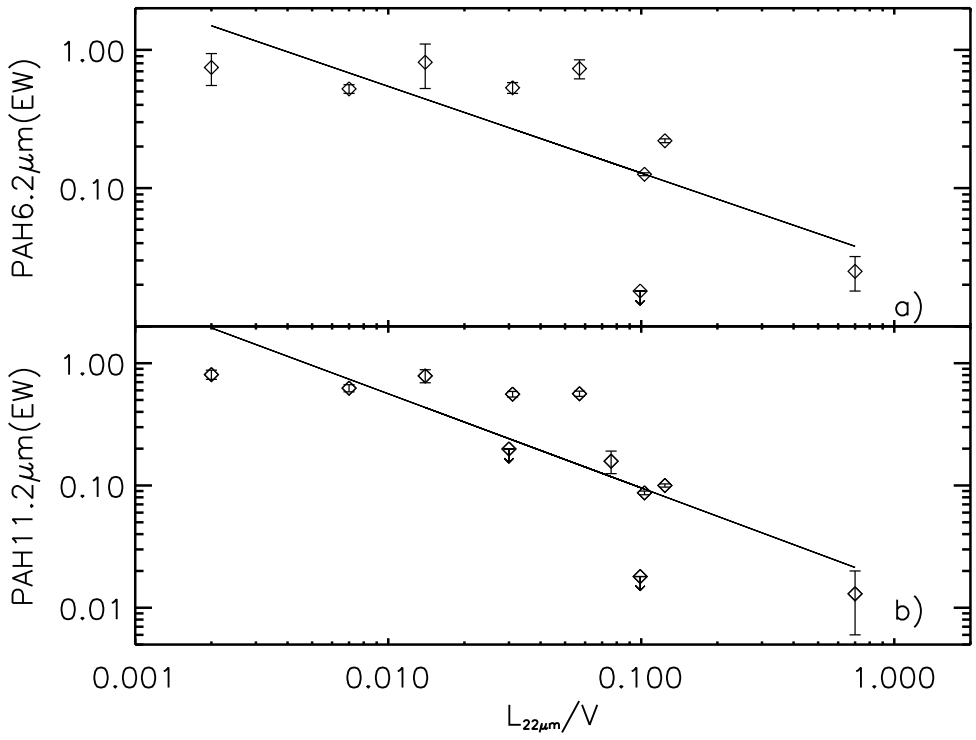

Figure 2.12 a) The EW of the 6.2 μm PAH vs the luminosity density indicated by $L_{22\mu m}/V$. We can see that there is a general trend that as the luminosity density of the galaxy increases, the PAH EW decreases. b) Same as a) but for the 11.2 μm PAH.

Table 2.5. Galaxy luminosity and volume

Object	$f_{22\mu m}$[a] (Jy)	Radius[b] (arcsec)	$L_{22\mu m}$[c] ($\times 10^8 L_\odot$)	Volume ($\times 10^9 pc^3$)	$L_{22\mu m}$/Volume ($L_\odot/pc^3$)
IZw18	0.006	7.2	0.01	0.2	0.007
SBS0335-052	0.080	3.8	3.8	3.9	0.099
UM461	0.030	6.8	0.1	0.4	0.030
Haro11	2.307	9.9	249.7	241.4	0.103
Mrk1450	0.053	5.9	0.1	0.2	0.076
IIZw40	1.482	9.5	2.1	0.3	0.700
NGC1569	2.596	55.4	0.2	0.1	0.124
Mrk1499	0.030	6.1	0.6	4.6	0.014
NGC1140	0.279	28.0	1.8	5.8	0.031
UGC4274	0.120	30.5	0.1	0.1	0.057
CG0598	0.025	5.9	20.8	1185.6	0.002
CG0752	0.149	9.9	16.9	258.3	0.007

[a]The 22 μm flux density are calculated using the "synthetic" method.

[b]The radius of the galaxy is measured using the optical image retrieved from the Digitized Sky Survey(DSS) for point sources. For the four extended sources mentioned earlier, we used their mid-IR size measured from the 22 μm images.

[c]The 22 μm luminosity in the red peak-up filter(18.5-26.0 μm).

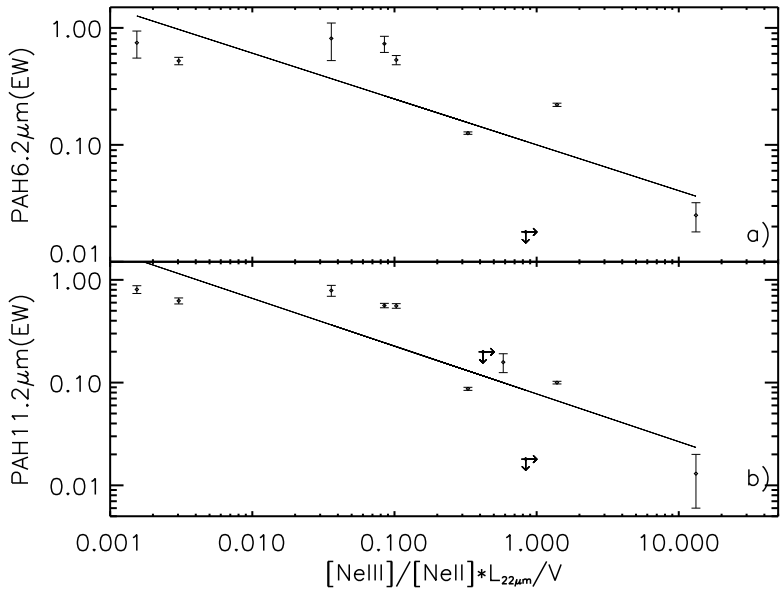

Figure 2.13 a) The dependence of the 6.2 μm PAH EW on the ([NeIII]/[NeII])$\times$($L_{22\mu m}$/V). It is clear that the PAH EW decreases as this quantity increases, indicating that for the same physical volume a more luminous starburst with harder radiation, destroys the PAHs. b) Same as a) but for the 11.2 μm PAH.

more PAH molecules. The fact that we are seeing a better correlation on Figure 2.13 than in Figure 2.11 or Figure 2.12 suggests that both the luminosity density and the hardness of the radiation field contribute to the destruction of PAHs.

2.4.6 PAHs: formation and destruction effects

We have shown in the previous section that there are generally weaker PAHs in metal-poor environments. We have also discussed the effects of the hardness of the radiation field and the luminosity density on the destruction of PAH molecules. Is the absence of PAHs in metal-poor galaxies solely due to formation effects or destruction effects or some combination? To examine this we plot the PAH EW as a function a new quantity: ([NeIII]/[NeII])$\times$($L_{22\,\mu m}$/V)$\times$(1/Z), where the product of the neon ratio and the luminosity density represents the destruction effect and

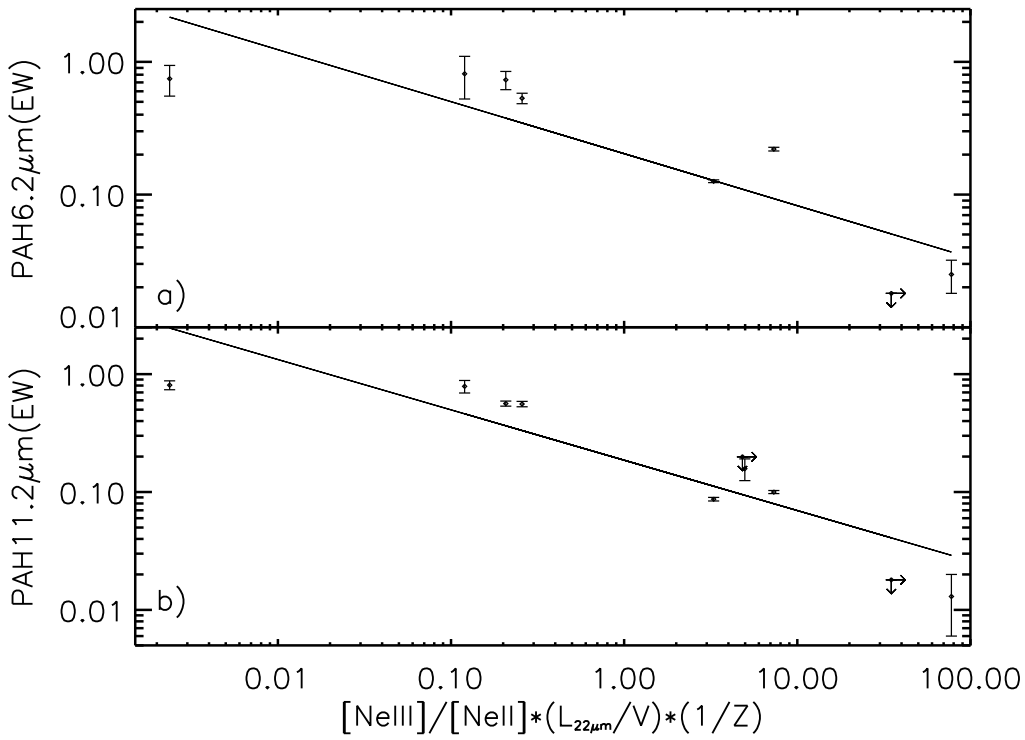

Figure 2.14 a) The PAH EW at 6.2 μm vs the product of the hardness of the radiation field and the luminosity density, divided by the metallicity of the galaxy. We can see that there is a strong anti-correlation where the PAH EW decreases when the factor ([NeIII]/[NeII])$\times$($L_{22\mu m}$/V)$\times$(1/Z) increases. b) Same as a) but for the 11.2 μm PAH.

Z, the metallicity of the galaxy, represents the formation effect. We can see in Figure 2.14 that there is a much tighter anti-correlation on this plot as compared to the previous series of plots on the PAH EW we have shown. A least-squares fit (logarithmic) gives a slope of N=-0.39$\pm$0.09 for the 6.2 μm PAH and N=-0.43$\pm$0.08 for the 11.2 μm PAH. We conclude that both the formation effects (Z) and the destruction effects ([NeIII]/[NeII])$\times$($L_{22\,\mu m}$/V) contribute to the weak PAH EW.

2.5 Conclusions

We have explored the mid-IR properties of blue compact dwarf galaxies with *Spitzer IRS*. We obtained broad band images at 16 and 22 μm from the *IRS* peak-up camera. Using the low-resolution *IRS* spectra, we detected emission from PAHs, at 6.2, 7.7, 8.6, 11.2 and 12.8 μm, for most of our galaxies though the strength varies considerably. We also detected a number of fine structure lines in our mid-IR spectra, including [SIV], [NeII], [NeIII] and [SIII] and found that for metallicities ranging between 1/50 $Z_\odot$ to 0.65 $Z_\odot$, the line ratios, [NeIII]/[NeII] and [SIV]/[SIII], which measure the hardness of the ionization field, vary inversely with metallicity. Our study yielded the following conclusions:

1) The ratio of f_{22}/f_{16} is $\sim$2.5$\pm$0.6 on average, but it does not show any dependence on metallicity.

2) Both the emission of PAHs and a hot dust component affect the f_{22}/f_8 (or f_{24}/f_8) ratio in a similar way. These effects are difficult to disentangle without mid-IR spectra or measurements of the mid-IR fluxes at several wavelengths. Predictions of the strength of PAHs based on a single pair of mid-IR broad band fluxes may be problematic and should be used with caution (see Figure 2.5 and 2.6).

3) The emission of PAHs in metal-poor BCDs is generally suppressed (see Figure 2.7).

4) The product of the hardness of the radiation field as traced by the neon line ratio with the mid-IR luminosity density, a "stand in" for the intensity of UV luminosity, correlates well with the PAH EW (see Figure 2.13).

5) The product of the hardness of the radiation field and the luminosity density divided by the metallicity of the galaxies has a strong correlation with the PAH EW. This suggests that the absence of PAHs in metal-poor environment is due to a combination of formation effects and destruction effects (Figure 2.14).

Acknowledgements We would like to thank D. Devost, L. Armus, Aigen Li and G.S. Sloan for insightful discussions. We also thank the anonymous referee whose careful reading and detailed comments greatly improved this manuscript. The IRS was a collaborative venture between Cornell University and Ball Aerospace Corporation funded by NASA through the Jet Propulsion Laboratory and the Ames Research Center. Support for this work was provided by NASA through Contract Number 1257184 issued by JPL/Caltech.

BIBLIOGRAPHY

Armus, L., et al. 2004, ApJS, 154, 178

Arp, H., & Sandage, A. 1985, AJ, 90, 1163

Arp, H., & Oconnell, R. W. 1975, ApJ, 197, 291

Arp, H. 1965, ApJ, 142, 402

Baldwin, J. A., Spinrad, H., & Terlevich, R. 1982, MNRAS, 198, 535

Brandl, B. R., et al. 2004, ApJS, 154, 188

Brandl, B. R., et al. 2005, submitted

Bergvall, N., Masegosa, J., Östlin, G., & Cernicharo, J. 2000, A&A, 359, 41

Brinks, E., Klein, U. 1988, MNRAS, 231, 63p

Charmandaris, V., et al. 2004, ApJS, 154, 142

Cairós, L. M., Caon, N., Vílchez, J. M., González-Pérez, J. N., & Muñoz-Tuñón, C. 2001, ApJS, 136, 393

Calzetti, D. 1997, AJ, 113, 162

Cerviño, M., & Mas-Hesse, J. M. 1994, A&A, 284, 749

Cohen, M., Megeath, T.G., Hammersley, P.L., Martin-Luis, F., & Stauffer, J. 2003, AJ, 125, 2645

Conti, P. S. 1991, ApJ, 377, 115

Cruzen, S. T., Weistrop, D., & Hoopes, C. G. 1997, AJ, 113, 1983

Dale, D. A. et al. 2005, ApJ, 633, 857

De Vaucoulers, G., De Vaucoulers, A., Corwin Jr., H. G., Buta, R. J. Paturel, G., & Fouque, P. 1991, Third Reference Catalogue of Bright Galaxies, version 3.9

Deeg, H.-J., Duric, N., & Brinks, E. 1997, A&A, 323, 323

Denicoló, G., Terlevich, R., & Terlevich, E. 2002, MNRAS, 330, 69

Dwek, E. 2004, in "The Spectral Energy Distribution of Gas-Rich Galaxies: Confronting Models with Data", Heidelberg, 4-8 Oct. 2004, eds. C.C. Popescu and R.J. Tuffs, AIP Conf. Ser., in press, astro-ph/0412344

Doublier, V., Comte, G., Petrosian, A., Surace, C., & Turatto, M. 1997, A&AS, 124, 405

Doublier, V., Caulet, A., & Comte, G. 1999, A&AS, 138, 213

Draine, B. T. 2003, ARA&A, 41, 241

Engelbracht, C. W., Gordon, K. D., Rieke, G. H., Werner, M. W., Dale, D. A., & Latter, W. B. 2005, ApJ, 628, L29

Förster Schreiber, N. M., Roussel, H., Sauvage, M., & Charmandaris, V. 2004, A&A, 419, 501

Gallego, J., Zamorano, J., Rego, M., & Vitores, A. G. 1997, ApJ, 475, 502

Galliano, F., Madden, A. P., Jones, C. D., Wilson, J.-P., & F. Le Peintre 2003, A&A, 407, 159

Galliano, F., Madden, S. C., Jones, A. P., Wilson, C. D., & Bernard, J.-P. 2005, A&A, 434, 867

Gil de Paz, A. 2000, Ph.D thesis

Gil de Paz, A., Madore, B. F., & Pevunova, O. 2003, ApJS, 147, 29

Guseva, N. G., Papaderos, P., Izotov, Y. I., Green, R. F., Fricke, K. J., Thuan, T. X., & Noeske, K. G. 2003, A&A, 407, 91

Guseva, N. G., Papaderos, P., Izotov, Y. I., Green, R. F., Fricke, K. J., Thuan, T. X., & Noeske, K. G. 2003, A&A, 407, 105

Heisler, C. A., & Vader, J. P. 1994, AJ, 107, 35

Heisler, C. A., & Vader, J. P. 1995, AJ, 110, 87

Higdon, S. J. U., et al. 2004, PASP, 116, 975

Ho, L. C., Filippenko, A. V., & Sargent, W. L. W. 1997, ApJS, 112, 315

Ho, L. C., Filippenko, A. V., & Sargent, W. L. 1995, ApJS, 98, 477

Hogg, D. W., Tremonti, C. A., Blanton, M. R., Finkbeiner, D. P., Padmanabhan, & N., Quintero, A. D., Schlegel, D. J., & Wherry, N. 2005, ApJ, 624, 162

Houck, J. R, et al. 2004, ApJS, 154, 18

Houck, J. R., et al. 2004, ApJ, 154, 211

Hunt, L., Bianchi, S., & Maiolino, R. 2005, A&A, 434, 849

Hunter, D. A., Gallagher, J. S., Rice, W. L., & Gillett, F. C. 1989, ApJ, 336, 152

Hunter, D. A., O'Connell, R. W., & Gallagher, J. S. 1994, AJ, 108, 84

Israel, F. P. 1988, A&A, 198, 109

Izotov, Y. I., Foltz, C. B., Green, R. F., Guseva, N. G., & Thuan, T. X. 1997, ApJ, 487, L37

Izotov, Y. I., Lipovetsky, V. A., Chaffee, F. H., Foltz, C. B., Guseva, N. G., & Kniazev, A. Y. 1997, ApJ, 476, 698

Izotov, Y. I., & Thuan, T. X. 1999, ApJ, 511, 639

Izotov, Y. I., & Thuan, T. X. 2004, ApJ, 616, 768

Izotov, I. I., Thuan, T. X, & Gauseva, N. G. 2005, Aj accepted

Jarrett, T. H., Chester, T., Cutri, R., Schneider, S. E., & Huchra, J. P. 2003, AJ, 125, 525

Kinman, T. D., & Davidson, K. 1981, ApJ, 243, 127

Kinney, A. L., Bohlin, R. C., Calzetti, D., Panagia, N., & Wyse, R. F. G. 1993, ApJS, 86, 5

Kirshner, R. P., Oemler, A., Schechter, P. L. & Shectman, S. A., 1981, ApJ, 248, l57

Kniazev, A. Y., Pustilnik, S. A., Grebel, E. K., Lee, H., & Pramskij, A. G. 2004, ApJS, 153, 429

Kniazev, A. Y., Pustilnik, S. A., Ugryumov, A. V., & Pramsky, A. G. 2001, A&A, 371, 404

Kniazev, A. Y., et al. 2000, A&A, 357, 101

Kniazev, A.Y., Pustilnik, S.A., Ugryumov, A.V. 1998, Bull. Special Astrophys. Obs., 46, 23

Kobulnicky, H. A., & Skillman, E. D. 1997, ApJ, 489, 636

Kunth, D. & Östlin, G. 2000, A&A Rev., 10, 1

Lamb, S. A., Hjellming, M. S., Gallagher, J. S., & Hunter, D. A. 1986, Star Formation in Galaxies, ed. J. C. Lonsdale persson(NASA CP-2466), 259

Lauberts, A., & Valentijn, E. A. 1989, Garching: European Southern Observatory, —c1989

Legrand, F., Kunth, D., Roy, J.-R., Mas-Hesse, J. M., & Walsh, J. R. 1997, A&A, 326, L17

Madden, S. C. 2000, New Astronomy Review, 44, 249

Madden, S. C. Galliano, F., Jones, A. P., Sauvage, M. 2006, A&A, 446, 877

Mas-Hesse, J. M., & Kunth, D. 1999, A&A, 349, 765

Masegosa, J., Moles, M. & Campos-Aguilar, A. 1994, apj, 420, 576

Meier, D. S., Turner, J. L., Crosthwaite, L. P., & Beck, S. C. 2001, AJ, 121, 740

Papaderos, P., Izotov, Y. I., Fricke, K. J., Thuan, T. X., & Guseva, N. G. 1998, A&A, 338, 43

Peimbert, M., & Torres-Peimbert, S. 1992, A&A, 253, 349

Petrosian, A. R., Movsessian, T., Comte, G., Kunth, D., & Dodonov, S. 2002, A&A, 391, 487

Plante, S. & Sauvage, M. 2002, AJ, 124, 1995

Popescu, C. C., & Hopp, U. 2000, A&AS, 142, 247

Pustilnik, S. A., Kniazev, A. Y., Masegosa, J., Márquez, I. M., Pramskij, A. G., & Ugryumov, A. V. 2002, A&A, 389, 779

Roche, P. F., Aitken, D. K., Smith, C. H., & Ward, M. J. 1991, MNRAS, 248, 606

Rosenberg, J. L., Ashby, M. L. N., Salzer, J., & Huang, Jia-sheng, ApJ, 636, 742

Sanders, D. B, & Mirabel, I. F. 1996, ARA&A, 34,749

Sanduleak, N., & Pesch, P. 1987, ApJS, 63, 809

Sargent, W. L. W., & Searle, L. 1970, ApJ, 162, L155

Searle, L. & Sargent, W. L. W. 1972, ApJ, 173, 25

Skillman, E. D. & Kennicutt, R. C. 1993, ApJ, 411,655

Spinoglio, L., Malkan, M. A., Rush, B., Carrasco, L., & Recillas-Cruz, E. 1995, ApJ, 453, 616

Stasinska, G., & Leitherer, C. 1996, ApJS, 107, 661

Takeuchi, T. T., Buat, V., Iglesias-Páramo, J., Boselli, A., & Burgarella, D. 2005, A&A, 432, 423

Thornley, M. D., Schreiber, N. M. F., Lutz, D., Genzel, R., Spoon, H. W. W., Kunze, D., & Sternberg, A. 2000, ApJ, 539, 641

Thuan, T. X., Sauvage, M., & Madden, S. 1999, ApJ, 516, 783

Thuan, T. X., Izotov, Y. I., & Lipovetsky, V. A. 1997, ApJ, 477, 661

Thuan, T. X. 1983, ApJ, 268, 667

Tully, R. B., Boesgaard, A. M., Dyck, H. M., & Schempp, W. V. 1981, ApJ, 246, 38

Vader,J. P., Frogel, J. .A. Terndrup, D. A., & Heisler, C. A. 1993, AJ, 106, 1743

Vennik, J., Hopp, U., & Popescu, C. C. 2000, A&AS, 142, 399

Vitores, A. G., Zamorano, J., Rego, M., Alonso, O., & Gallego, J. 1996, A&AS, 118, 7

Waller, W. H. 1991, ApJ, 370, 144

Werner, M., et al. 2004, ApJS, 154,1

Wu, Yanling, et al. 2006, ApJ, in preparation

Young, C. K., & Currie, M. J. 1998, A&AS, 127, 367

Zwicky, F. 1966, ApJ, 143, 192

CHAPTER 3

ELEMENTAL ABUNDANCES OF BLUE COMPACT DWARFS FROM MID-IR SPECTROSCOPY WITH *SPITZER*[*]

Abstract We present a study of elemental abundances in a sample of thirteen Blue Compact Dwarf (BCD) galaxies, using the ∼10–37μm high resolution spectra obtained with Spitzer/IRS. We derive the abundances of neon and sulfur for our sample using the infrared fine-structure lines probing regions which may be obscured by dust in the optical and compare our results with similar infrared studies of starburst galaxies from ISO. We find a good correlation between the neon and sulfur abundances, though sulfur is under-abundant relative to neon with respect to the solar value. A comparison of the elemental abundances (neon, sulfur) measured from the infrared data with those derived from the optical (neon, sulfur, oxygen) studies reveals a good overall agreement for sulfur, while the infrared derived neon abundances are slightly higher than the optical values. This indicates that either the metallicities of dust enshrouded regions in BCDs are similar to the optically accessible regions, or that if they are different they do not contribute substantially to the total infrared emission of the host galaxy.

3.1 Introduction

Blue Compact Dwarf Galaxies (BCDs) are dwarf galaxies with blue optical colors resulting from one or more intense bursts of star-formation, low luminosities ($M_B > -18$) and small sizes. The first BCD discovered was I Zw 18 by Zwicky (1966), which had the lowest oxygen abundance observed in a galaxy (Searle & Sargent 1972), until the recent study of the western component of SBS0335-052 (Izotov et al. 2005). Although BCDs are defined mostly by their morphological parameters,

[*]Originally published as: Yanling Wu, J. Bernard-Salas, V. Charmandaris, V. Lebouteiller, Lei Hao, B. R. Brandl, J. R. Houck, (2008), *The Astrophysical Journal*, 673, 193

they are globally found to have low heavy element abundances as measured from their HII regions ($1/30\,Z_{\odot}$~$1/2\,Z_{\odot}$). The low metallicity of BCDs is suggestive of a young age since their interstellar medium is chemically unevolved. However, some BCDs do display an older stellar population and have formed a large fraction of their stars more than 1Gyr ago (see Loose & Thuan 1985; Aloisi et al. 2007). The plausible scenario that BCDs are young is intriguing within the context of Cold Dark Matter models which predict that low-mass dwarf galaxies, originating from density perturbations much less massive than those producing the larger structures, can still be forming at the current epoch. However, despite the great success in detecting galaxies at high redshift over the past few years, bona fide young galaxies still remain extremely difficult to find in the local universe (Kunth & Sargent 1986; see the review by Kunth & Östlin 2000; Madden et al. 2006). This is likely due to the observational bias of sampling mostly luminous more evolved galaxies at high redshifts. If some BCDs are truly young galaxies, they would provide an ideal local laboratory to understand the galaxy formation processes in the early universe.

Over the past two decades, BCDs have been studied extensively in many wavelengths using ground-based and space-born instruments (see the review by Kunth & Östlin 2000). In the FUV, the Far Ultraviolet Spectroscopic Explorer (FUSE) has been used to study the chemical abundances in the neutral gas in several BCDs (Thuan et al. 2002; Aloisi et al. 2003; Lebouteiller et al. 2004). Optical spectra have been obtained for a large number of BCDs and display strong narrow emission lines resulting from the intensive star-formation processes that take place in these systems (Izotov et al. 1997; Izotov & Thuan 1999b; Pustilnik et al. 2005; Salzer et al. 2005). The Infrared Space Observatory (ISO) revealed unexpectedly that despite their low metallicities, BCDs, such as SBS 0335-052E, could still have copious emission from dust grains (Thuan et al. 1999; Madden 2000; Madden et

al. 2006; Plante & Sauvage 2002). More recently, the Spitzer Space Telescope (Werner et al. 2004) has been used to observe these metal-poor dwarf systems in order to study their dust continuum properties and the polycyclic aromatic hydrocarbon (PAH) features (Houck et al. 2004b; Hogg et al. 2005; Engelbracht et al. 2005; Rosenberg et al. 2006; Wu et al. 2006; O'Halloran et al. 2006; Hunt et al. 2006; Wu et al. 2007). Finally, radio observations have also been performed for several BCDs to study their HI kinematics and distribution (Thuan et al. 2004) and thermal/non-thermal continuum emission properties (Hunt et al. 2005).

Metallicity is a key parameter that influences the formation and evolution of both stars and galaxies. Detailed studies of the elemental abundances of BCDs have already been carried out by several groups (Izotov & Thuan 1999b; Kniazev et al. 2003; Shi et al. 2005) and the well known metallicity-luminosity relation has also been studied in detail in the environment of dwarf galaxies (Skillman et al. 1989; Hunter & Hoffman 1999; Melbourne & Salzer 2002). However, because these studies were performed in the optical, they were limited by the fact that the properties of some of the deeply obscured regions in the star-forming galaxies may remain inaccessible due to dust extinction at these wavelengths. In fact, Thuan et al. (1999), using ISO, have shown that the eastern component of SBS 0335-052 does have an embedded super star cluster (SSC) that is invisible in the optical while contributing $\sim$75% to the bolometric luminosity (see also Plante & Sauvage 2002; Houck et al. 2004b), even though it has very low metallicity (12+log(O/H)=7.33), which would in principle imply a low dust content. In addition to probing the dust enshrouded regions, emission in the infrared also has the advantage that the lines accessible at these wavelengths are less sensitive to the electron temperature fluctuations than the corresponding optical lines of the same ion. In the infrared, more ionization stages of an element become available as well. The improved

sensitivity of the Infrared Spectrograph (IRS[1]) (Houck et al. 2004a) on Spitzer has enabled us to obtain for the first time infrared spectra for a much larger sample of BCDs than was previously possible (Thuan et al. 1999; Madden 2000; Verma et al. 2003; Martín-Hernández et al. 2006), thus motivating this study to probe the heavy element abundances in BCDs.

In this paper, we analyze Spitze/IRS spectra of thirteen BCDs and present elemental abundances of neon and sulfur, which are both primary elements produced by the same massive stars in the nuclear synthesis processes. In section 2, we describe the sample selection, observations and data reduction. We present our results on the chemical abundances in section 3, followed by a comparison of the optical and infrared derived abundances in section 4. We show the interplay between the abundances and PAH emission in section 5. Finally, we summarize our conclusions in section 6.

3.2 Observations and Data Reduction

As part of the *IRS* Guaranteed Time Observation (GTO) program, we have compiled a large sample of BCD candidates selected from the Second Byurakan Survey (SBS), Bootes void galaxies (Kirshner et al. 1981; Popescu & Hopp 2000), and other commonly studied BCDs. Details on the low-resolution spectra of the sample have been published by Wu et al. (2006).

We acquired the targets using the red (22μm) IRS peak-up camera in high accuracy mode to locate the mid-IR centroid of the source and then offset to the appropriate slit using the standard IRS staring observing mode. Subsequently, we obtained the 10$-$37 μm spectra for our sources using the *IRS* Short-High (SH, 9.9-

[1]The IRS was a collaborative venture between Cornell University and Ball Aerospace Corporation funded by NASA through the Jet Propulsion Laboratory and the Ames Research Center.

19.6 μm) and Long-high (LH, 18.7-37.2 μm) modules. No spectra of the background were obtained. The AORkey and on-source integration time of the twenty-two sources for which we obtain high-resolution spectroscopy are given in Table 6.1. In this paper, we focus on the description and analysis of thirteen BCDs from our program which have a signal-to-noise ratio (SNR) high enough for our elemental abundance study.

The data were processed by the *Spitzer* Science Center (SSC) pipeline version 13.2. The three-dimensional data cubes were converted to two-dimensional slope images after linearization correction, subtraction of darks, and cosmic-ray removal. The reduction of the spectral data started from intermediate pipeline products "droop" files, which only lacked stray light and flat-field correction. Individual pointings to each nod position of the slit were co-added. The data from SH and LH were extracted using the full slit extraction method of a script version of *IRS* data analysis package SMART (Higdon et al. 2004) from the median of the combined images. The 1-dimensional spectra were flux calibrated by multiplying by a relative spectral response function (RSRF), which was created from the *IRS* standard star, ξ Dra, for which accurate templates were available (Cohen et al. 2003; Sloan et al. 2007). As a final cosmetic step the ends of each order where the noise increases significantly were manually clipped. No scaling was needed between the adjacent orders within the same module. For faint sources, the spectra taken at nod position 1 are severely affected by fringing problems, thus we only use the data at nod position 2 for these sources in our study.

The fine-structure lines, [SIV] λ10.51μm, [NeII] λ12.81μm, [NeIII] λ15.55μm and [SIII] $\lambda\lambda$18.71μm, 33.48μm are clearly present in the majority of the BCDs in our sample[2]. We measure the line fluxes by fitting them with a Gaussian profile. Even though the [SIII] line is visible in both SH and LH we only use the

[2]See Figure 3 of Wu et al. (2006), or Hao et al. 2008 in preparation for the reduced spectra.

Table 3.1. Observing Parameters of the Sample

Object Name	RA (J2000)	Dec (J2000)	AORKEY	Observation Date	Redshift	On-source Time (Seconds) SH	LR
Haro11	00h36m52.5s	-33d33m19s	9007104	2004-07-17	0.0206	480	240
NGC1140	02h54m33.6s	-10d01m40s	4830976	2004-01-07	0.0050	480	240
SBS0335-052E	03h37m44.0s	-05d02m40s	11769856	2004-09-01	0.0135	1440	960
NGC1569	04h30m47.0s	+64d50m59s	9001984	2004-03-01	~ 0	480	240
IIZw40	05h55m42.6s	+03d23m32s	9007616	2004-03-01	0.0026	480	240
UGC4274	08h13m13.0s	+45d59m39s	12076032	2004-10-23	0.0015	120	56
			12626688	2004-11-11		120	56
IZw18	09h34m02.0s	+55d14m28s	9008640	2004-03-27	0.0025	480	240
			16205568	2005-12-16		2880	1440
VIIZw403	11h27m59.9s	+78d59m39s	9005824	2004-12-09	~ 0	480	240
Mrk1450	11h38m35.6s	+57d52m27s	9011712	2004-12-12	0.0032	480	240
UM461	11h51m33.3s	-02d22m22s	9006336	2005-01-03	0.0035	480	240
			16204032	2006-01-14		1440	...
SBS1210+537A	12h12m55.9s	+53d27m38s	8989952	2004-06-06	...	480	240
Tol1214-277	12h17m17.1s	-28d02m33s	9008128	2004-06-28	0.0260	480	240
Tol65	12h25m46.9s	-36d14m01s	4829696	2004-01-07	0.0090	480	240
UGCA292	12h38m40.0s	+32d46m01s	4831232	2004-01-07	0.0010	480	240
Tol1304-353	13h07m37.5s	-35d38m19s	9006848	2004-06-25	0.0140	480	240
Pox186	13h25m48.6s	-11d37m38s	9007360	2004-07-14	0.0039	480	240
CG0563	14h52m05.7s	+38d10m59s	8992512	2005-05-30	0.0324	240	120
CG0598	14h59m20.6s	+42d16m10s	8992256	2005-03-19	0.0575	480	240
CG0752	15h31m21.3s	+47d01m24s	8991744	2005-03-19	0.0211	480	240
Mrk1499	16h35m21.1s	+52d12m53s	9011456	2004-06-05	0.0090	480	240
[RC2]A2228-00	22h30m33.9s	-00d07m35s	9006080	2004-06-24	0.0052	480	240

Note. — The coordinates and redshifts of the objects are cited from the NASA/IPAC Extragalactic Database (NED). In this paper, we only include the analysis of thirteen out of twenty-two sources which have SNRs sufficient for our abundance study. CG0563, CG0598 and CG0752 are included in the original sample as BCD candidates, however, they appear to be more starburst like (see Hao et al. 2007). Thus even though they have high SNR, we do not include these three sources in this study.

18.71 μm line for deriving the ionic abundance. This is because by using lines within the same module (SH), we remove uncertainties due to the different sizes of the SH and LH slits. Furthermore, the [SIII] λ33.48μm line is near the cut off of the LH module where the sensitivity drops dramatically, making its measurement more uncertain in some cases.

3.3 Elemental Abundances of BCDs

In this section, we derive the neon and sulfur abundances using the new infrared data of our BCD sample. The elemental abundances of the compact HII regions in our Galaxy (Martín-Hernández et al. 2002; Simpson et al. 2004), in the Magellanic Clouds (Vermeij et al. 2002), as well as in starburst galaxies (Verma et al. 2003; Martín-Hernández et al. 2006) have already been studied extensively in the past using ISO, and more recently with *Spitzer* (Rubin et al. 2007). There are several methods to derive the chemical abundances (for a review see Stasińska 2007). Here we use an empirical method, which derives ionic abundances directly from the observed lines of the relavent ions. To do so, we need to have the flux of at least one hydrogen recombination line, the dust extinction, as well as the electron temperature and density of the interstellar medium (ISM).

3.3.1 Electron density and temperature

The electron density (N_e) could in principle be determined by comparing the measured ratio of [SIII]18.71μm/33.48μm to the expected theoretical value using the corresponding S-curve (see Houck et al. 1984). However, the values for the ratio are in the horizontal part of the S-curve and as a result we cannot use these two lines to accurately constrain the electron density of these systems. Furthermore,

the 33.48 μm [SIII] line is located at the edge of the LH slit, where the sensitivity drops dramatically, and considering that these emission lines are weak, the measured line flux for the 33.48 μm [SIII] has a large uncertainty. Since the infrared determination of elemental abundances does not depend strongly on the density, we adopted the optically derived electron densities from the literature, which range from 10 to 3000 cm^{-3} (see Table 3.2). For sources where such information is not available, we adopt a typical electron density of 100 cm^{-3} in this paper.

Since BCDs in general have low metallicities, it is expected that BCDs would have relatively high electron temperatures (T_e). Fortunately, the infrared lines are much less sensitive to the uncertainties in the electron temperature compared to the optical (Bernard Salas et al. 2001). As a result we adopt electron temperatures derived from the optical studies found in the literature. For sources which do not have direct measurements (which happen to be high metallicity sources in our sample, e.g. NGC1140, UGC4274), we use a representative temperature of $T_e = 10{,}000$ K (see Table 3.2).

3.3.2 Ionized hydrogen flux estimates

In order to derive the ionic abundances, we also need to obtain information on at least one hydrogen recombination line (usually Hβ). For sources in which the Humphreys α (Huα, 12.37 μm) line is detected, we use it to convert to Hβ. From the extinction corrected Huα flux, we estimate the Hβ flux using the values given in the tables of Hummer & Storey (1987) for Case B recombination. This has the advantage that we do not need to correct for aperture effects because the neon and sulfur lines we use to derive the abundances also reside in the same module (SH). The 12.37 μm line is generally very weak and it is detected in six of our thirteen sources. For SBS0335-052E and IZw18, which have radio continuum data, we

Table 3.2. Optical Properties of the Sources

Object	F(Hβ) ($\times 10^{-14}$ergs s^{-1}cm^{-2})				E_{B-V}	T_e	N_e	ref
	Huα-derived	Hα-derived	radio-derived	optical	mag	K	cm^{-3}	
Haro11	252±40	···	···	···	0.41	13700	10	(1)
NGC1140	67±9	···	···	···	0.10	10000	100	(2)[a]
SBS0335-052E	<22.4	···	6.5±0.06	···	2.76	20000	200	(3),(4),(5)
NGC1569	393±19	···	···	···	0.65	12000	100	(6)
IIZw40	363±10	282±22	···	···	0.79	13000	190	(2),(7)
UGC4274	<59.6	11.5±1.0	···	···	0	10000	62	(7),(8)[a]
IZw18	<12.6	8.0±0.6	6.1±0.6	···	0.08	19000	100	(7),(9),(10)
VIIZw403	<24.6	11.8±1.2	···	···	0	14800	100	(7),(11)
Mrk1450	<14.8	15.8±1.4	···	···	0.10	12500	100	(7),(12)
UM461	<21.0	···	···	13.6±0.6	0.08	16100	200	(13),(14)
Tol1214-277	23.3±2.8	···	···	···	0.03	19790	400	(15)
Tol65	<18.2	9.3±0.4	···	···	0.08	17320	50	(7),(15)
Mrk1499	14.6±1.9	15.1±1.3	···	···	0.17	12600	3267	(7),(16)

Note. — When no data are available in the literature, the electron temperature and densities are assumed to be 10 000 K (for NGC1140 and UGC4274) and 100 cm^{-3} (for NGC1140 and NGC1569) respectively. When the Hu α line is detected, the Hβ flux is preferentially derived from this line. The upper limits are listed for the non-detections. For the remaining sources, we derived the Hβ flux either from the thermal component of the radio continuum, or from the extinction corrected Hα flux inside the SH slit. For UM461, the Hβ flux is for the whole galaxy from the integrated optical spectra.

References. — (1) Bergvall & Östlin (2002), (2) Guseva et al. (2000), (3) Izotov et al. (2006), (4) Hunt et al. (2004), (5) Houck et al. (2004b), (6) Kobulnicky & Skillman (1997), (7) Gil de Paz et al. (2003), (8) Ho et al. (1997), (9) Cannon et al. (2005), (10) Izotov et al. (1999a), (11) Izotov et al. (1997), (12) Izotov et al. (1994), (13) Moustakas & Kennicutt (2006), (14) Izotov & Thuan (1998), (15) Izotov et al. (2001), (16) Kong et al. (2002)

calculate the Hβ flux from the thermal free-free emission using the fraction included in the aperture of our SH slit at the time of the observation, and no correction for extinction is needed. For the remaining four sources which have Hα images available from Gil de Paz et al. (2003), we overlay the SH slit on each Hα image to calculate what fraction of the Hα emission is included in our slit. Then we derive the corresponding Hβ flux inside the SH slit from the extinction-corrected Hα flux. Finally, for UM461, we use the Hβ flux of the whole galaxy from the integrated spectra (Moustakas & Kennicutt 2006). UM461 is a very compact source, thus fully encompassed within the SH slit.

3.3.3 Extinction correction

All our measurements, both the fluxes from the Hα images, as well as the infrared lines, have been corrected for extinction. From the low-resolution spectra of our BCDs (Wu et al. 2006), we find that most of the sources do not show a strong 9.7 μm silicate feature, thus indicating an intrinsically relatively low dust extinction. Due to the faintness of our targets at λ <9.7 μm, the determination of the continuum on the blue side of the 9.7 μm feature is often poor and the uncertainties in estimating the mid-IR extinction from this are rather large (see discussion in Spoon et al. 2007). Thus for sources where optical spectra are available, we adopt the E_{B-V} values calculated from the hydrogen recombination lines in the literature. Only for SBS 0335-052E, which has a high quality mid-IR spectrum and evidence for an embedded SSC, the optical E_{B-V} is not a good estimate of its extinction, thus we use the extinction estimated from the depth of the silicate feature (Houck et al. 2004b). Throughout this paper, we adopt the Fluks et al. (1994) extinction law, though using the Draine (2003) law would produce very similar results. The E_{B-V} magnitudes are provided in Table 3.2.

3.3.4 Neon and sulfur abundances determination

We use the electron density and temperature given in Table 3.2, together with the fine structure lines detected in the *IRS* high-resolution spectra, to calculate the abundances of neon and sulfur. The equation used to determine the ionic abundance is described in Bernard Salas et al. (2001) and it is:

$$\frac{N_{\rm ion}}{N_{\rm p}} = \frac{I_{\rm ion}}{I_{\rm H_\beta}} N_{\rm e} \frac{\lambda_{\rm ul}}{\lambda_{\rm H_\beta}} \frac{\alpha_{\rm H_\beta}}{A_{\rm ul}} \left(\frac{N_{\rm u}}{N_{\rm ion}} \right)^{-1} \tag{3.1}$$

where $\rm I_{ion}/I_{H\beta}$ is the measured flux of the fine-structure line normalized to Hβ; $\rm N_P$ is the density of the ionized hydrogen; $\lambda_{\rm ul}$ and $\lambda_{\rm H\beta}$ are the wavelengths of the line and Hβ; $\alpha_{\rm H\beta}$ is the effective recombination coefficient for Hβ; $\rm A_{ul}$ is the Einstein spontaneous transition rate for the line and $\rm N_u/N_{ion}$ is the ratio of the population of the level from which the line originates to the total population of the ion. This ratio is determined by solving the statistical equilibrium equation for a five level system and normalizing the total number of ions to be unity (Osterbrock 1989). The effective collisional strengths used to derive the population of levels were obtained from the appropriate reference of the IRON project (Hummer et al. 1993)[3].

The most important ionization stages of neon and sulfur are available in the infrared. We detected [SIV] $\lambda 10.51\,\mu$m and [NeIII] $\lambda 15.56\,\mu$m in all of our BCDs while the [NeII] $\lambda 12.81\,\mu$m line is detected in nine objects and [SIII] $\lambda 18.71\,\mu$m in twelve sources (see Table 3.3). For sulfur, SII has its strongest emission lines in the optical. Vermeij et al. (2002) have shown that SII is typically less than 10% of SIII in the Magellanic cloud HII regions they studied. Because BCDs are typically high-excitation objects, we do not expect to have a significant contribution from SII. The optical studies reveal that the ionic abundance of SII is typically 10−20% of

[3]http://www.usm.uni-muenchen.de/people/ip/iron-project.html

that of SIII (Izotov et al. 1994, 1997), thus we keep in mind that this might result in a $\sim$10% underestimate in our infrared derived sulfur abundance. This is addressed further in the following subsection where we discuss the properties of the individual objects. The presence of the [OIV] λ25.89 μm line in most of our sources (except for VIIZw403, UM461, Tol65 and Mrk1499) indicates that some [NeIV] might be present, even though the [OIV] line is typically weak. For example, in Tol1214-277, where [OIV] is detected, the flux of [NeIV]λ4725 from optical spectra is less than 1% of that of [NeIII]λ3868 (Izotov & Thuan 2004), indicating that the contribution of [NeIV] is not significant. Tsamis & Péquignot (2005) also have shown in their photoionization modelling study of 30 Doradus that the contribution from NeIV to the total neon abundance is much less than 1%. As a result, rather than applying ionization correction factors (ICFs) which could introduce an unknown systematic uncertainty in our study, we sum the corresponding ionic abundances for the most important ionization stages to determine the total element abundance and the results are shown in Table 3.3.

Two successive stages of ionization of a given element (X) can be used to measure the state of the ionization of the ISM, which, on first order, depends on the ionization parameter, U, and the hardness of the ionizing radiation (Vilchez & Pagel 1988). For a given U, the ratio X^{+i+1}/X^{+i} is an indicator of the hardness of the stellar radiation field. Here we use the ionic pairs of Ne^{++}/Ne^{+} and S^{+3}/S^{++} as indicators of the hardness of the ionization field and plot them in Figure 3.1. It is clear from the figure that these two ratios increase proportionally. This indicates that the hardening of the radiation field affects similarly the various elements in the full range of the ionizing continua.

The major uncertainty in our study of the elemental abundances originates from the Hβ fluxes used as references. For sources where the 12.37 μm Huα line

Table 3.3. Fine-structure Line Fluxes and Ionic Abundances

Object	Line Fluxes ($\times 10^{-14}$ergs cm^{-2} s^{-1})				Ionic Abundances ($\times 10^{-6}$)			
	[SIV](10.51μm)	[NeII](12.81μm)	[NeIII](15.55μm)	[SIII](18.71μm)	N_{SIV}/N_p	N_{NeII}/N_p	N_{NeIII}/N_p	N_{SIII}/N_p
Haro11	43.95±0.14	31.23±0.23	98.14±0.65	45.24±0.25	0.353±0.056	15.4±2.4	23.2±3.7	1.89±0.30
NGC1140	12.14±0.13	11.41±0.20	37.79±0.32	20.04±0.11	0.375±0.051	22.5±3.0	35.5±4.8	3.56±0.48
SBS0335-052E	1.56±0.03	<0.14	1.43±0.02	0.43±0.03	0.527±0.011	<2.27	11.2±1.6	0.535±0.038
NGC1569	147.26±0.55	15.70±0.17	175.85±0.59	72.70±0.23	0.817±0.040	5.28±0.26	28.2±1.4	2.12±0.10
IIZw40	185.72±1.73	6.24±0.11	112.65±0.83	45.80±0.21	1.12±0.03	2.23±0.07	19.3±0.6	1.37±0.04
UGC4274	4.18±0.12	8.87±0.11	12.84±0.12	12.63±0.11	0.743±0.068	102±9	70.3±6.1	13.2±1.2
IZw18	0.48±0.03	0.09±0.01	0.46±0.02	0.23±0.02	0.125±0.015	1.41±0.21	3.56±0.38	0.276±0.036
VIIZw403	0.99±0.05	<0.142	0.88±0.02	0.87±0.02	0.311±0.035	<2.79	8.41±0.88	1.39±0.14
Mrk1450	7.34±0.04	1.34±0.03	9.61±0.04	4.37±0.03	0.928±0.223	10.70±2.57	36.9±8.9	2.98±0.71
UM461	4.58±0.04	0.16±0.02	2.83±0.03	0.812±0.03	0.636±0.029	1.38±0.18	11.8±0.5	0.563±0.032
Tol1214-277	0.88±0.02	<0.10	0.61±0.02	<0.19	0.061±0.007	<0.413	1.23±0.15	<0.059
Tol65	0.69±0.02	<0.14	0.90±0.02	0.32±0.02	0.129±0.007	<1.62	5.07±0.25	0.293±0.022
Mrk1499	1.74±0.02	1.88±0.03	5.03±0.03	2.91±0.02	0.286±0.037	16.5±2.2	21.6±2.8	2.28±0.30

Note. — The observed line fluxes are measured from the IRS high resolution spectra of the sources. Background emission has not been subtracted, but this does not affect the flux of the fine-structure lines.

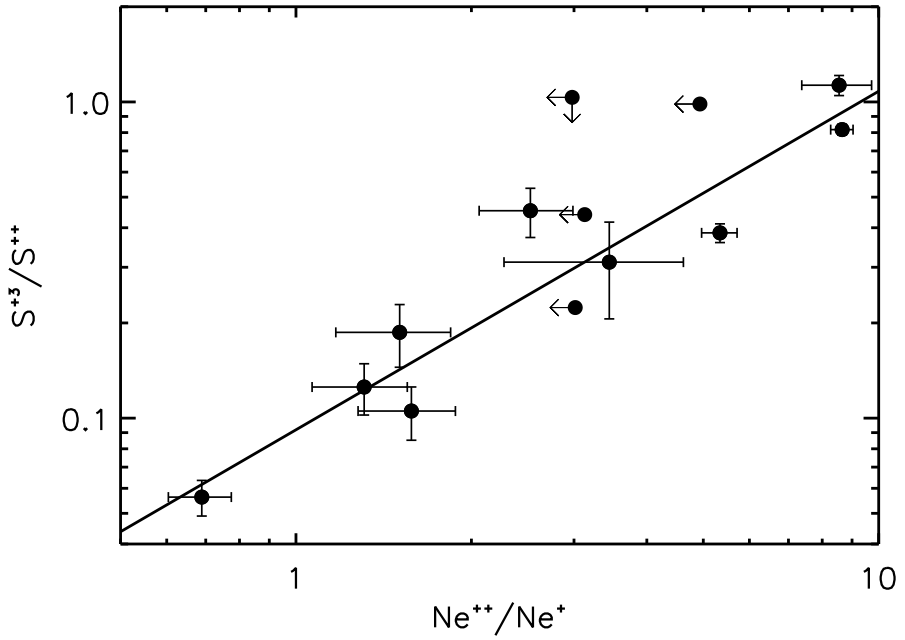

Figure 3.1 A plot of Ne^{++}/Ne^{+} vs S^{3+}/S^{++}, which traces the hardness of the radiation field. The solid line is a fit to the data.

is detected, we have no uncertainties from matching the slit apertures, and the extinction correction is very small. For sources where we estimate the Hβ flux from the thermal radio continuum emission, we are free of extinction corrections, even though we still need to properly account for the radio emission which falls within the IRS slit. For BCDs with no Hu α emission or radio data available in the literature, we estimate the Hβ flux using archival Hα images of the objects. This is clearly more challenging because in addition to the aperture corrections, the extinction correction is higher which could introduce a systematic uncertainty as large as 25%. In the following analysis, we indicate the sources with or without the detection of Hu α line using different symbols on the plots (see Figure 3.2, 3.3 and 3.4). The measurement uncertainties in the infrared lines are typically only a few percent, but could grow to $\sim$10% in the case of fainter sources. The uncertainties we list in Table 3.3 only account for measurement uncertainties.

Table 3.4. Elemental Abundances

Object	Ne/H($\times10^{-6}$)	S/H ($\times10^{-6}$)	O/H ($\times10^{-5}$)	Ne ($Z_\odot$)	S ($Z_\odot$)	O ($Z_\odot$)	ref (O/H)
Haro11	38.6±4.4	2.24±0.31	7.94	0.33±0.04	0.16±0.02	0.16	(1)
NGC1140	58.0±5.7	3.94±0.48	28.8	0.48±0.05	0.28±0.03	0.59	(2)
SBS0335-052E	[11.2, 13.5][a]	1.06±0.04	1.95±0.09	[0.09, 0.11][a]	0.08±0.003	0.03±0.001	(3)
NGC1569	33.5±1.4	2.94±0.11	15.8±0.5	0.28±0.01	0.21±0.01	0.32±0.01	(4)
IIZw40	21.5±0.6	2.49±0.05	12.2±0.4	0.17±0.005	0.18±0.004	0.25±0.01	(2)
UGC4274	172.3±10.9	13.94±1.20	33.3	1.4±0.1	1.0±0.1	0.68	(5)
IZw18	5.0±0.4	0.40±0.04	1.47±0.09	0.04±0.003	0.03±0.003	0.03±0.002	(6)
VIIZw403	[8.4, 11.2][a]	1.70±0.14	4.90±0.11	[0.07, 0.09][a]	0.12±0.01	0.10±0.002	(7)
Mrk1450	47.6±9.2	3.98±0.74	9.55±0.11	0.40±0.08	0.28±0.06	0.19±0.002	(8)
UM461	13.2±0.5	1.20±0.04	6.10±0.40	0.11±0.01	0.09±0.003	0.12±0.01	(9)
Tol1214-277	[1.2, 1.6][a]	[0.06,0.12][b]	3.45±0.10	[0.010, 0.013][a]	[0.004, 0.008][b]	0.07±0.002	(10)
Tol65	[5.1, 6.7][a]	0.42±0.07	3.48±0.10	[0.04,0.06][a]	0.03±0.002	0.07±0.02	(10)
Mrk1499	38.1±3.6	2.57±0.30	13.2	0.32±0.03	0.18±0.02	0.27	(11)

Note. — We adopt the following values for the solar abundances: $(Ne/H)_\odot=1.2\times10^{-4}$, $(S/H)_\odot=1.4\times10^{-5}$ and $(O/H)_\odot=4.6\times10^{-4}$ (See section 4.1).

[a]We provide a range for the neon abundance by taking as the lower value the ionic abundance of NeIII, while to obtain the upper value we add the upper limit for NeII.

[b]We provide a range for the sulfur by taking as the lower value the ionic abundance of SIV, while to obtain the upper value we add the upper limit of SIII.

References. — (1) Bergvall & Östlin (2002), (2) Guseva et al. (2000), (3) Izotov et al. (2006), (4) Kobulnicky & Skillman (1997), (5) Ho et al. (1997), (6) Izotov et al. (1999a), (7) Izotov et al. (1997), (8) Izotov et al. (1994), (9) Izotov & Thuan (1998), (10) Izotov et al. (2001), (11) Kong et al. (2002)

3.3.5 Individual Objects

Some details on the individual objects and how we measured the necessary parameters are provided in the following paragraphs.

Haro11: The 12.37 μm Huα line is clearly detected in the SH spectrum. The source has multiple nuclei, designated as A, B and C (Bergvall & Östlin 2002). The optical spectra from which the oxygen abundance was derived corresponds to the central region. Because all the lines we are using are from the SH spectrum, we are relatively free from extinction problems and there is no need for aperture correction. The contribution of SII may add ∼10% to the total sulfur abundance.

NGC1140: As with Haro11, the 12.37 μm Huα line is also clearly detected in the SH spectrum of NGC1140. No measurement was found in the literature for the electron temperature or density for this source, thus we assume 10000 K and 100 cm^{-3} respectively, which are typical for BCDs. However, because its oxygen abundance is more than half solar, the electron temperature could also be lower. If we use a T_e of 5000 K and re-derive the abundances, we find that the neon abundance would increase from 5.8× 10^{-5} to 8.5×10^{-5} and the sulfur abundance from 3.9×10^{-6} to 5.5×10^{-6}. The contribution of SII may add ∼10% to the total sulfur abundance.

SBS0335-052E: We do not detect the 12.37 μm Huα line in the SH spectrum. We use the thermal component of the 5 GHz radio continuum from Hunt et al. (2004) to convert to the Hβ flux, and thus no extinction correction is needed. [NeII] is not detected and we provide the upper limit in Table 3.3. The ionic abundance of SII is ∼25% of the SIII determined from the optical study of Izotov et al. (2006) and may add 12% to the total sulfur abundance. We also find higher neon and sulfur abundances compared with the oxygen and possible implications are discussed in Houck et al. (2004b).

NGC1569: The 12.37 μm Huα line is clearly detected in the SH spectrum, thus providing a direct estimate of the Hβ flux inside the SH slit. This galaxy is extended in the mid-IR (see Figure 4 in Wu et al. 2006) and optical spectra have been taken for several of the bright knots by Kobulnicky & Skillman (1997) in order to study the chemical gradient and inhomogeneities of the source. These authors found very little variation in the metallicity. Our infrared-derived abundances are in rough agreement with the optical results. The ionic abundance of SII is $\sim$13% that of the SIII estimated from the optical study (Kobulnicky & Skillman 1997) and may add 9% to the total sulfur abundance.

IIZw40: We use the 12.37 μm Huα line to convert to Hβ flux. The derived neon and sulfur abundances agree with each other but appear to be lower than oxygen with respect to the solar values. If we estimate the Hβ flux from the Hα image of Gil de Paz et al. (2003), we find a value $\sim$22% lower than the first, which would increase the neon and sulfur abundances by 22% accordingly. This suggests, that when using the Hβ flux derived from Hα image, the systematic error in our measurement is probably no better than 25%. The ionic abundance of SII is $\sim$13% that of SIII from the optical study of Guseva et al. (2000) and may add 7% to the total sulfur abundance.

UGC4274: We use an Hβ flux derived from the Hα image of Gil de Paz et al. (2003). Similarly to NGC1569, the galaxy is extended and the peak of the infrared centroid is displaced from the optical peak position. The derived neon and sulfur abundances are both super solar. The oxygen abundance is not directly available from the literature, thus we use the [NII]/Hα method (Ho et al. 1997; Denicoló et al. 2002) to derive O/H, which bears a large uncertainty. The contribution of SII may add $\sim$10% to the total sulfur abundance.

IZw18: The Hβ flux is derived from the thermal component of the radio continuum inside the SH slit. The ionic abundance of SII is $\sim$21% that of SIII from the optical study of Izotov et al. (1999a) and may add 15% to the total sulfur abundance. A more detailed discussion on this object can be found in Wu et al. (2007).

VIIZw403: The Hβ flux is derived by using the Hα image from Gil de Paz et al. (2003). The optical and infrared centroids do not overlap. The SH spectrum for this source is noisy and [NeII] λ12.81 μm is not detected, thus we have only a lower limit on the neon abundance. The upper limit of the [NeII] line indicates that it could add less than 25% to the total elemental abundance of neon which is presented in Table 3.4. The ionic abundance of SII is $\sim$24% that of SIII from the optical work of Izotov et al. (1997) and may add 20% to the total sulfur abundance.

Mrk1450: As with VIIZw403, we use the hydrogen flux as given by the Hα flux included in the SH slit. Neon and sulfur abundances appear to be higher than the oxygen abundance with respect to the solar values. The ionic abundance of SII is $\sim$18% that of SIII from the optical study of Izotov et al. (1994) and may add 12% to the total sulfur abundance.

UM461: The Hβ flux is estimated from the integrated spectra of Moustakas & Kennicutt (2006), and the source is small enough to be fully included by the SH slit. The derived neon and sulfur abundances are in good agreement with oxygen metallicity from the optical. The ionic abundance of SII is $\sim$17% that of SIII from the optical (Izotov & Thuan 1998) and may add 8% to the total sulfur abundance.

Tol1214-277: The 12.37 μm Huα line is marginally detected in the SH spectrum, and we use this line to derive the Hβ flux. The spectrum is very noisy and no [NeII] λ12.81 μm or [SIII] λ18.71 μm lines are visible. We use the ionic abundances of [NeIII] and [SIV] as the lower limits of the neon and sulfur abundances. The

upper limit of [NeII] amounts to 33% of the ionic abundance of [NeIII] while the upper limit of [SIII] is nearly as much as the abundance of [SIV]. We give the range of their elemental abundances in Table 3.4. The ionic abundance of SII is ∼18% that of SIII from the optical study of Izotov et al. (2001) and may add ∼9% to the total sulfur abundance.

Tol65: We use the Hα image (Gil de Paz et al. 2003) to calculate the Hβ flux. [NeII] λ12.81 μm is not detected in the SH spectrum, thus our derived neon abundance is a lower limit. The upper limit of NeII is ∼32% of the ionic abundance of NeIII, and the range of neon abundance is provided in Table 3.4. The metallicity of sulfur relative to solar is lower than oxygen. The ionic abundance of SII is ∼26% that of SIII from the optical (Izotov et al. 2001) and may add 19% to the total sulfur abundance.

Mrk1499: The 12.37 μm Huα line is detected in the SH spectrum. There was a bad pixel at the peak of this line and we interpolated its value using adjacent pixel values. The infrared centroid appears to be slightly shifted from the optical one. The Hβ flux inside the SH slit derived from the Hα image is very similar to that derived from the Huα line (within ∼10%). The contribution of SII may add ∼10% to the total sulfur abundance.

3.4 Discussion

In this section, we compare the abundances derived from the IR spectra with the results from the optical studies.

3.4.1 Solar abundances

The solar photospheric abundances have changed drastically over the past few years (see discussion in Pottasch & Bernard-Salas 2006). In some cases, the solar abundance estimates for the same element from different authors could differ by a factor of two. In this paper, when we quote the elemental abundance in solar units (e.g. Table 3.4), we adopt the following values: $(Ne/H)_{\odot}=1.2\times10^{-4}$ from Feldman & Widing (2003), $(S/H)_{\odot}=1.4\times10^{-5}$ from Asplund et al. (2005), and $(O/H)_{\odot}=4.9\times10^{-4}$ from Allende Prieto et al. (2001). We should note though that Asplund et al. (2005) have also reported that $(Ne/H)_{\odot}=6.9\times10^{-5}$ and Grevesse & Sauval (1998) have given $(S/H)_{\odot}=2.1\times10^{-5}$, while Anders & Grevesse (1989) have reported that $(O/H)_{\odot}=8.5\times10^{-4}$. These values represent the extremes for the solar neon, sulfur and oxygen abundance determinations. Pottasch & Bernard-Salas (2006) have shown that the higher neon solar value is favored in their sample of planetary nebulae (PNe). In the present paper we indicate the range of solar abundances in our plots and we also discuss the impact of different solar values on our results.

3.4.2 Neon and sulfur abundances

As discussed in Thuan et al. (1995), it is assumed — and has been shown in the optical — that the α-element-to-oxygen abundance ratios do not vary with oxygen abundance. This is due to the fact that those elements are produced by the same massive stars ($M>10M_{\odot}$) responsible for oxygen production. We test this assumption in the infrared by studying the abundances of neon and sulfur as derived from our IRS data.

In Figure 3.2, we plot the abundances of neon and sulfur as derived from our high-resolution data. Verma et al. (2003) have found a positive correlation between

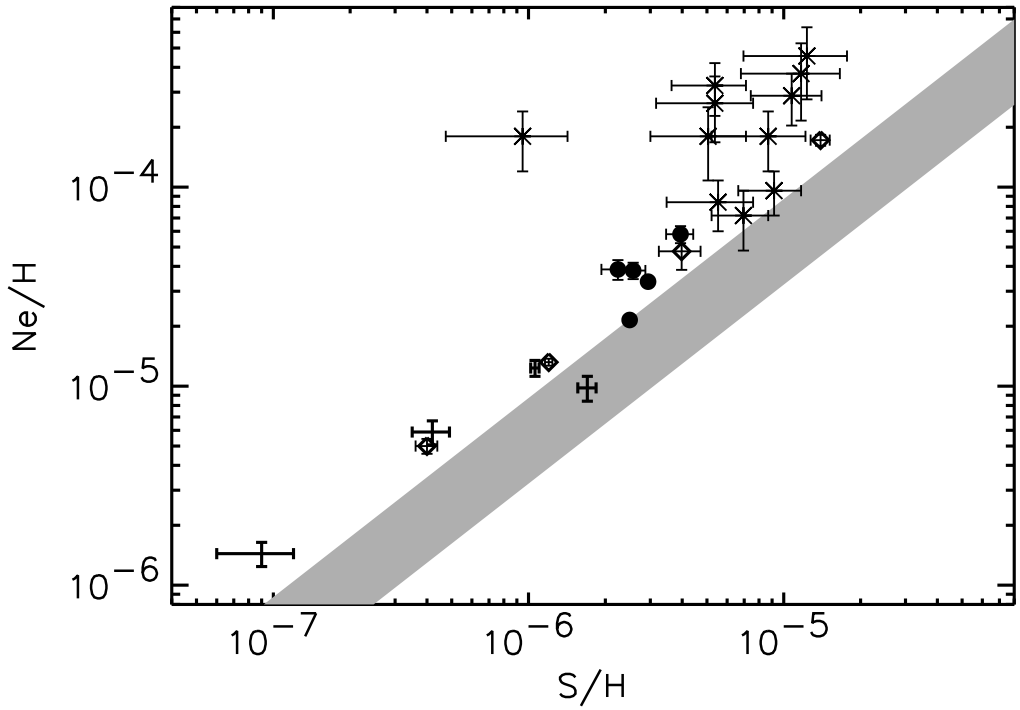

Figure 3.2 A plot of the Ne/H vs S/H abundance. Our BCDs are indicated by the filled circles if Hu α is detected and by diamonds if it is not detected. The sources that are shown by only the error bars are those that have non-detection of [NeII] or [SIII] (See note of Table 3.4). The starburst galaxies from Verma et al. (2003) are marked with the stars. We use the grey band to indicate the locus on the plot where the ratio of Ne/S would be consistent with the different solar values for neon and sulfur abundances.

the neon and argon abundances for their sample of starburst galaxies while their data show no correlation between the sulfur and neon and/or argon abundances (indicated as stars on Figure 3.2). However, our sources show that the neon and sulfur abundances scale with each other. In the same figure, we also plot the proportionality line of the ratio for $(\mathrm{Ne/S})_{\odot}$. The maximum and minimum values of the solar neon and sulfur abundances are indicated by the width of the grey band, and we find that most of our BCDs have ratios above those values.

In Figure 3.3, we examine the ratio of Ne/S[4] as a function of Ne/H derived from

[4]For sources of which their abundances are shown as a range, i.e., [x,y], in Table 4, we assume

the IRS data. We see no correlation between the ratio of Ne/S with respect to Ne/H, in agreement with the results of Thuan et al. (1995). The average Ne/S ratio we found for these BCDs is 12.5±3.1. This is similar with the Ne/S ratio of 14.3 in the Orion Nebula (Simpson et al. 2004). The Ne/S ratios found in the HII regions of M83 are higher (∼24−42) and decrease with increasing deprojected galactocentric radii (Rubin et al. 2007). These authors have also found that the Ne/S ratios in M33 are ∼12−21 (Rubin et al. 2006). We notice that all the BCDs, as well as the HII regions in M33, M83 and the Orion Nebula, have larger Ne/S ratios than those found in the solar neighborhood, while their Ne/S ratios from optical measurements are more consistent with the solar ratios. The higher Ne/S ratios from infrared studies have already been found in other type of objects, including PNe, starburst galaxies, and other HII regions (Marigo et al. 2003; Verma et al. 2003; Henry et al. 2004; Pottasch & Bernard-Salas 2006). Some of these works point out that the solar sulfur abundance could have been underestimated and they also appear to favor the higher values for the solar neon abundance. It could also be due to a differential depletion of sulfur onto dust grains compared to neon as suggested by several studies (Simpson & Rubin 1990; Verma et al. 2003; Pottasch & Bernard-Salas 2006; Bernard Salas et al. 2008).

3.4.3 Comparison with optically derived abundances

As has been discussed earlier in this paper, one of the major advantages of using IR lines for estimating abundances is that one can probe emission from dust enshrouded regions without the uncertainties introduced from extinction corrections. In this subsection, we compare the newly derived neon and sulfur abundances of our BCD sample using the infrared data, with the abundances of the same ele-

the average of (x+y)/2 as their abundance when calculating the Ne/S ratios.

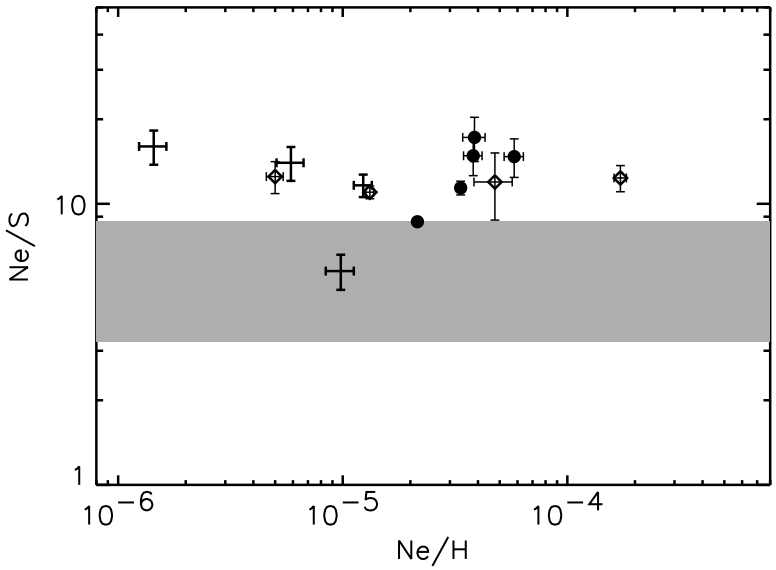

Figure 3.3 The abundance ratio of Ne/S as a function of Ne/H. The symbols are the same as in Fig. 3.1. The grey area indicates the range for the values of the Ne/S ratio encountered in the solar neighborhood.

ments as well as those for oxygen estimated from optical studies available in the literature.

In order to determine elemental abundances, the optical studies usually adopt a two-zone photoionized HII region model: a high-ionization zone with temperature T_e(OIII) and a low-ionization zone with temperature T_e(OII). Because the infrared lines are much less sensitive to variations in T_e (which affect the calculation on the population of the various atomic levels), in the subsequent calculations, we assume a constant electron temperature for our analysis.

In Figure 3.4 we compare the infrared derived neon and sulfur abundances of the BCD sample with their optical metallicities, using the oxygen abundances from the literature (see also Table 3.4). The infrared neon abundances with respect to solar are slightly higher than the oxygen (see Figure 3.4a), but overall, there is a good agreement between the infrared measurements and the optical results.

This indicates that there is little dust enshrouded gas, or that these regions have similar metallicities, or that they do not contribute much to the total integrated emission of the galaxies. In SBS0335-052E, as well as Mrk1450, UGC4274 and Haro11, the infrared derived metallicity of neon is more than twice that of oxygen compared to the solar values. This could be due to the different regions we are probing using the infrared, which could be obscured in the optical. SBS0335-052E is known to have an embedded super star cluster that is invisible in the optical (see Houck et al. 2004b). Both Haro11 and UGC4274 are somewhat extended, and detailed spectroscopy over the whole galaxy would be needed to directly compare the infrared results with the optical ones. For Mrk1450, which is a point source for Spitzer/IRS, the abundance we derived using the infrared data is higher than the optical value and it is likely due to the fact that the optical estimates are more susceptible to the uncertainties in the electron temperature. If we lower T_e from 12 500 K to 10 000 K, the oxygen abundance calculated from the optical data would double, while the neon abundance measured from the infrared would only increase by 5%. In Figure 3.4b we show that the infrared derived sulfur abundances agree well with the oxygen abundance relative to solar.

For nine out of the thirteen objects we studied, optically derived neon and sulfur abundances are also available in the literature. The optical data have matched apertures, in most cases an accurate T_e measurement, a direct measure of the Hβ flux, and reddening derived from the same data. Our infrared results are less sensitive to the electron temperature, but affected by the uncertainty in the Hβ flux if the Hu α line is not detected and the uncertainty could be as large as 25%. In Figure 3.5a, we plot the optically derived Ne/H against the infrared Ne/H. The solid line is the 1:1 proportion line for the infrared and optical derived abundances and we find that most of the sources are located above this line. A possible

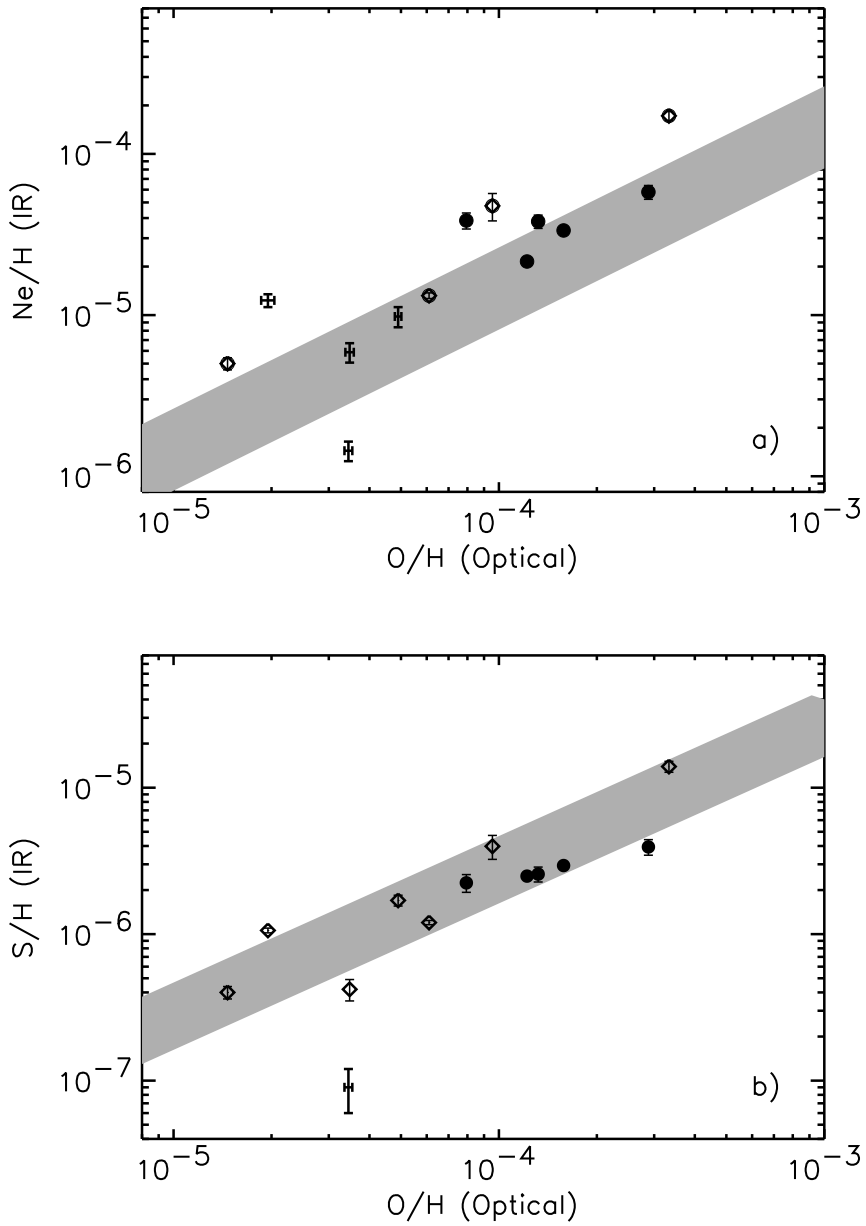

Figure 3.4 a)The Ne/H vs O/H abundances. The symbols are the same as in Fig. 1. The grey band represents the locus on the plot where sources of different metallicities would have a Ne/O intrinsic ratio similar to the values found in the solar neighborhood. b) Same as a), but for S/H vs O/H abundances.

explanation for the higher infrared derived neon abundances could be the presence of dust enshrouded regions which might have higher heavy element abundances. This could explain the higher infrared metallicity found in SBS0335-052E, but if this were true for the whole sample, it should also apply to the sulfur abundances. However, when we plot the S/H (Optical) against the S/H (IR) in Figure 3.5b, we find that the sources are located on both sides of the 1:1 proportion line. Alternatively, this could be due to the difference in the determination of element abundance using the infrared and optical methods. Because only NeIII is detected in the optical regime, the total elemental abundance of neon from the optical study is heavily dependent on the adopted ICF. In the infrared the [NeII] line is detected in most of our sources and we do not use any ICF for our study. Thus the higher neon abundances derived from the infrared data compared to the optical results could also be due to the large uncertainty in the ICF used in the optical studies. Another possibility is that the temperature of the NeIII ion is lower than that of the OIII ion as found in some PNe (Bernard Salas et al. 2002). Because the optical studies are based on T_e(OIII) when calculating the ionic abundance of NeIII, that could also result in an underestimate of its abundance.

Finally, we explore the variation in the ratio of Ne/S as derived from the infrared and the optical data, and plot them as a function of O/H in Figure 3.6. Interestingly, we find that with the exception of VIIZw403, in all BCDs, the infrared derived Ne/S ratios are higher than the corresponding optical values. Izotov & Thuan (1999b) indicate an average Ne/S ratio of 6.9 for the 54 super giant HII regions they study in 50 BCDs using optical spectroscopy. The average of the optically derived Ne/S ratio for the nine sources in our sample is 6.5$\pm$1.8 while the corresponding ratio from the infrared data is 11.4$\pm$2.9, statistically higher than the optical results. As we mentioned earlier, no SII abundances could be determined

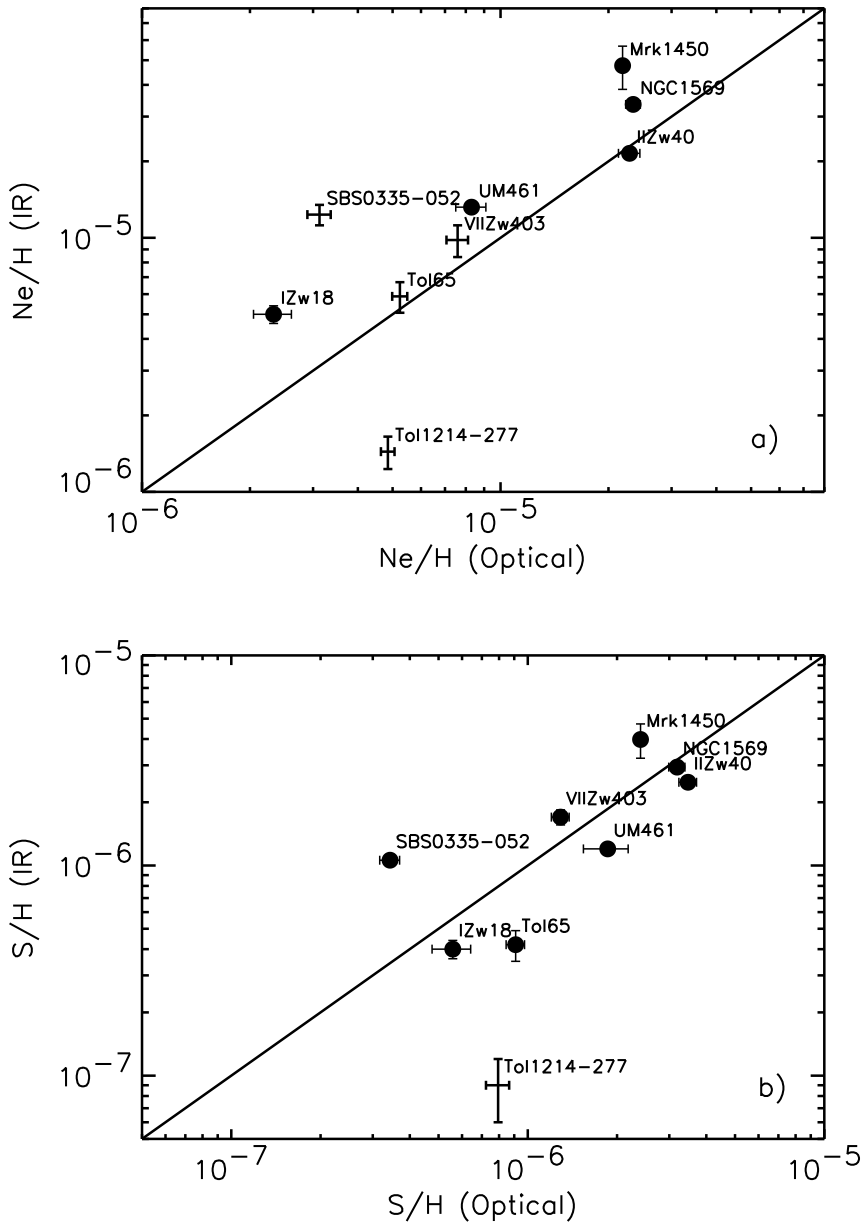

Figure 3.5 a)The infrared derived Ne/H as a function of the optical Ne/H abundances. The sources shown with only the error bars are those where [NeII] or [SIIII] is not detected. The solid line represents the 1:1 line for the optical and IR derived abundances. b) Same as a), but for S/H (Optical) vs S/H (IR) abundances.

with the Spitzer/IRS data. However, in high-excitation objects such as BCDs, SII does not contribute much ($\sim$10%) to the total elemental abundance, thus it could not account for the factor of two difference in the ratio of Ne/S. Furthermore, such a discrepancy is not a result of metallicity because we see no correlation in the dispersion between the infrared and optically derived ratios of Ne/S with respect to O/H. If we divide the sources into a high-excitation group with sources that have a detectable [OIV]λ25.89 μm line and a low-excitation group with sources without any detection of [OIV], we still see no clear trend. Thus the ionization field cannot explain the difference in the Ne/S ratios either. Moreover, no correlation is found between the Ne/S ratio and the extinction to the source. Even though the largest uncertainty in the infrared derived abundances comes from the uncertainty in the Hβ flux in cases where no Hu α is detected, when calculating the ratio of Ne/S, the Hβ flux cancels out, thus our infrared determined values for Ne/S should be fairly reliable. One possibility for the observed discrepancy could be that the difference in the infrared and optical results is again due to the ICF adopted in the optical studies.

3.5 Metallicities and PAHs

The observed suppression of PAH emission in low metallicity environment is still an open topic (Madden 2000; Madden et al. 2006; Engelbracht et al. 2005; Wu et al. 2006; O'Halloran et al. 2006). One explanation on the absence of PAHs is that there is not enough carbon to form into PAH molecules in such metal-poor environments while an alternative possibility could be that the strong ionization field in low metallicity environments may destroy the fragile PAH rings.

Previous studies relating the PAHs and metallicity were all based on the oxygen abundance measured from the optical, which could be associated with regions

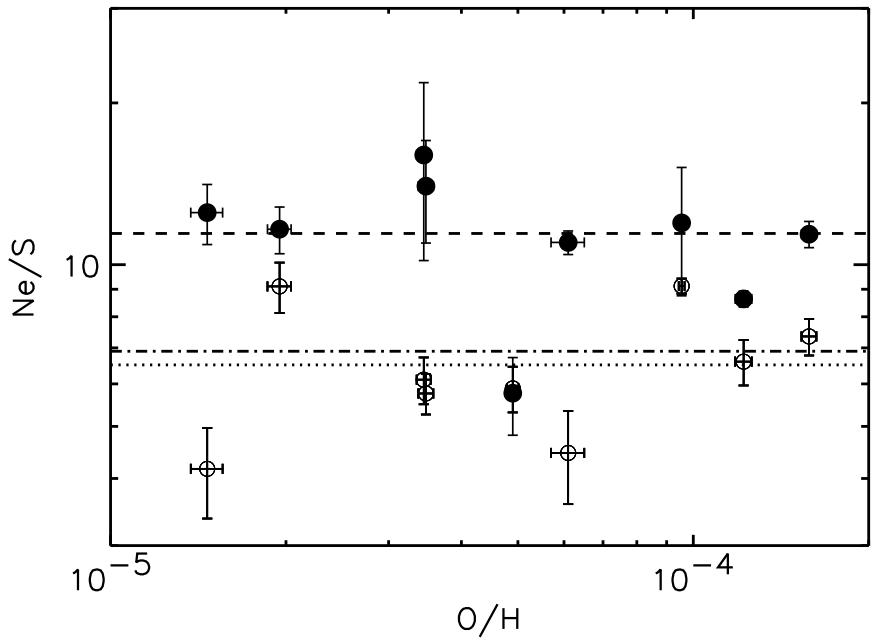

Figure 3.6 The abundance ratio of Ne/S as a function of O/H. The infrared derived Ne/S ratios are indicated by the filled circles while the optical derived Ne/S ratios are shown by the open circles. The dashed line is the average Ne/S ratio from the infrared derived elemental abundances while the dotted line is average Ne/S ratio from the optical derived elemental abundances. The dash-dotted line represents the average Ne/S ratio from Izotov & Thuan (1999b).

that are different from the ones where PAH emission originates. Because we have obtained the infrared measured neon and sulfur abundances, it is particularly interesting to compare the PAH strength with our metallicity estimates. Several BCDs in our sample do show PAH emission features and an analysis of the PAH properties of our sample based on IRS low resolution spectra was presented in Wu et al. (2006). We have obtained deeper spectra for some of the sources, so for consistency, we have re-measured all features in our sample and the results are given in Table 3.5. None of the sources with metallicity lower than $\sim$0.12 $Z_{\odot}$ show any detectable PAHs. For the sources where PAHs were detected, we calculate the equivalent widths (EWs) of the 6.2,7.7,8.6 and 11.2 μm features and find that the correlation between the PAH EWs and the metallicity is weak. This is not unexpected because as discussed in Wu et al. (2006), the strength of PAHs in low-metallicity environments is a combination of creation and destruction effects. As a result the dependency of PAH strength on the metallicity alone could have a substantial scatter.

3.6 Conclusions

We have studied the neon and sulfur abundances of thirteen BCDs using Spitzer/IRS high-resolution spectroscopy. Our analysis was based on the fine-structure lines and the hydrogen recombination line detected in the SH spectra of the *IRS*, combined with the radio continuum, Hα images and integrated optical spectral data in some cases. We find a positive correlation between the neon and sulfur abundances, though sulfur appears to be more under-abundant than neon (with respect to solar). The ratio of Ne/S for our sources is on average 12.5$\pm$3.1, which is consistent with what has been found in other HII regions using infrared data. However, this average ratio appears to be higher than the corresponding

Table 3.5. PAH measurements of the sample

Object Name	PAH EW (μm)				Integrated Flux ($\times10^{-14}$ergs cm^{-2} s^{-1})			
	6.2 μm	7.7 μm	8.6 μm	11.2 μm	6.2 μm	7.7 μm	8.6 μm	11.2 μm
Haro11	0.120±0.003	0.227±0.005	0.042±0.003	0.099±0.002	78.3±1.8	180±4	25.4±1.6	67.2±1.3
NGC1140	0.479±0.033	0.568±0.024	0.091±0.006	0.525±0.032	42.1±1.4	78.3±1.8	11.1±0.7	50.2±2.5
SBS0335-052E	<0.035	···	···	<0.015	<1.7	···	···	<1.0
NGC1569	0.232±0.013	0.380±0.019	0.007±0.005	0.129±0.008	50.4±2.4	118±6	2.7±1.6	68.1±4.3
IIZw40	0.044±0.007	0.044±0.006	0.006±0.005	0.033±0.006	13.2±2.1	19.0±2.8	2.8±1.2	21.1±3.7
UGC4274	0.423±0.032	0.497±0.049	0.105±0.012	0.495±0.021	23.2±1.2	43.3±2.3	7.7±0.9	29.1±0.9
IZw18	<0.233	···	···	<0.116	<0.4	···	···	<0.1
Mrk1450	0.207±0.045	0.337±0.143	0.084±0.020	0.112±0.017	1.8±0.4	2.8±0.9	0.7±0.2	1.6±0.2
UM461	<0.663	···	···	<0.134	<1.5	···	···	<1.6
Mrk1499	0.408±0.040	0.526±0.016	0.156±0.011	0.721±0.035	5.5±0.3	10.9±0.3	2.3±0.2	7.3±0.2

Note. — Contrary to Wu et al. (2006), the wavelengths which we have chosen to determine the underlying continuum are fixed in the above measurements, which explains the minor discrepancies between these two studies. The symbol " ··· " indicates that no PAH EW measurement was possible and it is mostly due to the low SNR of the corresponding spectrum. In this case, the determination of the continuum is highly uncertain and could significantly affect the value of the PAH EW. For SBS0335-052E, the SNR is high enough, but no PAH features can be identified in its mid-IR spectrum. We do not derive upper limits for the PAH EWs at 7.7 μm and 8.6 μm, because no reliable templates for those features are available.

optical value of 6.5±1.8 (in BCDs), which could be due to the adopted ICFs in the optical studies. When comparing the newly derived neon and sulfur abundances with the oxygen abundances measured from the optical lines, we find a good overall agreement. This indicates that there are few completely dust enshrouded HII regions in our BCDs, or if such HII regions are present, they have similar metallicities to the ones probed in the optical. Finally, the infrared derived neon and sulfur abundances also correlate, with some scatter, with the corresponding elemental abundances derived from the optical data.

Acknowledgments We thank Robert Kennicutt whose detailed comments help to improve this manuscript. We also thank Shannon Gutenkunst and Henrik Spoon for helpful discussions as well as an anonymous referee whose insightful suggestions helped to improve this manuscript. This work is based in part on observations made with the Spitzer Space Telescope, which is operated by the Jet Propulsion Laboratory, California Institute of Technology, under NASA contract 1407. Support for this work was provided by NASA through Contract Number 1257184 issued by JPL/Caltech.

BIBLIOGRAPHY

Anders, E., & Grevesse, N. 1989, Geochim. Cosmochim. Acta, 53, 197

Allende Prieto, C., Lambert, D. L., & Asplund, M. 2001, ApJ, 556, L63

Aloisi, A. et al. 2007, astro-ph/0702216, Proceedings of the IAU Symp. 241 "Stellar Populations as Building Blocks of Galaxies"

Aloisi, A., Savaglio, S., Heckman, T.M., Hoopes, C. G., Leitherer, C., & Sembach, K. R. 2003, ApJ, 595, 760

Asplund, M., Grevesse, N., & Sauval, A. J. 2005, Cosmic Abundances as Records of Stellar Evolution and Nucleosynthesis, 336, 25

Bergvall, N., & Oumlstlin, G. 2002, A&A, 390, 891

Becker, R. H., White, R. L., & Helfand, D. J. 1995, ApJ, 450, 559

Bernard Salas, J., et al. 2008, ApJ, 672, 274

Bernard Salas, J., Pottasch, S. R., Feibelman, W. A., & Wesselius, P. R. 2002, A&A, 387, 301

Bernard Salas, J., Pottasch, S. R., Beintema, D. A., & Wesselius, P. R. 2001, A&A, 367, 949

Cannon, J. M., Walter, F., Skillman, E. D., & van Zee, L. 2005, ApJ, 621, L21

Cohen, M., Megeath, S. T., Hammersley, P. L., Martín-Luis, F., & Stauffer, J. 2003, AJ, 125, 2645

Denicoló, G., Terlevich, R., & Terlevich, E. 2002, MNRAS, 330, 69

Draine, B. T. 2003, ARA&A, 41, 241

Engelbracht, C. W., Gordon, K. D., Rieke, G. H., Werner, M. W., Dale, D. A., & Latter, W. B. 2005, ApJ, 628, L29

Feldman, U., & Widing, K. G. 2003, Space Science Reviews, 107, 665

Fluks, M. A., Plez, B., The, P. S., de Winter, D., Westerlund, B. E., & Steenman, H. C. 1994, A&AS, 105, 311

Gil de Paz, A., Madore, B. F., & Pevunova, O. 2003, ApJS, 147, 29

Grevesse, N., & Sauval, A. J. 1998, Space Science Reviews, 85, 161

Guseva, N. G., Izotov, Y. I., & Thuan, T. X. 2000, ApJ, 531, 776

Hao, L., et al., 2007, in preparation

Henry, R. B. C., Kwitter, K. B., & Balick, B. 2004, AJ, 127, 2284

Higdon, S. J. U., et al. 2004, PASP, 116, 975

Ho, L. C., Filippenko, A. V., & Sargent, W. L. W. 1997, ApJS, 112, 315

Hogg, D. W., Tremonti, C. A., Blanton, M. R., Finkbeiner, D. P., Padmanabhan, N., Quintero, A. D., Schlegel, D. J., & Wherry, N. 2005, ApJ, 624, 162

Houck, J. R., et al. 2004a, ApJS, 154, 18

Houck, J. R., et al. 2004b, ApJS, 154, 211

Houck, J. R., Shure, M. A., Gull, G. E., & Herter, T. 1984, ApJ, 287, L11

Hummer, D. G., Berrington, K. A., Eissner, W., Pradhan, A. K., Saraph, H. E., & Tully, J. A. 1993, A&A, 279, 298

Hummer, D. G., & Storey, P. J. 1987, MNRAS, 224, 801

Hunt, L. K., Thuan, T. X., Sauvage, M., & Izotov, Y. I. 2006, ApJ, 653, 222

Hunt, L., Bianchi, S., & Maiolino, R. 2005a, A&A, 434, 849

Hunt, L. K., Dyer, K. K., Thuan, T. X., & Ulvestad, J. S. 2004, ApJ, 606, 853

Hunter, D. A., & Hoffman, L. 1999, AJ, 117, 2789

Izotov, Y. I., Thuan, T. X., & Lipovetsky, V. A. 1994, ApJ, 435, 647

Izotov, Y. I., Thuan, T. X., & Lipovetsky, V. A. 1997, ApJS, 108, 1

Izotov, Y. I., & Thuan, T. X. 1998, ApJ, 500, 188

Izotov, Y. I., Chaffee, F. H., Foltz, C. B., Green, R. F., Guseva, N. G., & Thuan, T. X. 1999, ApJ, 527, 757

Izotov, Y. I., & Thuan, T. X. 1999, ApJ, 511, 639

Izotov, Y. I., Chaffee, F. H., & Green, R. F. 2001, ApJ, 562, 727

Izotov, Y. I., Papaderos, P., Guseva, N. G., Fricke, K. J., & Thuan, T. X. 2004, A&A, 421, 539

Izotov, Y. I., Thuan, T. X., & Guseva, N. G. 2005, ApJ, 632, 210

Izotov, Y. I., Schaerer, D., Blecha, A., Royer, F., Guseva, N. G., & North, P. 2006, A&A, 459, 71

Kirshner, R. P., Oemler, A., Jr., Schechter, P. L., & Shectman, S. A. 1981, ApJ, 248, L57

Kniazev, A. Y., Grebel, E. K., Hao, L., Strauss, M. A., Brinkmann, J., & Fukugita, M. 2003, ApJ, 593, L73

Kobulnicky, H. A., & Skillman, E. D. 1997, ApJ, 489, 636

Kong, X., Cheng, F. Z., Weiss, A., & Charlot, S. 2002, A&A, 396, 503

Kunth, D. & Östlin, G. 2000, A&A Rev., 10, 1

Kunth, D., & Sargent, W. L. W. 1986, ApJ, 300, 496

Lebouteiller, V., Kunth, D., Lequeux, J., Lecavelier des Etangs, A., Désert, J.-M., Hébrard, G., & Vidal-Madjar, A. 2004, A&A, 415, 55

Loose, H.-H., & Thuan, T. X. 1985, Star-Forming Dwarf Galaxies and Related Objects, 73

Madden, S. C., Galliano, F., Jones, A. P., & Sauvage, M. 2006, A&A, 446, 877

Madden, S. C. 2000, New Astronomy Review, 44, 249

Marigo, P., Bernard-Salas, J., Pottasch, S. R., Tielens, A. G. G. M., & Wesselius, P. R. 2003, A&A, 409, 619

Martín-Hernández, N. L., et al. 2002, A&A, 381, 606

Martín-Hernández, N. L., Schaerer, D., Peeters, E., Tielens, A. G. G. M., & Sauvage, M. 2006, A&A, 455, 853

Melbourne, J., & Salzer, J. J. 2002, AJ, 123, 2302

Moustakas, J., & Kennicutt, R. C., Jr. 2006, ApJS, 164, 81

O'Halloran, B., Satyapal, S., & Dudik, R. P. 2006, ApJ, 641, 795

Osterbrock, D. E. 1989, Astrophysics of gaseous nebulae and active galactic nuclei. Research supported by the University of California, John Simon Guggenheim Memorial Foundation, University of Minnesota, et al. Mill Valley, CA, University Science Books, 1989, 422p

Peimbert, M., & Torres-Peimbert, S. 1992, A&A, 253, 349

Plante, S., & Sauvage, M. 2002, AJ, 124, 1995

Popescu, C. C., & Hopp, U. 2000, A&AS, 142, 247

Pottasch, S. R., & Bernard-Salas, J. 2006, A&A, 457, 189

Pustilnik, S. A., et al. 2005, A&A, 442, 109

Rosenberg, J. L., Ashby, M. L. N., Salzer, J. J., & Huang, J.-S. 2006, ApJ, 636, 742

Rubin, R. H., et al. 2007, MNRAS, 377, 1407

Rubin, R. H. et al. 2006, in *Galaxy Evolution Across the Hubble Time*, IAU Symposium 235, Eds.F. Combes & J. Palous, (Cambridge U. Press) (in press)

Salzer, J. J., Jangren, A., Gronwall, C., Werk, J. K., Chomiuk, L. B., Caperton, K. A., Melbourne, J., & McKinstry, K. 2005, AJ, 130, 2584

Searle, L., & Sargent, W. L. W. 1972, ApJ, 173, 25

Shi, F., Kong, X., Li, C., & Cheng, F. Z. 2005, A&A, 437, 849

Simpson, J. P., & Rubin, R. H. 1990, ApJ, 354, 165

Simpson, J. P., Rubin, R. H., Colgan, S. W. J., Erickson, E. F., & Haas, M. R. 2004, ApJ, 611, 338

Skillman, E. D., Kennicutt, R. C., & Hodge, P. W. 1989, ApJ, 347, 875

Sloan,G., et al., 2007, in prep

Smith, J. D. T., et al. 2007, ApJ, 656, 770

Spoon, H. W. W., Marshall, J. A., Houck, J. R., Elitzur, M., Hao, L., Armus, L., Brandl, B. R., & Charmandaris, V. 2007, ApJ, 654, L49

Stasiń'ska, G. 2007, astro-ph/0704.0348, Lectures given at the XVIII Canary Island Winterschool "The emission line Universe", to be published by Cambridge University Press

Thuan, T. X., Hibbard, J. E., & Lévrier, F. 2004, AJ, 128, 617

Thuan, T. X., Lecavelier des Etangs, A., & Izotov, Y. I. 2002, ApJ, 565, 941

Thuan, T. X., Sauvage, M., & Madden, S. 1999, ApJ, 516, 783

Thuan, T. X., Izotov, Y. I., & Lipovetsky, V. A. 1995, ApJ, 445, 108

Tsamis, Y. G., & Péquignot, D. 2005, MNRAS, 364, 687

Verma, A., Lutz, D., Sturm, E., Sternberg, A., Genzel, R., & Vacca, W. 2003, A&A, 403, 829

Vermeij, R., Peeters, E., Tielens, A. G. G. M., & van der Hulst, J. M. 2002, A&A, 382, 1042

Vilchez, J. M., & Pagel, B. E. J. 1988, MNRAS, 231, 257

Werner, M., et al. 2004, ApJS, 154,1

Wu, Y., Charmandaris, V., Hao, L., Brandl, B. R., Bernard-Salas, J., Spoon, H. W. W., & Houck, J. R. 2006, ApJ, 639, 157

Wu, Y., et al. 2007, ApJ, 662, 952

Zwicky, F. 1966, ApJ, 143, 192

CHAPTER 4

BLUE COMPACT DWARF GALAXIES WITH SPITZER: THE INFRARED/RADIO PROPERTIES*

Abstract We study the correlation between the radio, mid-infrared and far-infrared properties for a sample of 28 blue compact dwarf (BCD) and low metallicity star-forming galaxies observed by *Spitzer*. We find that these sources extend the same far-infrared to radio correlation typical of star forming late type galaxies to lower luminosities. In BCDs, the 24μm (or 22μm) mid-infrared to radio correlation is similar to starburst galaxies, though there is somewhat larger dispersion in their q_{24} parameter compared to their q_{FIR}. No strong correlations between the q parameter and galaxy metallicity or effective dust temperature have been detected, though there is a hint of decreasing q_{24} at low metallicities. The two lowest metallicity dwarfs in our sample, IZw18 and SBS0335-052E, despite their similar chemical abundance, deviate from the average q_{24} ratio in opposite manners, displaying an apparent radio excess and dust excess respectively.

4.1 Introduction

More than 35 years ago, a correlation between the 10μm mid-infrared (mid-IR) and 1.4 GHz luminosities in galactic nuclei was first noticed by van der Kruit (1971). In 1983, the launch of the *Infrared Astronomical Satellite (IRAS)* brought a new era in collecting large samples of data in the infrared, and sparked numerous studies investigating the above mentioned correlation in star forming galaxies. Both the radio and infrared emission are closely related to star formation activities. The radio continuum is known to originate from two processes: thermal free-free emission from ionized gas in HII regions and non-thermal synchrotron radiation

*Originally published as: Yanling Wu, V.Charmandaris, J.R.Houck, B. Bernard-Salas, V. Lebouteiller, B. R.Brandl, D. Farrah (2008), *The Astrophysical Journal*, 676, 970

from relativistic electrons that are accelerated in the supernovae remnants (SNRs) (see Condon 1992, for a review). The thermal emission usually has a rather flat spectrum with $f_\nu \propto \nu^{-0.1}$ while the non-thermal component often has a much steeper spectral slope with $f_\nu \propto \nu^{-0.8}$. In normal galaxies the relative contribution of the two components varies with frequency and at 1.4 GHz the radio continuum is dominated (at nearly $\sim$90%) by the non-thermal component. The infrared emission is due to the thermal re-radiation of starlight from dust surrounding HII regions (Harwit & Pacini 1975). Based mostly on *IRAS* data, it has been shown that the far-infrared (FIR, 40-120 μm) to radio correlation holds well over a remarkably wide range of star forming galaxies, spanning several orders of magnitude in luminosities (Helou et al. 1985; de Jong et al. 1985; Condon et al. 1991; Yun et al. 2001). The availability of deep observations of distant galaxies by the *Infrared Space Observatory (ISO)* and recently by *Spitzer* (Werner et al. 2004) showed that the correlation between the IR and radio emission is not limited to the local universe but also extends in galaxies at higher redshifts (Garrett 2002; Appleton et al. 2004). It was also revealed that in addition to the FIR, the mid-IR emission at $\sim$24μm correlates with the 20cm radio continuum, though with more scatter (Elbaz et al. 2002; Gruppioni et al. 2003; Appleton et al. 2004; Wu et al. 2005). A number of very deep *Spitzer* mid-IR and FIR surveys can now probe a population of galaxies with low infrared luminosities for which ancillary data, including deep radio imaging, are becoming available (e.g. Jannuzi & Dey 1999; Sanders et al. 2007; Rosenberg et al. 2006). This is particularly interesting since in the near future $\sim$ 20μm is the longest wavelength which will likely be probed by the James Web Space Telescope. It is thus instructive to examine the mid-IR to radio correlation in more detail in these low luminosity nearby systems, for which little is known to date.

As ubiquitous as the FIR/radio correlation appears to be, there are a few sig-

nificant deviations from it. Radio excess exists in some instances, such as galaxies hosting an active galactic nucleus (AGN). External magnetic field compression due to the interaction with nearby galaxies could also produce extra emission in the radio continuum (Miller & Owen 2001). Conversely, synchrotron deficiency has been found in some nascent starburst galaxies studied by Roussel et al. (2003, 2006) which was attributed to the lack of time for massive young stars to evolve into supernovae (SN) since these galaxies are just at the onset of a starburst episode. On the other hand, in the infrared, dust emission can be damped in an optically-thin environment, because the ultraviolet (UV) and optical light may not be fully reprocessed by the dust, as seen in low luminosity dwarf galaxies.

Blue compact dwarf galaxies are a group of extra-galactic objects that are characterized by their blue optical colors, small sizes ($\leq$1 kpc) and low luminosities (M_B >-18). These galaxies do not display any AGN signature[1] and have recent bursts of star formation in a relatively unevolved chemical environment. As such they have been proposed as nearby analogs of star formation in young galaxies in the early universe. In a metal poor environment, star forming regions are usually optically thin and emit less in the infrared. However, Devereux & Eales (1989) suggested that in a low luminosity galaxy, the radio emission also decreases, and probably faster than the infrared. The deficiency in both the non-thermal radio and FIR emission may counterbalance each other and result in a similar FIR/radio ratio to the one observed in normal spiral galaxies (Klein et al. 1991). This was examined by a study of star formation rates (SFRs) in BCDs performed by Hopkins et al. (2002), in which the authors found an excellent agreement between the SFRs estimated from 1.4 GHz and 60 μm luminosities. As Bell (2003) has pointed out though, the FIR/radio correlation is almost linear, not because the IR and radio

[1]A possible exception among our sources is CG0752 in which the high ionization lines [NeV]λ14.3/24.3μm are detected (see Hao et al. 2007).

emission reflect the SFRs correctly, but because in low luminosity galaxies they are both underestimated by similar factors. This is in agreement with Helou & Bicay (1993), who found from their modelling work in disk galaxies that the transparency of the disk was about the same to both re-emission processes. Hunt et al. (2005a) in their analysis of the spectral energy distributions (SEDs) of low metallicity BCDs, noticed that these systems do not follow several of the usual correlations between the mid-IR, FIR and radio emission and display a scatter of a factor of ∼10.

The *Spitzer* Space telescope has enabled us to study the infrared properties of a large sample of BCDs, probing the lower end of the luminosity and metallicity range. In this paper, the fifth in a series (Houck et al. 2004b; Wu et al. 2006, 2007, 2008), we examine their mid-IR and FIR to radio correlation extending the work of Hopkins et al. (2002). We describe the sample selection and the observational data in §2. A detailed study of mid-IR and FIR/radio correlation, as well as its dependence with other parameters, such as metallicity and dust temperature are presented in §3. We also discuss two extreme cases, IZw18 and SBS0335-052 in §3. We summarize our conclusions in §4.

4.2 Observations

As part of the IRS[2] (Houck et al. 2004a) Guaranteed Time Observation (GTO) program (PID: 85), we have compiled a sample of BCD candidates (∼64) selected from the Second Byurakan Survey (SBS), Bootes void galaxies (Kirshner et al. 1981; Popescu & Hopp 2000), and other commonly studied BCDs. These sources are known to have low metallicities ranging from $0.03\,Z_{\odot}$ to $0.5\,Z_{\odot}$[3]. Their $22\,\mu$m

[2]The IRS was a collaborative venture between Cornell University and Ball Aerospace Corporation funded by NASA through the Jet Propulsion Laboratory and the Ames Research Center.

[3]Here we adopt the new oxygen solar abundance of 12+log(O/H)=8.69 (Allende Prieto et al. 2001). Wu et al. (2008) have derived neon and sulfur abundances for a sample of BCDs using the infrared data, but these abundances are not available for all of the sources in this study.

fluxes have been published in Wu et al. (2006). We also include 10 galaxies from Engelbracht et al. (2005) (PID: 59), which are mostly BCDs and starburst galaxies, and span a larger metallicity range ($0.03\,Z_{\odot}$~$1.5\,Z_{\odot}$)[4]. For all galaxies with 22 (24) μm detections, we searched the literature as well as the public archives (NVSS and FIRST) for 1.4GHz radio continuum data. We restirct our sample to sources with both mid-IR and radio detections which results in a sample of 23 galaxies. Finally, we also include 5 galaxies that have 22 μm detections and 1.4 GHz upper limits published by Hopkins et al. (2002) for comparison between ours and Hopkins' samples. Note that the sample was not selected based on infrared properties, but merely on BCD-type objects and the availability of both infrared and radio data. As a result, our sample is not complete, but the large number of sources that only became detectable in the infrared with *Spitzer*, allows us to probe the properties of low luminosity dwarf galaxies, and provide statistically meaningful results. The observational information for this sample and previously published data are presented in Table 4.1, which includes the positions of the sources, their mid-IR, FIR and 1.4GHz flux densities, as well as the oxygen abundances of the ionized gas.

All sources in this study have mid-IR flux measurements either at 22μm with the IRS red peak-up camera and/or at 24 μm with MIPS (Rieke et al. 2004). The photometric fluxes of these two bands differ by less than 10% for galaxies in the local universe. This was confirmed by using a suite of ~100 spectra of nearby galaxies from our IRS/GTO database and calculating their synthetic 22 and 24μm fluxes after convolving the spectra with the corresponding filter response curves. For consistency, in our analysis we use the MIPS 24 μm measurements, and the 22 μm values are only used when the 24 μm values are not available. For

[4]The galaxies in PID 59 partly overlap with the BCDs in PID 85. We have also excluded some galaxies which the authors derived their 24 μm fluxes by doing a color correction to the *IRAS* 25 μm fluxes because of the aperture difference between these two band filters.

sources above the IRS 22μm and MIPS 24μm saturation limits we use the IRS low resolution spectrum to estimate a synthetic 24 μm flux. We also obtained far-infrared fluxes for our sample from the archival *IRAS* 60 and 100 μm data (Moshir & et al. 1990; Sanders et al. 2003).

Most of the 1.4 GHz radio continuum data are from the NRAO VLA Sky Survey (NVSS) (Condon et al. 1998), while one is from the Faint Images of the Radio Sky at Twenty cm (FIRST) (Becker et al. 1995), along with some individual observations (references in Table 4.1). A total of seven sources were too faint and were not included in the NVSS catalogue. For those we used the values of Hopkins et al. (2002) who studied a similar BCD sample and remeasured the 1.4GHz fluxes using the images from NVSS and FIRST, providing radio detections for 2 sources and better upper limits for another five sources that overlaps with the galaxies in our sample.

Our final sample consists of 28 galaxies, all of which have *Spitzer* mid-IR 24 μm and/or 22 μm flux measurements. Among these galaxies, 23 sources have 1.4GHz radio continuum data and 5 have measured upper limits. *IRAS* 60 μm and 100 μm fluxes are available for 16 sources and 3 more are detected only at 60 μm. We list the photometry of our sources in Table 4.1. The uncertainty in the 22 μm or 24 μm photometry is less than 5%. The *IRAS* 60 μm and 100 μm fluxes typically have less than a few percent of error, but could go up to $\sim$15% for some of the fainter sources. The rms noise level for NVSS is $\sim$0.5 mJy beam^{-1}.

Table 4.1. Properties of the Sample

ID	Object Name	RA J2000	Dec J2000	Flux (mJy) 1.4 GHz	24(22) μm	60 μm	100 μm	12+log(O/H)	References 1.4 GHz	24 μm	IRAS	Z
1	Haro11	00h36m52.5s	-33d33m19s	26.8	1900	6880	5040	7.9	(1)	(2)	(3)	(4)
2	NGC1140	02h54m33.6s	-10d01m40s	23.6	316.6	3358	4922	8.5	(1)	(5)	(6)	(7)
3	SBS0335-052E	03h37m44.0s	-05d02m40s	0.46	66	···	···	7.3	(8)	(2)		(9)
4	NGC1569	04h30m47.0s	+64d50m59s	336.3	2991	54360	55290	8.2	(1)	(2)	(3)	(10)
5	IIZw40	05h55m42.6s	+03d23m32s	32.5	1500	6570	5270	8.1	(1)	(2)	(3)	(7)
6	UGC4274	08h13m13.0s	+45d59m39s	10.5	240	3236	6448	8.5	(1)	(2)	(6)	
7	He2-10	08h36m15.2s	-26d24m34s	83.8	4900	···	···	8.9	(1)	(2)		(11)
8	NGC2782	09h14m05.1s	+40d06m49s	124.5	960	9170	13760	8.8	(1)	(2)	(3)	(12)
9	NGC2903	09h32m10.1s	+21d30m03s	444.5	2200	60540	130430	9.3	(1)	(2)	(3)	(11)
10	IZw18	09h34m02.0s	+55d14m28s	1.83	5.5	···	···	7.2	(13)	(2)		(9)
11	SBS0940+544	09h44m16.7s	+54d11m33s	<2.3	2.3	···	···	7.5	(14)	(5)		(15)
12	NGC3077	10h03m19.1s	+68d44m02s	29.0	1500	15900	26530	8.6	(1)	(2)	(3)	(16)
13	Mrk153	10h49m05.0s	+52d20m08s	4.0	29	280	<480	7.8	(1)	(2)	(6)	(17)
14	VIIZw403	11h27m59.9s	+78d59m39s	1.2	28	···	···	7.7	(18)	(2)		(9)
15	Mrk1450	11h38m35.6s	+57d52m27s	<2.0	48	279	<575	8.0	(14)	(2)	(6)	(7)
16	UM448	11h42m12.4s	+00d20m03s	32.6	560	4139	4321	8.0	(1)	(2)	(6)	(7)
17	UM461	11h51m33.3s	-02d22m22s	<2.6	30	···	···	7.8	(14)	(2)		(9)
18	UM462	11h52m37.3s	-02d28m10s	5.8	110	944	896	8.0	(1)	(2)	(6)	(9)
19	SBS1159+545	12h02m02.4s	+54d15m50s	<2.3	6.4	···	···	7.5	(14)	(5)		(19)
20	NGC4194	12h14m09.5s	+54d31m37s	100.7	3100	23200	25160	8.8	(1)	(2)	(3)	(16)
21	NGC4670	12h45m17.1s	+27d07m32s	13.7	210	2634	4470	8.2	(1)	(2)	(6)	(12)

Table 4.1 (continued)

ID	Object Name	RA J2000	Dec J2000	Flux (mJy) 1.4 GHz	24(22) μm	60 μm	100 μm	12+log(O/H)	References 1.4 GHz	24 μm	IRAS	Z
22	SBS1415+437	14h17m01.4s	+43d30m05s	4.3	19.6	···	···	7.6	(14)	(5)		(9)
23	Mrk475	14h39m05.4s	+36d48m21s	<2.7	10.8	···	···	7.9	(14)	(5)		(9)
24	CG0563	14h52m05.7s	+38d10m59s	6.2	97.0	870	1900	8.7	(1)		(6)	
25	CG0752	15h31m21.3s	+47d01m24s	4.8	138.9	837	1059	···	(1)	(5)	(6)	
26	SBS1533+574	15h34m13.8s	+57d17m06s	4.2	53.4	257	405	8.1	(14)	(5)	(6)	(9)
27	Mrk1499	16h35m21.1s	+52d12m53s	1.5	33.8	256	617	8.1	(20)	(5)	(6)	(21)
28	Mrk930	23h31m58.3s	+28d56m50s	12.2	170	1245	<2154	8.1	(1)	(2)	(6)	(7)

References. — (1) Condon et al. (1998), (2) Engelbracht et al. (2005), (3) Sanders et al. (2003), (4) Bergvall & Östlin (2002), (5) Wu et al. (2006), (6) Moshir & et al. (1990), (7) Guseva et al. (2000), (8) Hunt et al. (2004), (9) Izotov & Thuan (1999), (10) Kobulnicky & Skillman (1997), (11) Kobulnicky & Johnson (1999), (12) Heckman et al. (1998), (13) Hunt et al. (2005a), (14) Hopkins et al. (2002), (15) Thuan & Izotov (2005), (16) Storchi-Bergmann et al. (1994), (17) Kunth & Joubert (1985), (18) Leroy et al. (2005), (19) Izotov & Thuan (1998), (20) FIRST catalog, (21) Shi et al. (2005)

4.3 Results

4.3.1 Mid-IR and FIR to Radio Correlation in BCDs

The sensitivity and efficiency of the *Spitzer* Space Telescope has allowed us to probe the correlation between the mid-IR and radio luminosities for a large number of galaxies. Using the 24 μm and 70 μm MIPS imaging data of the First Look Survey, Appleton et al. (2004) have demonstrated the first direct evidence for the universality of the mid-IR/radio and FIR/radio correlation to z$\sim$1. Wu et al. (2005) have also studied the mid-IR/radio correlation in a sample of star-forming galaxies and found that both the 8 μm and 24 μm luminosity are clearly correlated with the 1.4GHz radio luminosity. Their sample included only a few (3) dwarf galaxies and suggested that there may be a slope change for dwarf galaxies, which could be due to the lower dust-to-gas ratios and lower metallicities of the dwarfs. A detailed analysis of the spatial distribution of the infrared to radio correlation using *Spitzer* data on a sample of nearby late type spiral galaxies has been performed by Murphy et al. (2006a,b) in which the authors found that the ratio of the mid-IR and FIR to radio emission does vary from one region to the other. In general though, the dispersion is small and the ratio decreases with surface brightness and galactocentric radius.

Using the data from this sample of low metallicity dwarf galaxies we plot in Figure 4.1 the radio luminosity of the sample as a function of the FIR luminosity. The luminosities of the sources we study span nearly 4 orders of magnitudes, but the correlation between the FIR and the radio is remarkably tight. The scatter in the ratio of the FIR and radio luminosities is 0.23 dex, i.e. less than a factor of 2. We performed a least-squares bisector fit to the data and found: $\log[L_{1.4GHz}(WHz^{-1})]=1.09\times\log(L_{FIR}/L_{\odot})+10.75$. For comparison, we have in-

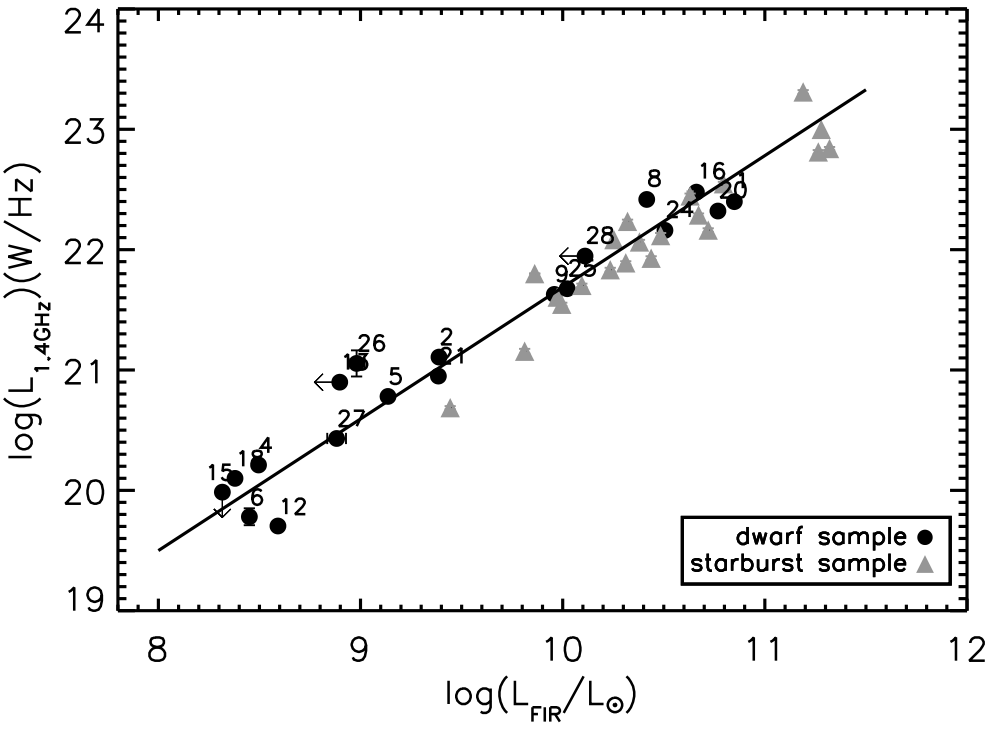

Figure 4.1 The FIR to 1.4 GHz radio luminosity correlation for this sample. Our data are presented with filled circles. The numbers next to each symbol correspond to their IDs in Table 4.1. The solid line is the best fit to this sample excluding the upper limits. For comparison, we have also include the starburst galaxies of Brandl et al. (2006), indicated with triangles.

cluded in the plot the starburst galaxies from Brandl et al. (2006) marked with triangles, which has an identical slope (within 1σ). This slope of 1.09±0.07 for the dwarf galaxy data agrees well with the slope of 1.10±0.04 found by Bell (2003) for a sample of 162 galaxies, as well as the slope of 1.11±0.02 for the infrared selected sources from the *IRAS* Bright Galaxy Sample (BGS) (Condon et al. 1991). This is also in agreement with Hopkins et al. (2002) and would suggest that globally our BCDs have a very similar FIR/radio correlation to normal galaxies.

Another way to parameterize the IR/radio correlation is to calculate the ratio of FIR to radio luminosity $q_{\rm FIR}$ according to the Helou et al. (1985) formula as well as the q_{24} following the definition of Appleton et al. (2004)[5]. We plot the q_{24} values for our sample as a function of the 24μm luminosity of the galaxies in Figure 4.2. For this sample we find that $q_{\rm FIR}$ = 2.4±0.2, consistent with the value of normal galaxies of $q_{\rm FIR}$ = 2.3±0.2 found by Condon (1992). When using the mid-IR 24μm data, we find that q_{24} =1.3±0.4 (see Table 4.2). The standard deviation in q_{24} is ∼twice that of $q_{\rm FIR}$. This is not unexpected given that the spectrum of star forming galaxies shows substantially larger variations in spectral slope in the mid-IR (see Brandl et al. 2006) than in the FIR (Dale et al. 2006). A small change in the geometry of the emitting regions would affect $F_\nu(24\,\mu{\rm m})$ and thus q_{24} ratio much more than the FIR emission and $q_{\rm FIR}$. A similar result has also been noticed by Appleton et al. (2004) and Murphy et al. (2006a) who found a larger dispersion in q_{24} as compared to q_{70}[6] and suggested that this is probably due to a larger intrinsic dispersion in the IR/radio correlation at shorter wavelengths. Interestingly, the Appleton et al. (2004) values for q_{24} = 0.84±0.28 or the k-corrected q_{24} of 0.94±0.23 are somewhat smaller than our results, though

[5]We use $q_{\rm FIR}$=log[1.26×10^{-14} (2.58$S_{60\mu m}$+$S_{100\mu m}$)/(3.75 ×10^{12} $F_{1.4GHz}$)] where $S_{60\mu m}$ and $S_{100\mu m}$ are in Jy and $F_{1.4GHz}$ is in $Wm^{-2}Hz^{-1}$ (Helou et al. 1985). We also define q_{24}= log ($S_{24\mu m}/S_{1.4GHz}$) where $S_{24\mu m}$ and $S_{1.4GHz}$ are in Jy as in Appleton et al. (2004).

[6]We define q_{70}= log ($S_{70\mu m}/S_{1.4GHz}$) where $S_{70\mu m}$ and $S_{1.4GHz}$ are in Jy as in Appleton et al. (2004).

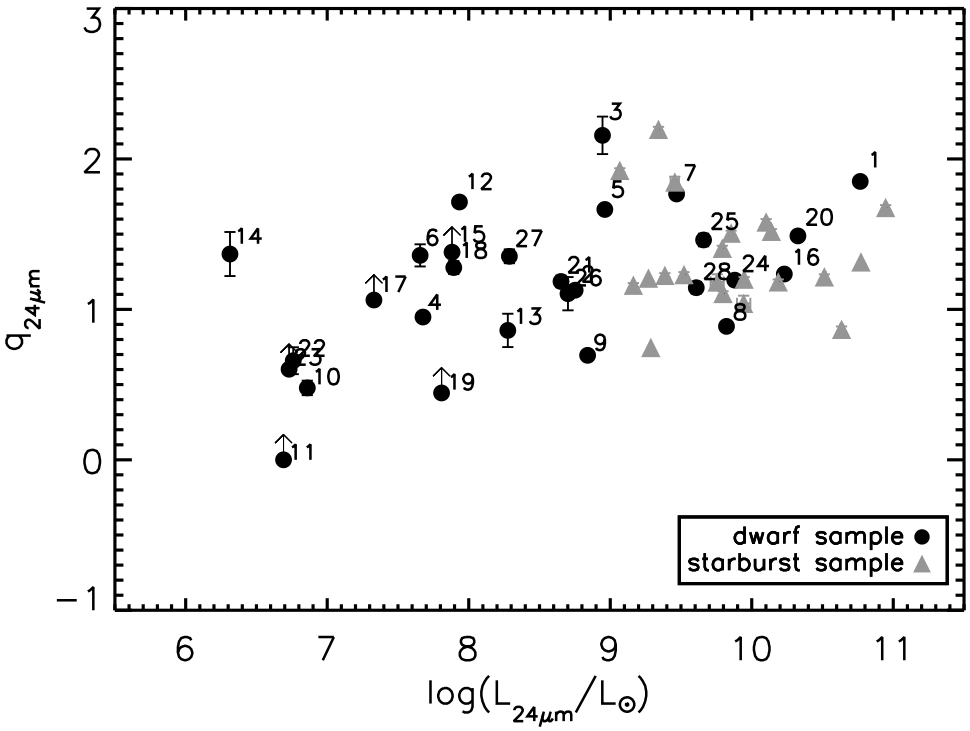

Figure 4.2 The q_{24} as a function of the the 24 μm monochromatic luminosity L_{24}. The symbols are the same as in Figure 1.

consistent within 2σ. One possible explanation is that the dust temperature of low luminosity dwarf galaxies tends to peak at shorter wavelength than normal star forming galaxies, which would result in an elevated 24 μm based luminosity. An alternative explanation is that due to the peculiar morphology of dwarf galaxies, more electrons escape from the galaxy because of the cosmic ray diffusion. Boyle et al. (2007) have also found a high q_{24}=1.39±0.02 for the sources they studied, and postulated that this may be due to a change in the mean q_{24} ratio for objects with $F_\nu(24\,\mu m)$ <1 mJy, however, their sources are much further away and may not be comparable to the low metallicity star forming galaxies we study in the local universe.

Table 4.2. Derived Quantities of the Sample

ID	Object Name	Distance[a] (Mpc)	$L_{1.4GHz}$ ($\times 10^{20}$ W Hz^{-1})	$L_{24\mu m}$ ($\times 10^{8} L_{\odot}$)	L_{FIR} ($\times 10^{8} L_{\odot}$)	q_{24}	q_{FIR}
1	Haro11	88	250.5	584.2	706.3	1.85	2.46
2	NGC1140	21.2	12.8	5.6	24.4	1.13	2.29
3	SBS0335-052E	58	18.7	8.8	···	2.16	···
4	NGC1569	2.0	1.6	0.5	3.1	0.95	2.29
5	IIZw40	12.4	6.0	9.2	13.7	1.66	2.36
6	UGC4274	6.9	0.6	0.5	2.8	1.36	2.68
7	He2-10	12	15.6	29.9	···	1.77	···
8	NGC2782	41.7	216.3	66.3	260.4	0.89	2.00
9	NGC2903	8.9	42.5	6.9	90.9	0.69	2.34
10	IZw18	18.2	0.7	0.07	···	0.48	1.31[b]
11	SBS0940+544	23	< 1.5	0.05	···	>0.00	···
12	NGC3077	3.8	0.5	0.9	3.9	1.71	2.89
13	Mrk153	40.5	7.9	1.9	<7.9	0.86	<2.00
14	VIIZw403	4.3	0.03	0.02	···	1.37	···
15	Mrk1450	20.0	<1.0	0.8	<2.1	>1.38	···
16	UM448	87.4	300.6	188.9	458.6	1.23	2.19
17	UM461	13.4	<0.6	0.2	···	>1.06	···
18	UM462	13.4	1.3	0.8	2.4	1.28	2.29
19	SBS1159+545	50	<7.0	0.6	···	>0.44	···
20	NGC4194	41.5	209.3	212.0	586.0	1.49	2.45
21	NGC4670	23.2	8.9	4.5	24.3	1.19	2.44
22	SBS1415+437	8.7	0.4	0.06	···	0.66	···
23	Mrk475	11.2	<0.4	0.05	···	>0.60	···
24	CG0563	139	144.6	74.4	320.5	1.19	2.35
25	CG0752	90	47.3	45.1	105.3	1.46	2.35
26	SBS1533+574	47	11.3	4.7	9.6	1.10	1.93
27	Mrk1499	39	2.7	2.0	7.6	1.35	2.46
28	Mrk930	77.5	88.4	40.5	<129.0	1.14	<2.17

[a]The distances to the galaxies of the sample are adopted from Moustakas & Kennicutt (2006) when available, while the rest of the sources are calculated from the redshifts taken from NED, assuming a ΛCDM cosmology with $H_0 = 70$ km s^{-1} Mpc^{-1}, $\Omega_m = 0.3$ and $\Omega_\lambda = 0.7$. For IZw18, we adopt the newly derived distance by Aloisi et al. (2007). The average uncertainty in the distances is ∼5%, mainly due to the value of H_0.

[b]This is calculated based on the "equivalent" *IRAS* 60 and 100 μm fluxes (see Section 3.4).

4.3.2 Metallicity and Dust Temperature Effects on q_{IR}

A number of physical parameters, such as the metallicity, dust grain size distribution, and temperature may affect the shape of the infrared SED. Consequently, we search for correlations between the q ratios of the galaxies in our sample with those parameters. Our sample covers a metallicity range of $7.2 \leq 12+\log(O/H) \leq 8.9$. In low metallicity galaxies, the dust content is usually low, even though there are notable exceptions such as SBS0335-052E (Houck et al. 2004b), thus the emission of UV light might not be fully reprocessed by the dust and re-emitted at the infrared wavelengths. However, these galaxies might have a quenched synchrotron radiation. This can be attributed to various reasons including a lack of supernovae remnants which accelerate particles producing radio emission, the escape of fast cosmic rays from the galaxy, etc. These two competing factors, dust and radio emission, counter balance each other (see Bell 2003). BCDs though, are typically small, less than $\sim$1 kpc in size, and have fewer HII regions with massive stars (w.r.t. normal galaxies) which heat the dust and go supernovae to produce cosmic rays. As a result the averaging effects in the sampling of the properties of the interstellar medium which result from the limited spatial resolution in dense galactic disks is not so prominent in BCDs. Furthermore, the small number of statistics may also contribute to the observed higher dispersion in q_{24} ratios in metal-poor dwarf galaxies. We investigate how metallicity affects the q_{24} ratios by dividing the dwarf galaxies in our sample into two groups: a lower metallicity group with $12+\log(O/H) \leq 8.0$ and a higher metallicity group with $12+\log(O/H) > 8.0$. This metallicity threshold was selected following Rosenberg et al. (2008) who noticed a change in the properties of the star-forming dwarf galaxies they studied around this metallicity value. We find a mean $q_{24} = 1.1 \pm 0.1$[7] for the first group and $q_{24} =$

[7]Here we use the standard error of the mean (SEM) to quantify the dispersion in the mean value.

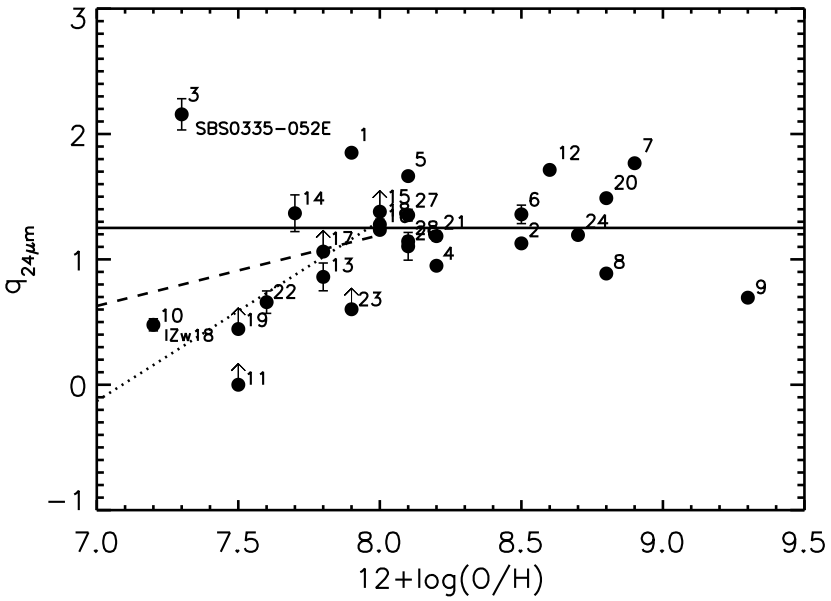

Figure 4.3 The q_{24} ratio plotted as a function of the oxygen abundance of the BCDs. The mean q_{24} value for all the sources is indicated by the solid line. A fit to the low metallicity sources (12+log(O/H)≤8.0) is indicated by the dashed line; while the dotted line is the same fit excluding SBS0335-052E.

1.3±0.1 for the second one. If we calculate the q_{24} for the low metallicity group without including SBS0335-052E, we find a much lower q_{24} = 0.9±0.1. We also notice that it appears q_{24} generally decreases with reduced metallicity for sources with 12+log(O/H)<8.0, with SBS035-052E as a clear outlier, and the slope flattens out at 12+log(O/H)>8.0 (see Figure 4.3). This scatter in q_{24} at higher metallicities could be attributed to the more dispersion in the mid-IR emission in these sources and is consistent with a number of other studies that have found increased dispersion in the q ratios for very high luminosity galaxies (which usually have higher metallicities) (Condon et al. 1991; Yun et al. 2001; Bell 2003).

Hummel et al. (1988) have found evidence that, for a given galaxy, there is a small decrease in F(100 μm)/S(20 cm) when the dust temperature increases. The latter can be traced by the ratio of F(60 μm)/F(100 μm). Roussel et al. (2003) reached a similar result for the starburst galaxies they studied, in which they de-

tected an anti-correlation of q_{FIR} with F(60 μm)/F(100 μm). However, performing the same test for the q_{24} ratios on our dwarf galaxy sample which spans a range of flux ratios -0.4 <log(F(60 μm)/F(100 μm))<0.2 we find no such clear trend. It is conceivable that this is partly because our sample is too small to identify a trend due to the intrinsic scatter in q_{24}.

4.3.3 Star Formation Rate Estimates

Both the radio and infrared emission can be used to estimate the star formation rates (SFRs) in galaxies. However, these correlations depend on a number of parameters including dust content, optical depth and metallicity. This topic and potential caveats have been discussed extensively in the literature (see Condon 1992; Kennicutt 1998, and references therein). For dwarf galaxies, the topic has been addressed in detail by Hopkins et al. (2002). The recent wealth of data from *Spitzer* has also provided sufficient motivation to establish a calibration for the SFR using the infrared. Wu et al. (2005) and more recently Calzetti et al. (2007) have explored this topic using a large sample of star forming regions and nearby galaxies.

In Figure 4.4 we plot the IR estimated SFR for our sample using the calibrations proposed by Wu et al. (2005) and Calzetti et al. (2007) respectively:

$$\mathrm{SFR}_{24}(M_{\odot}yr^{-1}) = \frac{\nu L_{\nu}(24\mu m)}{6.66 \times 10^{8} L_{\odot}} \tag{4.1}$$

$$\mathrm{SFR}_{24}(M_{\odot}yr^{-1}) = 1.27 \times 10^{-38}[L_{24}(ergs^{-1})]^{0.885} \tag{4.2}$$

as a function of the well-known radio to SFR formula of Condon (1992):

$$\mathrm{SFR}_{1.4\mathrm{GHz}} = 5.5 \times \frac{L_{1.4\mathrm{GHz}}}{4.6 \times 10^{21}(\mathrm{WHz}^{-1})} \tag{4.3}$$

The Wu et al. (2005) work is based on a global correlation without separating the low metallicity sources from metal rich galaxies. As can be seen in Figure 4.4, a good agreement exists between the radio and IR estimated SFRs (indicated by diamonds). If we use the more recent calibration by Calzetti et al. (2007) on SFRs from 24 μm luminosities, we find that most of the mid-IR estimated SFRs (marked as filled circles) are located below the 1:1 proportionality line, and thus they are consistently lower than both the SFRs estimated from the radio or from Wu et al. (2005). This is not unexpected since eq. 2 is calibrated based on the high metallicity sources that have significant 24 μm emission, while most of our sources are metal-poor galaxies. We should also note that Calzetti et al. (2007) measure the SFR in individual HII regions in apertures within disks and subtract a "disk background", which could partly explain the deviations we see from our analysis. These authors have also mentioned that the SFRs of low metallicity galaxies would be underestimated by a factor of 2–4 depending on how metal-poor the galaxies are. This deviation from a linear correlation is likely due to the lower opacities for decreasing metal content (Walter et al. 2007). When we fit the filled circles on Figure 4.4, we find that log(SFR[IR])=0.94×log(SFR[1.4GHz]/3.98), which is consistent with the metallicity correction factor suggested by Calzetti et al. (2007). We should stress once more though that as Bell (2003) has noted, the good agreement between the IR and radio estimates of SFRs does not necessarily mean that these are the "true" SFRs for the dwarf galaxies we study, but rather the competition of the lower dust content and suppressed synchrotron emission balances each other.

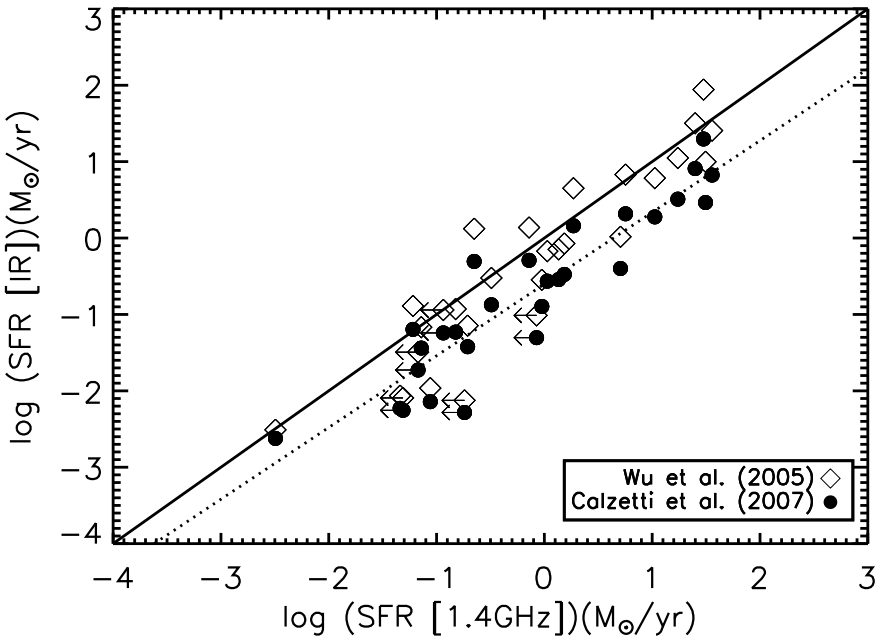

Figure 4.4 A plot of the SFR based on the 24 μm luminosity as a function of the corresponding SFR estimated from the 1.4 GHz radio continuum emission for each galaxy in our sample. The open diamonds indicate the SFRs calculated using the 24 μm fluxes following Wu et al. (2005) (eq.1), the filled circles are those using eq.2 from Calzetti et al. (2007). The solid line is the 1:1 proportionality line. The dotted line is a fit to the filled circles.

4.3.4 The Two Extremes: IZw18 and SBS0335-052E

Despite this overall agreement between the IR/radio correlation in our dwarf sample and the corresponding values of normal galaxies, the two lowest metallicity galaxies in our sample, IZw18 and SBS0335-052E, deviate markedly from the correlations and in opposite directions (see Figure 4.3[8]). As the two most well-studied BCDs, it is interesting to inspect the IR/radio properties of these two galaxies and a comparison of their physical parameters can be found in Table 4.3.

As indicated by the *Spitzer* IRS spectrum of SBS0335-052E (Houck et al. 2004b), the SED of the galaxy has an unusually flat mid-IR slope that peaks at $\sim$28μm. Hunt et al. (2005a) used *DUSTY* models (Ivezić et al. 1999) to fit its SED and found a q_{FIR} value of 2.0 for this galaxy, lower than the typical q_{FIR} of $\sim$2.3 expected for late type systems. These calculations are based on a 1.4GHz continuum flux of $\sim$0.46 mJy, which corresponds to the compact part (6″) of SBS0335-052E (Dale et al. 2001; Hunt et al. 2004). Similarly, if we simply calculate the q ratio independent of any modelling work and only use the observable parameters, we find a $q_{70} = 2.1\pm0.1$ (assuming that the MIPS 70 μm flux density is 51.1$\pm$4.8 mJy, Engelbracht et al. 2008). This is in good agreement with the $q_{70} = 2.16\pm0.17$ for the sources in the First Look Survey studied by Appleton et al. (2004).

However, when we examine the q_{24} for SBS0335-052E, adopting a MIPS 24 μm flux of 66 mJy, we find a q_{24} ratio of 2.2$\pm$0.1. We see a 2σ excess in the q parameter compared with the mean q_{24} of 1.3$\pm$0.4 in the dwarf sample. If this excess is real, it would be consistent with the unique shape of the SED of the galaxy, which suggests that the dust grain distribution is dominated by small grains with temperatures of $\sim$150K and a total dust mass of $\sim 10^3$ $M_\odot$(Houck et al. 2004b). Whether the

[8]In Figure 4.2 the "outlier" status of SBS0335-052E does not appear as prominent as in Figure 4.3, because its high 24 μm luminosity places it in a region of the plot where other sources with higher metallicity and higher luminosity are located.

Table 4.3. Comparison of SBS 0335-052E and I Zw 18

	SBS 0335-052E	I Zw 18	Ratio[a]
12+log(O/H)	7.32	7.17	1.4
D (Mpc)	58	18	3
R (pc)	560[b]	870[c]	∼0.6
SFR($M_\odot\,yr^{-1}$)	7×10^{-1}	5×10^{-2}	14
SNR(yr^{-1})	6×10^{-3}	$2\times10-4$	30
$L_{H\alpha}(L_\odot)$	5.6×10^{7}[d]	1.6×10^{6}	35
$L_{24\mu m}(L_\odot)$	9×10^{8}	7×10^{6}	120
$L_{IR}(L_\odot)$	$\sim4\times10^{9}$	$\sim4\times10^{7}$	100
$L_{1.4GHz}(W\,Hz^{-1})$	2×10^{20}	8×10^{19}	2.5
M(Ks)(mag)	-18.3	-16.1	∼80[e]

[a]Ratio of the relative quantities in SBS0335-052E to IZw18.

[b]This is the size of the six super star clusters in SBS0335-052E, which has a size of 2″ (Thuan et al. 1997). At a distance of 58 Mpc, 1″ ∼280 pc.

[c]This indicate the largest projected linear extend of the total star-forming regions in this galaxy (∼10″, Hunt et al. 2005b). At a distance of 18 Mpc, 1″ ∼ 87 pc.

[d]Flux in 1″ slit multiplied by a factor of 2 to correct for aperture effects.

[e]This is the approximate mass ratio of the two sources assuming that their mass scales with K-band luminosity and that both sources have the same M/L_{Ks} (see Bell & de Jong 2001).

large grains were never created or they were destroyed by shocks is unknown. The elevated q_{24} ratio could also be due to the lack of synchrotron emission. Roussel et al. (2003, 2006) have shown their study of three starburst galaxies, all of which have q_{FIR} more than 3σ higher the mean q_{FIR} and categorized them to be nascent starbursts. SBS0335-052E though, could also be a candidate of this group. It is based partly on the high q_{24} value, as well as its low Hα luminosity as compared to the infrared or radio luminosities (see Table 4.3). Finally, Hunt et al. (2004) have shown the existence of free-free absorption in the radio spectrum of SBS0335-052E, which is usually caused by young, dense and heavily embedded clusters[9].

IZw18, despite its similar metallicity to SBS0335-052E (12+log(O/H)=7.17 and 7.32 respectively), shows a rather different q ratio. It also has an IR luminosity of $L_{IR}\sim10^7 L_\odot$, just 1% of the L_{IR} in SBS0335-052E. In low luminosity galaxies, radio emission is known to decrease faster than dust emission (Devereux & Eales 1989), and high IR/radio ratios have been observed in low luminosity dwarf galaxies (Klein et al. 1984). In IZw18 though, we find a rather low infrared to radio ratio. The q_{24} is found to be 0.5 ± 0.1, nearly 2σ lower than the average value of our sample. At longer wavelengths, IZw18 is faint and no *IRAS* FIR data are available. However, as noted by Wu et al. (2007) (see their Figure 4.5), it has a very similar 5–38μm continuum slope to the typical starburst galaxy NGC7714 (Brandl et al. 2004). If we were to assume that this similarity extends to the FIR and scale down the *IRAS* 60 and 100 μm flux densities of NGC7714 by a factor of 375 so that its corresponding 22 μm flux density matches the one of IZw18, we find its "equivalent" *IRAS* 60 and 100 μm flux density to be 29.8 and 32.8 mJy respectively. This would result in q_{FIR} of 1.3 for the galaxy, which deviates from the average q_{FIR} ratio of 2.3 ± 0.2 calibrated by Condon (1992) by nearly 5σ. If we were to

[9]Note, that if we could properly account for the self-absorption of the radio continuum, the intrinsic q ratio would decrease. However, the exact fraction for absorption is not known and more data at ν <1.5GHz would be needed to determine that number.

use the MIPS 70 μm detection of 34 mJy for IZw18 (Engelbracht et al. 2008) and calculate its q ratio, we would find q_{70}=1.4, again 5σ away from the average q_{70} suggested by Appleton et al. (2004).

A number of plausible scenarios were considered to explain this result, though none appears convincing. As discussed in Wu et al. (2007), because the optical depth of IZw18 is small, it could be that a significant fraction of the UV light has leaked out without being absorbed by the dust, thus resulting in a damped 24 μm emission. Alternatively, IZw18 may simply have an unusually high radio luminosity at 1.4 GHz. Could it be that IZw18 is observed at a special moment right after the explosion of a supernovae event? Radio supernovae fade by more than a factor of 10 within $\sim$3 yr (Chevalier 1982). The radio continuum observations of IZw18 span over a period of more than 5 yrs (Hunt et al. 2005b; Cannon et al. 2005) but show no variation, thus this is not likely.

The recent results by Murphy et al. (2006b) provide another possible scenario. These authors analyzed a sample of nearby spiral galaxies and found that systems with higher disk-averaged SFRs ($\Sigma_{\rm SFR}$) have usually experienced a recent episode of enhanced star formation. As a result they contain a higher fraction of young cosmic ray electrons that have traveled only a few hundred parsecs from their acceleration sites in supernova remnants. This is perhaps the case for IZw18. However, other sources in our sample also have elevated $\Sigma_{\rm SFR}$ and show no radio excess. It could also be that the extremely low metal abundance of IZw18, 0.15 dex lower than that of SBS0335-052E, is below a critical threshold. The newly formed stars in the unpolluted interstellar medium may produce, and subsequently heat, less dust than electrons which are accelerated and contribute in the radio emission. We also note that the rate of SNR in IZw18 is a factor of $\sim$30 lower than that in SBS0335-052E (see Table 4.3) but its morphology is much more disturbed with

filamentary structure and outflows (see Izotov & Thuan 2004). If we were to assume that both sources have similar mass-to-light ratios and estimate their mass from their K-band luminosities, we find that the mass of IZw18 is almost a factor of 80 less than that of SBS0335-052E. Thus the rate of SNR normalized with mass in IZw18 would be $\sim$2.5 times that of SBS0335-052E. Could it be that the disturbed morphology of IZw18 in addition to its low metal content that it created the conditions in the interstellar medium for this abnormally high radio flux? The question remains open.

4.4 Conclusions

We have studied the mid-IR and FIR to radio correlation in a sample of dwarf star-forming galaxies spanning a metallicity range from 7.2<12+log(O/H)<8.9, using *Spitzer* IRS/MIPS, as well as radio 1.4 GHz data obtained from the literature. The BCD sample appears to follow the same FIR/radio correlation as normal star forming galaxies. The analysis based on mid-IR and radio data reveals a similar correlation, though the scatter is larger, probably due to an intrinsically higher variation in the 15-30μm SEDs of dwarf galaxies. When comparing the q_{24} ratios with metallicity or effective dust temperature, we find no strong correlation, though there is a general trend of lower q ratios at lower metallicity for galaxies with 12+log(O/H)<8.0 and the correlation flattens out toward higher metallicity. In general the SFRs estimated from the radio 1.4 GHz continuum and the mid-IR data are in good agreement. Two extremely metal poor BCDs, IZw18 and SBS0335-052E appear to deviate from the average q_{24} by $\sim 2\sigma$, with one displaying a radio excess and the other an infrared excess.

Acknowledgments The authors would like to thank P. Appleton and D. Calzetti for stimulating discussions. We would also like to thank G. Helou, L.K.

Hunt as well as an anonymous referee whose detailed comments and insightful suggestions have helped to improve this manuscript. This work is based in part on observations made with the *Spitzer* Space Telescope, which is operated by the Jet Propulsion Laboratory, California Institute of Technology, under NASA contract 1407. Support for this work was provided by NASA through Contract Number 1257184 issued by JPL/Caltech. VC would like to acknowledge the partial support from the EU ToK grant 39965.

BIBLIOGRAPHY

Allende Prieto, C., Lambert, D. L., & Asplund, M. 2001, ApJ, 556, L63

Aloisi, A. et al. 2007, ApJ, 667, L151

Appleton, P. N., et al. 2004, ApJS, 154, 147

Becker, R. H., White, R. L., & Helfand, D. J. 1995, ApJ, 450, 559

Bell, E. F., & de Jong, R. S. 2001, ApJ, 550, 212

Bell, E. F. 2003, ApJ, 586, 794

Bergvall, N., & Östlin, G. 2002, A&A, 390, 891

Brandl, B. R., et al. 2004, ApJS, 154, 188

Brandl, B. R., et al. 2006, ApJ, 653, 1129

Boyle, B. J., Cornwell, T. J., Middelberg, E., Norris, R. P., Appleton, P. N., & Smail, I. 2007, MNRAS, 376, 1182

Calzetti, D., et al. ApJ, 666,870

Cannon, J. M., Walter, F., Skillman, E. D., & van Zee, L. 2005, ApJ, 621, L21

Chevalier, R. A. 1982, ApJ, 258, 790

Condon, J. J., Anderson, M. L., & Helou, G. 1991, ApJ, 376, 95

Condon, J. J. 1992, ARA&A, 30, 575

Condon, J. J., Cotton, W. D., Greisen, E. W., Yin, Q. F., Perley, R. A., Taylor, G. B., & Broderick, J. J. 1998, AJ, 115, 1693

Dale, D. A., Helou, G., Neugebauer, G., Soifer, B. T., Frayer, D. T., & Condon, J. J. 2001, AJ, 122, 1736

Dale, D. A., et al. 2006, ApJ, 646, 161

de Jong, T., Klein, U., Wielebinski, R., & Wunderlich, E. 1985, A&A, 147, L6

Devereux, N. A., & Eales, S. A. 1989, ApJ, 340, 708

Elbaz, D., Cesarsky, C. J., Chanial, P., Aussel, H., Franceschini, A., Fadda, D., & Chary, R. R. 2002, A&A, 384, 848

Engelbracht, C. W., Gordon, K. D., Rieke, G. H., Werner, M. W., Dale, D. A., & Latter, W. B. 2005, ApJ, 628, L29

Engelbracht, C. W., Rieke, G. H., Gordon, K. D., Smith, J.-D. T., Werner, M. W., Moustakas, J., Willmer, C. N. A., & Vanzi, L. 2008, ApJ, 678, 804

Garrett, M. A. 2002, A&A, 384, L19

Gruppioni, C., Pozzi, F., Zamorani, G., Ciliegi, P., Lari, C., Calabrese, E., La Franca, F., & Matute, I. 2003, MNRAS, 341, L1

Guseva, N. G., Izotov, Y. I., & Thuan, T. X. 2000, ApJ, 531, 776

Hao, Lei, et al., 2007, in preparation

Harwit, M., & Pacini, F. 1975, ApJ, 200, L127

Heckman, T. M., Robert, C., Leitherer, C., Garnett, D. R., & van der Rydt, F. 1998, ApJ, 503, 646

Helou, G., Soifer, B. T., & Rowan-Robinson, M. 1985, ApJ, 298, L7

Helou, G., & Bicay, M. D. 1993, ApJ, 415, 93

Hopkins, A. M., Schulte-Ladbeck, R. E., & Drozdovsky, I. O. 2002, AJ, 124, 862

Houck, J. R., et al. 2004a, ApJS, 154, 18

Houck, J. R., et al. 2004b, ApJS, 154, 211

Hummel, E., Davies, R. D., Pedlar, A., Wolstencroft, R. D., & van der Hulst, J. M. 1988, A&A, 199, 91

Hunt, L. K., Dyer, K. K., Thuan, T. X., & Ulvestad, J. S. 2004, ApJ, 606, 853

Hunt, L., Bianchi, S., & Maiolino, R. 2005b, A&A, 434, 849

Hunt, L. K., Dyer, K. K., & Thuan, T. X. 2005a, A&A, 436, 837

Izotov, Y. I., & Thuan, T. X. 2004, ApJ, 616, 768

Izotov, Y. I., & Thuan, T. X. 1998, ApJ, 500, 188

Izotov, Y. I., & Thuan, T. X. 1999, ApJ, 511, 639

Ivezić, Z., Nenkova, M., & Elitzur,M. 1999, User Manual for *DUSTY*, University of Kentucky Internal Report,accessible at `http://www.pa.uky.edu/ moshe/dusty`

Jannuzi, B. T., & Dey, A. 1999, ASP Conf. Ser. 191: Photometric Redshifts and the Detection of High Redshift Galaxies, 111

Kennicutt, R. C., Jr. 1998, ARA&A, 36, 189

Kirshner, R. P., Oemler, A., Jr., Schechter, P. L., & Shectman, S. A. 1981, ApJ, 248, L57

Klein, U., Weiland, H., & Brinks, E. 1991, A&A, 246, 323

Klein, U., Wielebinski, R., & Thuan, T. X. 1984, A&A, 141, 241

Kobulnicky, H. A., & Skillman, E. D. 1997, ApJ, 489, 636

Kobulnicky, H. A., & Johnson, K. E. 1999, ApJ, 527, 154

Kunth, D., & Joubert, M. 1985, A&A, 142, 411

Leroy, A., Bolatto, A. D., Simon, J. D., & Blitz, L. 2005, ApJ, 625, 763

Miller, N. A., & Owen, F. N. 2001, AJ, 121, 1903

Moshir, M., & et al. 1990, IRAS Faint Source Catalogue, version 2.0 (1990)

Moustakas, J., & Kennicutt, R. C., Jr. 2006, ApJS, 164, 81

Murphy, E. J., et al. 2006a, ApJ, 638, 157

Murphy, E. J., et al. 2006b, ApJ, 651, L111

Popescu, C. C., & Hopp, U. 2000, A&AS, 142, 247

Rieke, G. H., et al. 2004, ApJS, 154, 25

Rosenberg, J. L., Ashby, M. L. N., Salzer, J. J., & Huang, J.-S. 2006, ApJ, 636, 742

Rosenberg, J. L., Wu, Yanling, Le Floc'h, E., Charmandaris, V., Ashby, M. L. N., Houck, J. R., Salzer, J. J. Willner, S.P. 2008, ApJ, 674, 814

Roussel, H., Helou, G., Beck, R., Condon, J. J., Bosma, A., Matthews, K., & Jarrett, T. H. 2003, ApJ, 593, 733

Roussel, H., et al. 2006, ApJ, 646, 841

Sanders, D. B., Mazzarella, J. M., Kim, D.-C., Surace, J. A., & Soifer, B. T. 2003, AJ, 126, 1607

Sanders, D. B., et al. 2007, ApJS, 172, 86

Shi, F., Kong, X., Li, C., & Cheng, F. Z. 2005, A&A, 437, 849

Storchi-Bergmann, T., Calzetti, D., & Kinney, A. L. 1994, ApJ, 429, 572

Thuan, T. X., & Izotov, Y. I. 2005, ApJS, 161, 240

Thuan, T. X., Izotov, Y. I., & Lipovetsky, V. A. 1997, ApJ, 477, 661

van der Kruit, P. C. 1971, A&A, 15, 110

Walter, F., et al. 2007, ApJ, 661, 102

Werner, M. W., et al. 2004, ApJS, 154, 1

Wu, H., Cao, C., Hao, C.-N., Liu, F.-S., Wang, J.-L., Xia, X.-Y., Deng, Z.-G., & Young, C. K.-S. 2005, ApJ, 632, L79

Wu, Y., Charmandaris, V., Hao, L., Brandl, B. R., Bernard-Salas, J., Spoon, H. W. W., & Houck, J. R. 2006, ApJ, 639, 157

Wu, Y., et al., 2007a, ApJ, 662, 952

Wu, Y., Bernard-Salas, J., Charmandaris,V. Lebouteiller, V., Hao, L., Brandl, B.R., Houck, J.R. 2008, ApJ, 673, 193

Yun, M. S., Reddy, N. A., & Condon, J. J. 2001, ApJ, 554, 803

CHAPTER 5

DUST PROPERTIES AND STAR FORMATION RATES IN STAR-FORMING DWARF GALAXIES*

Abstract We have used the *Spitzer Space Telescope* to study the dust properties of a sample of star-forming dwarf galaxies. The mid-infrared spectral energy distributions for these galaxies which, in general, are low metallicity systems, indicate a wide range of dust properties. These galaxies have more hot dust and/or very small grains and less PAH emission than either spiral or higher luminosity starburst galaxies. As has been shown in previous studies, there is a gradual decrease in PAH emission as a function of metallicity. Because much of the energy from star formation in galaxies is re-radiated in the mid-infrared, star-formation rate indicators based on both line and continuum measurements in this wavelength range are coming into more common usage. We show that the variations in the interstellar medium properties of galaxies in our sample, as measured in the mid-infrared, result in over an order of magnitude spread in the computed star-formation rates.

5.1 Introduction

Mid-infrared (MIR) observations probe the dusty interstellar medium and the dust-enshrouded star formation in galaxies. The spectral energy distribution in this region is shaped by this star formation, but can also be affected by the presence (or lack) of dust grains of varying size, by differences in metallicity, and by radiation from an older population of stars (Li and Draine 2002). One of the first studies of the MIR spectra of a large sample of galaxies including the low metallicity system II Zw 40 was performed by Roche et al. (1991). More recent observations have been

*Originally published as: J. L.Rosenberg, Yanling Wu, E.Le Ffloc'h, V. Charmandaris, M. L.N.Ashby, J. R.Houck, J. J.Salzer, S. P.Willner (2008), *The Astrophysical Journal*, 674, 814

used to understand how these different properties affect a galaxy's spectral energy distribution. With the advent of the *Spitzer Space Telescope* and the *Infrared Space Observatory*, the facilities are now available to make deep observations in the MIR. These data are being used to study the interstellar medium and to measure the star-formation rate (SFR) in galaxies both in the nearby and distant universe.

Some detailed, broadband, MIR observations of low metallicity galaxies have shown that these systems display a wide range of colors which implies a wide range of interstellar medium properties (Rosenberg et al. 2006; Engelbracht et al. 2005; Hogg et al. 2005). A more detailed examination of the dust properties of low metallicity galaxies has been performed for some of the best known low metallicity galaxies using infrared spectroscopy (Wu et al. 2007, 2006; Houck et al. 2004a; Hunt et al. 2005, 2006; Madden et al. 2006). These observations have provided evidence that there is a relationship between how much polycyclic aromatic hydrocarbon (PAH) emission is detectable in these systems and their metallicity. In the two lowest metallicity galaxies known, I Zw 18 and SBS 0335-052, no PAH emission is detected even in deep observations (Wu et al. 2007; Houck et al. 2004a; Thuan et al. 1999). Several models for the decrease in PAH emission with metallicity have been proposed including destruction by the hard radiation field in low metallicity systems because the dust opacity is low in these environments (Galliano et al. 2005; Madden et al. 2006), destruction in the shocks created by supernova blast waves (O'Halloran et al. 2006), and an intrinsic lack of PAH molecules in young systems because the PAHs are produced in low-mass stars that have not yet evolved (Dwek 2005; Galliano et al. 2008).

Using the measured MIR properties of galaxies to determine their star formation rates requires an understanding of the properties that affect the heating of the dust responsible for the MIR emission. At high redshift, in particular, the effect of

metallicity on the MIR emission may become more significant if a larger fraction of the galaxy population consists of low metallicity systems. The relationships between MIR flux density and SFR may not be the same as those for the more luminous and metal-rich systems for which the relationships were determined (e.g., Rosenberg et al. 2006; Wu et al. 2006; Engelbracht et al. 2005). Emission from very small grains and warmer dust is seen in low metallicity galaxies but much less emission from PAH molecules is detected relative to spiral and higher luminosity starburst galaxies (Madden and Galliano 2005; Hunt et al. 2005). For example, in the Small Magellanic Cloud where the metallicity is low, the dust properties, absorption, and emissivity are significantly different from what is seen in the Milky Way, indicating that metal-rich galaxies are not a proxy for their lower-metallicity counterparts (Li et al. 2006).

The star-forming dwarf galaxies that are discussed here have been studied previously in the *Spitzer*/IRAC bands and have been found to have a wide range in mid-infrared colors (Rosenberg et al. 2006). Here we look in greater detail at the spectral energy distributions for these systems as well as the relationship between dust properties and metallicity, and the measurements of star-formation in the mid-infrared and ultraviolet. The data are presented in §2. A detailed look at flux density ratios and the MIR SEDs of these galaxies are examined in §3 to answer the question, as best as the data will allow, do these galaxies exhibit PAH emission? The measured SFRs determined from the optical, MIR, and ultraviolet (UV) data are discussed and compared in §4, and the results are summarized in §5.

5.2 Data

5.2.1 Sample selection and optical data

The galaxies in this study are low luminosity star-forming galaxies selected from the KPNO International Spectroscopic Survey (KISS) in the Boötes field. These systems have been observed both as a part of the KISS survey and by several other surveys at optical, infrared, and ultraviolet wavelengths including the NOAO Deep Wide-Field Survey (NDWFS, Jannuzi and Dey 1999; Jannuzi 2007), the *Spitzer*/IRAC Shallow Survey (Eisenhardt et al. 2004), and a shallow *Spitzer*/MIPS survey. Rosenberg et al. (2006) provides a discussion of the *Spitzer*/IRAC Shallow Survey data for these objects.

KISS is a modern objective-prism survey. It combines the methodology of many of the classic wide-field color- and line-selected surveys (e.g., Markarian 1967; Smith et al. 1976; MacAlpine et al. 1977; Wasilewski 1983; Zamorano et al. 1994) with the higher sensitivity of a CCD detector. The survey method is described in detail by Salzer et al. (2000). KISS selects objects for inclusion in the survey lists if they possess a strong ($> 5\sigma$) emission line in their low-dispersion objective-prism spectra. The survey has been carried out in two distinct spectral regions: the blue portion (4800 – 5500 Å) where the primary line observed is [O III]λ5007, and the red region (6400 – 7200 Å) where galaxies are selected by their Hα emission. The current sample galaxies were chosen from the Jangren et al. (2005) list of of Hα emission-line galaxy (ELG) candidates (KR3). The objective prism passband imposes a redshift limit on the sample of $z \leq 0.095$. The selection criteria used to define the sample were that the galaxies exhibit spectra consistent with heating by star-formation processes (i.e., AGNs were excluded) and that they have a B-band absolute magnitude $M_B > -18.0$ (for $H_0 = 75$ km s^{-1} Mpc^{-1}, although four are

slightly brighter than this limit when they are corrected for extinction). Thus these galaxies are selected to be star-forming dwarf galaxies.

These criteria produced a list of 26 galaxies within the NDWFS Boötes area. However, of those 26 galaxies, only 19 overlap with the *Spitzer* Shallow Survey area because the *Spitzer* survey field is smaller than the NDWFS field. We discuss only these 19 galaxies in our analysis. Many of these galaxies also turn out to be low metallicity – the median metallicity of the sample is $\log[O/H] + 12 = 8.17$ ($0.32 Z_{\odot}$). With the exception of one super-solar and one slightly sub-solar galaxy, they are all significantly sub-solar ($< 0.6 Z_{\odot}$, see Rosenberg et al. 2006 for sample details).

All of the KISS ELG candidates in the Boötes field possess higher dispersion follow-up slit spectra (Salzer et al. 2005) that have been used to verify the reality of the putative emission lines seen in the objective-prism spectra, calculate accurate redshifts, and to distinguish between the various activity types that might be present in a line-selected sample (e.g., star-forming galaxies vs. AGNs). These follow-up spectra provide us with a great deal of useful information (e.g., accurate redshifts, emission-line fluxes and line ratios, reddening and metallicity estimates). The combination of the accurate B and V photometry from the original survey lists with these follow-up spectra allow for the construction of a fairly complete picture of the properties of the KISS ELGs.

Table 5.1 contains some of the optical parameters for the galaxies in this sample. More details about the KISS data and parameters can be obtained from KR3.

Table 5.1. Properties of KISS Galaxies

KISSR	RA J2000	Dec J2000	v_{hel}[a] km s^{-1}	M_{B0}[b]	$c_{H\beta}$[c]	$\log L_{H\alpha}$ ergs s^{-1}	$\log[O/H]+12$
2292	14:25:09.2	35:25:15.9	8659	-18.31	0.283	40.39	8.12
2300	14:26:08.9	33:54:19.8	10271	-16.09	0.154	40.52	7.89
2302	14:26:17.5	35:21:35.5	8342	-17.16	···	40.04	···
2309	14:26:53.6	34:04:14.5	7231	-17.12	0.284	40.09	7.98
2316	14:28:14.9	33:30:25.7	10685	-18.57	1.094	41.01	8.84
2318	14:28:24.6	35:10:21.5	22163	-17.88	···	41.15	···
2322	14:29:09.6	32:51:26.7	8574	-17.84	0.096	40.24	8.05
2326	14:29:32.7	33:30:40.3	7935	-17.14	0.151	40.65	8.21
2338	14:30:27.9	35:32:07.2	11689	-17.20	0.190	40.81	8.11
2344	14:31:03.6	35:31:14.8	4166	-17.75	0.248	40.12	8.17
2346	14:31:14.4	33:19:13.2	10819	-16.80	0.197	40.49	7.84
2349	14:31:20.0	34:38:03.8	4396	-16.63	-0.012	40.48	8.08
2357	14:31:39.2	33:26:32.3	10759	-17.67	0.504	40.40	8.37
2359	14:31:49.3	35:28:40.0	22512	-18.03	1.350	41.66	8.62
2368	14:32:18.9	33:02:53.7	10972	-17.05	0.193	40.84	8.03
2382	14:34:08.0	34:19:34.4	6813	-17.81	0.100	40.03	8.21
2398	14:36:33.1	34:58:04.4	9006	-18.01	0.187	40.33	8.42
2403	14:37:42.6	33:36:26.7	12047	-16.24	0.362	40.38	8.36
2406	14:38:27.8	35:08:59.0	8641	-17.89	0.185	40.38	8.35

[a]Heliocentric velocity

[b]B-band absolute magnitude corrected for Galactic extinction

[c]Optical reddening at Hβ

Table 5.2. Infrared and Ultraviolet Fluxes of KISS Galaxies

KISSR	f_{16} mJy	σ_{16} mJy	f_{24} mJy	σ_{24} mJy	f_{70} mJy	σ_{70} mJy	f_{160} mJy	σ_{160} mJy	f_{NUV} μJy	σ_{NUV} μJy	f_{FUV} μJy	σ_{FUV} μJy
2292	1.27	0.08	2.35	0.07	···	···	<120	···	74.98	0.69	···	···
2300	0.77	0.05	1.72	0.05	<15	···	<120	···	31.26	0.50	···	···
2302	<0.1	···	<0.24	···	<15	···	<120	···	92.42	0.84	···	···
2309	0.32	0.02	0.92	0.06	<15	···	<120	···	111.00	0.88	···	···
2316	3.39	0.20	4.09	0.10	52	4	150	33	19.40	0.33	···	···
2318	1.17	0.07	2.06	0.05	15	4	<120	···	7.96	0.29	···	···
2322	0.49	0.03	0.82	0.08	<15	···	<100	···	154.30	1.31	···	···
2326	1.43	0.08	3.77	0.05	29	3	<100	···	117.80	0.80	···	···
2338	2.85	0.17	6.56	0.09	25	5	<100	···	49.46	0.55	39.20	0.81
2344	1.41	0.08	3.73	0.03	71	6	210	33	581.44	2.04	439.02	2.47
2346	0.98	0.06	2.20	0.04	<15	···	<120	···	27.23	0.54	···	···
2349	10.72	0.64	26.20	0.09	154	7	190	33	276.85	1.53	···	···
2357	<0.3	···	0.48	0.06	<15	···	<120	···	75.33	0.95	···	···
2359	0.94	0.05	2.30	0.07	20	4	<100	···	11.87	0.31	7.88	0.34
2368	4.34	0.26	7.51	0.08	30	10	<120	···	113.90	1.24	···	···
2382	0.81	0.05	1.00	0.07	34	7	<120	···	242.74	1.40	140.28	5.80
2398	0.74	0.04	1.05	0.05	20	3	<120	···	128.21	0.36	92.40	0.44
2403	<0.2	···	0.47	0.04	<15	···	···	···	21.20	0.47	···	···
2406	1.00	0.06	2.09	0.08	27	6	<120	···	164.71	0.44	126.32	0.50

5.2.2 Spitzer multiband imaging photometer data

The far-IR observations of the Boötes field were performed using the "medium scan" mode of the MIPS instrument (Rieke et al. 2004) on-board the *Spitzer Space Telescope*. This mode allows for efficient coverage of large areas of sky with simultaneous observations at 24, 70, and 160μm. The MIPS detector at 24μm is characterized by a resolution of 2.″45 per pixel on an array of 128×128 elements; the 70μm detector has a resolution of 9.″98 per pixel on an array of 32×16 elements; and at 160μm, the effective array operates with two rows of 20 16″×18″ pixels separated by one row of non-functional pixels. The point spread function (PSF) in the MIPS images is characterized by a full width at half maximum of 6″, 18″ and 40″ at 24μm, 70μm and 160μm respectively. Data were reduced using the MIPS Data Analysis Tool (Gordon et al. 2005). The astrometry of the final mosaic was calibrated against the 2MASS survey (Jarrett et al. 2000) and is accurate to 0.3″ rms. The effective integration time per sky pixel was ∼90 s, ∼40 s, and ∼8 s at 24, 70, and 160μm respectively.

At 24 μm 18 of the 19 galaxies were detected while 11 galaxies were detected at 70 μm and only 3 were detected at 160 μm. Photometry was performed with PSF fitting using the IRAF/DAOPHOT software (Stetson 1987). At each wavelength an empirical PSF was constructed from the brightest objects found in the mosaic. The flux density of each source was derived from the scaled, fitted PSF plus a slight correction to account for the finite size of the modeled point spread function. For the cases where residual emission was found in the 24μm image after the PSF subtraction, aperture photometry was performed within a region large enough to account for the extended emission of the object. Only 5 sources show extended emission at 24μm and all of the targets appear unresolved at 70 and 160μm. For the non-detections at 70 and 160 μm, we adopted an upper limit based on the

noise. This noise was derived as the dispersion of the flux measured within fixed-diameter apertures randomly placed over blank sky regions of the image. The flux densities for all of the sources are presented in Table 5.2.

5.2.3 Spitzer 16 μm imaging

The galaxies in this sample were all imaged at 16μm with the blue peak-up camera on the *Spitzer* Infrared Spectrograph (IRS[1], Houck et al. 2004a; Werner et al. 2004). The targets were observed as part of the IRS guaranteed time observing program on 2006 January 18 and 19. The 19 galaxies were observed with a 5 position random dither pattern in order to oversample the point spread function (PSF) on the $1.8'' \times 1.8''$ pixels of the IRS Short-Low Si:As detector. The observing time was 30 seconds per position for a total on-source integration time per target of 157 seconds.

The data were processed by the *Spitzer* Science Center pipeline (version 13.2). The 2D images were converted from slopes after linearization correction, subtraction of darks, and cosmic ray removal. The resulting images were divided by the photometric flat and a world coordinate system was determined using the reconstructed pointing of the telescope. Final rectified, shifted, co-added image mosaics were produced by the pipeline. The astrometric accuracy of our images is better than $2''$ and the FWHM of the PSF is $3.5''$.

Photometry was performed using fixed apertures of 3 pixels in radius. The flux conversion factor was 0.01375 MJy sr^{-1} (e^{-}sec^{-1})$^{-1}$, and the aperture loss correction factor used was 1.38, as described in version 2.0 of the IRS Data Handbook[2]. Our photometric uncertainties are less than $\sim$6% based on the uncertainty in the

[1]The IRS was a collaborative venture between Cornell University and Ball Aerospace Corporation funded by NASA through the Jet Propulsion Laboratory and the Ames Research Center.

[2]http://ssc.spitzer.caltech.edu/irs/dh/

photometric calibrators that were used. Ultimately 16 of the 19 sources were detected in these images. The flux densities for all of the galaxies are presented in Table 5.2.

5.2.4 *Spitzer* Infrared Array Camera Data

The majority of the NOAO Deep Wide Field in Boötes was mapped in the 3.6, 4.5, 5.7, and 8.0 μm bands in January 2004 (Eisenhardt et al. 2004) using the Infrared Array Camera (IRAC) aboard the *Spitzer* Space Telescope. The IRAC coverage of 8.5 square degrees was reached by tiling the $5' \times 5'$ field-of-view over the region. Each position in the survey field was observed with three 30 second IRAC frames, resulting in a depth of 19.1, 18.3, 15.9, and 15.2 Vega magnitudes (5σ) at 3.6, 4.5, 5.8, and 8.0μm, respectively. A full discussion of the data and the reduction procedures is presented by Rosenberg et al. (2006). All 19 galaxies were detected in all four bands.

5.2.5 Galaxy evolution explorer data

Archival ultraviolet (UV) imaging for all of the galaxies in this sample was available from the Galaxy Evolution Explorer (GALEX) (Martin and The GALEX Team 2005). These images were taken as a part of the Deep Imaging Survey and span a wide range in exposure time. For all of the systems, near-UV (NUV) images in the 1750–2800 Å band are available, and for a small subset (6) of the objects, far-UV (FUV) imaging in the 1350–1750 Å band is available. The data have been processed though the standard GALEX reduction pipeline producing photometric images with an angular resolution of $5''.6$ (FWHM) in the NUV and 4" (FWHM) in the FUV.

Photometry was performed on the archival images using the ELLIPSE task in

the STSDAS module to IRAF. The regions around the galaxies were first masked to exclude the flux from neighboring sources. Most of the galaxies were then fit with circular apertures (for the 3 distinctly elliptical galaxies, KISSR 2302, 2357, and 2359, elliptical apertures were used to minimize the noise). In order to calculate the total UV counts for the galaxy, the size of the apertures was allowed to grow until the background was reached as determined by the curve of growth of the flux. The counts in each aperture were converted to fluxes using the GALEX calibration values[3] (Morrissey et al. 2005). The results are presented in Table 5.2.

5.3 Dust diagnostics

5.3.1 Do star-forming dwarf galaxies have PAHs?

The existence of polycyclic aromatic hydrocarbon (PAH) emission from dwarf and low metallicity galaxies has been discussed by several different groups (e.g., Wu et al. 2006; Rosenberg et al. 2006; Engelbracht et al. 2005; Madden et al. 2006; Hunt et al. 2005; Madden 2000). This subject is of increasing interest because these molecules provide a probe of the star-formation environment and, therefore, can be used as a measure of the star-formation rate in galaxies. Rosenberg et al. (2006) showed that the [3.6]-[8.0] colors of these galaxies span the full range of late-type galaxy colors. The presence of some star-forming dwarfs with very red infrared colors indicates that even some metal poor dwarf galaxies which have low line-of-sight reddening, as measured by the $c_{H\beta}$ parameter, have a significant amount of dust. Nevertheless, the only way to definitively determine whether a galaxy exhibits PAH emission is through infrared spectroscopy, but only a small number of sources are bright enough to be measured in this way.

[3]http://galexgi.gsfc.nasa.gov/FAQ/counts_background.html

To assess the degree to which PAH emission is present in the galaxies in this sample, information from broadband flux ratios was combined with an examination of the galaxies' spectral energy distributions (SEDs; description of the SED fitting procedures is presented in Appendix A). The relevant pieces of information are given in Table 5.3. The general trends in the data are presented here while a detailed description of the results for each galaxy in the sample are included in Appendix B. The template fitting approach used here is not ideal because it does not provide a physical measurement of the stars, dust, and PAHs and because the templates are not derived from low metallicity. As has been shown by Marshall et al. (2007) and Galliano et al. (2008), a proper analysis of the dust, PAH emission and stellar starburst component is not possible using only the IRAC and MIPS photometric points even in "simple" star forming galaxies because of the degeneracy in these component's contributions to the near-/mid-IR spectrum of the galaxy. As a result, these templates provide only a general guide to the properties of the galaxies and are used to answer two basic questions: (1) are the SEDs of dwarf starbursts similar to those of "normal" and starburst galaxies? and (2) do dwarf starbursts have PAH emission?

Figures 5.1 to 5.5 provide diagnostics of the PAH and dust emission properties of galaxies. The model template fits to the galaxy spectral energy distributions (which were not fit at 5.8 and 8.0 μm points where PAH emission has the largest impact) are shown in Figures 5.1, 5.2, and 5.3. The galaxies that have significant PAH emission (Figure 5.1) either exceed the models at 8 μm or have 8μm fluxes that are within 3σ of the models. Alternatively, all of the galaxies without PAH emission either have large reduced χ^2 for the template fits (the lowest $\chi^2_{red} = 9.8$) or the templates exceed the data by at least 30σ at 8μm. All of the other galaxies fall between these two criteria and are listed as having questionable PAH emission

which probably means that they have a low level of PAH emission. However, a definitive and/or quantitative assessment of the PAH emission from this intermediate category can not be made without spectroscopy. Note that there are also three galaxies for which SEDs are not plotted because the long wavelength data necessary to constrain the fits do not exist.

Figure 5.4 shows the relationship between ratios of the 8 μm emission and the dust continuum at shorter and longer wavelengths. The division of galaxies into systems exhibiting PAH emission and those that do not based on the relationship between the 8μm fluxes and the models as discussed above agree well with the divisions established by Engelbracht et al. (2005) based on the relationship between the 8 μm emission and the dust continuum. The 8 μm excess above the dust continuum for galaxies with PAH emission is reflected in the flux density ratio: $f_\nu(8.0)/f_\nu(24) > 0.3$. The galaxies for which the SEDs do not definitively determine the nature of the PAH emission populate both the "PAH" and "no-PAH" region of the plot. KISSR 2292, 2318, and 2322 look like galaxies with PAH emission using this measure while KISSR 2309 looks like galaxies without PAH emission and KISSR 2359 is on the boundary between the two regions.

Figure 5.5 shows how the ratio between the 8 μm emission and the hot dust continuum is related to the slope of the hot dust continuum. The 8 μm flux has been stellar subtracted assuming $f_\nu(8.0)_{stellar} = 0.232 f_\nu(3.6)$ (Helou et al. 2004, the correction at 8μm is very small and the stellar contribution at 16 and 24 μm is ignored because it is negligible.) The blackbody that was fit to the galaxy SEDs in §3.1 are not used for this subtraction because the templates also include some stellar light so this extrapolation from the 3.6 μm flux is more appropriate. In general the galaxies that do not exhibit PAH emission have small values for both of these ratios: $f_\nu(8.0)/f_\nu(24) < 0.2$ and $f_\nu(8.0)/f_\nu(16) < 0.3$ while all of the

galaxies that exhibit PAH emission have $f_\nu(8.0)/f_\nu(16) > 0.9$. The galaxies for which the SED fitting was not able to distinguish between PAH and no-PAH emission fall between these two groups in their $f_\nu(8.0)/f_\nu(16)$ ratio and all fall below the starburst galaxy model curves. The PAH and no-PAH galaxies are better separated in this plot than they are with the other MIR flux ratios. In particular the galaxies are well separated using the $f_\nu(8.0)/f_\nu(16)$ ratio.

For a small number of these galaxies, longer wavelength data exist and can be used to study the properties of the interstellar medium in greater detail using the models described in Draine and Li (2007). These models include PAH material in addition to dust which consists of a mixture of carbonaceous and amorphous silicate grains that have sizes consistent with the observed wavelength-dependent extinction in the Milky Way. Within the context of this model we can determine q_{PAH}, the fractional contribution of PAHs to the dust; the fractional dust mass exposed to starlight intensity, U parameterized by a linear component (1-γ)$M_{dust}\delta$(U-U_{min}) and power-law component $\gamma M_{dust}\ \frac{(\alpha-1)}{[U_{min}^{1-\alpha}-U_{max}^{1-\alpha}]}U^{-\alpha}$; and f_{PDR}, the fraction of the IR luminosity that is radiated in regions where $U > 10^2$. We follow the prescription in Draine and Li (2007) for estimating these quantities for the galaxies possessing enough data. For the galaxies without 160 μm detections we use the 3 σ value as an upper limit and obtain a lower limit by assuming that between 70 and 160 μm the galaxy's SED is Rayleigh-Jeans which defines $F_{70}/F_{160} = 11.94$.

For KISSR 2316 and 2344 which both have PAH emission, $U_{min} \sim 2$, q_{PAH} =3.2% and 1.8%, $\gamma \sim 0.01$ and 0.001, and f_{PDR} = 7.6% and 3.8% respectively. For several other PAH emitting galaxies with limits on the 160 μm flux the range of f_{PDR} can be computed. For KISSR 2406, f_{PDR} = 5.8-6.9% while for KISSR 2382 and 2398 the fraction is below the plot/fit range. Only a small

fraction of the dust in galaxies that exhibit clear PAH emission comes from high stellar intensity regions. The Draine and Li (2007) dust diagnostics for KISSR 2349, which does not show PAH emission, indicate that $U_{min} \sim 5$, q_{PAH} =1.12%, $\gamma \sim 0.09$ and $f_{PDR} = 40\%$. For galaxies for which we only have 160 μm limits, KISSR 2326, 2338, and 2368, f_{PDR} =15-20%, 31-35%, and 30-34% respectively. These galaxies which do not show PAH emission have model parameters indicating a stronger radiation field and with more of the IR luminosity originating in high intensity regions where it is more difficult for the PAHs to survive.

Why are high luminosity templates the best fits to some of these dwarf galaxies (specifically KISSR 2338, 2349, and 2368)? One of the primary reasons that the high luminosity templates fit these objects better is that they peak at shorter wavelengths and, in general, have a steeper (redder) spectral slope in the 8 to 70 μm range which is also observed in these dwarfs. In addition, the fits may be thrown off by minimal or absent PAH emission since all of the templates include the PAH features. This also explains why the fits to PAH-deficient sources are poor. A more physical reason for the poor fits may be that for these compact galaxies the specific SFRs (normalized) by mass are high so, like in the ultra-luminous infrared galaxies (ULIRGs), more of the PAHs are being destroyed in the high intensity radiation. In particular it may be that the area outside of the star-formation region, where most of the PAH emission originates, is smaller in the galaxies that lack PAH emission because the HII regions are beginning to overlap.

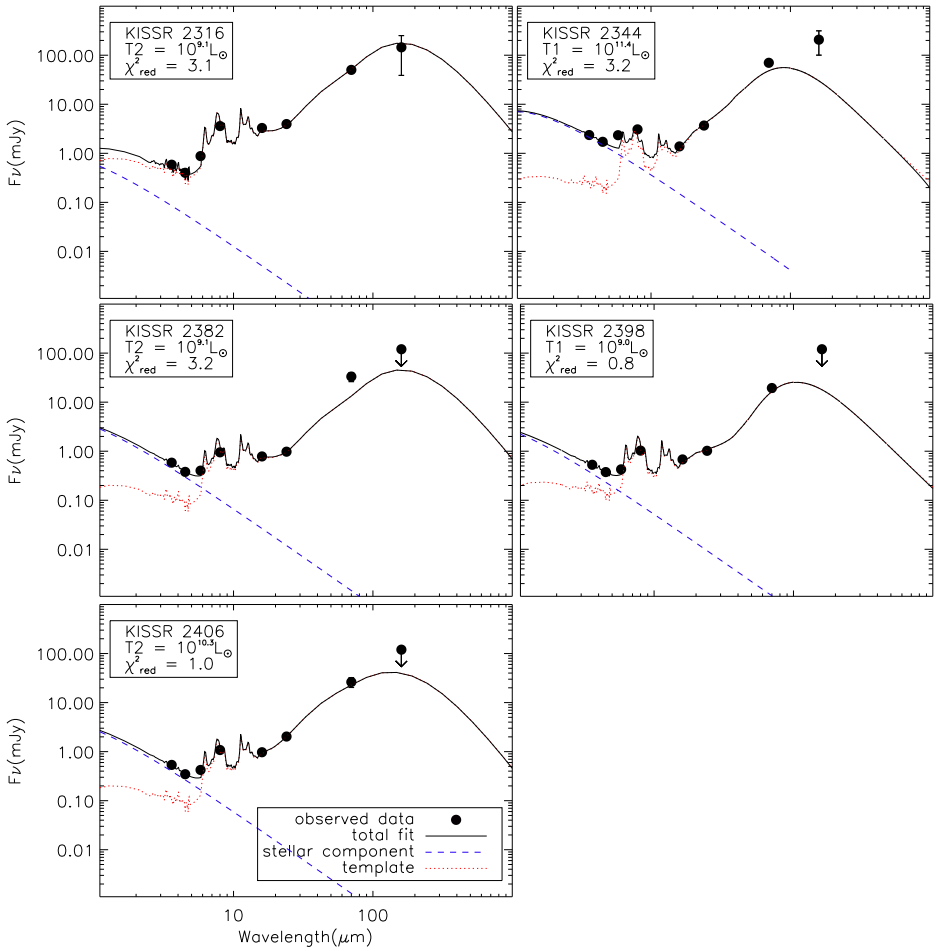

Figure 5.1 SEDs for the sample galaxies that show evidence for PAH emission. The points represent the observations. The blue dashed line shows the best-fit blackbody representing the stellar component of the model. The dotted red line shows the best-fit dust template from the Lagache et al. (2003) (T1) and Dale and Helou (2002) (T2) models. The solid line is the sum of the stellar and dust fits to the data. The values of T1 (Lagache templates) or T2 (Dale templates) in the legend refers to the best-fit template – it is a measurement of the shape of the spectrum not of the infrared luminosity as it is not dependent on the luminosity scaling. The dust templates are only fit longward of 8.0 μm (i.e., not including the 5.8 and 8.0 μm points). The reduced χ^2 values for the fits are given in the legends.

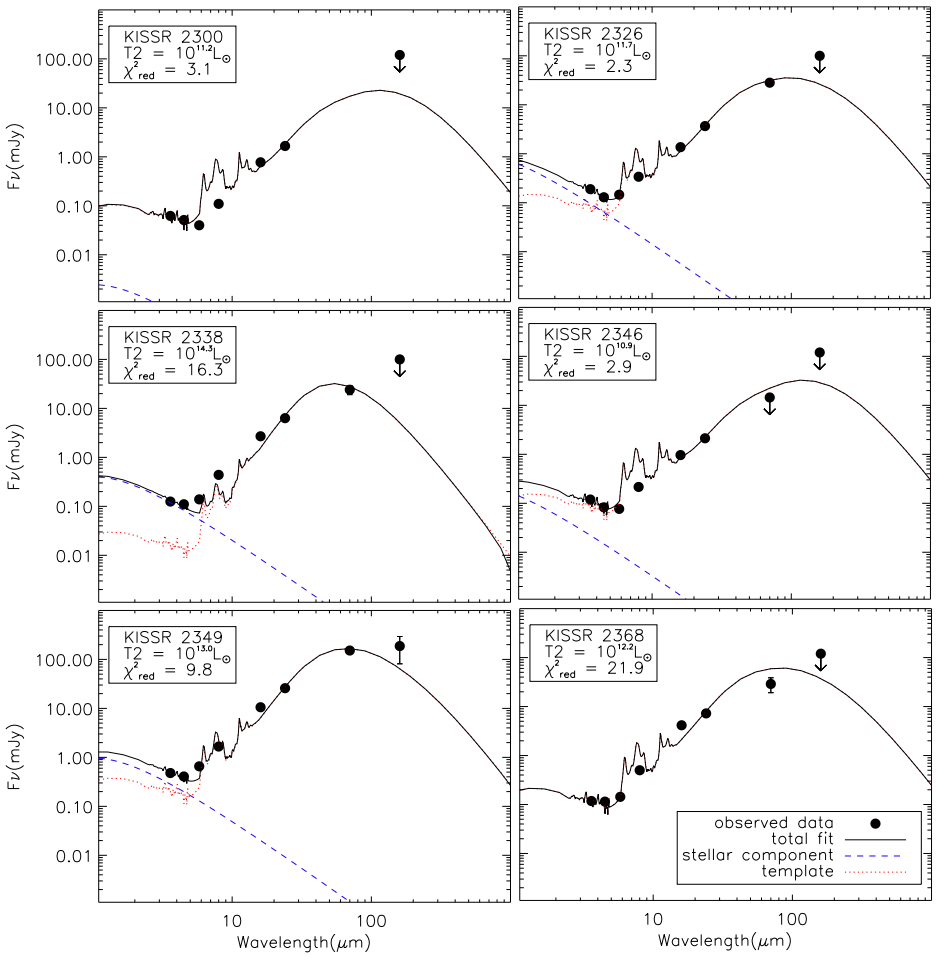

Figure 5.2 SEDs for the sample galaxies that do not show evidence for PAH emission. The points represent the observations. The blue dashed line shows the best-fit blackbody representing the stellar component of the model. The dotted red line shows the best-fit dust template using the Dale and Helou (2002) and Lagache et al. (2003) models. The solid line is the sum of the stellar and dust fits to the data. The values of T2 (Dale templates) in the legend refers to the best-fit template – it is a measurement of the shape of the spectrum not of the infrared luminosity as it is not dependent on the luminosity scaling. The dust templates are only fit longward of 8.0 μm (i.e., not including the 5.8 and 8.0 μm points). The reduced χ^2 values for the fits are given in the legends.

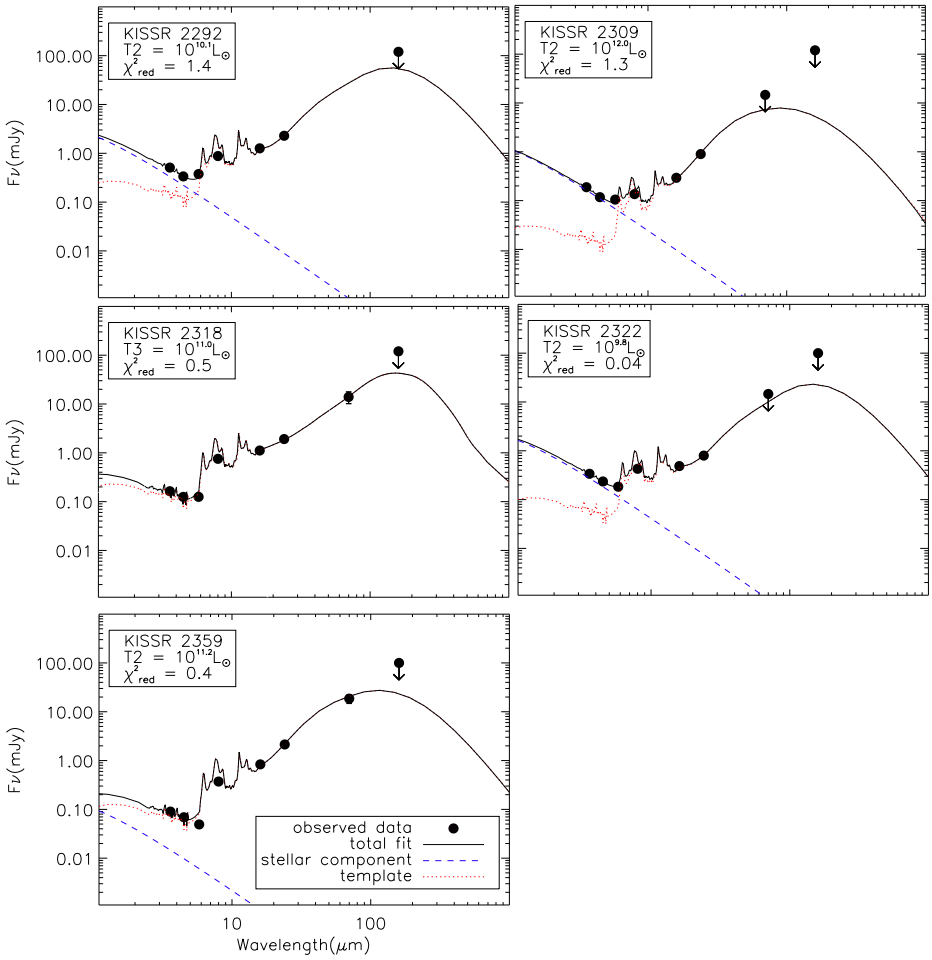

Figure 5.3 SEDs for the sample galaxies for which a determination can not be made as to whether PAH emission is present. The points represent the observations. The blue dashed line shows the best-fit blackbody representing the stellar component of the model. The dotted red line shows the best-fit dust template using the Dale and Helou (2002) and Lagache et al. (2003) models. The solid line is the sum of the stellar and dust fits to the data. The values of T2 (Dale templates) or T3 (normal galaxy template) in the legend refers to the best-fit template – it is a measurement of the shape of the spectrum not of the infrared luminosity as it is not dependent on the luminosity scaling. The dust templates are only fit longward of 8.0 μm (i.e., not including the 5.8 and 8.0 μm points). The reduced χ^2 values for the fits are given in the legends.

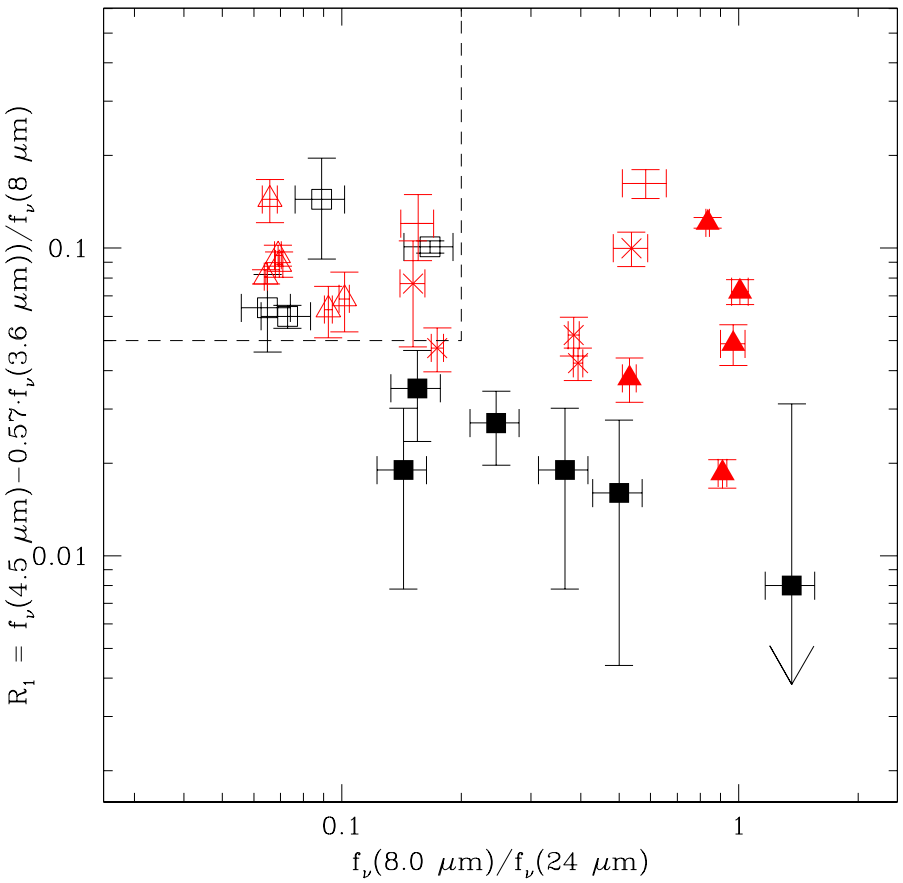

Figure 5.4 The relationship between two different MIR flux ratios for the galaxies. The 8 μm flux includes PAH, dust continuum, and stellar emission, but the stellar emission is very small and would not introduce a significant shift in these data. The y-axis ratio is the stellar subtracted 4.5μm continuum to the 8 μm flux. The region enclosed by the dashed lines is the "no-PAH" region as defined from the Engelbracht et al. (2005) sample. The black points are from Engelbracht et al. (2005) – the open squares are spectroscopically confirmed to lack PAH emission, the filled squares are spectroscopically confirmed to possess PAH emission. The red points show the galaxies from our sample. Even though none of them have *Spitzer*/IRS spectroscopy to determine the presence of PAH emission we mark in filled/open triangles the ones for which the SEDs indicate the presence/absence of PAH emission. The galaxies for which the presence or absence of PAH emission could not be determined are marked with $\times$s. For the galaxies that do not have enough data to construct SEDs, only errorbars are plotted.

Table 5.3. Properties Influenced by PAH Emission in KISS Galaxies

KISSR	f[8]$_{model}$[a] mJy	f[8]$_{data}$[b] mJy	f[8]$_{diff}$[c] mJy	σ[8][d] mJy	σ_{diff}[e]	χ^2_{red}[f]	f[8]/f[24][g]	f[8]/f[16][h]	R$_1$[i]	f$_{PDR}$[j] %	PAH?[k]
2344	1.99	3.07	-1.08	0.090	12	3.2	0.84	1.83	0.12	4	Y
2406	0.96	1.08	-0.12	0.034	4	1.0	0.53	0.98	0.04	6-7	Y
2316	3.49	3.61	-0.12	0.109	1	3.1	0.91	1.05	0.02	8	Y
2398	1.04	1.03	0.01	0.033	1	0.8	1.01	1.33	0.07	0	Y
2382	1.04	0.95	0.09	0.030	3	3.2	0.97	1.04	0.05	0	Y
2309	0.17	0.14	0.03	0.006	7	1.3	0.15	0.31	0.08	···	?
2322	0.54	0.43	0.11	0.015	7	0.04	0.54	0.72	0.10	···	?
2359	0.55	0.37	0.18	0.013	14	0.4	0.17	0.42	0.05	13	?
2318	1.03	0.75	0.28	0.024	12	0.5	0.39	0.64	0.04	···	?
2292	1.24	0.88	0.36	0.028	13	1.4	0.38	0.60	0.05	···	?
2326	0.67	0.37	0.30	0.010	30	2.3	0.09	0.22	0.06	15-20	N
2346	0.68	0.22	0.46	0.008	58	2.9	0.10	0.19	0.07	···	N
2300	0.46	0.11	0.35	0.005	70	3.1	0.07	0.12	0.14	···	N
2338	0.17	0.44	-0.27	0.015	18	16.3	0.07	0.15	0.09	31-35	N
2349	1.74	1.66	0.08	0.050	2	9.8	0.06	0.15	0.08	40	N
2368	0.94	0.50	0.44	0.017	26	21.9	0.07	0.11	0.09	30-34	N
2302	···		···		···	···	···	···	···	···	···
2357	···		···		···	···	0.58	···	0.16	···	···
2403	···		···		···	···	0.16	···	0.12	···	···

[a]The 8μm flux of the best-fit template SED

[b]The 8μm flux measured for the galaxy

[c]The difference between the model and the galaxy 8μm flux

[d]The error in the measured 8μm flux

[e]The number of σ difference between the model and the data at 8μm

[f]The reduced χ^2 of the fit between the data and the template SED

[g]The 8 to 24 μm flux ratio

[h]The 8 to 16 μm flux ratio

[i]R$_1$ = (f$_\nu$(4.5μm)-0.57f$_\nu$(3.6μm))/f$_\nu$(8μm)

[j]The fraction of the infrared emission coming from regions with U$> 10^2$ in the Draine and Li (2007) models

[k]The assessment of whether the galaxies has significant PAH emission

5.3.2 How do dust properties relate to metallicity?

Metallicity is a parameter that can shape the properties of the interstellar medium in galaxies and can span a wide range both within and between galaxies. We explore how metallicity affects properties of the dust observable in the mid-infrared emission from these systems.

Figure 5.6 shows the variations in the ratio of the PAH emission at 8.0 μm to the dust continuum at 24 μm with metallicity. Both the galaxies from this sample and the blue compact dwarf galaxies (Wu et al. 2006) show a weaker correlation (correlation coefficient $\rho_{XY} = 0.36$) than the systems in the Engelbracht et al. (2005) sample (correlation coefficient $\rho_{XY} = 0.75$). Star-forming dwarf galaxies span a wide range in 8 to 24 μm flux density ratio – over an order of magnitude at $\log[O/H]+12 = 8.2$. The transition from a high flux density ratio to a low ratio at $\log[O/H] + 12 = 8.2$, as claimed by Engelbracht et al. (2005), appears to be more of a slow transition with a large galaxy-to-galaxy variation at metallicities around this transition value. Several of the galaxies in the $\log[O/H] + 12 = 8.0$ to 8.2 range exhibit PAH emission and there is nearly two orders of magnitude spread in the 8 to 24 μm flux density ratio in this metallicity range.

Figure 5.7 shows the relationship between metallicity and 16 to 24 μm flux density ratio for this survey and the 16 to 22 μm flux density ratio for the blue compact dwarf galaxies (Wu et al. 2006). This flux density ratio is a measure of the continuum slope in these galaxies. Fluxes measured at 24 and 22 μm should be comparable because the bands are wide (5.5 and 7 μm respectively), the spectrum is fairly smooth in this flux range, and the relative K-corrections should be small – for a standard dust SED, the 16 to 22 μm flux density ratio would be slightly larger. There is an increase in the flux density ratio with increasing metallicity, but the spread at any given metallicity is large. For any given metallicity there is a wide

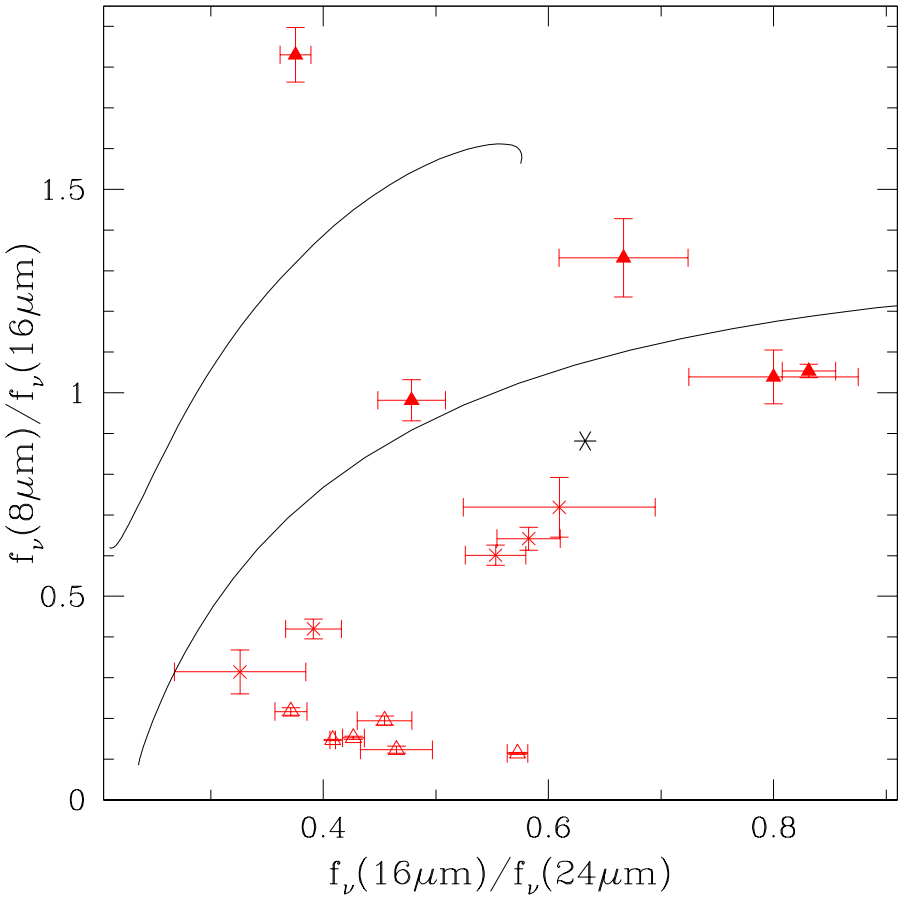

Figure 5.5 The mid-infrared color ratio for galaxies in our sample (red points). The filled symbols represent galaxies with PAH emission while the open symbols represent galaxies without PAH emission. Even though none of these galaxies have *Spitzer*/IRS spectroscopy to determine the presence of PAH emission we mark in filled/open triangles as determined by the SED fitting. The ×s are galaxies for which we were not able to determine the presence or absence of PAH emission from the SEDs. The solid lines are the tracks followed by star-forming galaxies from the Dale and Helou (2002) (lower line) and Lagache et al. (2003) (upper line) samples, all of which exhibit PAH emission. The higher luminosity galaxies are at the bottom right end of the tracks. The black star is the "normal" galaxy from Lagache et al. (2003).

range in the slope of the dust continuum, but on average the lower metallicity galaxies have a steeper slope. As mentioned previously, this steeper slope may be explained by higher radiation density and increased emission from very small grains in these dwarf galaxies.

Figures 5.6 and 5.7 demonstrate that these galaxies exhibit a wide range of dust properties at any given metallicity – there is a wide range in the PAH to continuum ratio (Figure 5.6) and in the continuum slope (Figure 5.7).

5.4 Star formation rate indicators

Star-formation rate plays an important role in the evolution of galaxies. As the high redshift universe becomes more and more accessible, star-formation and its evolution can be studied over a wider range of epochs (e.g., Madau et al. 1996; Steidel et al. 1999; Giavalisco et al. 2004). Estimates of the evolution in the star-formation rate come from indicators that span the spectrum from the rest-frame UV (e.g., Madau et al. 1996; Bouwens and Illingworth 2006) to the optical (e.g., Gallego et al. 2002; Hogg et al. 1998) to the infrared (e.g., Wu et al. 2005; Calzetti et al. 2005). All of the SFR indicators commonly used make assumptions about the metallicity, stellar make-up, star-formation history (continuous versus instantaneous star formation) and/or interstellar medium properties of the systems. In general the conversion from flux to star-formation rate assumes a standard IMF in a solar metallicity galaxy with interstellar medium properties consistent with a "normal" galaxy in the local universe. In order to use these indicators at higher redshift, where low metallicity star-forming galaxies may be more prevalent, the connection between flux and SFR must be evaluated for a range of metallicity and galaxy type. Because it contains a large fraction of low metallicity systems, this sample can be used to compare the affect of galaxy metallicity on the SFRs

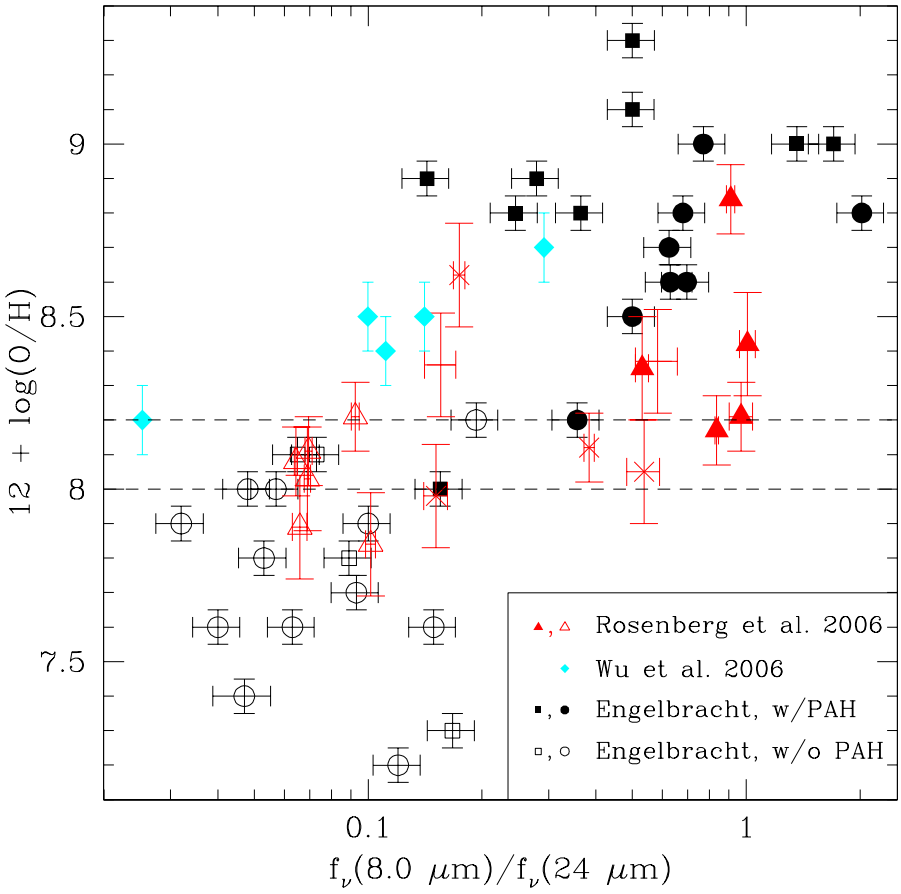

Figure 5.6 Galaxy metallicity as a function of the 8 to 24 μm flux density ratio. The black points are galaxies from Engelbracht et al. (2005), the blue diamonds are blue compact dwarfs from Wu et al. (2006), and the red points are star-forming dwarf galaxies in this sample. Open points are systems that lack PAH emission (determined from either spectra or Figure 5.4 for the galaxies from Engelbracht et al. (2005), from spectra for the galaxies from Wu et al. (2006), and from the broadband SEDs for the galaxies in this sample) while the solid points are thought to exhibit PAH emission. Errorbars with no points are galaxies in our sample that were not detected at the longer wavelengths so SEDs could not be constructed. The dashed lines delineate the region between $\log[O/H] + 12 = 8.0$ and 8.2

.

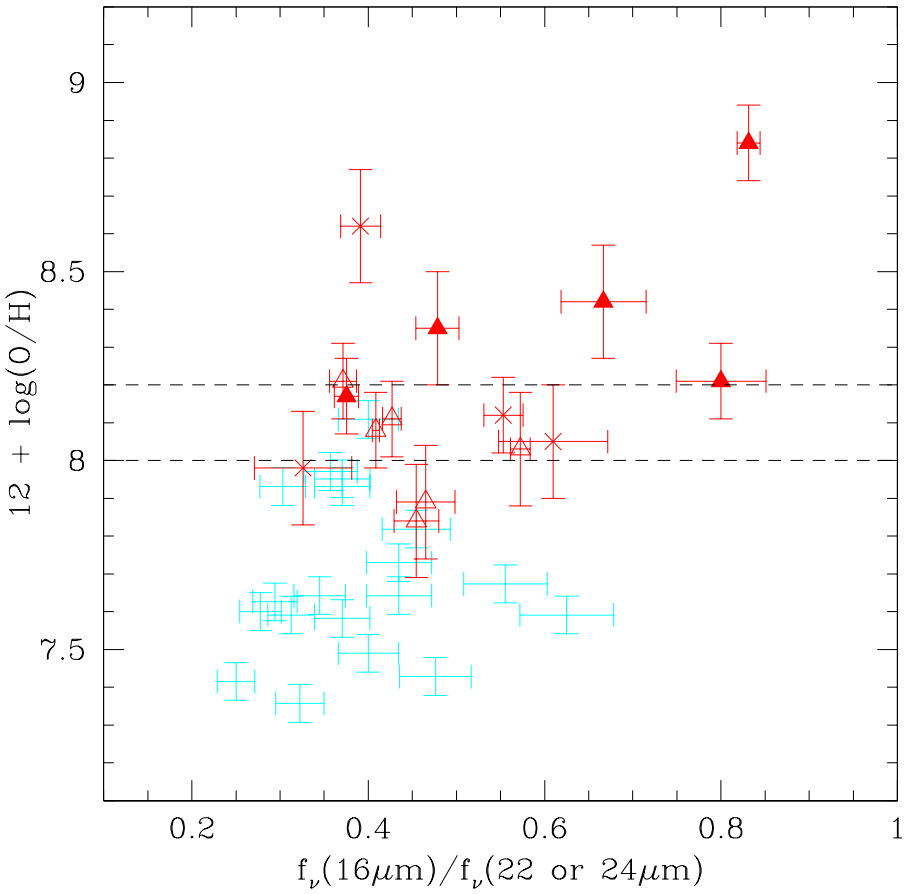

Figure 5.7 Galaxy metallicity as a function of the 22 or 24 to 16 μm flux ratio. The blue errorbars are blue compact dwarf galaxies from Wu et al. (2006) for which the presence or absence of PAH emission is unknown. The red points are galaxies in this sample. Filled points are galaxies that show evidence for PAH emission while open points do not. The $\times$s are galaxies for which the presence or absence of PAH emission could not be determined from the SED fitting. The dashed lines delineate the region with metallicities between $\log[O/H] + 12 = 8.0$ and 8.2

calculated at different wavelengths.

5.4.1 Description of star-formation rate indicators

Spitzer is now providing an unprecedented view of galaxies in the MIR over a wide range of redshifts. At these wavelengths, PAH emission and the dust continuum are the primary contributors to the flux. The dust emission at 12 μm was first shown to be linearly correlated with a galaxy's bolometric luminosity by Spinoglio et al. (1995) using data from IRAS. More recently correlations have been found between 15 μm emission and the total infrared luminosity (TIR, Chary and Elbaz 2001), between both 8 and 24 μm emission and the radio continuum emission from galaxies (Wu et al. 2005), and between combinations of 8 and 24 μm emission and TIR (Calzetti et al. 2005). In the ultraviolet (UV), GALEX (Martin and The GALEX Team 2005) is opening up another window on star formation in the local universe and providing a probe of the emission from the youngest and hottest stars in galaxies. This section is devoted to a comparison of star-formation rates derived using indicators from these different wavelengths ranges (see Table 5.3). Several of the methods are obviously inappropriate for these galaxies, but the goal is to understand the errors in the calculated SFR using standard techniques so we apply them for the sake of comparison.

- Several authors have built libraries of galaxy templates that can be used to estimate TIR from the 24 μm flux densities (Dale et al. 2001; Chary and Elbaz 2001; Dale and Helou 2002; Lagache et al. 2003; Chanial 2003) alone. For this measurement only the 24 μm flux density is used to predict the total infrared emission, not the full SED shape. As shown by Le Floc'h et al. (2005), these templates all produce similar results; we adopt the Chary and Elbaz (2001) results here without concern that this will bias our findings

significantly. A single template was derived for each luminosity bin (see Chary and Elbaz 2001 for details) and can be used to predict the TIR from the 24 μm luminosity. The Kennicutt (1998b) conversion was then used to derive the SFR from TIR. The galaxies that were used to derive these templates are Arp 220, NGC 6090, M82, and M51 which were selected to represent ULIRGs, LIRGs, "starbursts", and "normal galaxies" respectively. An additional set of far-infrared templates from Dale et al. (2001) were added to span a wider range of spectral shapes. In §3.1 we used a similar set of templates from Lagache et al. (2003) and Dale et al. (2001) to fit the sources in this sample and found that, in many of the cases, the shape of the low luminosity templates was not appropriate for fitting the galaxies. The difference between the low luminosity template shape and the galaxy SED will introduce an error in determining the SFR.

- Wu et al. (2005) used a sample of star-forming galaxies in the *Spitzer* First Look Survey to study the correlations between 8 μm and 24 μm luminosity with 1.4 GHz and Hα luminosities. These correlations were used to derive the 1.4 GHz luminosity from either 8 or 24 μm luminosities which was then used to calculate SFR using the Kennicutt (1998b) conversion. Most of the Wu et al. (2005) systems are normal galaxies but a few dwarfs are included and appear to show a different slope between the MIR and radio luminosity. The difference in the normal and dwarf galaxy slopes is probably driven by a lack of PAH emission (Figure 5.1 and 5.2) and the wide range of continuum slopes (Figure 5.7). The more recent calibration of the conversion between 24 μm luminosity and SFR from Calzetti (2007) does not produce significantly different results than the Calzetti et al. (2005) results plotted here.
- Calzetti et al. (2005) showed that there is a correlation between

$\log[\nu L_\nu(24)/\mathrm{TIR}]$ and $\log[L_\nu(8)/L_\nu(24)]$ for H II regions in NGC 5194. The SFR was calculated using the Kennicutt (1998b) conversion from TIR. Calzetti et al. (2005) use $\log[L_\nu(8)/L_\nu(24)]$ instead of just 8 or 24 μm luminosity because the scatter from the ratio is lower. However, there are still region-to-region differences in the correlation between flux density ratio and SFR for the H II regions in NGC 5194, all of which are high metallicity (they are consistent with $2 \lesssim Z \lesssim 3\ Z_\odot$) so the scatter is probably worse when studying objects that cover a range in metallicity.

- The total infrared star-formation rate has been calculated using the 24, 70, and 160 μm data for the three galaxies for which all of these data are available using the method for deriving TIR described by Dale et al. (2005). The SFR was then calculated using the Kennicutt (1998b) conversion from TIR. For the galaxies for which 24 and 70 μm data are available but the 160 μm observation was a non-detection (an additional 8 galaxies), we use the 3 σ upper limit at 160 μm to place an upper limit on the total infrared luminosity. We also obtain a lower limit on the luminosity of these galaxies by assuming that between 70 and 160 μm the galaxy's SED is Rayleigh-Jeans which defines $\mathrm{F}_{70}/\mathrm{F}_{160} = 11.94$.

- Star-formation rates for all of the galaxies in this sample have been computed from the Hα line fluxes measured from the KISS objective prism spectra. These spectra reflect the total Hα emission from the galaxy because they are derived from objective prism observations. A full description of the line flux measurements and calibration is given by Jangren et al. (2005). In order to compute the star-formation rate for these galaxies from the Hα flux, the measurements must be corrected for the presence of blended [N II] emission (these are low resolution spectra), and for absorption. These corrections are

derived from slit spectra. The absorption correction is derived using the reddening coefficient derived from the Balmer line ratios, $c_{H\beta}$. From the [N II] and absorption-corrected Hα fluxes, the SFRs were computed using the standard prescription from Kennicutt (1998a).

- In addition to using the standard methods for computing SFR from the Hα emission, we use a method that takes into account the harder radiation field in low metallicity galaxies (Lee et al. 2002). The stellar population synthesis models on which the standard conversion assume a softer radiation field than what exists in these low metallicity systems. This prescription was derived for a sample of KISS galaxies for which the selection criteria were the same as for these objects. The resulting star-formation rates are lower than what is obtained using the standard models because the harder radiation field produces more Hα emission for a given star-formation rate.

- The UV emission from galaxies comes from the youngest, hottest stars. Kennicutt (1998a) provides a conversion from the UV luminosity to SFR which can be computed across the UV-band because young stars produce a flat spectrum in this region. The UV SFR for these galaxies has not been corrected for absorption so it is a lower limit which measures only the amount of star formation not buried behind dust. Therefore, the SFR measured this way is complementary to that measured in the MIR where all of the emission is coming from the re-radiation from dust in the galaxy. We compute the total SFR as described in Bell et al. (2005) as: $\Psi/\ M_{\odot}\ yr^{-1} = 9.8 \times 10^{-11}$ (L_{IR}+2.2L_{UV}). We use the Calzetti et al. (2005) measurement of L_{IR} because the values are generally between the other MIR results. As with the infrared measurement, the sum of the MIR and UV measurement could overestimate the SFR if some PAH emission is excited by an older stellar population.

Table 5.4. Infrared, Optical, and UV SFRs of KISS Galaxies

KISSR	SFR_{CE}[a,b]	$SFR_{8\mu m}$[a,c]	$SFR_{24\mu m}$[a,d]	SFR_{Calz}[a,e]	$SFR_{H\alpha}$[a,f]	$SFR_{H\alpha_Z}$[a,g]	SFR_{TIR}[a,h]	SFR_{NUV}[a,i]	SFR_{FUV}[a,j]
2292	0.30	0.10	0.21	0.09	0.19	0.07	···	0.19	···
2300	0.32	0.02	0.22	0.02	0.26	0.08	···	0.11	···
2302	<0.05	0.01	<0.02	···	0.09	0.09	···	0.22	···
2309	0.09	0.01	0.06	0.01	0.10	0.03	···	0.20	···
2316	0.70	0.65	0.56	0.48	0.81	0.68	0.79	0.08	···
2318	1.66	0.61	1.21	0.54	1.12	1.12	0.5-2.1	0.13	···
2322	0.12	0.05	0.07	0.04	0.14	0.05	···	0.39	···
2326	0.38	0.03	0.28	0.04	0.35	0.15	0.1-0.3	0.25	···
2338	1.23	0.09	1.07	0.12	0.51	0.19	0.3-0.7	0.23	0.18
2344	0.12	0.08	0.08	0.06	0.10	0.04	0.16	0.34	0.26
2346	0.41	0.04	0.31	0.05	0.24	0.07	···	0.11	···
2349	0.64	0.05	0.61	0.06	0.24	0.09	0.32	0.18	···
2357	0.11	0.05	0.07	0.04	0.20	0.09	···	0.30	···
2359	1.87	0.31	1.40	0.32	3.59	2.09	0.6-2.0	0.21	0.14
2368	1.26	0.09	1.08	0.12	0.54	0.18	0.3-1.0	0.47	···

Table 5.4 (continued)

KISSR	SFR_{CE}[a,b]	$SFR_{8\mu m}$[a,c]	$SFR_{24\mu m}$[a,d]	SFR_{Calz}[a,e]	$SFR_{H\alpha}$[a,f]	$SFR_{H\alpha_Z}$[a,g]	SFR_{TIR}[a,h]	SFR_{NUV}[a,i]	SFR_{FUV}[a,j]
2382	0.09	0.07	0.06	0.05	0.08	0.04	0.1-0.2	0.38	0.22
2398	0.15	0.13	0.10	0.09	0.17	0.08	0.1-0.4	0.36	0.26
2403	0.13	0.02	0.08	0.02	0.19	0.09	···	0.10	···
2406	0.27	0.13	0.19	0.10	0.19	0.09	0.1-0.4	0.42	0.32

[a]The units are $M_\odot$ yr^{-1}

[b]SFR from the Chary and Elbaz (2001) models.

[c]SFR from the 8 μm Wu et al. (2005) relation.

[d]SFR from the 24 μm Wu et al. (2005) relation.

[e]SFR from a combination of 8 μm and 24 μm flux as described by Calzetti et al. (2005)

[f]Hα SFR from the Kennicutt (1998a) relation.

[g]Hα SFR from the Lee et al. (2002) relation which accounts for the harder radiation field in low metallicity galaxies.

[h]SFR from the 24, 70, and 160 μm fluxes using the Dale et al. (2005) and Kennicutt (1998a) relations.

[i]SFR calculated from the NUV flux using the Kennicutt (1998a) relation.

[j]SFR calculated from the FUV flux using the Kennicutt (1998a) relation.

5.4.2 Comparison of star-formation rates

Do all measurements of SFR give the same answer and, under what conditions are the derived SFRs comparable? The answer to this question is critical if measurements of SFR from the MIR and UV are going to be used along with Hα to compute SFR density over a wide range of redshift. Figure 5.8 shows the relationship between the MIR measurements of SFR and the metallicity-corrected Hα SFR (left-hand panel) and between SFR measured over a wide range of wavelengths and the metallicity-corrected Hα SFR (right-hand panel). The errors due to the galaxy photometry on all of these these data points (and those in the subsequent SFR plots), with the exception of the NUV values, are smaller than the points. The NUV SFRs are the exception because the values are all lower limits since no correction has been made for extinction. There is also a distance error associated with these measurements but they will only shift all of the points up or down without altering their relative separations (i.e., it will not change the spread between the points). These plots show that there is over an order of magnitude spread in the SFR measurement for a given galaxy and the disagreement occurs for both high and low SFR sources. However, the plot also shows that several of the methods give similar answers. The Chary and Elbaz (2001) and the 24 μm Wu et al. (2005) values are similar as are the 8 μm Wu et al. (2005) and the Calzetti et al. (2005) values. These values agree because they were derived in a consistent way for normal galaxies and are derived from the same fluxes (24 μm and 8 μm respectively). The spread in the derived SFRs points to a systematic difference in the calculation of these values due either to the intrinsic spread in the luminosity-SFR relationships or to a physical difference between these galaxies and those for which the luminosity-SFR relationship was derived.

In general, the measurements based on the 24 μm luminosity (Chary and Elbaz

2001 and 24 μm Wu et al. 2005) tend to indicate a higher SFR than the 8 μm (Wu et al. 2005) or 8 plus 24 μm (Calzetti et al. 2005) measurements. This result is consistent with the 8 μm to Hα correlation having a steeper slope for dwarf galaxies than it does for more luminous galaxies as was found in the Wu et al. (2005) study. For six galaxies in this sample the SFR derived from the 8 μm flux is about an order of magnitude lower than that derived from the 24 μm flux. All six of these galaxies are low metallicity systems (Z $\lesssim$0.25 Z$_\odot$) that have SEDs which show no evidence for PAH emission. KISSR 2359 which has low PAH emission, has an 8 μm derived SFR that is 4.5 times smaller than the 24 μm SFR. Clearly the 8 μm emission is not a good SFR indicator for low metallicity objects that may not exhibit PAH emission. Alternatively, the 24 μm SFR seems, in general, to overpredict the SFR in these galaxies relative to the Hα measurement. The galaxies in this sample are, in general, very compact systems with hard radiation fields because they tend to also be low metallicity systems. These conditions appear to be driving the heating of hot dust and/or very small grains that dominate in the region between 8 and 24 μm as has been seen previously in low metallicity systems (Madden et al. 2006). The difference between the 24 μm and Hα SFRs is certainly affected by the incorrect calibration of the 24 μm SFR for these galaxies which comes about because the SEDs shown in §5.3.1 are not well fit by the low luminosity templates.

The right-hand panel in Figure 5.8 shows the SFR computed using several different indicators including the Calzetti et al. (2005) MIR indicator and the NUV emission. The SFRs computed in the NUV have not been corrected for extinction. For the highest SFR systems (which are also the highest metallicity ones), the lack of an extinction correction has led to a low measurement of the SFR. However, for most of the systems, the SFR computed in the UV is larger than that computed from the Hα despite the fact that extinction has not been

taken into account. One factor in the high UV SFR may be that the there is a metallicity dependence that has not been accounted for. However, the significant excess in the UV SFR even for galaxies that have metallicities $\gtrsim 0.5 Z_{\odot}$, indicates that this is probably not the only factor. A higher SFR measured in the UV than in Hα, attributed to declining star-formation from a young but quasi-stellar burst, has also been seen for intergalactic star-forming regions in NGC 5291 (Boquien et al. 2007). A declining SFR in the KISS galaxies would explain the discrepancy between the Hα and UV SFRs since the timescale in the UV is about 10 times longer than it is in Hα. However, this timescale argument would not explain why the UV SFR is higher than the MIR SFR which does not decline as quickly. A different explanation would be that the interstellar medium has been blown out in these systems so that there is much less gas and dust surrounding the star-forming region. This explanation is consistent with the mid-infrared spectroscopic results for a similar sample of galaxies which provides evidence for supernova driven bubbles surrounding the star-formation regions O'Halloran et al. (2008). A much more detailed analysis would be required to assess whether there was a strong burst of star-formation in the recent past that could have blown away the gas and dust. The plot includes the combined MIR and NUV SFR using the Bell et al. (2005) formulation. For two of the galaxies, the total SFR is smaller than the Calzetti et al. (2005) MIR SFR alone because there is a small difference in the calibration in the two methods. This calibration uncertainty is a systematic error in all of the calculations and these results are consistent within that error.

Figure 5.9 shows the MIR SFR as a function of the Hα SFR with point type specifying those galaxies with and without PAH emission. For the galaxies that appear to have PAH emission, the 8 and 24 μm measurements of SFR are, in all but one case, in good agreement with the Hα values. For galaxies that do not

show evidence for PAH emission, the SFR computed from the 8 μm flux is lower than what is measured from the Hα emission, while the value computed from the 24 μm emission is higher in all but one case. The dispersion in the values of SFR computed in the mid-infrared for these galaxies appears to be driven by a difference in the properties of the interstellar medium in these galaxies. Both the PAH emission and the shape of the MIR continuum differ from those of normal galaxies both in a lack of PAH emission and in excess emission from hot dust and/or small grains.

Figure 5.10 shows the relationship between the SFR ratio – SFR from a given indicator divided by the metallicity corrected Hα SFR – as a function of metallicity. The left-hand panel shows this ratio for the MIR indicators. The right-hand panel shows the ratio for the Calzetti et al. (2005) MIR SFR, the NUV SFR, and the combination of the MIR and NUV SFRs. For the MIR SFRs, the two measures that are derived from the 24 μm emission are the most highly correlated with metallicity. For the 8 μm computed SFRs, a trend with metallicity is not clear in these data. The NUV SFR for the highest metallicity systems are low because of extinction, but there is no clear trend among the lower metallicity systems.

This sample has 3 galaxies that have the properties of dusty starbursts – KISSR 2316, 2318, and 2359. These systems all have SFRs calculated from the total infrared emission that are much higher than that calculated from the NUV (which is not corrected for extinction). These galaxies are some of the most luminous systems in the sample and the two with known metallicities are the highest metallicity systems. Since the derivation of the SFR indicators in the mid-infrared has generally been based on dusty starbursts one might expect the most consistency in the derived SFRs from these systems. The rates calculated from Hα, 8 μm, 24 μm, and the total infrared are fairly consistent for KISSR 2316 and 2318 (the UV

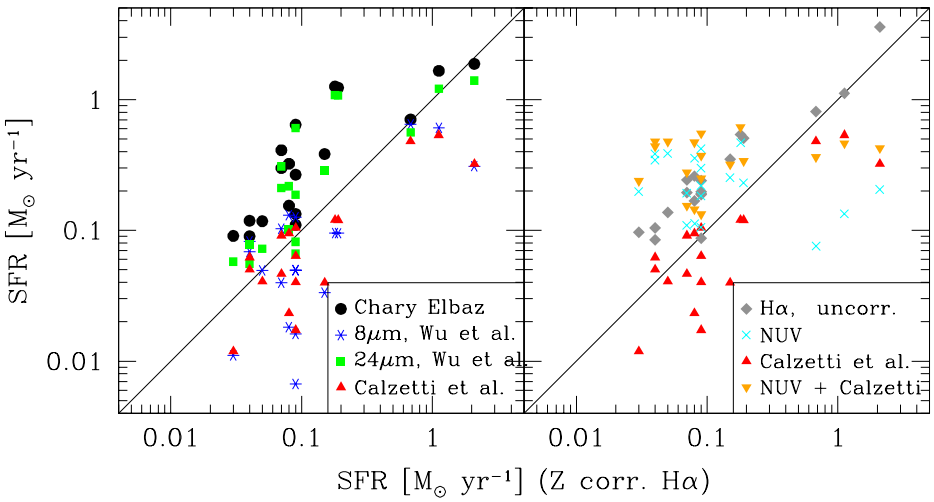

Figure 5.8 Comparison of SFR indicators with respect to the SFR calculated from Hα with a correction for metallicity. The left-hand panel shows a comparison of the MIR indicators while the right-hand panel shows the Hα not corrected for metallicity, the Calzetti et al. (2005) MIR values, the NUV measurement, and the combined NUV and MIR values. Because of a difference in the calibration between the Calzetti et al. (2005) MIR SFR and the Bell et al. (2005) combined MIR and NUV SFR, there are a couple of galaxies for which the Calzetti et al. (2005) MIR SFR is slightly higher than the combined SFR.

values are low because they are not corrected for extinction). However, the SFRs computed for KISSR 2359 are more problematic. This source has the highest Hα SFR, (3.59 M$_\odot$ yr^{-1}; not correcting for metallicity because the source is close to Z$_\odot$) in the sample. The 24 μm SFRs from the Chary and Elbaz (2001) models and from the Wu et al. (2005) correlation are 1.87 and 1.40 respectively. These are smaller than the Hα values, but given the spread in the models and correlation they are still consistent. However, the 8 μm SFR from the Wu et al. (2005) correlation is only 0.31, significantly less than what is measured from the other methods. The lower value for the 8 μm emission may be a reflection of a substantial portion of the infrared emission coming from a high intensity region where the PAHs are destroyed.

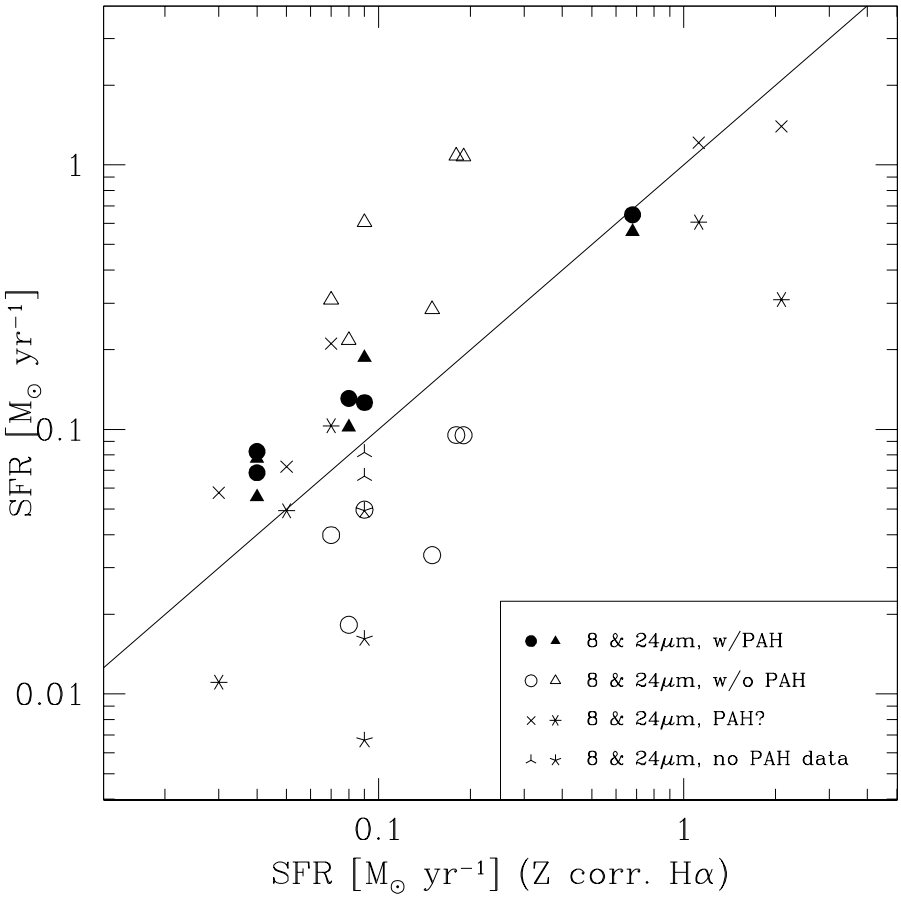

Figure 5.9 Comparison of MIR SFR indicators as a function of the metallicity corrected Hα SFR. The open symbols indicate objects that do not show evidence for PAH emission while the filled symbols indicate those which do have PAH emission. The crosses and stars indicate galaxies for which the PAH determination was uncertain from the SED fitting. The "no PAH data" points are galaxies for which the longer wavelength data were not available so no SED fitting could be done.

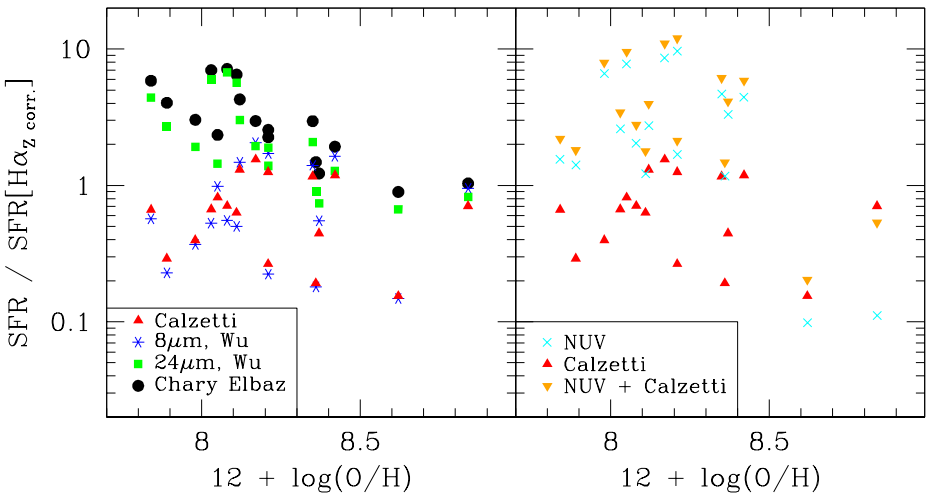

Figure 5.10 Comparison of SFR indicators, normalized by the Hα corrected SFR as a function of metallicity. The left-hand panel is a comparison of the MIR indicators. The right-hand panel is a comparison of the Calzetti et al. (2005), the NUV, and the combined NUV and MIR values. Because of a difference in the calibration between the Calzetti et al. (2005) MIR SFR and the Bell et al. (2005) combined MIR and NUV SFR, there are a couple of galaxies for which the Calzetti et al. (2005) MIR SFR is slightly higher than the combined SFR.

5.5 Summary

Star-forming dwarf galaxies have a wide range of dust properties that are quite different from those of the spiral and massive starburst galaxies. These differences most likely result from a combination of the harder radiation field, the more compact structure of these systems, possibly a lack of dust due to destruction in shocks or delayed injection, and either a different composition or different heating of the dust in the interstellar medium.

We have used broadband SEDs and color-color diagrams to determine the presence or absence of PAH emission in the sample galaxies. It appears that one of the best indicators of PAH emission may be the 8 to 16μm flux ratio. Mid-infrared spectroscopy, which is not available at this time, is required to confirm these results. Nevertheless, the combination of the SEDs and the color-color plots provide more information on the presence or absence of PAH emission than the trend of color

with metallicity that was evident from only the *Spitzer*/IRAC data (Rosenberg et al. 2006).

One of the most striking properties of the galaxies in this sample is that, despite their simplicity in being compact systems dominated by a small number of H II regions, they have a wide range of infrared properties. There are low metallicity systems that show some evidence for PAH emission (KISSR 2322, $Z=0.24Z_{\odot}$) and high metallicity systems for which PAH emission is uncertain (KISSR 2359, $Z=0.91Z_{\odot}$) indicating that metallicity is not the only parameter driving the presence and/or strength of the PAH emission features.

It is not only the PAH emission features in these star-forming dwarf galaxies that are different from the spirals and massive starbursts, but also the shapes of the mid-infrared continua. Many of these galaxies have steep, red mid-infrared continua similar to those observed by Gallais et al. (2004) in starburst galaxies, by Madden et al. (2006); Hunt et al. (2006) in low metallicity galaxies and modeled by Galliano et al. (2005) as being due to emission from very small grains.

Applying the model of Draine and Li (2007) it appears that the galaxies with lower PAH emission have more of their infrared emission coming from higher stellar intensity regions where PAHs are more likely to be destroyed. The smaller amounts of PAH emission could be an indication that the H II regions are beginning to overlap in these galaxies thereby decreasing the relative volume of the photodissociation region.

The effect of metallicity on the star-formation rate in galaxies is well studied (Lee et al. 2004; Kewley et al. 2004; Moustakas et al. 2006), primarily with respect to the optical indicators. At 24 μm we see a clear connection between the derived star-formation rate and metallicity, but the connection is not as clear at 8 μm where other factors must be dominating the dispersion in the relationship between

flux density and star-formation rate.

The differences between these star-forming dwarf galaxies and the majority of systems that have been studied in the infrared have two major consequences: (1) mid-infrared spectral templates do not provide a good fit to the systems, and (2) the methods that have been developed to determine the star-formation rate from mid-infrared observations do not work well in these systems. Because these galaxies are different from the majority of galaxies that have been studied in the mid-infrared, some caution needs to be exercised in fitting spectral templates and deriving mid-infrared star-formation rates, particularly at higher redshift where more information is often not available and where compact star-forming systems may be more prevalent.

Acknowledgements This work is based in part on observations made with the Spitzer Space Telescope, which is operated by the Jet Propulsion Laboratory, California Institute of Technology under a contract with NASA. Support for this work was provided by NASA through an award issued by JPL/Caltech. JLR acknowledges support from NSF grant AST-0302049. ELF's work was supported through NASA/JPL by the Spitzer Fellowship program. JJS gratefully acknowledges support for the KISS project from the NSF through grants AST 95-53020, AST 00-71114, and AST 03-07766.

APPENDIX

A. Description of SED Fitting Procedure

The spectral energy distributions were studied by fitting model templates to each galaxy. The 5.8 and 8.0 μm points which are most affected by PAH emission were excluded from the fitting so that we could compare the photometry with the models at these wavelengths. Note that $\sim$10% or less of the 8.0 μm emission in these galaxies is from stellar photospheres, most of the emission is from the dust continuum or PAH features.

The models consist of an ensemble of starburst galaxy model templates produced by Lagache et al. (2003) and normal star-forming galaxy templates by Dale and Helou (2002). Each template is identified by a galaxy luminosity. However, the templates are used to model the shape of the SED and are not necessarily dependent on the luminosity of the source (we ignore the luminosity scaling). These templates sample the MIR colors of both normal and ultra-luminous infrared galaxies. The Lagache et al. (2003) models also include a single "normal" (non-starburst) galaxy template. For many of the galaxies, the fits are constrained only by the 16 and 24 μm data points.

In order to fit the broadband data, "synthetic" data points for the IRAC 3.6, 4.5, IRS 16μm, and MIPS 24, 70 and 160μm bands were created by convolving the template spectra with the filter response functions. To fit the near-infrared portion of the SED, a blackbody spectrum with a temperature in the range 5000 K to 10000 K was added to the template model. A least squares technique was then used to determine the best fit template plus blackbody (steps of 1000 K were used to determine the best-fit temperature) with the appropriate scaling factors. The temperature of the chosen blackbody did not have a significant effect on the SED fit.

Out of the 19 sample galaxies, three are not detected at 16μm and one of these is also not detected at 24μm. Template fitting was not performed for these three sources because there were not enough long wavelength points to derive meaningful constraints.

B. Description of Individual Galaxy SEDs

B.1. Galaxies that show PAH emission

KISSR 2344: has 8μm emission that is significantly in excess of the best-fitting SED template model. As can be seen in Table 5.3, this galaxy also has one of the largest values for $f_\nu(8)/F_\nu(24)$, $f_\nu(8)/F_\nu(16)$, and R_1. While this galaxy probably does have some of the largest values for each of these parameters, differences in the size of the apertures used at each of these wavelengths could affect these numbers. A difference between the apertures would tend to increase the fluxes at the shorter wavelengths with respect to the longer wavelengths. This is the only galaxy in the sample for which this should be a significant issue since most of the others are unresolved or barely resolved.

KISSR 2406: has a metallicity of log[O/H]+12 = 8.3 and PAH emission in excess of the best-fit template models. In addition, this galaxy falls well within the PAH-emitting galaxy regions in Figures 5.4 and 5.5 and has a small fraction of its infrared luminosity coming from the highest intensity regions ($f_{PDR} = 6 - 7$).

KISSR 2316: is the highest metallicity system in the sample (log[O/H]+12 = 8.8) and has PAH emission that is only 1σ below the best-fit model template. As with KISSR 2406, the galaxy falls well within the PAH-emitting galaxy regions in Figures 5.4 and 5.5 and has a small fraction of its infrared luminosity coming from high intensity regions.

KISSR 2398: has a metallicity of log[O/H]+12 = 8.4 and 8μm emission that is

only 1σ below the best-fit model template. The diagnostics from the other plots, Figures 5.4 and 5.5, also agreeing with this being a PAH emitting galaxy.

KISSR 2382: has a metallicity of log[O/H]+12 = 8.2 and 8μm emission that is 3σ below the best-fit model template. However, the galaxy falls well within the PAH-emitting galaxy regions in Figures 5.4 and 5.5.

B.2. Galaxies that show no evidence of PAH emission

KISSR 2326: shows no evidence for PAH emission – the data are 30σ below the best-fit template at 8.0 μm in this log[O/H]+12 = 8.2 galaxy. This galaxy falls well within the no-PAH regions in Figures 5.4 and 5.5.

KISSR 2346: shows no evidence for PAH emission as the data are 58σ below the best-fit template at 7μm in this low metallicity (log[O/H]+12 = 7.8) galaxy. This galaxy falls well within the no-PAH regions in Figures 5.4 and 5.5.

KISSR 2300: shows no evidence for PAH emission. The best-fit dust template is 70σ above the 8.0 μm flux from this galaxy. There is no evidence for a rise in the spectrum above the continuum level at these wavelengths for this galaxy that has log[O/H]+12 = 7.9. In addition, this galaxy clearly occupies the no-PAH region in Figures 5.4 and 5.5.

KISSR 2338: shows no evidence for PAH emission in this log[O/H]+12 = 8.1 metallicity galaxy. Even the best-fit dust template, which is the template for an ultraluminous infrared galaxy (ULIRG), gives an extremely poor fit to these data (χ^2 = 16.3). This galaxy shows an excess at 5.8, 8.0, and 16 μm that seems to indicate an unusually large contribution from hot dust and/or very small grains. The galaxy falls well within the no-PAH regions in Figures 5.4 and 5.5.

KISSR 2349: shows no evidence for PAH emission in this galaxy which has a metallicity of log[O/H]+12 = 8.1. Even the best-fit template gives a poor fit to the data ($\chi^2 = 9.8$). Similar to KISSR 2338, the best-fit template is for an ULIRG

and there appears to be an excess (although not quite as great as for KISSR 2338) of hot dust and/or very small grain emission. This galaxy falls well within the no-PAH regions in Figures 5.4 and 5.5.

KISSR 2368: shows no evidence for PAH emission in this log[O/H]+12 = 8.0 galaxy. Even the best-fit dust template which, similar to KISSR 2338 and 2349, is a ULIRG template, provides an extremely poor fit ($\chi^2 = 21.9$). As with the other two galaxies, there is some evidence for an excess of hot dust and/or very small grains. This galaxy falls well within the no-PAH regions in Figures 5.4 and 5.5.

B.3. Galaxies for which the existence of PAH emission is uncertain

KISSR 2309: is a low metallicity galaxy (log[O/H]+12 = 8.0) which has an 8 μm flux density that is 7σ below the best-fit SED template. In Figure 5.4 the galaxy falls within the no-PAH region. In Figure 5.5, KISSR 2309 is the left-most galaxy in the no-PAH region with errorbars that touch the tracks for the spectral templates which include PAH emission.

KISSR 2322: is another low metallicity galaxy (log[O/H]+12 = 8.0) which has an 8 μm flux density that is 7σ below the best-fit SED template. In contrast to KISSR 2309, KISSR 2322 falls within the PAH-emitting region in Figure 5.4 and between the PAH and no-PAH galaxies in Figure 5.5.

KISSR 2359: is a high metallicity galaxy (log[O/H]+12 = 8.6) yet it has an 8 μm flux density that is 14σ below the best-fit SED template. In Figure 5.4 the galaxy falls just outside the no-PAH region, although the errorbars overlap with the region. In Figure 5.5 KISSR 2359 has the second lowest value of $f_\nu(8)/f_\nu(16)$ of the galaxies for which the PAH classification is uncertain, placing it closer to the no-PAH galaxies than the PAH emitting ones.

KISSR 2318: has an unknown metallicity and an 8 μm flux density that is 12σ below the best-fit SED template. Nevertheless, this galaxy falls well within the

PAH-emitting galaxy region in Figures 5.4 and has one of the higher $f_\nu(8)/f_\nu(16)$ ratios of the galaxies with uncertain PAH emission in Figure 5.5.

KISSR 2292: is another fairly low metallicity galaxy ($\log[O/H]+12 = 8.1$) which has an 8 μm flux density that is 13σ below the best-fit SED template. The galaxy falls in the PAH-emitting region in Figure 5.4 and has one of the higher $f_\nu(8)/f_\nu(16)$ ratios of the galaxies with uncertain PAH emission in Figure 5.5.

BIBLIOGRAPHY

Bell, E. F. et al. 2005, *ApJ* **625**, 23

Boquien, M., Duc, P. ., Braine, J., Brinks, E., Lisenfeld, U., and Charmandaris, V.: 2007, *A&A* **467**, 93

Bouwens, R. and Illingworth, G.: 2006, *New Astronomy Review* **50**, 152

Calzetti, D.: 2007, *ApJ* **666**, 870

Calzetti, D. et al. 2005, *ApJ* **633**, 871

Chanial, P.: 2003, *Ph.D. Thesis, Univ. Paris*

Chary, R. and Elbaz, D.: 2001, *ApJ* **556**, 562

Dale, D. A. et al. 2005, *ApJ* **633**, 857

Dale, D. A. and Helou, G.: 2002, *ApJ* **576**, 159

Dale, D. A., Helou, G., Contursi, A., Silbermann, N. A., and Kolhatkar, S.: 2001, *ApJ* **549**, 215

Draine, B. T. and Li, A.: 2007, *ApJ* **657**, 810

Dwek, E.: 2005, in R. Szczerba, G. Stasinska, and S. K. Gorny (eds.), *Planetary Nebulae as Astronomical Tools*, Vol. 804 of *American Institute of Physics Conference Series*, pp 197–203

Eisenhardt, P. R. et al. 2004, *ApJS* **154**, 48

Engelbracht, C. W., Gordon, K. D., Rieke, G. H., Werner, M. W., Dale, D. A., and Latter, W. B.: 2005, *ApJ* **628**, L29

Gallais, P., Charmandaris, V., Le Floc'h, E., Mirabel, I. F., Sauvage, M., Vigroux, L., and Laurent, O.: 2004, *A&A* **414**, 845

Gallego, J., García-Dabó, C. E., Zamorano, J., Aragón-Salamanca, A., and Rego, M.: 2002, *ApJ* **570**, L1

Galliano, F., Dwek, E., and Chanial, P.: 2008, *ApJ* **672**, 214

Galliano, F., Madden, S. C., Jones, A. P., Wilson, C. D., and Bernard, J.-P.: 2005, *A&A* **434**, 867

Giavalisco, M. et al. 2004, *ApJ* **600**, L103

Gordon, K. D. et al. 2005, *PASP* **117**, 503

Helou, G. et al. 2004, *ApJS* **154**, 253

Hogg, D. W., Cohen, J. G., Blandford, R., and Pahre, M. A.: 1998, *ApJ* **504**, 622

Hogg, D. W., Tremonti, C. A., Blanton, M. R., Finkbeiner, D. P., Padmanabhan, N., Quintero, A. D., Schlegel, D. J., and Wherry, N.: 2005, *ApJ* **624**, 162

Houck, J. R. et al. 2004a, *ApJS* **154**, 18

Houck, J. R. et al. 2004b, *ApJS* **154**, 211

Hunt, L., Bianchi, S., and Maiolino, R.: 2005, *A&A* **434**, 849

Hunt, L. K., Thuan, T. X., Sauvage, M., and Izotov, Y. I.: 2006, *ApJ* **653**, 222

Ivezic, Z., Nenkova, M., and Elitzur, M.: 1999, *ArXiv Astrophysics e-prints, arXiv:astro-ph/9910475*

Jangren, A., Salzer, J. J., Sarajedini, V. L., Gronwall, C., Werk, J. K., Chomiuk, L., Moody, J. W., and Boroson, T. A.: 2005, *AJ* **130**, 2571 (KR3)

Jannuzi, B. T. and Dey, A.: 1999, in *ASP Conf. Ser. 191: Photometric Redshifts and the Detection of High Redshift Galaxies*, pp 111–+

Jannuzi, R. T. et. al.: 2007, *submitted*

Jarrett, T. H., Chester, T., Cutri, R., Schneider, S., Skrutskie, M., and Huchra, J. P.: 2000, *AJ* **119**, 2498

Kennicutt, R. C.: 1998a, *ApJ* **498**, 541

Kennicutt, Jr., R. C.: 1998b, *ARA&A* **36**, 189

Kewley, L. J., Geller, M. J., and Jansen, R. A.: 2004, *AJ* **127**, 2002

Lagache, G., Dole, H., and Puget, J.-L.: 2003, *MNRAS* **338**, 555

Le Floc'h, E. et al. 2005, *ApJ* **632**, 169

Lee, J. C., Salzer, J. J., Impey, C., Thuan, T. X., and Gronwall, C.: 2002, *AJ* **124**, 3088

Lee, J. C., Salzer, J. J., and Melbourne, J.: 2004, *ApJ* **616**, 752

Li, A. and Draine, B. T.: 2002, *ApJ* **572**, 232

Li, A., Misselt, K. A., and Wang, Y. J.: 2006, *ApJ* **640**, L151

MacAlpine, G. M., Smith, S. B., and Lewis, D. W.: 1977, *ApJS* **34**, 95

Madau, P., Ferguson, H. C., Dickinson, M. E., Giavalisco, M., Steidel, C. C., and Fruchter, A.: 1996, *MNRAS* **283**, 1388

Madden, S. C.: 2000, *New Astro. Rev.*,**44**,249

Madden, S. C. and Galliano, F.: 2005, in D. C. Lis, G. A. Blake, and E. Herbst (eds.), *IAU Symposium*, pp 198–+

Madden, S. C., Galliano, F., Jones, A. P., and Sauvage, M.: 2006, *A&A* **446**, 877

Markarian, B. E.: 1967, *Astrofizika* **3**, 55

Marshall, J. A., Herter, T. L., Armus, L., Charmandaris, V., Spoon, H. W. W., Bernard-Salas, J., Houck, J. R.: 2007, *ApJ* **670**, 129

Martin, C. and The GALEX Team: 2005, in M. Colless, L. Staveley-Smith, and R. A. Stathakis (eds.), *IAU Symposium*, pp 221–+

Morrissey, P. et al. 2005, *ApJ* **619**, L7

Moustakas, J., Kennicutt, Jr., R. C., and Tremonti, C. A.: 2006, *ApJ* **642**, 775

O'Halloran, B., Satyapal, S., and Dudik, R. P.: 2006, *ApJ* **641**, 795

O'Halloran, B., Madden, S. C., Satyapal, S., Abel, N. : 2008, *ApJ* in press, astro-ph/0803.3403

Rieke, G. H. et al. 2004, *ApJS* **154**, 25

Roche, P. F., Aitken, D. K., Smith, C. H., and Ward, M. J.: 1991, *MNRAS* **248**, 606

Rosenberg, J. L., Ashby, M. L. N., Salzer, J. J., and Huang, J.-S.: 2006, *ApJ* **636**, 742

Salzer, J. J. et al. 2000, *AJ* **120**, 80

Salzer, J. J., Jangren, A., Gronwall, C., Werk, J. K., Chomiuk, L. B., Caperton, K. A., and McKinstry, K.: 2005, *AJ* **130**, 2584

Smith, M. G., Aguirre, C., and Zemelman, M.: 1976, *ApJS* **32**, 217

Spinoglio, L., Malkan, M. A., Rush, B., Carrasco, L., and Recillas-Cruz, E.: 1995, *ApJ* **453**, 616

Steidel, C. C., Adelberger, K. L., Giavalisco, M., Dickinson, M., and Pettini, M.: 1999, *ApJ* **519**, 1

Stetson, P. B.: 1987, *PASP* **99**, 191

Thuan, T. X., Sauvage, M., and Madden, S.: 1999, *ApJ* **516**, 783

Wasilewski, A. J.: 1983, *ApJ* **272**, 68

Werner, M. W. et al. 2004, *ApJS* **154**, 1

Wu, H., Cao, C., Hao, C.-N., Liu, F.-S., Wang, J.-L., Xia, X.-Y., Deng, Z.-G., and Young, C. K.-S.: 2005, *ApJ* **632**, L79

Wu, Y., Charmandaris, V., Hao, L., Brandl, B. R., Bernard-Salas, J., Spoon, H. W. W., and Houck, J. R.: 2006, *ApJ* **639**, 157

Wu, Y., Charmandaris, V., Hunt, L. K., Bernard-Salas, J., Brandl, B. R., Marshall, J. A., Lebouteiller, V., and Houck, J. R.: 2007, *ApJ* **662**, 952

Zamorano, J., Rego, M., Gallego, J. G., Vitores, A. G., Gonzalez-Riestra, R., and Rodriguez-Caderot, G.: 1994, *ApJS* **95**, 387

CHAPTER 6

DUST IN THE EXTREMELY METAL-POOR BLUE COMPACT DWARF GALAXY I ZW 18: THE *SPITZER* MID-INFRARED VIEW*

Abstract I Zw 18, a blue compact dwarf (BCD) galaxy with the 2nd lowest metallicity measured in a star-forming object, has been observed with all three instruments on board the Spitzer Space Telescope. We present the deepest $5-36\,\mu$m mid-infrared (mid-IR) spectrum of this galaxy as yet obtained, as well as $3.6\,\mu$m to $70\,\mu$m imaging results. As with SBS 0335-052E, another BCD with similar metallicity, I Zw 18 shows no detectable emission from polycyclic aromatic hydrocarbons (PAHs). However, the continuum emission, from 15 to $70\,\mu$m, of I Zw 18 has a much steeper slope, more characteristic of a typical starburst galaxy of solar abundance. The neon abundance as measured from the infrared fine-structure lines is $\sim 1/23\,Z_\odot$, and the sulfur abundance is $\sim 1/35\,Z_\odot$, generally consistent with the nebular oxygen abundance of $1/30\,Z_\odot$ derived from optical lines. This suggests that the extinction to the infrared emitting regions of this galaxy is low, also in agreement with the optical Balmer line ratios.

6.1 Introduction

Low-metallicity galaxies may have been the first sites of star formation in the early universe (White & Rees 1978; Dekel & Silk 1986). Consequently understanding their properties may provide valuable insights into the formation of the first generation of normal stars and the subsequent enrichment of the interstellar medium. However, finding truly primordial galaxies in the distant universe is beyond the

*Originally published as: Yanling Wu, V.Charmandaris, L.K. Hunt, J. Bernard-Salas, B. R.Brandl, J. A.Marshall, V. Lebouteiller, Lei Hao, J. R.Houck (2007), *The Astrophysical Journal*, 662, 952

reach of current technology. At high redshift, observational limitations introduce biases toward the detection of high-mass high-luminosity systems in which the short time-scales of massive star formation lead to the identification of systems that are already chemically enriched (i.e., Maiolino et al. 2003). An alternative approach is to identify and study unevolved galaxies in the local universe. Such a sample are the blue compact dwarf galaxies (see the review by Kunth & Östlin 2000).

Since its discovery by Zwicky (1966) and the seminal paper of Searle & Sargent (1972), I Zw 18 has been studied extensively at many wavelengths. With an oxygen abundance determined from the optical lines in HII regions of 12+log(O/H)=7.17 (Skillman & Kennicutt 1993; Izotov & Thuan 1999), or $\sim$1/30 $Z_\odot$[1], it has remained the lowest metallicity BCD for over two decades until the recent study of the western component of SBS 0335-052 (Izotov et al. 2005; Papaderos et al. 2006), which has slightly lower metallicity (12+log(O/H)=7.12). Distance estimates to I Zw 18 range from $\sim$10 Mpc (Hunter & Thronson 1995), $\sim$12.6 Mpc (Östlin 2000), and up to $\sim$15 Mpc (Izotov & Thuan 2004). Here we adopt a distance of 12.6 Mpc ($1''\sim$61 pc). I Zw 18 consists of two bright knots of star-formation, a northwest (NW) component and a southeast (SE) one, together they form the "main body" of the system. Both the NW and SE components contain numerous young star clusters, with ages ranging from 3 to 10 Myr, but the age of the underlying stellar population in I Zw 18 is still a matter of debate, with maximum ages ranging from 500 Myr to 5 Gyr (Aloisi et al. 1999; Östlin 2000; Recchi et al. 2002; Hunt et al. 2003; Izotov & Thuan 2004; Momany et al. 2005). Approximately 22″ northwest of the "main body", there is a blue irregular low surface brightness star-forming region, called the "C component", which is embedded in a common HI envelope

[1]Izotov & Thuan (1999) give 1/50 $Z_\odot$. Here, we use the new oxygen solar abundance of 12+log[O/H]=8.69 (Allende Prieto et al. 2001), which results in a metallicity of 1/30 $Z_\odot$.

(van Zee et al. 1998; Izotov & Thuan 2004).

It is well known that some BCDs are forming stars at a rate that can only be maintained for ∼1/10 of Hubble time given their store of available hydrogen. SBS 0335-052E, which has a similar metallicity (12+log[O/H]=7.31), is forming stars at a high rate in dense compact regions (Houck et al. 2004b). I Zw 18 is forming stars at a slower rate in complexes which are diffuse and extended (Hunt et al. 2005a). These differences have been attributed to different star-formation modes. SBS 0335-052E is in an "active" mode with relatively high star-formation rate (SFR) in compact dense regions, while in I Zw 18 star-formation occurs in a "passive" mode in more extended regions with a relatively low SFR (Hirashita & Hunt 2004).

In this paper, we present a detailed analysis of the infrared properties of the "main body" of I Zw 18 based on the current deepest mid-IR spectra for this galaxy, obtained using the infrared spectrograph (IRS, Houck et al. 2004a) on the Spitzer Space Telescope (Werner et al. 2004). We also discuss the results of photometric observations with IRAC (Fazio et al. 2004) and MIPS (Rieke et al. 2004) observations. We describe the observation and data analysis in §2. The Spitzer images and spectra are discussed in §3, along with the observed morphologies and abundance estimates. A discussion of the SFR of I Zw 18 is given in §4 and we summarize our conclusions in §5.

6.2 Observations

6.2.1 Spitzer/IRS Spectroscopy

I Zw 18 was observed as part of the IRS[2] Guaranteed Time Observation program on 27 March 2004 using all four instrument modules. It was re-observed on 23 April 2005 with the short-low (SL) and long-low (LL) modules with increased integration time to achieve a higher signal-to-noise ratio (SNR) over the $5-36\,\mu$m mid-IR continuum. A third even longer observation was made on 16 December 2005 with all four IRS modules. The target was acquired using the 22μm (red) peak-up camera in high-accuracy mode, and the details of the observations are presented in Table 6.1.

The data were processed at the *Spitzer* Science Center (SSC) (pipeline version 14.0). The two-dimensional image data were converted to slope images after linearization correction, subtraction of darks, and cosmic-ray removal. Finally, the data were co-added. In order to increase the SNR of the subtracted background for SL and LL, we combined the background observed in off-order and off-nod positions. A detailed explanation for this method on faint source extraction can be found in Weedman et al. (2006). After subtracting the background, the one-dimensional spectra were extracted from images with a script version of the Spectral Modeling, Analysis and Reduction Tool (SMART, ver. 6.0.4, Higdon et al. (2004)). We used tapered column extraction starting from intermediate pipeline product droop files, which only lack stray light and flat-field correction. The data from short-high (SH) and long-high (LH) droop files used the full slit extraction method from the mean of the combined images. We calibrated the flux densities by multiplying the extracted spectrum with the relative spectral response

[2]The IRS was a collaborative venture between Cornell University and Ball Aerospace Corporation funded by NASA through the Jet Propulsion Laboratory and the Ames Research Center.

Table 6.1. Spizer Observations of I Zw 18

AORKEY	Date	Instrument	On-source Time (sec)
9008640	2004-03-27	IRS (SL)	84
		IRS (LL)	120
		IRS (SH)	240
		IRS (LH)	120
4330759	2004-04-03	IRAC (3.6 μm)	120
		IRAC (4.5 μm)	120
		IRAC (5.8 μm)	120
		IRAC (8.0 μm)	120
4349184	2004-04-07	MIPS (24 μm)	48
		MIPS (70 μm)	231
		MIPS (160 μm)	42
12622848	2005-04-23	IRS (SL)	480
		IRS (LL)	240
16205568	2005-12-16	IRS (SL)	2040
		IRS (LL)	840
		IRS (SH)	2880
		IRS (LH)	1440

function (RSRF), which was created from the IRS standard stars, HR6348 for SL, HD173511 for LL and ξ Dra for SH and LH, for which accurate templates are available (Cohen et al. 2003).

6.2.2 Spitzer Imaging with IRAC and MIPS

The galaxy was imaged at 3.6, 4.5, 5.8 and 8 μm using IRAC on 3 April 2004, as well as at 24, 70 and 160 μm using MIPS on 7 April 2004 (Engelbracht et al. 2005) (PID:59) (See Table 6.1). The IRAC high dynamic range mode was used with a 4 point small cycling pattern of 30 seconds exposure time for each frame. This resulted in an on-source time of 120 seconds for each IRAC filter. The MIPS photometry mode was used in small fields with 1 cycle $\times$ 3 seconds at 24 μm and 2 cycles $\times$ 10 seconds at both 70 and 160 μm. Two offset positions ($\pm 12''$) were used to allow proper subtraction of bad pixels. The total on-source times were 48, 231 and 42 seconds for the MIPS 24, 70 and 160 μm bands. The imaging data were processed by the SSC pipeline version 14.0 and the final mosaics were obtained from the Spitzer archive.

6.3 Results

6.3.1 Mid-IR Morphology

Many ground-based and space-born instruments have been used to obtain optical/UV to near-IR data for I Zw 18 (Hunter & Thronson 1995; Aloisi et al. 1999; Östlin 2000; Cannon et al. 2002; Hunt et al. 2003; Izotov & Thuan 2004). Hunter & Thronson (1995) first resolved the "main body" of I Zw 18 into stars using the *Hubble* Space Telescope (HST). They have also detected filaments of ionized gas

up to 450 pc from the center of the galaxy. Keck II spectra revealed Hα emission as far as $\sim$1800 pc from the "main body" of I Zw 18. Izotov et al. (2001) have also shown that the equivalent widths of emission lines are large in this extended envelope. This, together with the optical and near-IR colors, suggests that ionized gas dominates the emission in the outermost regions.

In Figure 6.1 we present images of the "mainbody" of I Zw 18 in four infrared bands (3.6, 4.5, 8 and 24 μm). At 3.6 μm, where most of the light is due to the stellar photospheric emission, the morphology of I Zw 18 is very similar to that in deep near-IR imaging (Hunt et al. 2003) and broad band optical optical imaging (Izotov & Thuan 2004). The NW component is noticeably more extended and brighter than the SE one. At 8μm the components are still clearly resolved while the contrast in the brightness between the two components has decreased. In normal star forming galaxies the emission sampled by the IRAC 8 μm filter is typically dominated by dust continuum, and PAH emission when PAHs are present. Some continuum emission from the nearly Rayleigh-Jeans tail of stellar photospheric emission may also be present, even though its contribution is typically small in late type or irregular galaxies (see Smith et al. 2007). As we discuss in the following section, no PAH features are detected in the IRS spectrum of I Zw 18 down to our 1 σ $\sim$0.2 mJy sensitivity limit. To estimate the contribution of the stellar continuum to the observed 8 μm flux density we follow the approach of Jackson et al. (2006) and apply a scale factor of 0.4 in the 4.5 μm emission from the galaxy. This suggests that no more than $\sim$25% of the 8 μm flux can be attributed to the stars (Engelbracht et al. 2005). This was also to be expected given the observed steeply rising slope of the mid-IR spectrum. Therefore most of the "mainbody" emission seen in the 8μm band is due to dust continuum emission. Hence we interpret this gradual shift in brightness from the NW to the SE component to

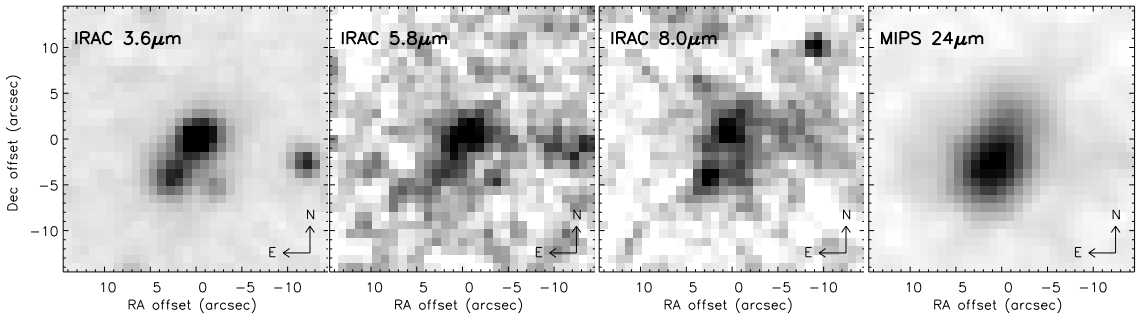

Figure 6.1 IRAC 3.6, 5.8, 8 μm and MIPS 24 μm images of I Zw 18 as observed by *Spitzer*. The galaxy is resolved into a NW and a SE component at 3.6 μm which gradually become blended to a single extended source at 24 μm. At the distance of 12.6 Mpc, 1″ corresponds to ∼61 pc. The image is centered on the optical centroid of the galaxy (α =09°34′02.0″, δ =55°14′28″). Note the change in morphology and peak of the emission as the wavelength increases.

the probable presence of more embedded star formation in the SE component which was obscured in the optical broad band imaging. Interestingly, while optical recombination line ratios give an average extinction of only $A_V \sim 0.2$ mag, there are also statistically significantly high Hα/Hβ flux ratios (∼3.4, corresponding to $A_V \sim 0.5$ mag) in the SE component (Cannon et al. 2002), suggesting the existence of an appreciable amount of dust within the galaxy. Moreover, as can be seen in Figure 6.2, there is some extended 8μm emission, though at low levels, to the west of the NW component. This emission has similar morphology as the radio continuum emission detected in the X-band and L-band by Cannon et al. (2005) and Hunt et al. (2005b), which has been attributed to low-frequency flux from a synchrotron halo.

In Figure 6.2, we show contour overlays of the 8 μm and 24 μm emission on the *HST* V-band image of the "main body" of I Zw 18. At 8 μm, the source is clearly resolved into two components. The centroids of the two components, especially the NW one, are slightly displaced from their optical counterparts. Moreover, this displacement becomes even more pronounced at longer wavelengths. At 24 μm,

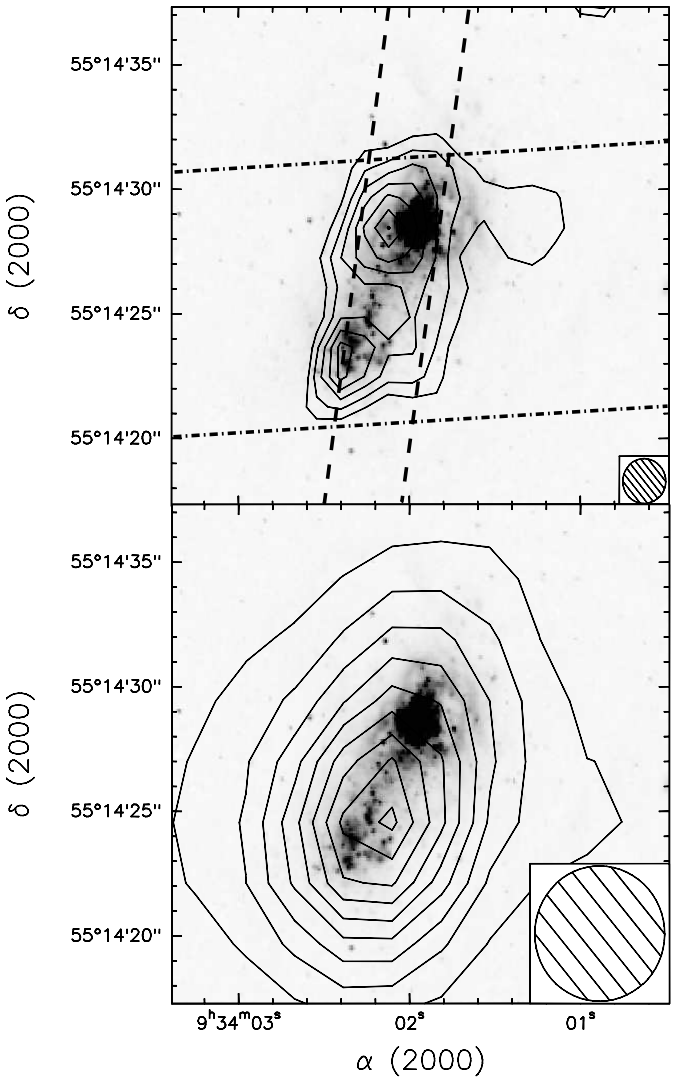

Figure 6.2 a) Top: Contour overlay of the IRAC 8 μm image on the *HST*/WFPC2 F555W image taken from the HST archive. The astrometric calibration of the HST image has been derived using stars from the U.S. Naval Observatory Astrometric Catalog B1.0, and is the same image as used in Hunt et al. (2005b). The contours range from 4σ (σ=0.03 MJy sr^{-1}) above the sky level (1.40 MJy sr^{-1}) to the peak value of 1.71 MJy sr^{-1}. The location of the IRS SL (3.6″ in width) and LL (10.5″) slits, are also indicated with the dashed and dash-dotted lines respectively. Note that due to the extent of the galaxy, and the fixed position angle of the slit, part of both the NW and SE components are not fully covered by the SL slit. The size of the PSF at 8 μm (1.8″) is also shown at the lower right of the panel. b) Bottom: the same optical image with the contours of MIPS 24 μm emission (from 4σ and above). The size of the PSF is 5.4″.

the two components are blended into a single source, the centroid of which is located slightly closer to the SE region. This displacement is real and indicates the presence of more 24 μm dust emission in the SE cluster. To confirm this change in morphology we convolved the 8 μm image to the $\sim 5.4''$ size of the 24 μm point-spread-function (PSF). Even though the resulting marginally resolved source is also elongated in the SE to NW direction, the peak emission was further to the NW than the peak of the 24μm image. This suggests an actual change in the spatial distribution of the various dust temperature components in the galaxy. In Figure 6.2, we also overlay the IRS SL/LL slit on the image of the galaxy. As one can see, since the SL slit is only $3.6''$ wide, some of the flux from both components is not properly sampled, resulting in an underestimate of the extended emission from the galaxy. However, because the spectrograph is not sensitive to the low-surface brightness emission from the areas denoted by the lowest 8 μm contours, this does not bias our analysis of the global spectral properties of the system or affects any of conclusions drawn.

6.3.2 Mid-IR Spectral Features

Figure 6.3 shows the 5.3-36 μm low-resolution spectrum of I Zw 18 as observed by the IRS. The SNR is $\sim$3 times higher than that shown by Wu et al. (2006). As we will discuss in §3.4, the global shape of the mid-IR spectrum, reveals that the IRS spectrum of I Zw 18 continues to rise steeply with wavelength from 5 μm all the way to 36 μm. This is unlike the case of SBS 0335-052E (Houck et al. 2004b), the third lowest metallicity galaxy to date, which has a nearly flat continuum peaking at $\sim$28 μm in f_ν.

The improved SNR of the new spectrum enables us to detect for the first time several mid-IR forbidden lines. Fine structure lines, such as [SIV] at 10.51 μm

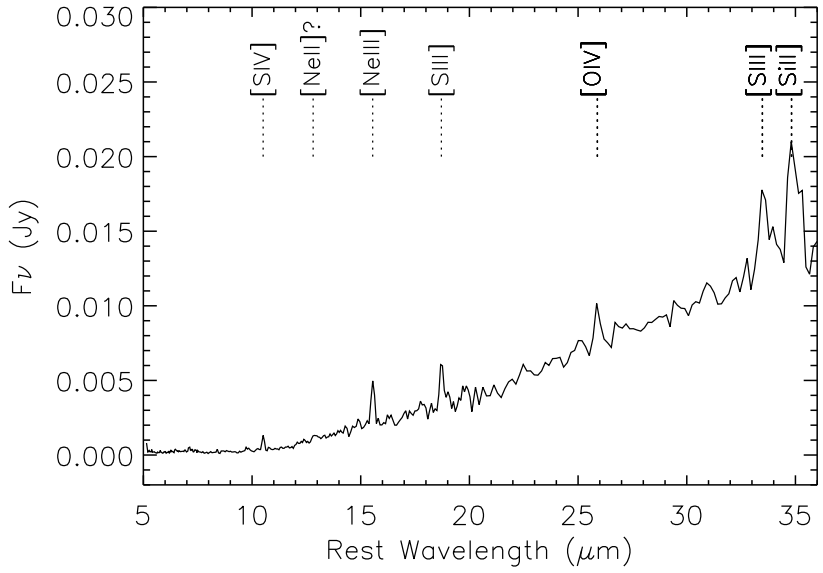

Figure 6.3 *Spitzer/IRS* 5-36 μm low-resolution spectrum of I Zw 18. No scaling factors have been applied to stitch the different orders and modules. We indicate several of the well known mid-IR fine structure emission lines, detected in the spectrum (see also Fig. 4).

and [NeIII] at 15.55 μm can clearly be seen, even in the low-resolution spectrum. Several additional forbidden lines, such as [NeII] at 12.81 μm, [SIII] at 18.71 and 33.48 μm, as well as [SiII] at 34.82 μm are identified in the high-resolution spectrum (see Figure 6.4). [OIV] at 25.89 μm and [FeII] at 25.99 μm are blended in LL, but clearly be resolved in LH. The line fluxes measured from the IRS high-resolution spectrum are reported in Table 6.2. The observed line ratio of [NeIII]/[NeII] is ~ 5 and the ratio of [SIV]/[SIII](18.71 μm) is ~ 2. This indicates that the radiation field in I Zw 18 is much harder than in a typical starburst galaxy, where [NeIII]/[NeII] is usually ≤ 1 (Brandl et al. 2006), and even harder than the majority of the BCDs observed so far (Hunt et al. 2006; Wu et al. 2006).

As was the case with SBS 0335-052E, the 5-15 μm spectrum of I Zw 18 does not show any detectable Polycyclic Aromatic Hydrocarbon (PAH) emission. Using the new mid-IR spectrum, we measure a 3σ upper limit of 3.5×10^{-22}Wcm^{-2} for the

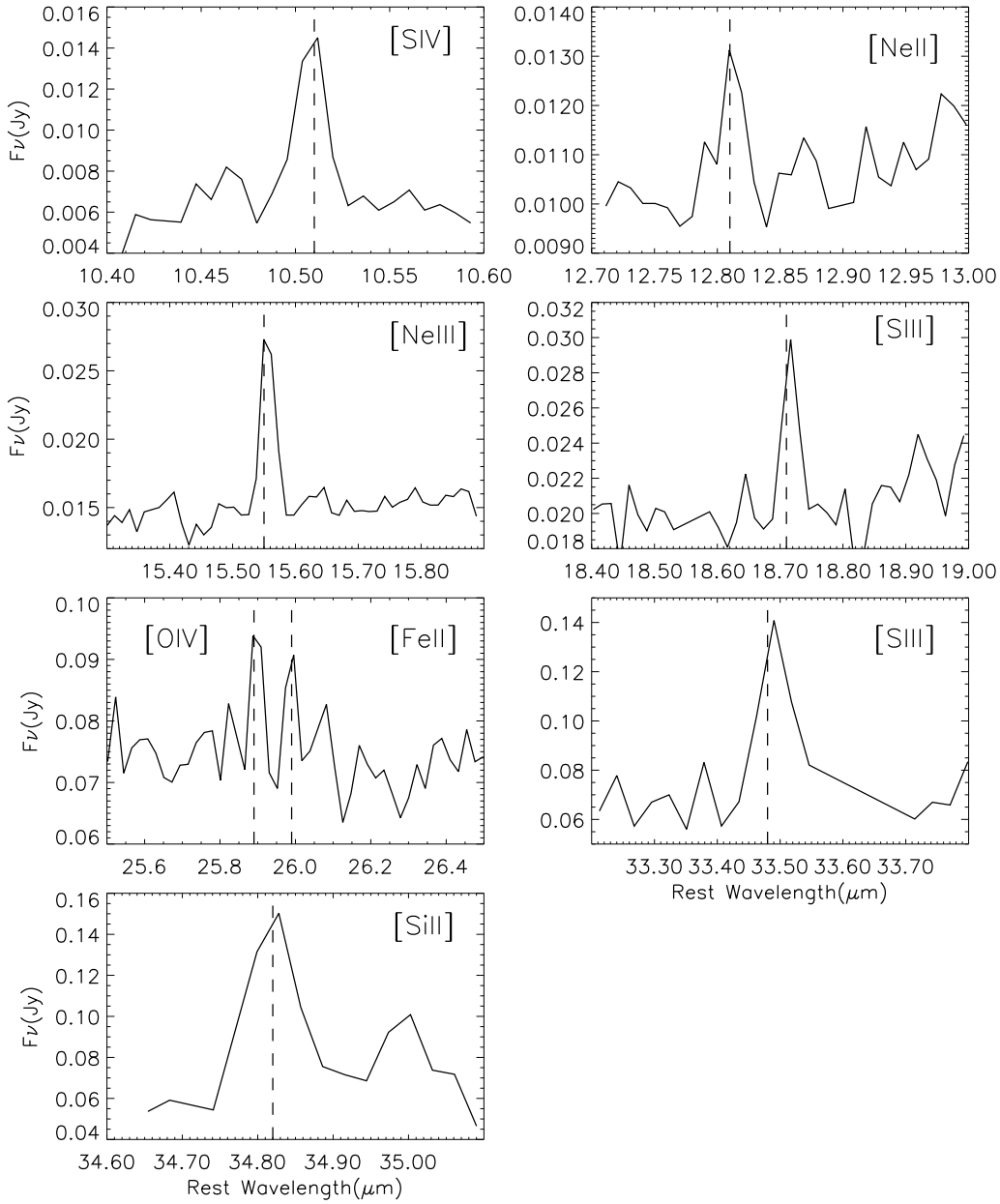

Figure 6.4 Mid-IR fine structure lines of [SIV] (10.51μm), [NeII] (12.81μm), [NeIII] (15.55μm), [SIII](18.71, 33.42μm) [OIV] (25.89μm), [FeII] (25.99μm) and [SiII] (34.82μm) from the high-resolution spectrum of I Zw 18. Note that the sky emission has not been subtracted.

Table 6.2. Fluxes and ionic abundances[a]

$\lambda_{\rm rest}$	Feature	Obs. Flux[b]	$N_{\rm ion}/N_{\rm p}$[c]
10.51	[S IV]	4.8±0.3	1.3×10^{-7}
12.81	[Ne II]	0.9±0.1	1.4×10^{-6}
15.55	[Ne III]	4.6±0.2	3.6×10^{-6}
18.71[d]	[S III]	2.3±0.2	2.8×10^{-7}
25.89	[O IV]	4.9±0.3	···
25.99	[Fe II]	3.4±0.3	···
33.48[d]	[S III]	12.0±1.2	···
34.82	[Si II]	15.8±1.8	···

[a]Only the abundances of ions used to calculate the metallicities in this work are listed in this table.

[b]In units of 10^{-15} erg cm^{-2}s^{-1}.

[c]Ionic abundance relative to hydrogen.

[d]Here we use the [S III] at 18.71 μm when calculating the sulfur abundance because this line is in the SH module and provides us a more reliable measurement as compared to the 33.48 μm line which is at the edge of the LH module and is noisy.

6.2 μm PAH feature, as well as an equivalent width (EW) of <0.23 μm. The 11.2 μm PAH emission has an upper limit of 1.3×10^{-22}Wcm^{-2} and EW of <0.12 μm. The decreasing strength of the PAH features in low metallicity environment is a current topic of interest (see Engelbracht et al. 2005; Wu et al. 2006; O'Halloran et al. 2006; Jackson et al. 2006; Madden et al. 2006; Beirão et al. 2006). The exact reason why PAHs tend to be absent in low-metallicity, high-excitation star-forming regions is not yet clear, although it almost certainly has to do with a combination of several effects, such as low carbon abundance, shock destruction of grains by supernovae, high ionization or excitation resulting from low metallicity and/or extreme radiation field intensity.

6.3.3 Neon and Sulfur Abundances

The fine-structure lines of sulfur and neon measured in the high-resolution spectrum can be used to derive the ionic abundances relative to hydrogen. To derive these abundances one needs at least one hydrogen recombination line (usually Hβ), as well as an estimate of the electron temperature (T_e) and electron density (N_e). The Hβ fluxes for I Zw 18 reported in the literature often correspond to small regions of the galaxy or of one of the two components. The IRS SH slit from which the IR lines were measured contains part of both components. We derive the Hβ flux from the thermal component of the 3.6 cm continuum (Cannon et al. 2005), which is not affected by extinction effects and encompasses the entire "main body". The SH slit includes ∼52% of the total Hβ emission and this gives an Hβ flux of 6.1×10^{-14}ergs cm^{-2}s^{-1}. The reported electron temperatures in the literature range from 18 000 to 20 000 K for O II and O III (Skillman & Kennicutt 1993; Izotov & Thuan 1999; Thuan & Izotov 2005; Shi et al. 2005), with a slightly lower value for S II (T_e ∼15 500 K). The infrared lines are less sensitive to T_e and here we

adopt an average temperature of 19 000 K. An electron density (N_e) of 100 cm^{-3} was assumed (Shi et al. 2005; Izotov & Thuan 1999). Using the above quantities and resolving the population of the levels for each ion, the ionic abundances can be derived (see Bernard Salas et al. (2001), their eq. 1).

The calculated ionic abundances are presented in Table 6.2. The elemental abundances can be obtained by adding the contribution of each ion. In the case of neon, only Ne II and Ne III are observed. The presence of O IV suggests that some Ne IV may be present. Assuming that the contribution of Ne IV is 10% of that of Ne III as has been found in some planetary nebulae (PN[3], Bernard-Salas et al. (2003)), the total neon abundance is 5.3×10^{-6}, which is 1/23 $Z_\odot$. Similarly, adding up the ionic abundance of S III and S IV, the total sulfur abundance is 4.0×10^{-7}, which is 1/35 $Z_\odot$. However, this might be a lower limit because sulfur abundance as derived from galactic planetary nebulae and HII regions is lower than the solar sulfur abundance (Pottasch & Bernard-Salas 2006; Maciel & Costa 2003), probably due to an overestimate of the solar value. Comparing directly with the ionic abundance from the optical (Izotov & Thuan 1999), our Ne III abundance is nearly twice as high while S III abundance agrees quite well. The difference in Ne III could come from the electron temperature that is used to derived the ionic abundance. The optical is more affected by the change in temperature as compared to the infrared. Lowering T_e from 19000 K to 15000 K would double the Ne III abundance derived from the 3869$\mathring{A}$ line. It is known that in some PN, the temperature obtained from the Ne III ion is lower than that from the O III (Bernard Salas et al. 2002). Another possible explanation is that there are some regions with dust obscuring the optical emission lines. Overall, the neon (1/23 $Z_\odot$) and sulfur (1/35 $Z_\odot$) abundances we derive using the infrared lines are consistent

[3]The high excitation and densities in BCDs are a closer match to PN than the typical H II regions found in normal starburst galaxies.

with the nebular oxygen abundance ($1/30\,Z_\odot$), which supports the low extinction (A_V=0.2 mag) derived from hydrogen recombination lines by Cannon et al. (2002).

6.3.4 Comparison with SBS 0335-052E and NGC7714

I Zw 18 and SBS 0335-052E share some properties but are very different in other aspects. Perhaps the most salient difference between their spectral energy distribution (SED) is the fraction of their luminosities emitted in the IR. Using the 15 μm and 30 μm flux densities of I Zw 18 and applying an empirical relation in starburst galaxies (Brandl et al. 2006), we derive $L_{IR}=1.8\times10^7\,M_\odot$. While SBS 0335-052E has $L_{IR}\sim10^9\,L_\odot$ and $L_{IR}/L_B\sim1.3$, I Zw 18 has $L_{IR}\sim10^7\,L_\odot$ and $L_{IR}/L_B\sim0.3$; the relative infrared luminosity is a factor of 4 times greater in SBS 0335-052E. Another important difference in the infrared SEDs of I Zw 18 and SBS 0335-052E is the peak wavelength of the SED. The SED of SBS 0335-052E peaks at $\sim$28 μm in f_ν space (Houck et al. 2004b), indicating very little cold dust. I Zw 18 has a clear detection of 34$\pm$2.4 mJy at 70 μm(Engelbracht et al. 2007, in preparation), and the ratio of f_{70}/f_{24} is more than a factor of 5 while the same ratio in SBS 0335-052 is less than 1. This suggests that contrary to SBS 0335-052E, which is a similarly low metallicity BCD, there is a significant amount of cold dust in I Zw 18.

We can further compare the properties of I Zw 18 with higher-luminosity and more metal-rich starbursts. In Figure 6.5, we present the spectra of I Zw 18 and SBS 0335-052E, together with a typical starburst galaxy, NGC7714 (Brandl et al. 2004), all of which have been normalized to the flux density of I Zw 18 at 22 μm. Setting aside the strong PAH emission features present in NGC7714, there is a striking similarity between the mid-IR continuum of I Zw 18 and NGC7714, although the latter has a metallicity of more than half solar. At short mid-IR wavelengths (λ <10μm), the warm dust component dominates and it does not

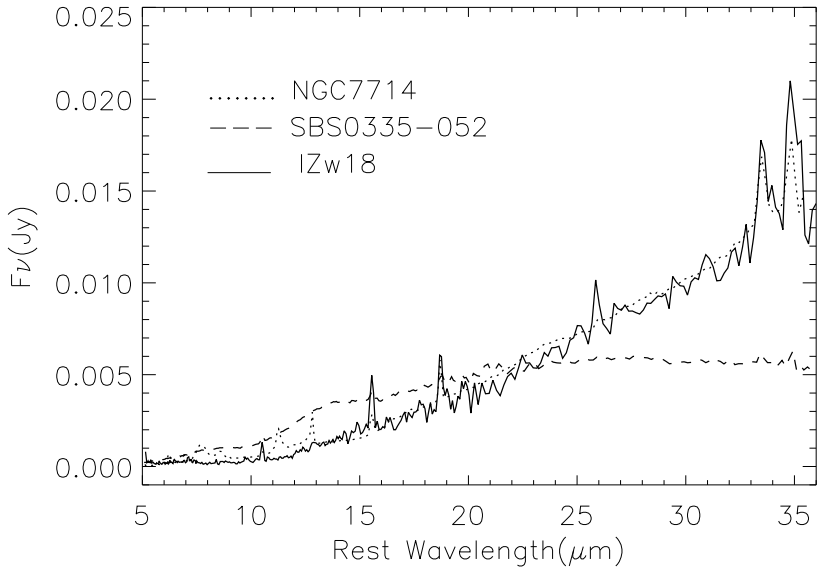

Figure 6.5 The mid-IR spectra of I Zw 18, SBS 0335-052E and NGC7714 between 5-36 μm. The spectra have been normalized to the flux density of I Zw 18 at 22 μm. SBS 0335-052E stands out as having a very flat continuum in the mid-IR, indicating there is much less cold dust in this galaxy. I Zw 18 and NGC7714 display a striking resemblance in this wavelength range.

change much even for an extended starburst galaxy (Brandl et al. 2006). At longer wavelengths, emission from larger cooler grains is dominant. After normalization at 22 μm, the 70 μm flux of I Zw 18 differs less than 20% when compared to the 70 μm flux of 9.53 Jy (Engelbracht, private communication) or the *IRAS* 60 μm flux of 11.16 Jy for NGC7714. Figure 6.5 suggests that similarly low metallicity galaxies can have both very flat or very steep spectral slope, while in the latter case, the spectral slope can be as steep as that of a typical starburst. This leads us to conclude that metallicity is not the main parameter driving the difference in the shape of the mid-IR spectral slope (Wu et al. 2006) and the infrared part of the SEDs.

Based on the new Spitzer measurements of the mid- and far-infrared emission from I Zw 18 one could in principle attempt to model the global SED of the galaxy.

Table 6.3. Star Formation Rate Estimates of I Zw 18

SFR indicator	SFR ($M_\odot yr^{-1}$)	Reference [a]
$L_{H\alpha}$ [b]	0.05	(1)
$L_{H\alpha}$ [c]	0.03	(2)
L_{TIR}	0.003	(3)
$L_{24\mu m}$	0.006	(4)
L_{IR+UV}	0.02	(5)
$L_{thermal}$	0.1	(6)
$L_{non-thermal}$	0.03	(6)

[a]References: 1) Kennicutt et al. (1994), 2) Lee et al. (2002) 3) Kennicutt (1998) 4) Wu et al. (2005) 5) Bell et al. (2005) 6) Condon (1992).

[b]Not corrected for low-metallicity effects.

[c]After correcting the low-metallicity effects.

We did explore this avenue using modelling tools such as DUSTY (Ivezić et al. 1999), but with only limited success. The complex geometry of IZw18 and the large number of free parameters in the available models prevented us from significantly constraining the physical conditions of the dust. We thus refrain from elaborating on these results until more data are available.

6.4 Star Formation Rate in I Zw 18

Deriving the star formation rate in nearby galaxies from various observational indicators and understanding the possible variations in the results is extremely useful for "predicting" the properties of high-redshift galaxy populations, where only sparse data are available. Using the available data, we calculated the SFRs of I Zw 18 from different indicators and we present our results in Table 6.3.

The SFR estimated from the Hα luminosity gives a value of $0.05\,M_{\odot}yr^{-1}$ (Kennicutt et al. 1994; Cannon et al. 2002). However, I Zw 18 has only $1/30\,Z_{\odot}$ and lower metallicities may result in a reduced SFR for a given Hα luminosity (Lee et al. 2002; Rosenberg et al. 2006). Using the metallicity correction recipe of Lee et al. (2002), the SFR would be $\sim$$0.03\,M_{\odot}yr^{-1}$.

The radio continuum emission is another important diagnostic of star-formation process and it is not affected by dust extinction effects. The thermal free-free emission is a direct indicator of SFR and it is typically only $\sim$10% of the total radio continuum at 1.4 GHz for normal galaxies (Condon 1992). However, in I Zw 18, the fraction of thermal component is three times the typical value ($\sim$30%: Hunt et al. 2005b; Cannon et al. 2005). Using the relation between radio free-free emission and SFR, we derive a SFR=$0.1\,M_{\odot}yr^{-1}$ (Hunt et al. 2005b). The non-thermal component of the radio continuum can also be used to calculate SFR and we derive a SFR of $0.03\,M_{\odot}yr^{-1}$ (Condon 1992), a factor of 3 lower than the thermally-derived SFR. This difference is a direct consequence of the unusual value of the "thermal/non-thermal" fraction in I Zw 18. This is an important caveat that should be considered when applying the standard correlations, which have been established for normal star forming galaxies, in very young low-metallicity systems.

Finally, the SFRs estimated from the infrared are significantly lower. Using the total infrared luminosity of $1.8\times10^{7}\,L_{\odot}$, we derive a SFR=$0.003\,M_{\odot}yr^{-1}$ (Kennicutt 1998), while using the 24 μm emission, we find that SFR=$0.006\,M_{\odot}yr^{-1}$ (Calzetti et al. 2005; Wu et al. 2005). This is probably because the dust content in I Zw 18 is so low while the above relations have been calibrated for sources of high optical depth, where virtually all of the UV radiation is converted to infrared luminosity. A simple calculation using the reddening curve of the Small Magellanic Cloud assuming an A_V=0.2 mag suggests that a significant amount of UV light has leaked out without

being absorbed by the dust, thus the lower SFRs estimated from the infrared are not unexpected. The readers should be aware of these complications when applying the canonical infrared relations for estimating the SFR in environments with low dust optical depth. If we were to assume that L_{IR} accounts for the bolometric luminosity of the obscured populations while L_{UV} (Kinney et al. 1993) represents the contribution of the unobscured stars, and use the eq.1 of Bell et al. (2005)[4], we find a SFR of $0.02\,M_{\odot}yr^{-1}$, more consistent with the SFRs derived using the Hα or radio luminosities.

6.5 Conclusions

We have explored the mid-IR and far-IR properties of the archetype BCD I Zw 18 based on Spitzer data:

1.Using the low-resolution modules of the IRS, we have acquired the deepest mid-IR spectrum of this galaxy obtained so far. No PAH emission is found which confirms the absence of PAHs in low metallicity systems. However, the mid- to far-IR spectral slope of I Zw 18 is surprisingly similar to NGC7714, a typical starburst galaxy with half solar metallicity. This, especially the MIPS 70 μm detection, would suggest the presence of a significant amount of cold dust in I Zw 18.

2.Variations in the morphology of the galaxy from 3.6 to 24μm imaging imply that more dust emission is present in its SE component than in the NW one. This agrees well with the results of Cannon et al. (2002).

3. The mid-IR fine-structure lines identified in the high-resolution spectrum of I Zw 18 imply a neon and sulfur abundance of 1/23 and 1/35 $Z_{\odot}$ respectively, consistent with the optically derived oxygen abundance of $1/30\,Z_{\odot}$.

4. Estimates of the star formation rates calculated from different indicators

[4]SFR=9.8×10^{-11} (L_{IR}+2.2 L_{UV})

show considerable scatter. L_{IR} and $L_{24\mu m}$ give lower SFRs when compared with results using Hα or $L_{1.4GHz}$, probably because the low dust content in this galaxy can only convert a small fraction of the UV radiation emitted by stars into L_{IR}. This should be considered when interpreting star formation rates derived for high-redshift low metallicity galaxies.

Acknowledgments We thank Chad Engelbracht for graciously providing the IRAC and MIPS photometric measurements for our source before publishing the data. We also thank Rob Kennicutt for insightful discussions. We thank the anonymous referee, whose careful reading and detailed comments greatly improved this manuscript. Support for this work was provided by NASA through Contract Number 1257184 issued by JPL/Caltech.

BIBLIOGRAPHY

Allende Prieto, C., Lambert, D. L., & Asplund, M. 2001, ApJ, 556, L63

Aloisi, A., Tosi, M., & Greggio, L. 1999, AJ, 118, 302

Anders, E. & Grevesse, N. 1989, Geochim. Cosmochim. Acta, 53, 197

Beirão, P., Brandl, B. R., Devost, D., Smith, J. D., Hao, L., & Houck, J. R. 2006, ApJ, 643, L1

Bell, E. F., et al. 2005, ApJ, 625, 23

Bernard Salas, J., Pottasch, S. R., Feibelman, W. A., & Wesselius, P. R. 2002, A&A, 387, 301

Bernard Salas, J., Pottasch, S. R., Beintema, D. A., & Wesselius, P. R. 2001, A&A, 367, 949

Bernard-Salas, J., Pottasch, S. R., Wesselius, P. R., & Feibelman, W. A. 2003, A&A, 406, 165

Brandl, B. R., et al. 2004, ApJS, 154, 188

Brandl, B. R., et al. 2006, ApJ, 653, 1129

Calzetti, D., et al. 2005, ApJ, 633, 871

Cannon, J. M., Skillman, E. D., Garnett, D. R., & Dufour, R. J. 2002, ApJ, 565, 931

Cannon, J. M., Walter, F., Skillman, E. D., & van Zee, L. 2005, ApJ, 621, L21

Cohen, M., Megeath, T.G., Hammersley, P.L., Martin-Luis, F., & Stauffer, J. 2003, AJ, 125, 2645

Condon, J. J. 1992, ARA&A, 30, 575

Dekel, A., & Silk, J. 1986, ApJ, 303, 39

Devereux, N. A., & Eales, S. A. 1989, ApJ, 340, 708

Engelbracht, C. W., Gordon, K. D., Rieke, G. H., Werner, M. W., Dale, D. A., & Latter, W. B. 2005, ApJ, 628, L29

Fazio, G. G., et al. 2004, ApJS, 154, 10

Higdon, S. J. U., et al. 2004, PASP, 116, 975

Hirashita, H., & Hunt, L. K. 2004, A&A, 421, 555

Hopkins, A. M., Schulte-Ladbeck, R. E., & Drozdovsky, I. O. 2002, AJ, 124, 862

Houck, J. R., et al., 2004, ApJS, 154, 18

Houck, J. R., et al., 2004, ApJS, 154, 211

Hunt, L. K., Thuan, T. X., & Izotov, Y. I. 2003, ApJ, 588, 281

Hunt, L., Bianchi, S., & Maiolino, R. 2005a, A&A, 434, 849

Hunt, L. K., Dyer, K. K., & Thuan, T. X. 2005b, A&A, 436, 837

Hunt,L. K., Thuan, T. X., Sauvage, M., Izotov, Y. I., 2006, ApJ, 653, 222

Hunter, D. A., & Thronson, H. A., Jr. 1995, ApJ, 452, 238

Ivezić, Z., Nenkova, M., & Elitzur,M. 1999, User Manual for *DUSTY*, University of Kentucky Internal Report,accessible at `http://www.pa.uky.edu/ moshe/dusty`

Izotov, Y. I., Foltz, C. B., Green, R. F., Guseva, N. G., & Thuan, T. X. 1997, ApJ, 487, L37

Izotov, Y. I. & Thuan, T. X. 1999, ApJ, 511, 639

Izotov, Y. I., Chaffee, F. H., Foltz, C. B., Thuan, T. X., Green, R. F., Papaderos, P., Fricke, K. J., & Guseva, N. G. 2001, ApJ, 560, 222

Izotov, Y. I., & Thuan, T. X. 2004, ApJ, 616, 768

Izotov, Y. I., Thuan, T. X., & Guseva, N. G. 2005, ApJ, 632, 210

Jackson, D. C., Cannon, J. M., Skillman, E. D., Lee, H., Gehrz, R. D., Woodward, C. E., & Polomski, E. 2006, ApJ, 646, 192

Kennicutt, R. C., Jr. 1998, ARA&A, 36, 189

Kennicutt, R. C., Jr., Tamblyn, P., & Congdon, C. E. 1994, ApJ, 435, 22

Kinney, A. L., Bohlin, R. C., Calzetti, D., Panagia, N., & Wyse, R. F. G. 1993, ApJS, 86, 5

Klein, U., Weiland, H., & Brinks, E. 1991, A&A, 246, 323

Kunth, D. & Östlin, G. 2000, A&A Rev., 10, 1

Lee, J. C., Salzer, J. J., Impey, C., Thuan, T. X., & Gronwall, C. 2002, AJ, 124, 3088

Maciel, W. J., & Costa, R. D. D. 2003, IAU Symposium, 209, 551

Madden, S. C., Galliano, F., Jones, A. P., & Sauvage, M. 2006, A&A, 446, 877

Maiolino, R., Juarez, Y., Mujica, R., Nagar, N. M., & Oliva, E. 2003, ApJ, 596, L155

Momany, Y., et al. 2005, A&A, 439, 111

Östlin, G. 2000, ApJ, 535, L99

O'Halloran, B., Satyapal, S., & Dudik, R. P. 2006, ApJ, 641, 795

Papaderos, P., Izotov, Y. I., Guseva, N. G., Thuan, T. X., & Fricke, K. J. 2006, A&A, 454, 119

Pottasch, S. R., & Bernard-Salas, J. 2006, A&A, 457, 189

Recchi, S., Matteucci, F., D'Ercole, A., & Tosi, M. 2002, A&A, 384, 799

Rieke, G. H., et al. 2004, ApJS, 154, 25

Rosenberg, J. L., Ashby, M. L. N., Salzer, J. J., & Huang, J.-S. 2006, ApJ, 636, 742

Searle, L. & Sargent, W. L. W. 1972, ApJ, 173, 25

Shi, F., Kong, X., Li, C., & Cheng, F. Z. 2005, A&A, 437, 849

Skillman, E. D., & Kennicutt, R. C., Jr. 1993, ApJ, 411, 655

Smith, J.D. T., et al. 2007, ApJ, 656, 770

Thuan, T. X., & Izotov, Y. I. 2005, ApJS, 161, 240

van Zee, L., Westpfahl, D., Haynes, M. P., & Salzer, J. J. 1998, AJ, 115, 1000

Weedman, D. W., Le Floc'h, E., Higdon, S. J. U., Higdon, J. L., & Houck, J. R. 2006, ApJ, 638, 613

Werner, M., et al. 2004, ApJS, 154, 1

White, S. D. M., & Rees, M. J. 1978, MNRAS, 183, 341

Wu, H., Cao, C., Hao, C.-N., Liu, F.-S., Wang, J.-L., Xia, X.-Y., Deng, Z.-G., & Young, C. K.-S. 2005, ApJ, 632, L79

Wu, Y., Charmandaris, V., Hao, L., Brandl, B. R., Bernard-Salas, J., Spoon, H. W. W., & Houck, J. R. 2006, ApJ, 639, 157

Zwicky, F. 1966, ApJ, 143, 192

CHAPTER 7

CONCLUSIONS AND FUTURE WORK

The research presented in this thesis is aimed at understanding the general physics of low metallicity star-forming galaxies, the blue compact dwarfs. This is for the first time, a large sample of BCDs can be studied systematically in the infrared, inspecting their properties in many different aspects, thanks to the unprecedented sensitivity of the *Spitzer* Space Telescope.

The Polycyclic Aromatic Hydrocarben emission in BCDs

The superb sensitivity of the IRS on board *Spitzer* has provided us a wonderful tool to investigate the PAH features in low-metallicity environment. PAHs have been found ubiquitously in many types of objects, such as galactic HII regions, reflection nebular, star-forming galaxies, etc. PAH emission is prominent in starburst galaxies, however, it is missing in the extremely metal poor BCDs, SBS0335-052E and IZw18. Whether the absence of PAH molecules in metal-poor environment is due to a deficit of carbon atoms, the intensive UV radiation field, or some other effects, is still not proven. We obtained high quality $5-36\,\mu$m low-resolution spectra for 12 BCDs using IRS, and measured the equivalent widths (EWs) of PAH features at 6.2, 7.7, 8.6 and $11.2\,\mu$m, which later were used to correlate with several physical parameters of the galaxies. We found that the strength of the PAH emission varies in the environment of BCDs and is best represented by a combination of formation (characterized by metallicity) and destruction (described by the hardness and the intensity of the interstellar radiation field) effects (Wu et al. 2006).

Elemental Abundance Determination with the IRS

As we have mentioned in the introduction chapter, even though BCDs are defined based on their morphological properties, the majority of them are found

to have low, sub-solar metallicities. Since the low elemental abundances are an important charactersitics of BCDs, an accurate determination of abundances is critical for studying these objects. The infrared fine structure lines can be used to derive the elemental abundances. The infrared observations are much less affected by extinction effects, thus allowing us to probe the dust enshrouded regions in galaxies. The fine-structure lines are also less sensitive to the uncertainties in the electron temperatures as compared to the optical. The most important ionization stages of neon and sulfur are available in the infrared, thus avoids the need of ionization correction factors. For the 13 BCDs we studied using IRS high-resolution spectroscopy, the neon and sulfur abundances correlate very well with each other. Overall, the infrared and optical derived elemental abundances also agree well, though neon is slightly higher than the optical values (Wu et al. 2008a). This indicates that either the metallicities of the dust enshrouded region are similar to the optically accessible regions, or that if they are different they do not contribute substantially to the total infrared emission of the host galaxy.

IR/radio Correlation in Low luminosity Galaxies

The FIR/radio correlation is well-known to be ubiquitous among late type star forming galaxies as revealed by the *IRAS* mission (Helou et al. 1985; Condon 1992). However, little could been done for low luminosity systems (Hopkins et al. 2002). Recently, a number of deep *Spitzer* mid-IR and FIR surveys can now probe a population of galaxies with low infrared luminosities, for which ancillary data including deep radio imaging are becoming available. We have compiled a sample of 28 low luminosity star forming dwarf galaxies and studied the IR/radio correlation in these sources (Wu et al. 2008b). We found that BCDs follow the same mid-IR/radio and FIR/radio correlation typical of normal galaxies, though the scatter in the ratio of $\log(f_{24}/f_{1.4GHz})$ is significantly higher than the dispersion

in the FIR/radio correlation, which we attribute to the higher intrinsic variation in the 15∼30 μm SEDs of dwarf galaxies. Moreover, the star formation rates (SFRs) estimated from the radio and mid-IR data are in good agreement. This indicates that in these low metallicity systems, the competition of the lower dust content and the suppressed synchrotron emission balance each other and results in underestimating the SFRs by similar factors (Bell 2003).

Future Work

Using *Spitzer* observations, we have found that the strength of PAH emission varies subtantially in metal-poor environment, and it is probably due to a combination of formation and destruction effects, however, the exact constraints on these parameters are not clear yet due to the limited amount of data available in the early of the *Spitzer* mission. Now a much larger sample of low-metallicity star-forming galaxies have been observed by *Spitzer* in the past five years, and in addition to that, data on individual HII regions in star-forming galaxies have been collected or being collected from *Spitzer* Legacy surveys, such as the SING and LVL. This will allow us to investigate and quantify the impact of different physical parameters, thus leading to a better understanding to the abundance of PAH features in metal-poor galaxies.

Another problem that still remains unsolved is what triggers the star formation in BCDs. An intriguing explanation is the galaxy merging scenario. An interaction with another galaxy or HI cloud ignites the star formation in one BCD, which is the one that have been captured by us now, while the other companion still remains quiescent. This has been suggested for SBS03350-052, of which the eastern component is strongly forming stars, while the western component is extremely faint and only become detectable recently with deep optical spectroscopy. While (**?**) have suggested that the majority, perhaps as many as 80% or more of the BCDs

are involved in interactions, only a small fraction of them display clear tidal tails and other obvious distortions characteristics of larger scale mergers. I suggest taht identifying companions of BCDs via deep imaging and calculating the correlation function may provide an answer to the merger hypothesis for the star formation in BCDs.

In the next few years, several new instruments will be launched. The HERSCHEL Space Telescope is scheduled to fly in sping 2008, which will extend our capability of obtaining IR spectrsocopy to the far-infrared wavelengths. The James Webb Space Telescope will be launched in 2013, providing better sensitivity as well as better spatial resolution in the mid-infrared. A new era for studying the BCDs in the infrared is yet to come !

BIBLIOGRAPHY

Bell, E. F. 2003, ApJ, 586, 794

Condon, J. J. 1992, ARA&A, 30, 575

Helou, G., Soifer, B. T., & Rowan-Robinson, M. 1985, ApJ, 298, L7

Hopkins, A. M., Schulte-Ladbeck, R. E., & Drozdovsky, I. O. 2002, AJ, 124, 862

Wu, Y., Charmandaris, V., Hao, L., Brandl, B. R., Bernard-Salas, J., Spoon, H. W. W., & Houck, J. R. 2006, ApJ, 639, 157

Wu, Y., Bernard-Salas, J., Charmandaris, V., Lebouteiller, V., Hao, L., Brandl, B. R., & Houck, J. R. 2008, ApJ, 673, 193

Wu, Y., Charmandaris, V., Houck, J. R., Bernard-Salas, J., Lebouteiller, V., Brandl, B. R., & Farrah, D. 2008, ApJ, 676, 970